

# STRESS-ENHANCED FERROELECTRIC MATERIALS AND STRUCTURES

## Final Report

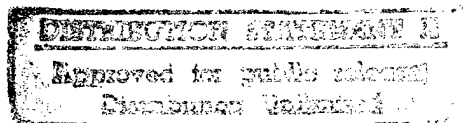
Period: June 1, 1996 to June 14, 1997

## OFFICE OF NAVAL RESEARCH

Grant No. N00014-94-1-0563

Principal Investigator: Gene Haertling  
Co-Investigator: Eugene Furman  
Guang Li

Supporting Investigators: Bret Barron  
Youngwoo Moon  
William Paradise  
David Dausch



July 9, 1997



The Gilbert C. Robinson  
Department of Ceramic Engineering

College of Engineering

## REPORT DOCUMENTATION PAGE

FORM APPROVED  
OMB No. 0704-0188

Public reporting burden for this collection of information is estimated to average 1 hour per response, including the time for reviewing instructions, searching existing data sources, gathering and maintaining the data needed and completing and reviewing the collection of information. Send comments regarding this burden estimate or any other aspect of the collection of information, including suggestions for reducing the burden to Washington Headquarters Services, Directorate for Information Operations and Reports, 1215 Jefferson Davis Highway, Suite 1204, Arlington, VA 22202-4302 and to the Office of Management and Budget, Paperwork Reduction Project (0704-0188), Washington, DC 20503

1. AGENCY USE ONLY (Leave blank)	2. REPORT DATE 9 July 97	3. REPORT TYPE AND DATES COVERED Final: 1 June 96-14 June 97	
4. TITLE AND SUBTITLE OF REPORT Stress-Enhanced Ferroelectric Materials and Structures		5. FUNDING NUMBERS N00014-94-1-0563	
6. AUTHOR(S) G. Haertling, E. Furman, Guang Li, B. Barron, Y. Moon, W. Paradise and D. Dausch			
7. PERFORMING ORGANIZATION NAME(S) AND ADDRESS(ES) Clemson University Clemson, SC 29634-0907		8. PERFORMING ORGANIZATION REPORT NUMBER:	
9. SPONSORING/MONITORING AGENCY NAME(S) AND ADDRESS(ES) Office of Naval Research Arlington, VA 22217-5660		10. SPONSORING/MONITORING AGENCY REPORT NUMBER:	
11. SUPPLEMENTARY NOTES:			
12a. DISTRIBUTION AVAILABILITY STATEMENT No restrictions		12b. DISTRIBUTION CODE	
13. ABSTRACT (Maximum 200 words) <p>This report details work performed in the Ceramic Engineering Department of Clemson University over the period from June 1, 1996 to June 14, 1997. The work described in this report covers the final year of a three-year program involving stress-enhanced ferroelectric materials and structures. It is presented in ten parts dealing with Rainbows, Cerambows and electrooptic and ferroelectric thin films, processing, characterization and published work. The Rainbow and Cerambow actuator technologies are relatively recent materials developments involving new processing techniques for preparing pre-stressed piezoelectric and electrostrictive ceramic materials for high displacement actuators. During this period, PLZT Rainbow and Cerambows were characterized with respect to (1) the formation of their distinctive curvature, (2) the grain size dependence of their nonlinear properties, (3) nonlinear piezoelectric behavior, (4) electrostrictive butterfly loops and (5) vibration control and noise suppression applications. Studies of the effect of intelligent processing and externally applied stress on the properties of electrooptic thin films were finalized this period. Properties such as dielectric constant, remanent polarization, coercive field and optical birefringence were found to be highly dependent upon the magnitude and sign (tensile or compressive) of the stress.</p>			
14. SUBJECT TERMS Ferroelectrics, Rainbows, Cerambows, Thin Films, Piezoelectric actuators		15. NUMBER OF PAGES: 288	
		16. PRICE CODE	
17. SECURITY CLASSIFICATION OF REPORT: Unclassified	18. SECURITY CLASSIFICATION OF THIS PAGE Unclassified	19. SECURITY CLASSIFICATION OF ABSTRACT Unclassified	20. LIMITATION OF ABSTRACT UL

# **STRESS-ENHANCED FERROELECTRIC MATERIALS AND STRUCTURES**

## **Final Report**

Period: June 1, 1996 to June 14, 1997

## **OFFICE OF NAVAL RESEARCH**

Grant No. N00014-94-1-0563

Principal Investigator: Gene Haertling  
Co-Investigator: Eugene Furman  
Guang Li

Supporting Investigators: Bret Barron  
Youngwoo Moon  
William Paradise  
David Dausch

July 9, 1997

---

---

19970808 060

---

---



The Gilbert C. Robinson  
Department of Ceramic Engineering

College of Engineering

## **Table of Contents**

Introduction .....	Summary
Part I. ....	Investigation of Curvature Formation in Rainbow Ceramics
Part II. ....	Effect of Grain Size on the Nonlinear Dielectric Properties of PLZT
Part III. ....	Characterization of Nonlinear Piezoelectric Behavior of Rainbows
Part IV. ....	Quantitative Characterization of Electrostrictive Butterfly Loops
Part V. ....	Characterization of Rainbow Ceramics for Active Vibration Control
Part VI. ....	Stress Effects in Cerambow Actuators
Part VII. ....	Voltage-Induced Displacement Properties of Cerambow Actuators
Part VIII. ....	Intelligent Processing and Stressing of Electrooptic Thin Films
Part IX. ....	Effects of Rapid Photothermal Annealing of PLZT
Part X. ....	Publications



## Introduction

This report details work performed in the Ceramic Engineering Department of Clemson University over the period from June 1, 1996 to June 14, 1997 under Grant No. N00014-94-1-0563. The work described in this report covers the final year of a three-year program involving stress-enhanced ferroelectric materials and structures. It is presented in ten parts dealing with Rainbows, Cerambows and electrooptic and ferroelectric thin films, processing, characterization and published work.

The Rainbow actuator technology is a relatively new materials development which had its beginning in 1992. It involves a new processing technique for preparing pre-stressed, high lead containing piezoelectric and electrostrictive ceramic materials. Ceramics fabricated by this method produce bending-mode actuator devices which possess several times more displacement and load bearing capacity than present-day benders; i.e., unimorphs and bimorphs. Since they can also be used in sensor applications, Rainbows are part of the family of materials known as smart ceramics. During this period, PLZT Rainbow ceramics were characterized with respect to (1) the formation of their distinctive curvature, (2) the grain size dependence of their nonlinear properties, (3) nonlinear piezoelectric behavior, (4) electrostrictive butterfly loops and (5) vibration control and noise suppression applications.

The Cerambow development essentially comprises a pre-stressed structural composite for actuators and sensors consisting of a ferroelectric, piezoelectric, antiferroelectric or electrostrictive materials and a metal or plastic substrate suitably bonded to one of the major surfaces such that the thermal expansion/contraction mismatch between the ceramic and substrate produces an internal stress which acts to amplify electromechanical displacement and to increase its load-bearing capability. Termed a Cerambow (CERAMic Biased Oxide Wafer), this composite actuator structure is fabricated by bonding together a ceramic wafer and a substrate at an elevated temperature of approximately 250 to 300°C and allowed to cool to room temperature. The resulting internal stresses produced from the thermal contraction mismatch and any domain reorientation effects act to deform the originally planar wafer into a dome or curved structure which is similar in characteristics and operation to a Rainbow device. Like a Rainbow, this pre-stressed composite has amplified displacement and greater than normal load bearing capability. Results on the characterization of Cerambows and their comparison to Rainbows as actuators are included in this report. In general, the Cerambow has proven to be a viable strain-amplification device for piezoelectric applications, producing displacements of approximately 75% of Rainbow elements of similar dimensions.

Studies of the effect of intelligent processing and externally applied stress on the properties of electrooptic thin films were finalized this period. Properties such as dielectric constant, remanent polarization, coercive field and optical birefringence were found to be highly dependent upon the magnitude and sign (tensile or compressive) of the stress. Improvements of varying degrees were observed in the properties of films processed via rapid photothermal annealing.

**Part I.**

**Investigation of Curvature Formation in Rainbow Ceramics**

Submitted by :

Guang Li  
Gene Haertling

# **Investigation of Curvature Formation in Rainbow Ceramics**

## **1. Introduction**

Recent studies of the Rainbow ceramic have demonstrated that this new device possesses great potential for stress sensing and actuation applications [1-4]. Many of the peculiar features and properties of Rainbow ceramics have been found to be closely related to the unique technique of the Rainbow process which involves local chemical reduction of a high-lead-containing piezoelectric or electrostrictive ceramic wafer at an elevated temperature. Such a process leads to a dome-shaped structure when the Rainbow is cooled to room temperature. A large physical displacement can be produced in the axial direction of a Rainbow when a voltage is applied across its unreduced layer. Because of the dome shape and the accompanying internal stress, Rainbows are capable of sustaining a load or pressure much larger than normal. Furthermore, when made from a piezoelectric composition, these devices can also be utilized for detection and measurement of external stresses or forces. Stress-sensing sensitivities of over two orders of magnitude greater than the unreduced ceramic of the same composition have been obtained from the Rainbows operated in the dome mode [5].

Generally, the occurrence of the dome curvature for a Rainbow can be regarded as a consequence of the dimensional mismatch between the unreduced and reduced layers created during the chemical reduction process, although detailed mechanisms are much more complex. Three major contributors to the curvature onset have been proposed in the previous investigations. They are: (1) volume change in the reduced region imposed by the reduction process, (2) difference in thermal expansion coefficients of the unreduced and reduced layers,

and (3) dimensional change caused by the phase transition at the Curie temperature. The extent of the curvature of a Rainbow can be simply represented by its dome height which is measured as the height of the domed structure relative to the edge. The magnitude of the dome height for a given Rainbow sample is dependent on the original oxide composition, sample dimensions and the ratio of the reduced thickness to the total thickness (thickness ratio).

The mechanisms mentioned above for the curvature formation were derived on the basis of the experimental observations of the curvature development during the Rainbow processing. No quantitative evaluations have yet been carried out as for the relative magnitude of each contribution and the influence of sample composition and reduction conditions on it. In addition, possible effects on the curvature formation of high-temperature creep occurring during the reduction process has not been considered. Given the high internal stress deduced from the magnitude of the curvature, creep may have a marked impact on the curvature development. Moreover, in a few unusual cases, a spontaneous reversal of the curvature from a positive value (reduced side concave), which is normally seen for a ferroelectric composition, to a negative value was observed. It is worthwhile mentioning that the curvature for an antiferroelectric composition usually exhibits a negative value [4].

The current work was aimed to achieve a more thorough understanding of some of the issues relevant to the formation and change of the domed structure of the Rainbow ceramic. These issues are concerned with the effect of high-temperature creep, the relative magnitude of each mechanism for the curvature formation, and the spontaneous curvature reversal.

## **2. Sample Preparation**

A number of compositions from the PLZT systems were chosen, which include PLZT 1.0/53/47, 5.5/56/44, and 9.5/65/35. Conventional mixed-oxide processing techniques were employed to prepare the sample powders, which were sintered in an oxygen atmosphere or by hot-pressing. Details of the preparation procedure were reported elsewhere [1]. The sintered sample slugs were sliced into wafers or strips of different dimensions. The ceramic wafers were then chemically reduced to obtain the Rainbow samples via the standard Rainbow processing route. Some of the samples were fully reduced for the determination of creep characteristics in the reduced layer. Commercial PZT-based ceramics were also used to produce some of the specimens.

### **3. Experimental Results and Discussion**

#### ***3.1 Effect of High-Temperature Creep on Rainbow Curvature***

In order to assess the possible influence of high-temperature creep on the evolution of Rainbow's domed structure, creep characteristics of both unreduced and fully reduced samples were examined and analyzed. Strip-shaped samples with dimensions of 25×5×0.5 mm were tailored from the unreduced and fully reduced wafers. These samples were placed across two zirconia setters on a refractory plate with a separation of 20 mm, as is depicted schematically in Figure 1. The assembly was introduced into a furnace and the samples were thermally treated under the same conditions as those used in the Rainbow processing (e.g., 975°C for 60-120 minutes). For the fully reduced samples an inert atmosphere with flowing argon gas was maintained to minimize the reoxidation that otherwise would completely reoxidize the sample if testing were carried out in air. This thermal treatment lead to a permanent bending deformation

of the samples as a result of the high-temperature creep driven by the sample's self-weight. In some test cases, an alumina ball of 5.5 grams was placed on the samples, as shown in Figure 1(b), to enhance the creep process. After cooling down to room temperature, the bending deflection in the middle of a sample was measured on a setup equipped with an LVDT.

Table 1 displays the data of creep-induced bending deflection divided by the thickness of the sample. Without external loading the bending deflection was only a few percent of the thickness for all the unreduced samples tested. The deflection value for PLZT 5.5/56/44 was approximately twice as large as those for PLZT 1.0/53/47 and PLZT 9.5/65/35. Dramatic increase in the bending occurred when a load of merely 5.5 grams was applied to the samples during test. In this case, the bending deflection for sample PLZT 5.5/56/44 was found to be more than three times of its thickness. Meanwhile, the difference in the deflection magnitude between PLZT 5.5/56/44 and the other two compositions became much more appreciable. It is clear from these results that the unreduced PLZT 5.5/56/44 has a much stronger creep effect than PLZT 1.0/53/47 and PLZT 9.5/65/35. The creep characteristics for the fully reduced samples, however, were very similar regardless of the original PLZT compositions, as is clearly shown in the table. This is not surprising since the microstructure and composition in the reduced samples, as indicated in our previous work, are very similar for a wide range of PLZT compositions. Table 1 also shows the dependence of the creep-generated bending deflection with temperature. An accelerated increase of creep with increasing temperature was observed.

Generally speaking, the high-temperature creep in the PLZT oxide layer of a Rainbow tends to undermine the Rainbow's curvature by adapting a shape that effectively releases the dimensional mismatch between the unreduced and the reduced regions and consequently reduce the internal stress. The same process is also expected to happen in the reduced layer which

should be more pronounced since the reduced layer contains a great deal of metallic lead phase. On quite contrary to these expectations, experiments showed that the Rainbow samples made of PLZT 5.5/56/44, which has a much stronger creep effect suggested in the above analyses, exhibited a larger dome curvature than those Rainbow samples produced from PLZT 1.0/53/47 and PLZT 9.5/65/35. In addition, no noticeable influence of creep in the reduced layer on the curvature could be deduced from these experiments.

To further explore any effect of high-temperature creep on the curvature development, the reduced layer of several Rainbow samples made from these compositions was carefully removed using sandpaper, and the curvature of the remaining oxide layer was determined. It was found that for samples made from compositions 5.5/53/47 and 9.5/65/35 the oxide layers straightened out almost completely to its original flat state after removal of the reduced region, while for composition 1.0/53/47 a small curvature was retained on the oxide layer. The latter was considered to result from the preferential domain alignment created by the initial internal stress, which has been confirmed by the fact that the retained curvature disappeared after heating the sample slightly over its Curie point. This result appears to further suggest that no significant effect of creep was present during the Rainbow process.

The unexpectedly insignificant influence of creep on the curvature formation seems difficult to perceive considering the high levels of the internal stress. A possible explanation may be related to the fact that the Rainbow process involves dynamic creep behavior which probably can not be interpreted solely on the basis of the steady state creep characteristics. A better understanding of this phenomenon apparently demands further experimental efforts.

### *3.2 Development of Domed Configuration during Rainbow Processing*

An investigation of the evolution of the dome-shaped configuration in Rainbow ceramics should be of help to understand the reduction kinetics involved as well as to obtain deep insights into the mechanisms responsible for the curvature occurrence. To this end, the curvature of Rainbow samples with different compositions was monitored during the cool down step and their dome height was determined *in situ* with the help of a setup depicted schematically in Figure 2. In this experiment, a sample wafer was reduced at an elevated temperature for 1-3 hours via the standard process procedure. The sample together with the graphite block and the protecting zirconia disk was pulled out of the furnace and placed on a refractory brick. A thermocouple was immediately inserted into the carbon block through a hole in another zirconia disk next to the Rainbow sample. Two alumina rods that each terminated with a dial micrometer were positioned to the respective zirconia disks on the carbon block. This arrangement was designed to ensure that the recorded temperature closely represents the actual temperature on the Rainbow sample being measured. The change of the dome height with temperature during cooling was determined from the difference in the readings of the two micrometers. In a similar setup, two samples with different compositions were chemically reduced on the same carbon block and a series of pictures were taken as the sample temperature dropped.

Figure 3 shows the variation of the dome height with temperature during the cool down step for a number of Rainbow samples having different compositions. The designations for RB1053HP and RB1053S denote Rainbow samples made from wafers prepared by hot-pressing and sintering routes, respectively. The main difference between them is that the hot-pressed wafers have a higher density (close to the theoretical density) than that of the sintered wafers (about 96% the theoretical). As shown in Figure 3, the RB1053S sample showed no noticeable curvature at the reduction temperature and remained fairly flat until a temperature close to the



Curie point, which was approximately 350°C for this composition, was reached. Significant curvature began to develop as the sample underwent a phase transition. The curvature continued to grow gradually as the sample temperature steadily dropped to room temperature. A very similar behavior was observed for sample RB1053HP, except in this case that a small curvature was already present before cooling.

Unlike composition 1.0/53/47, RB5556S and RB9565S showed a significant curvature before the cool down process. There were only slight changes in the dome height as these samples cooled down to room temperature. The relatively sudden increase of the dome height for RB5556S at around 200°C was attributed to the paraelectric to ferroelectric phase transition. No such change, however, was observed for RB9565S because of the relaxor nature of this composition which leads to a diffuse phase transition. Using the results in Figure 3, the relative contributions of three mechanisms mentioned in the Introduction can be estimated quantitatively. Taking RB1053HP as an example, the data were replotted in Figure 4, with two dashed lines drawn across the figure to make intercepts at the vertical axis. Of these two lines, the horizontal one indicates the portion of the dome height developed at the reduction temperature, and the other line shows the average slope of the curve excluding the effect of the phase transition. Clearly, the three sections of the dome height created by the intercepts, as is shown in Figure 4, correspond to the three different contributions, namely the volume change in the reduced layer, the difference in thermal expansion coefficients between the oxide and reduced layers, and the dimensional change at the Curie point.

The relative contribution of each mechanism for those samples shown in Figure 3 was determined with the aforementioned method and the results are given in Table 2. As can be seen,

the volume change due to the reduction process was dominant for RB5556 and RB9565 samples whereas for RB1053 samples the curvature was mainly caused by the dimensional change at the phase transition.

Pictures in Figures 5 and 6 display changes of the curvature with temperature for a number of Rainbow samples during the cool down process. The significant dome height at the reduction temperature and the curvature change near the Curie point were clearly evident in these figures. It is worth mentioning that in a similar experiment where a sample of composition 1.0/54/47 was reduced for a much longer time, e.g. 180 minutes, an appreciable curvature was also observed at the reduction temperature. This suggests that the contribution to the curvature formation also depends on the reduction conditions.

### *3.3 Spontaneous Curvature Reversal*

In a few unusual situations, Rainbow samples were found to change spontaneously from its initial curvature with a concave reduced side to a curvature with a convex reduced side. In other words, the curvature is gradually reversed without external influences in these samples. It was found that this curvature reversal process proceeded very slowly. It usually took more than a year for the curvature to become totally reversed. At the present time this phenomenon was exclusively seen in the Rainbow samples made from PZT-based ceramics. It is apparent that an understanding of this behavior of Rainbow ceramics is vital for long-term use of this new device.

At the first glance, the curvature reversal process seems running against the minimum energy principle of a system. It would be more perceivable if the curvature change ceases when the sample becomes flat. The spontaneous curvature reversal may result from a spontaneous dimensional change of either the oxide layer or reduced layer, or both. But careful examinations

revealed that the reduced regions were most likely to be expanding. Given the fact that the curvature reversal was very significant in the samples that exhibited such an effect, the reversal process must involve occurrence of new phase(s) and/or structural transformation of the initial phases into the phases with a larger unit cell volume. With this consideration, focus was first placed on the possibility of any compositional and structural changes in the reduced layer as time passes.

Figure 7 shows the X-ray diffraction spectra of the Rainbow samples in which the spontaneous curvature reversal was observed. In this figure, the PZT Rainbow samples were made from wafers provided by a commercial company. The exact composition for them was not clear. The PLZT Rainbow sample was obtained from hot-pressed wafers of composition 1.0/53/47, which can also be regarded as a PZT-based composition. A strong peak in the X-ray diffraction spectrum of the PLZT Rainbow, which corresponds to  $\text{Pb}_2\text{O}_3$ , was discovered. This same peak was either very weak or simply did not exist for the Rainbows of the same composition that show no tendency of a spontaneous curvature reversal. Similarly, the X-ray diffraction peaks of  $\text{Pb}_2\text{O}_3$  were observed in the PZT Rainbow samples as shown in Figure 7. Based on these findings, it was speculated that the gradual inversion of the curvature may originate from the slow transformation of the PbO phases (lithorge and masscot) to  $\text{Pb}_2\text{O}_3$  in the help of ambient oxygen. This appears reasonable since the latter has a larger unit cell volume than the former [6]. It should be noted that the relative intensity of the peaks in the X-ray patterns displayed in Figure 7 is not necessarily proportional to the amount of the phase that they refer to. In addition to the phase content, the peak intensity also depends heavily on some other factors such as sample surface states and grain sizes. For this reason, the phase content generally can not be derived on the basis of the peak intensities.

Similar X-ray diffraction analyses were carried out on the oxide layer of the Rainbow samples that exhibited a curvature reversal and on the unreduced samples of the same composition. The results are displayed in Figure 8, which indicate from the same X-ray patterns of the two cases that no structural change and/or phase transformation have occurred in the oxide layer.

The above speculation on the possible origin of the spontaneous curvature reversal needs to be confirmed by careful quantitative analysis of the relative concentration of each phase as a function of time. Moreover, other mechanisms are also possible, which include, for example, gradual decomposition of an existing phase into other existing phases (e.g.,  $\text{ZrTiO}_4$  into  $\text{TiO}_2$  and  $\text{ZrO}_2$ ), since such a process will not be revealed from the conventional X-ray spectrum. The spontaneous curvature reversal has never been observed in PLZT Rainbow samples with a lanthanum concentration greater 2 atm%. It is interesting to note that a slight increase in the lanthanum content has such a profound impact on the curvature reversal phenomenon. Further work is required for a clearer picture of this issue.

#### **4. Summary and Conclusions**

Several issues associated with the onset and development of the unique domed structure of the Rainbow ceramic have been investigated using samples made from a number of different PLZT compositions and commercial PZT ceramics with intent to obtain a more thorough understanding of the factors that influence the magnitude and sign of the dome curvature. It appears that the effect of the high-temperature creep on the curvature is insignificant based on the creep characteristics determined from the reduced and unreduced samples of a series of compositions. The major contributors to the curvature formation are those proposed in our

previous work, which are the volume change in the reduced layer, the thermal expansion mismatch between the unreduced and reduced layers, and the dimensional change at the Curie point. It was found that the relative magnitude of each contribution to the curvature depends strongly on the composition of the unreduced wafer in addition to the reduction conditions. For PLZT 1.0/53/47 wafers, the curvature is predominantly determined by the dimensional change at the Curie temperature. This contribution decreases drastically with increasing lanthanum content. On the other hand, the contribution from the volume change in the reduced layer becomes increasingly dominant as the La content increases. The contribution from the mismatch in the thermal expansion coefficients between the unreduced and reduced layers account for an approximately equal amount for compositions PLZT 5.5/56/44 and PLZT 9.5/65/35, while that for PLZT 1.0/53/47 is insignificant.

The mechanism underlying the spontaneous curvature reversal has not been fully established, although efforts have been made in this study to identify the formation of any new phases which were considered to be most likely the origin of this unusual phenomenon. An extra peak corresponding to  $\text{Pb}_2\text{O}_3$  was found in the X-ray spectra of the reduced layer of the Rainbow samples exhibiting the curvature reversal. The presence of this new phase is probably associated with the spontaneous curvature reversal in these samples. But careful quantitative analyses are needed before any solid conclusion can be drawn on this issue.

## References

- [1] Haertling G H 1994 Rainbow ceramics - a new type of ultra-high-displacement actuator *Am. Ceram. Soc. Bull.* 73 93-96

- [2] Furman E, Li G and Haertling G H 1994 An investigation of the resonance properties of Rainbow devices *Ferroelectrics* **160** 357-69
- [3] Sherrit S, Wiederick H D, Mukherjee B K and Haertling G H 1994 The dielectric, piezoelectric and hydrostatic properties of PLZT based Rainbow ceramics *Proceedings of the Ninth IEEE International Symposium on Applications of Ferroelectrics* 390-393
- [4] Li G, Furman E and Haertling G H 1996 Fabrication and properties of PSZT antiferroelectric Rainbow actuators *Ferroelectrics* **188** 223-236
- [5] Li G and Haertling G H 1996 The piezoelectric, pyroelectric and photoelectronic properties of PLZT Rainbow ceramics *Proceedings of the Tenth IEEE International Symposium on Applications of Ferroelectrics*, to be published
- [6] Samsonov G V 1973 The oxide handbook, IFI/PLENUM, NewYork-Washington-London

Table 1. Creep-induced bending deflection divided by sample thickness obtained under different temperatures and load conditions (data are given in percentage).

	Unreduced Sample				Chemically Reduced
	<i>With Load</i>		<i>Without Load</i>		<i>Without Load</i>
	975°C	950°C	975°C	1000°C	975°C
<i>PLZT 1.0/53/47</i>	28.9	2.1	2.4	3.5	6.2
<i>PLZT 5.5/56/44</i>	309.6	5.0	6.0	7.7	4.8
<i>PLZT 9.5/65/35</i>	24.6	2.8	3.1	3.8	6.6

Sample dimensions = 25×5 ×0.5 mm; load = 5.5 grams.

Table 2. Relative contribution of three different mechanisms for the curvature formation.

Sample	Volume Change in the Reduced Layer.	Thermal Expansion Mismatch	Phase Transition at the Curie Point
<i>RB1053HP</i>	11%	15%	74%
<i>RB1053S</i>	0%	3%	97%
<i>RB5556S</i>	67%	14%	19%
<i>RB9565S</i>	77%	15%	8%

Sample dimensions: 31.75×0.675 mm; Reduction conditions: 975°C for 90 minutes.

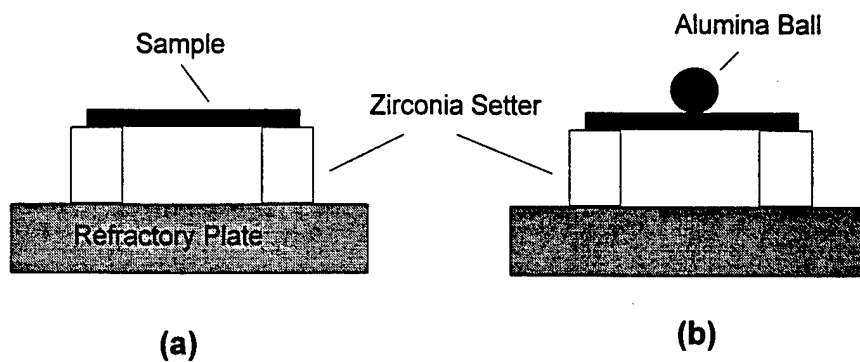


Figure 1. Schematic diagram of setup for determination of the creep characteristics of unreduced and reduced ceramics.

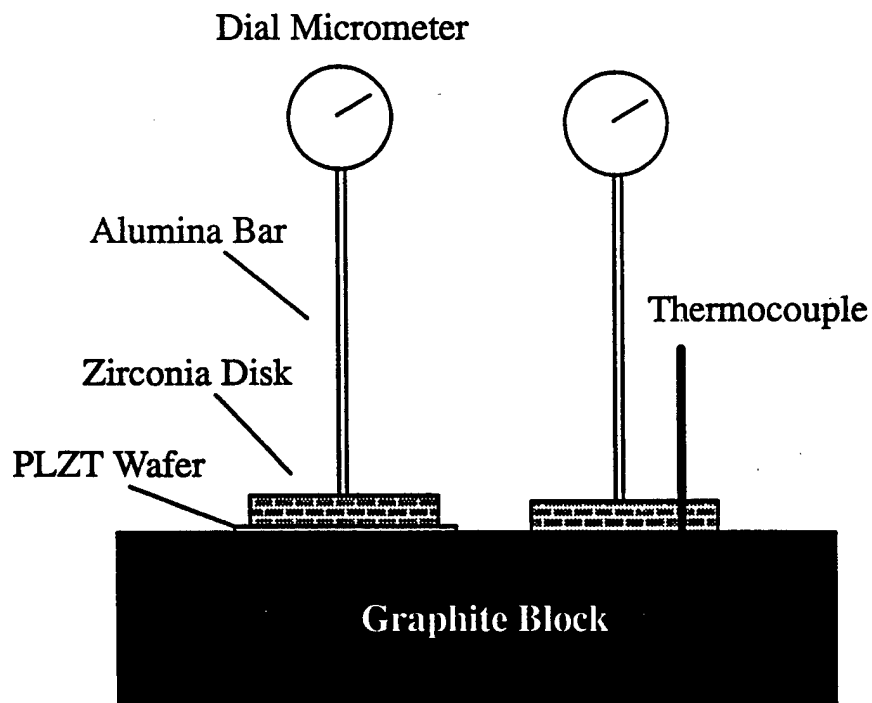


Figure 2. Schematic of measuring setup for temperature dependence of dome height.



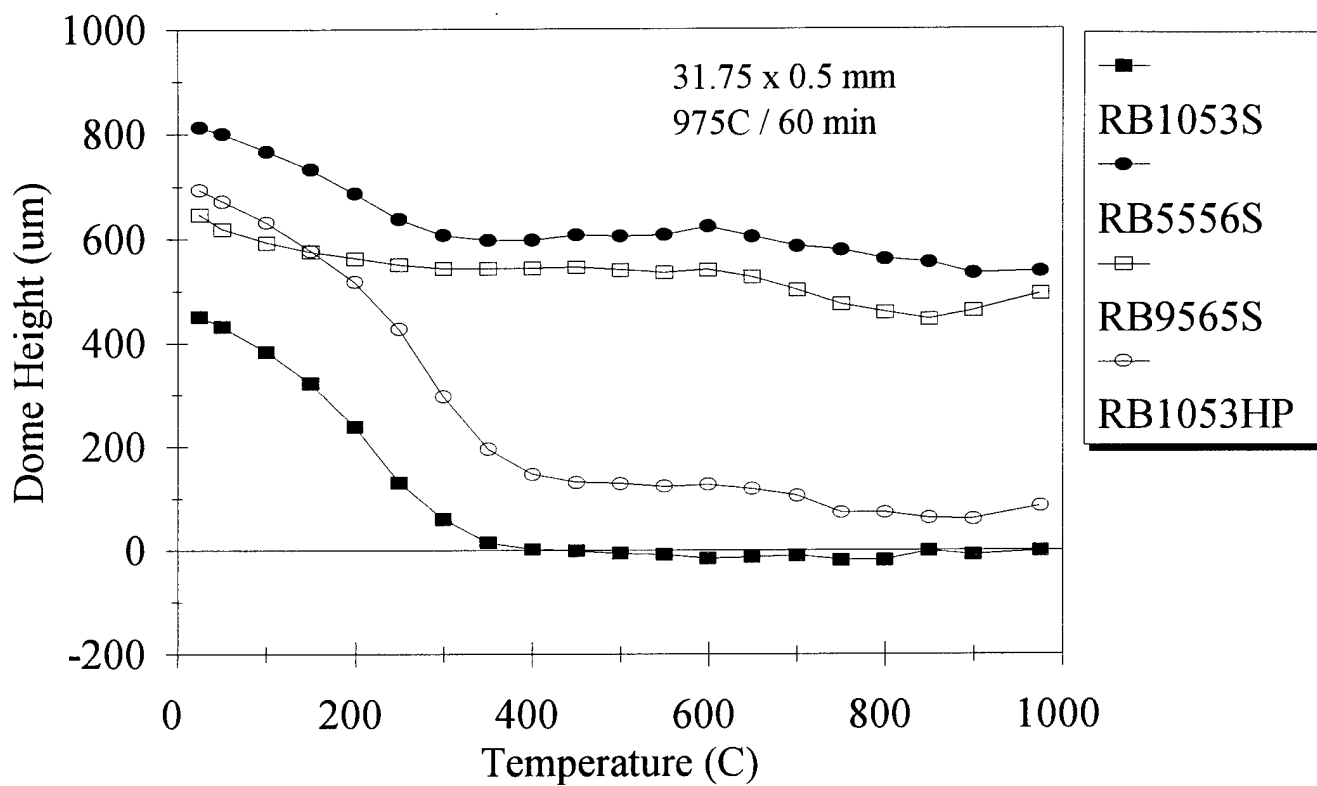


Figure 3. Change of the dome curvature with temperature during the cool down step.

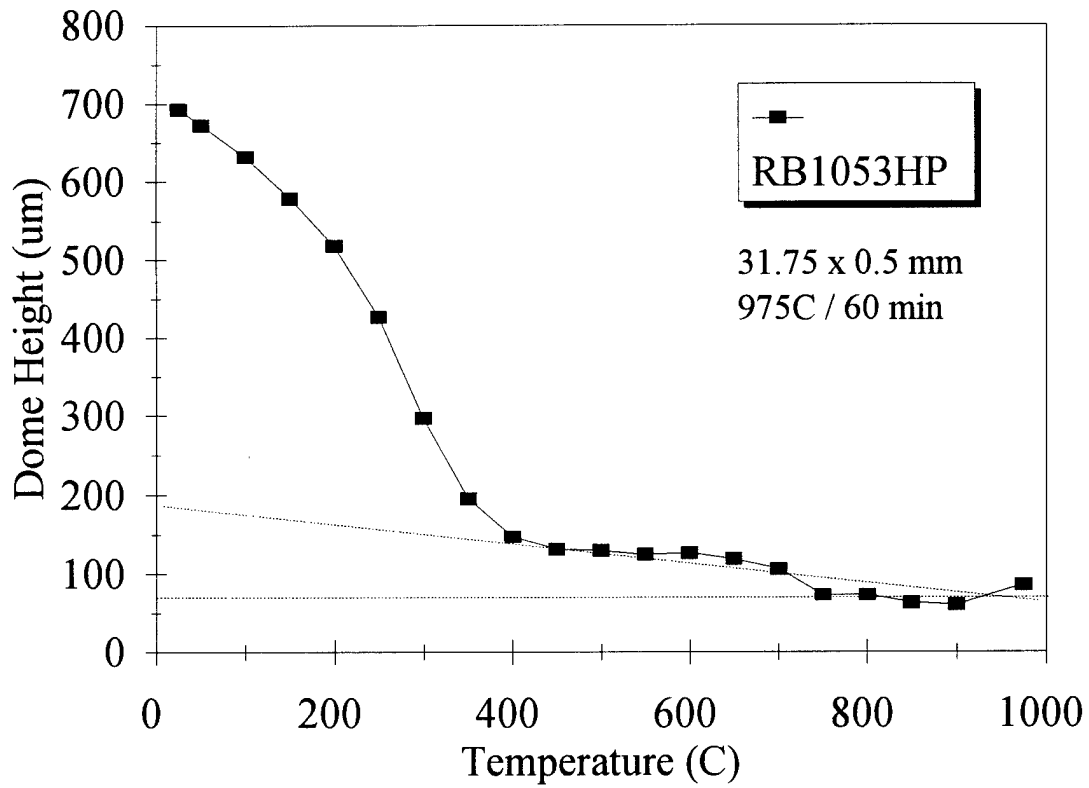


Figure 4. Relative contribution of each mechanism to the curvature formation derived from the variation of the dome height with temperature for RB1053HP.

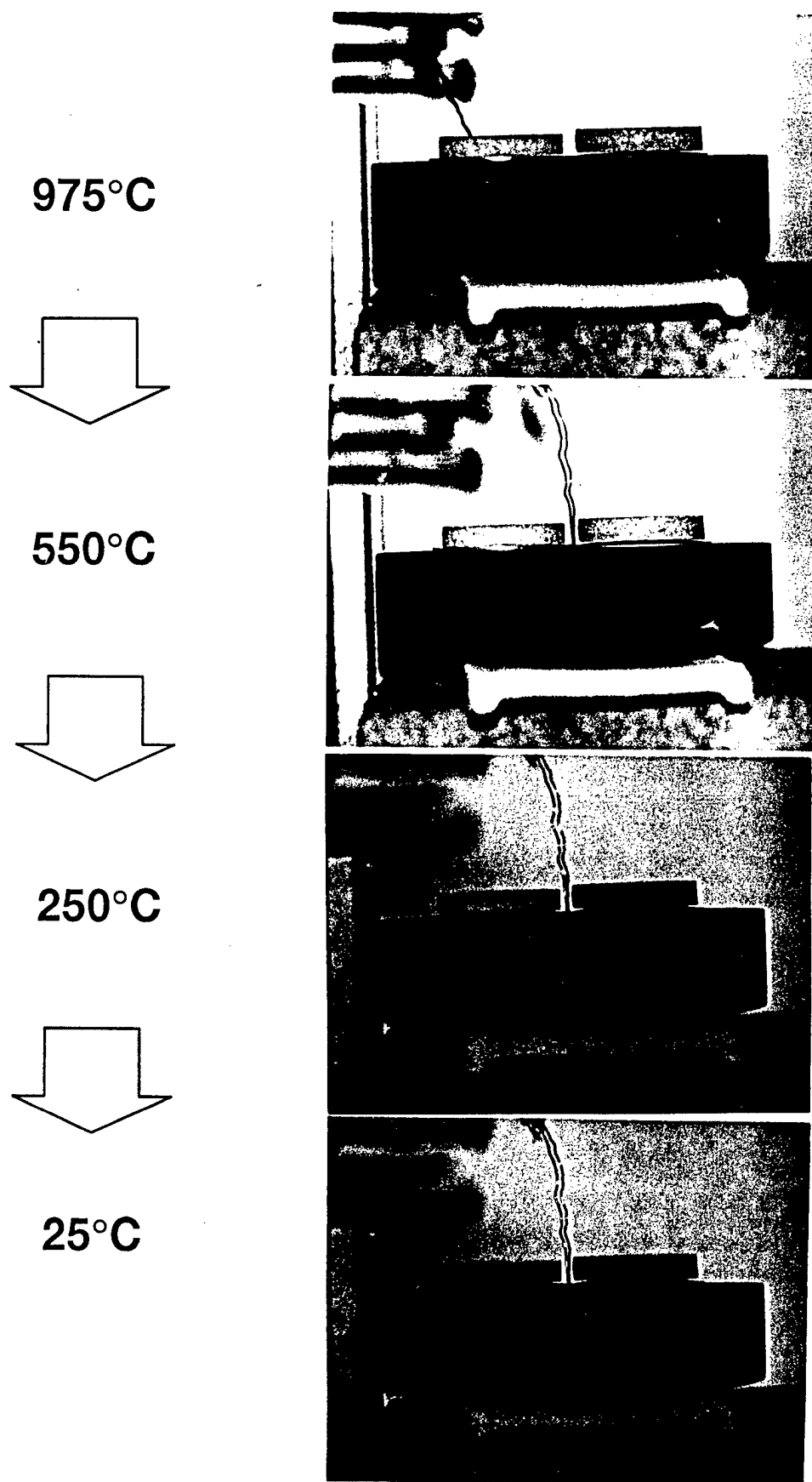
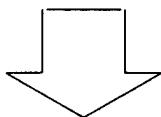


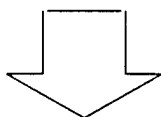
Figure 5. Photo pictures showing the curvature development of RB1053S and RB5556S samples at different temperatures during the cool down step.

PLZT1.0/53/47HP PLZT 9.5/65/35

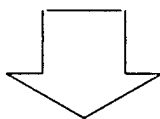
975°C



550°C



250°C



25°C

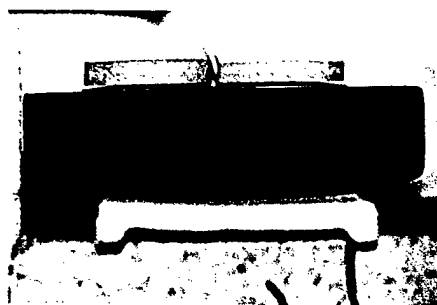
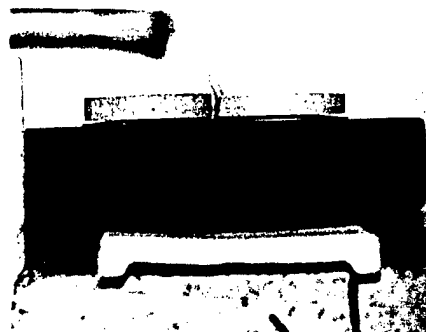
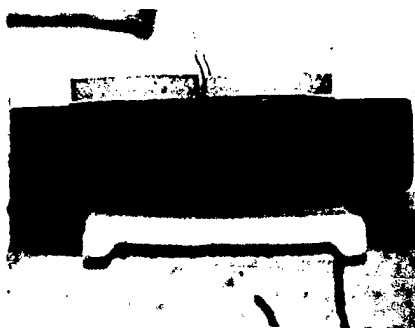


Figure 6. Photo pictures showing the curvature development of RB1053HP and RB9565S samples at different temperatures during the cool down step.

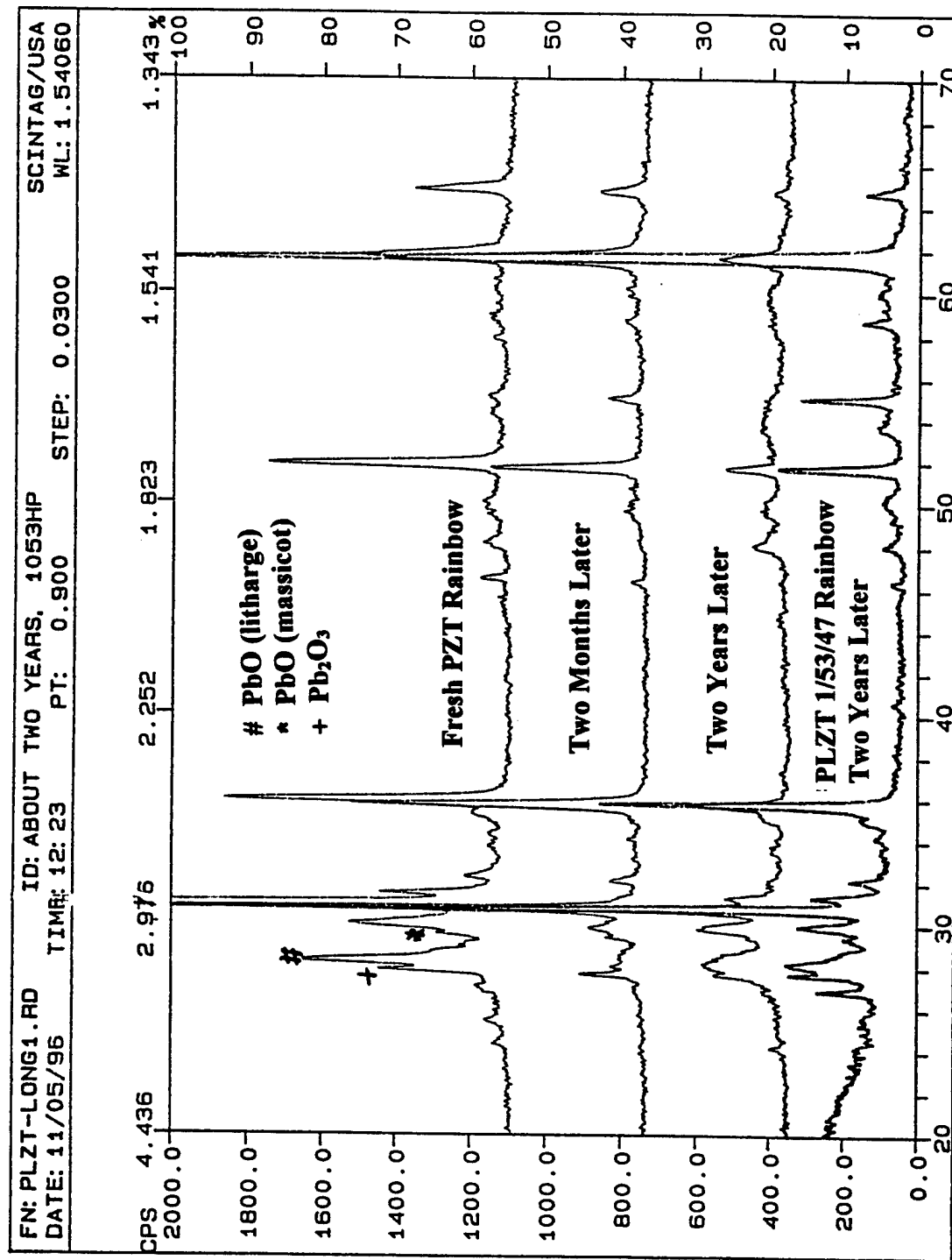


Figure 7. X-ray diffraction patterns of the reduced layer for PZT and PLZT 1/53/47 Rainbow samples that show spontaneous curvature reversal. The diffraction patterns were obtained at different times after the sample was made.

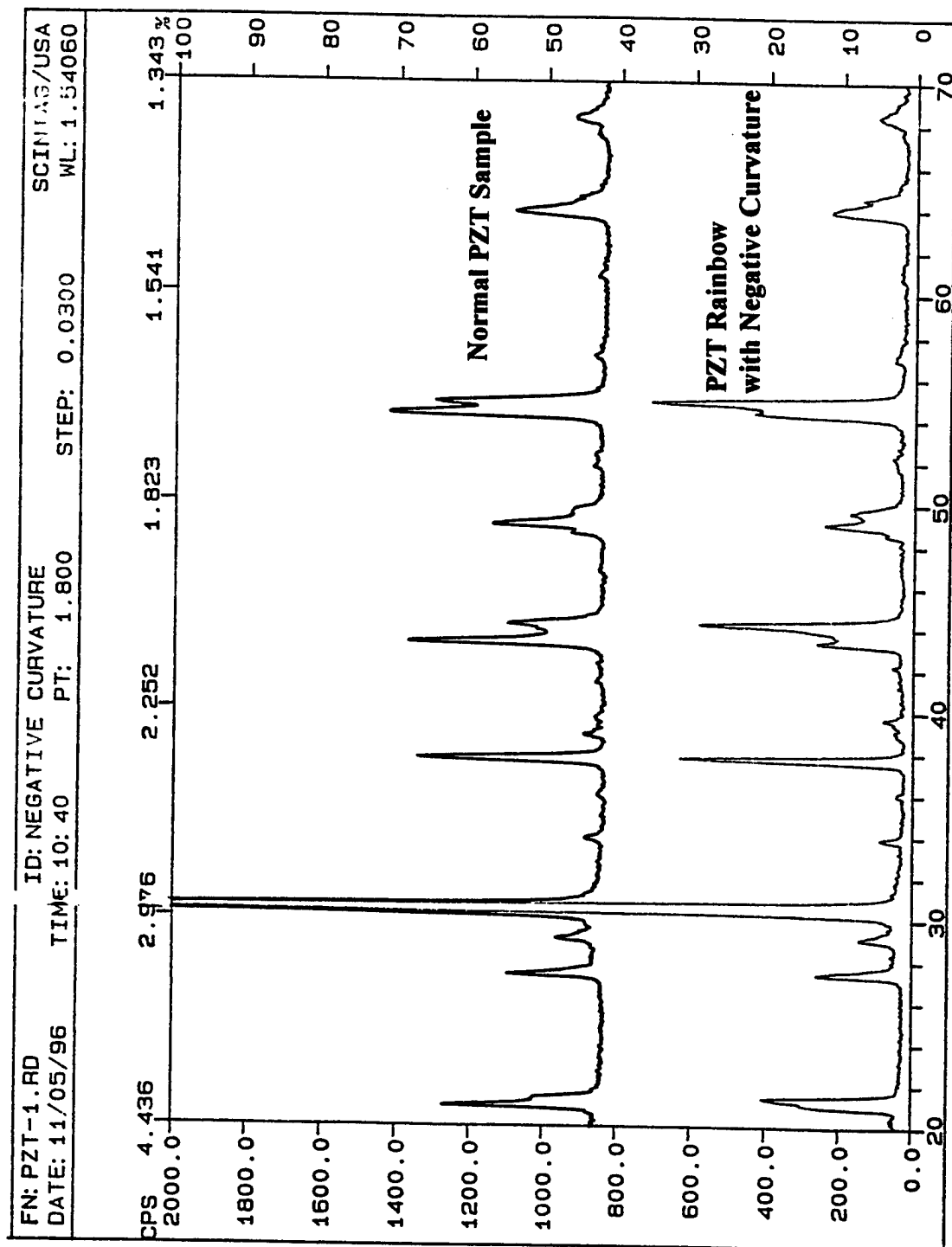


Figure 8. X-ray diffraction patterns of the unreduced layer for the PZT Rainbow samples showing spontaneous curvature reversal.

## **Part II.**

### **Effect of Grain Size on the Nonlinear Dielectric Properties of PLZT**

# **Effect of Grain Size on the Nonlinear Dielectric Properties of PLZT Ceramics**

Y.W. Moon<sup>\*</sup>, G. Li, and G. Haertling,

Department of Ceramic Engineering, Clemson University, Clemson,



## Abstract

Dielectric nonlinear behavior was investigated for 1/53/47 PLZT ceramics with different grain sizes. Different grain sizes were achieved by employing various sintering conditions. By measuring the dielectric constant as a function of ac electric field at various temperatures and frequencies, it was found that the dielectric nonlinearity was affected by grain size, i.e. the samples having larger grains showed a higher degree of dielectric nonlinearity. In addition, the dielectric nonlinearity was found to be influenced substantially by the frequency of applied field and sample temperature. Analysis of x-ray diffraction along with other experimental results indicates that a variation of  $90^\circ$  domain wall contribution is the main cause of the variation of dielectric nonlinearity.

## Introduction

Nonlinear behavior of ferroelectric ceramics has been studied over many decades in association with their practical application.[1-3] As a terminology, nonlinearity means that material properties such as permittivity and piezoelectric constants vary as a function of applied electric field or stress. In ferroelectric ceramics, the piezoelectric and dielectric constants are commonly observed to increase with an increase of the applied field.[1] This nonlinearity becomes more significant as driving field increases. In this nonlinear region, the constitutive equations which are applicable at low fields may no longer be applicable, and thus the nonlinearity becomes one of the limiting factors for proper design of ferroelectric devices. Therefore, further information and more fundamental treatment of

the nonlinear behavior is required for the proper application of ferroelectric ceramic materials.

The dielectric nonlinearity of ferroelectric ceramics can be described by incremental changes in permittivity which is induced by electric field. This increment of permittivity begins to increase when the applied electric field exceeds a certain value.[4] Although, the nonlinear behavior of dielectric properties can be generally observed in most ferroelectric ceramics, the quantitative incremental change of dielectric constant was found to be strongly dependent upon composition.[5,6] For example, the increase of dielectric constants measured from PZT-4, -5, and -8 under elevated electric field were quite different.[1] In case of the soft PZT-5, the dielectric constant increased faster than those of the other compositions.

It is known that the dielectric nonlinear behavior of ferroelectric ceramics is affected by factors such as sample temperature, frequency of applied field, and stress conditions.[1,7,8] Experimental results showed that the degree of dielectric nonlinearity of PZT-5 increased as temperature increased, provided the temperature is below the Curie point.[1]. The effect of frequency on nonlinear behavior can be found from several experimental results.[7,8] It was reported that nonlinear behavior was observed at all frequencies when a large electric field was applied to the ferroelectric samples. In addition, the dielectric nonlinearity became less appreciable at high frequencies. These described experimental results were considered to indicate the dependency of dielectric nonlinearity on sample temperature and frequency of electric field.

The theory which could predict the nonlinear behavior of ferroelectric ceramics has not yet been developed. However, according to present experimental results,[1,6,8] 90°

domain wall motion is commonly considered to be the main cause of the nonlinear phenomenon in ferroelectric ceramics. Arlt et.al. proposed the theoretical model which explained the nonlinear variation of permittivity on the basis of movement of  $90^\circ$  domain walls.[9] In their model, they suggested that the additional switching of  $90^\circ$  domain walls induces the change of polarization and strain. Recently, several studies investigated the domain wall contribution by employing x-ray techniques and analyzing hysteresis loops.[4,7] In their investigation, the x-ray peak intensities of the (002) and (200) planes were measured under elevated electric fields. It was reported that the peak intensity ratio between the (002) and (200) planes increased with an increase of electric field. This result was accepted as evidence of  $90^\circ$  domain activity.

Material properties of ferroelectric ceramics are influenced by microstructure as well as composition. Previous studies regarding the effect of grain size showed that material properties such as remanent polarization ( $P_R$ ), coercive field ( $E_C$ ), and Curie point ( $T_C$ ) vary as a function of grain size.[10,11] Dielectric constants measured on  $\text{BaTiO}_3$  having various grain sizes exhibited a maximum at a grain size of around  $1\text{ }\mu\text{m}$ . [12] This variation of dielectric constant as a function of grain size was explained on the basis of the variation of the internal stress and formation of domain structure which was considered to depend on grain size.[12,13]

This study focused on the effect of grain size on the nonlinear dielectric behavior of ferroelectric ceramics. Although many studies have been performed to investigate effects of grain size on the material properties at low electric field, only limited studies has been reported regarding the effect of grain size on nonlinear behavior which occurs at high electric field. In this study, the composition 1/53/47 PLZT, which has a ferroelectric

phase, was selected. Dielectric constants were measured from the samples having various grain sizes as a function of ac electric field at different temperatures and frequencies. To analyze the contribution of  $90^\circ$  domains on the dielectric nonlinear behavior, XRD techniques were employed to show the variation of the peak intensities of the (002) and (200) planes. These  $90^\circ$  domains were considered to be the main cause of the dielectric nonlinearity.

## Experimental

PLZT 1/53/47 ceramics having different grain sizes were prepared in order to investigate the effect of grain size on the dielectric nonlinearity in ferroelectric ceramics. Samples were prepared employing the conventional mixed-oxide method. Appropriate amounts of PbO, La<sub>2</sub>O<sub>3</sub>, ZrO<sub>2</sub>, and TiO<sub>2</sub> powders were weighed out, calcined at 925 °C and ground using a ball mill and distilled water as a grinding media. The prepared powder was pressed in a cylindrical die and sintered in an electric furnace. In order to obtain various grain sizes, the sintering temperature and time were controlled in the range of 1150 - 1250 °C and 5 - 15 hrs, respectively.

Because the material properties of PLZT ceramics may be influenced by the density of samples which, in turn, depend on the sintering conditions, an effort was made to control the grain size of the samples without a serious variation of density. To obtain high density samples, a setting powder (1:1 mixture of PbO and ZrO<sub>2</sub> powder) and oxygen atmosphere were used during the sintering process.[9] Table 1 shows the density and grain sizes of the samples prepared under various conditions. As shown in Table 1, the samples

with different grain sizes were fabricated without serious loss of the density, thus the obtained results could be considered to be primarily due to grain size. The grain sizes of the prepared samples were measured using the line intercept method. For better accuracy, the average value determined from 10 measurements was accepted as the grain size of the sample.

The dielectric constants of the samples having different grain sizes were measured as a function of ac field in order to investigate the effect of grain size on nonlinear dielectric behavior. With increasing ac electric field, the variation of dielectric constant was measured using an LCR meter (HP 4284A). An ac electric field of up to 400 v/cm was applied at a frequency of 1 kHz. Because the dielectric nonlinearity can be affected by the temperature of the sample which may increase under high electric field, the measurements were carried out in an oil bath to keep the sample temperature constant.

The effects of sample temperature and frequency of applied field, which were known to influence to the dielectric nonlinear behavior, were investigated by the determination of dielectric constants as a function of ac electric field at various samples temperatures and frequencies of the applied field. The investigated range of the frequency and temperature were 20 Hz - 10 kHz and 25 to 160 °C, respectively.

As reported in previous studies, because the dielectric nonlinearity was considered to be related to a contribution of 90° domain wall, the x-ray peak intensity of (002) and (200) plane were investigated. The intensity ratios of the (002) and (200) planes were measured for the samples having various grain sizes at different dc electric fields (0 and 9 kv/cm). The measured intensity ratios at two different conditions were plotted as a function of grain size. For analysis of the contribution of 90° domains to the dielectric

plotted as a function of ac electric field. Because the increment of dielectric constant becomes significant over the threshold field ( $E_t$ ),  $\Delta K/\Delta E$  values were calculated from a difference of the dielectric constant measured at threshold field and 400 v/cm, which can be described as

$$\frac{\Delta K}{\Delta E} = \frac{K(E = 400) - K(E_t)}{400 - E_t}$$

where  $K(E = 400)$  and  $K(E_t)$  are dielectric constants at  $E = 400$  v/cm and  $E_t$ , respectively.

The change of dielectric constants ( $\Delta K$ ) which were measured from the poled samples having different grain sizes were plotted as a function of ac field in Fig. 2. The nonlinear dielectric behavior of PLZT ceramics is clearly evident. The increment was negligible when the field strength was low. However, an appreciable increment was obtained at elevated field strength. It is noted that the increment of dielectric constant was dependent on the grain size. For quantitative comparison of dielectric nonlinearity obtained from the samples having different grain sizes, the average change of dielectric constant ( $\Delta K/\Delta E$ ) occurring at elevated ac field was plotted as a function of grain size in Fig. 3. As is shown in Fig. 3, the  $\Delta K/\Delta E$  increased with increasing grain size. The obtained results showed that the dielectric nonlinearity of the PLZT ceramics was influenced by grain size.

The threshold field ( $E_t$ ), plotted as a function of grain size, is shown in Fig. 4 as another parameter for evaluation of the dielectric nonlinearity. As described, the values were obtained from the increment plot in Fig. 2 as the field strength where  $\Delta K$  reaches

2.5% of the dielectric constant at low field. Fig. 4 shows the threshold field plotted as a function of grain size at two different temperature conditions. The threshold field obtained from both conditions decreased as a function of increasing grain size. Combined with the results shown in Fig. 2, the decrease of  $E_t$  was considered to imply that the samples having larger grains show higher dielectric nonlinearity.

The experimental results obtained at various temperatures and frequencies show a substantial dependence of the dielectric nonlinearity on temperature and frequency. In addition, the dependence of dielectric nonlinearity on both factors was also observed to vary as a function of grain size. The  $\Delta K/\Delta E$  was calculated from the plot of  $\Delta K$  vs. ac electric field obtained at different temperatures. The tested temperatures were 25, 100, and 160 °C which were lower than the Curie temperature, thus the samples have ferroelectric phases. As shown in Fig. 5, the variations of the  $\Delta K/\Delta E$  were plotted as a function of the sample temperature which were obtained from several samples having different grain sizes. All of the samples showed an increase of the  $\Delta K/\Delta E$  values with an increase of temperature. This result indicated that the dielectric nonlinearity is enhanced with increasing temperature. In order to investigate the grain size effect, the variation of the  $\Delta K/\Delta E$  caused by the variation of the temperature was plotted as a function of grain size in Fig. 6. Each plot in Fig. 6 represents the difference of  $\Delta K/\Delta E$  caused by two different sample temperatures which are indicated on the plots. These plots show that the larger difference of  $\Delta K/\Delta E$  occurred in the samples having larger grains, when the sample temperatures increased. The obtained results imply that the influence of temperature on the dielectric nonlinearity was greater when the grain size was larger.

To investigate the effect of frequency, the increment of dielectric constant ( $\Delta K$ ) was measured as a function of ac field at frequencies between 20 Hz and 10 kHz. The  $\Delta K/\Delta E$  was calculated from these measurements as a parameter for evaluation of the dielectric nonlinearity. As plotted in Fig. 7, the  $\Delta K/\Delta E$  obtained from the samples having different grain sizes decreased as a function of frequency. It was observed that the slope of the  $\Delta K/\Delta E$  varied as a function of grain size. The difference of  $\Delta K/\Delta E$  induced by the variation of frequency increased with increase of grain size (Fig. 8). This result was also considered to show that the samples having the larger grains possess greater dependence of dielectric nonlinearity on the frequency of the applied electric field.

The variation of  $E_t$  shown in Fig. 4 is also considered to be evidence of the dependence of dielectric nonlinearity on the sample temperature. As plotted in Fig. 4, the threshold field ( $E_t$ ) values measured at two different temperatures gave different values. The  $E_t$  was found to decrease as the sample temperature increased. These results are considered to be another evidence that the dielectric nonlinearity is substantially affected by sample temperature. In addition, the difference of  $E_t$  measured at two different temperatures was observed to be greater with increasing grain size. It can be mentioned that the dependence of dielectric nonlinearity on the sample temperature was greater in the samples having larger grain.

In poled ferroelectric ceramics, a significant amount of domains are aligned with the poling direction. The amount of alignment depends on the crystal structure.[14] This alignment process may be influenced by the microstructure, including grain size and porosity. When an electric field is applied to a poled sample, additional domain switching can be induced corresponding to the strength of the applied field. It is known that  $90^\circ$



domain switching causes variations of polarization and strain,[3] and the additional domain switching may cause variation of material properties of ferroelectric ceramics such as dielectric and piezoelectric constants. Therefore, the nonlinear behavior which is observed at high electric fields is considered to be associated with the contribution of domain switching occurring at high electric fields.

The domain switching process under an applied field may be influenced by the temperature of the sample and frequency of the field. Because the switching of domains is related to the movement of atoms constituting the unit cell in response to the electric field, the switching process can be activated by additional thermal energy. Also, the response of a domain exhibits a time dependent characteristic which is usually called an electric relaxation. Due to this relaxation, the domain switching is influenced by the frequency of applied field. Consequently, the dielectric properties can vary as a function of temperature and frequency.

The domain structure is considered to be configured in a manner to minimize strain energy induced during a phase transition from cubic to ferroelectric phases (tetragonal, rhombohedral) which occurs below the Curie temperature. It was reported that there were several types of energy related to the formation of a domain structure.[15] They were domain wall energy, elastic energy caused by deformation of grain, and grain boundary energy originating from mismatched configuration between grains. Therefore, characteristics of domains such as density and mobility of domain walls may vary as a function of grain size. When an electric field is applied to a ferroelectric ceramic, the response of the domains to an applied field may depend on the characteristics of the

domains. Consequently, the domain switching process occurring at high applied field is considered to be affected by the grain size of samples.

The effect of grain size on dielectric nonlinearity which is observed in these experiments are considered to be related to the different contribution of  $90^\circ$  domain walls. The experimental results plotted in Figs. 2, 3, and 4 show that the dielectric nonlinearity increases as a function of grain size. These are considered to be a result of increased contribution of the  $90^\circ$  domain with increasing grain size.

The nonlinear dielectric behavior observed at various temperatures and frequencies is also explainable on the basis of domain wall contribution. The increase of nonlinearity at high temperatures (Figs. 4, 5 and 6) may be induced by the thermal activation of domain switching. The increase of nonlinearity in larger grain samples at high temperature (Fig. 6) can be explained as a result of the increased contribution of  $90^\circ$  domain walls. Regarding the effect of frequency, the decrease of nonlinearity shown in Fig. 7 is considered to be caused by domain relaxation. The variations of nonlinearity plotted as a function of grain size (Fig. 8) can be considered as additional evidence for the increase of the contribution of  $90^\circ$  domain walls with increasing grain size.

Variation of  $90^\circ$  domain wall contribution could be detected by crystallographic investigations performed by using X-ray techniques. The obtained results show the evidence of  $90^\circ$  domain contribution to the dielectric nonlinear behavior of the samples having different grain sizes. Fig. 9 shows the peak intensity ratios of the (002) to (200) planes obtained from the poled samples having different grain sizes. As shown in Fig. 9 (a), the ratio increased as a function of grain size at both bias conditions (bias free and 9 kv/cm ). When the strength of the applied field is greater, the intensity ratio of the (002) to

(200) planes was larger in every sample having a different grain size. As shown in Fig. 9 (b), it is noticeable that the variation of the ratios between zero field and field applied increases with increasing grain size. This means that more  $90^\circ$  domain switching is induced in the samples having larger grains under an applied electric field.

## Conclusion

The effect of grain size on dielectric nonlinearity was investigated in ferroelectric ceramics. For the investigation, 1/53/47 PLZT ceramics having different grain sizes were used. The grain size could be controlled in the range of 3.4 to 10  $\mu\text{m}$  by changing sintering conditions. It was found that the dielectric nonlinearity increased gradually with increasing grain size. There was a substantial variation of dielectric nonlinearity according to the sample temperature and frequency of the applied field. Obtained results could be explained on the basis of the contribution of  $90^\circ$  domains which were induced at elevated electric field. A crystallographic investigation employing XRD techniques gave good evidence of the contribution of  $90^\circ$  domains to the obtained dielectric nonlinearity of the ferroelectric samples. In the samples having large grain size, the contribution of  $90^\circ$  domains was found to be enhanced.

## References

1. R. S. Woollett and Charles L. LeBlanc, *IEEE Transaction on Sonics and Ultrasonics*, **SU-20(1)**, 24 (1973)
2. Litvin, M. M. Pikalev, V. A. Dorochenko and V. Z. Borodin, *Ferroelectrics*, **51**, 159 (1984)
3. Berlincourt, D. R. Curran and H. Jaffe, *Physical Acoustic*, **1(A)**, 109 (1964)
4. S. Li, W. Cao, and L. E. Cross, *J. Appl. Phys.*, **69(10)**, 7219 (1991)
5. Gerson, J. *Appl. Phys.* **13(1)**, 1960
6. Robels, C. H. Zadon, and G. Arlt, *Ferroelectrics*, **133**, 163 (1992)
7. Beige and G. Schmidt, *Ferroelectrics*, **41**, 39 (1982)
8. S. Li, W. Cao, R. E. Newnham and L. E. Cross, *Ferroelectrics*, **139**, 25 (1993)
9. Arlt and H. Dederichs, *Ferroelectrics*, **29**, 47 (1980)
10. Okasaki and K. Nagata, *J. Amer. Ceram. Soc.*, **56**, 82 (1973)
11. Burggraaf and K. Keizer, *Mat. Res. Bull.*, **10**, 521 (1975)
12. Arlt, D. Hennings, and G. de With, *J. Appl. Phys.* **58(4)**, 1619 (1985)
13. R. Buessem, L. E. Cross, and A. K. Goswami, *J. Amer. Ceram. Soc.*, **49**, 33 (1966)
14. Baerwald, *Phys. Rev.* **105**, 480 (1957)
15. Arlt and N. A. Pertsev. *J. Appl. Phys.* **70(4)**, 2283, (1991)

Table 1. The density and grain size of PLZT samples fabricated at various sintering conditions.

Sintering Conditions	1150°C 5hrs	1175°C 5hrs	1200°C 5hrs	1225°C 5hrs	1250°C 5hrs	1250°C 15hrs
Density (g/cm <sup>3</sup> )	7.8	7.8	7.75	7.79	7.72	7.65
Grain Size (μm)	3.4	4.5	5.5	6.2	7.4	10.0

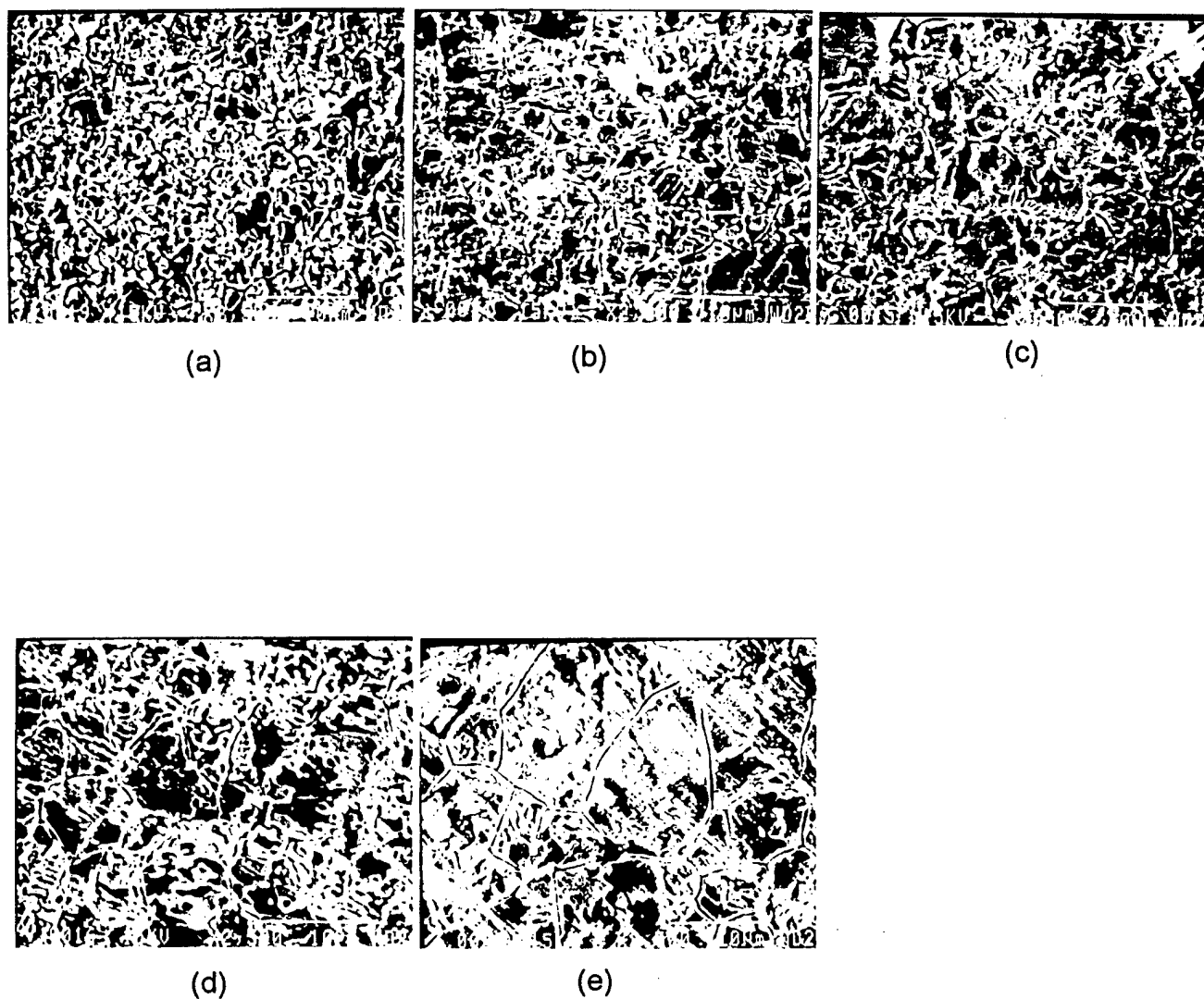


FIGURE 1 SEM micrographs of 1/53/47 PLZT ceramics sintered at various conditions  
(x2,500)  
(a) 1100 °C, 5hrs (b) 1150 °C, 5hrs (c) 1200 °C, 5hrs  
(d) 1250 °C, 5hrs (e) 1250 °C, 15hrs

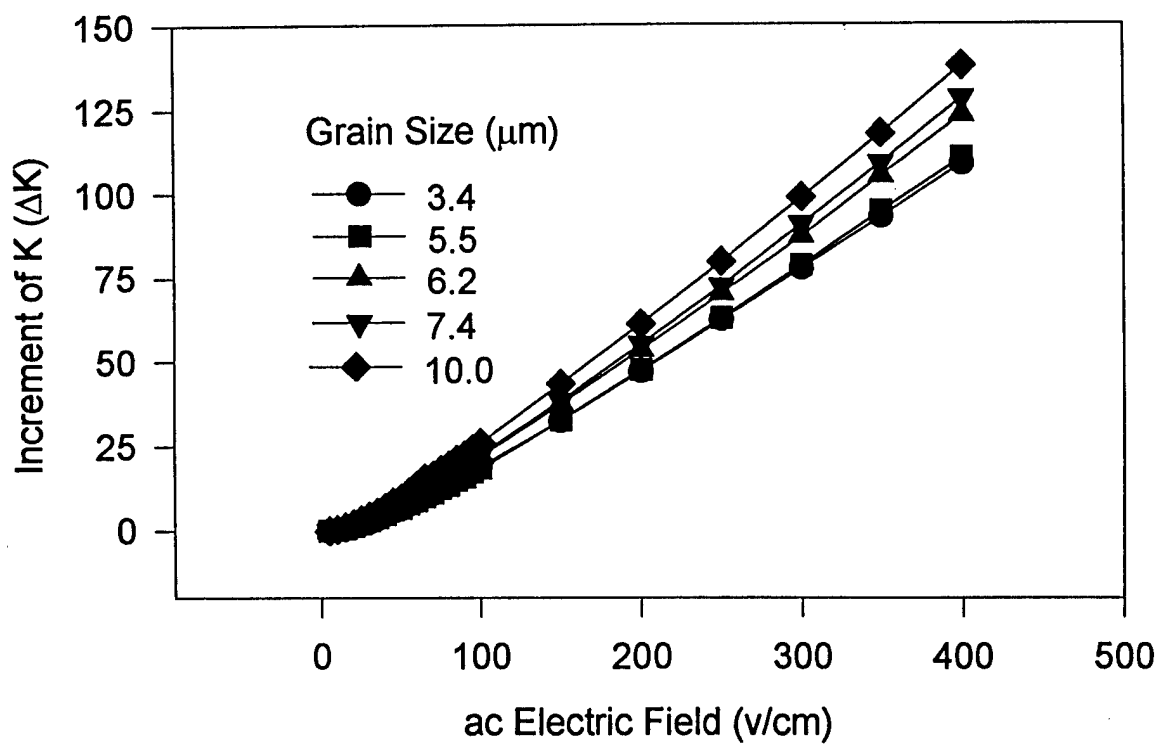


FIGURE 2 Increase of dielectric constant as a function of ac electric field measured for samples having different grain sizes

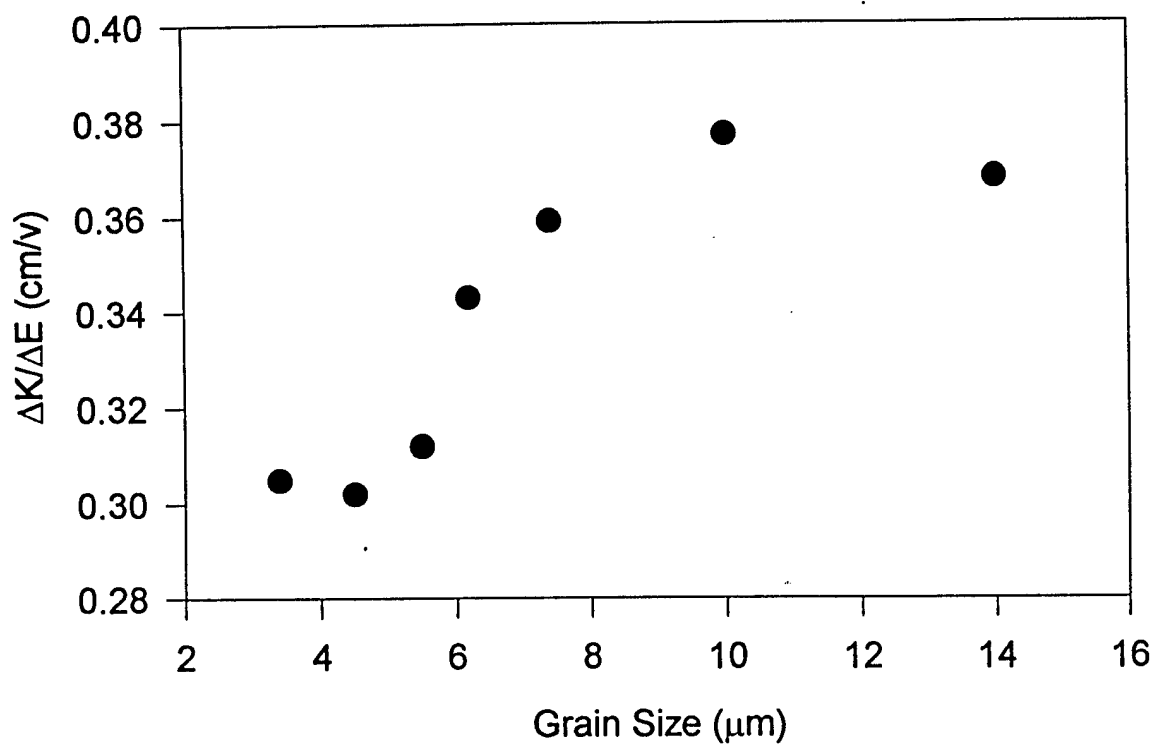


FIGURE 3 Variation of average change of dielectric constant ( $\Delta K/\Delta E$ ) as a function of grain size



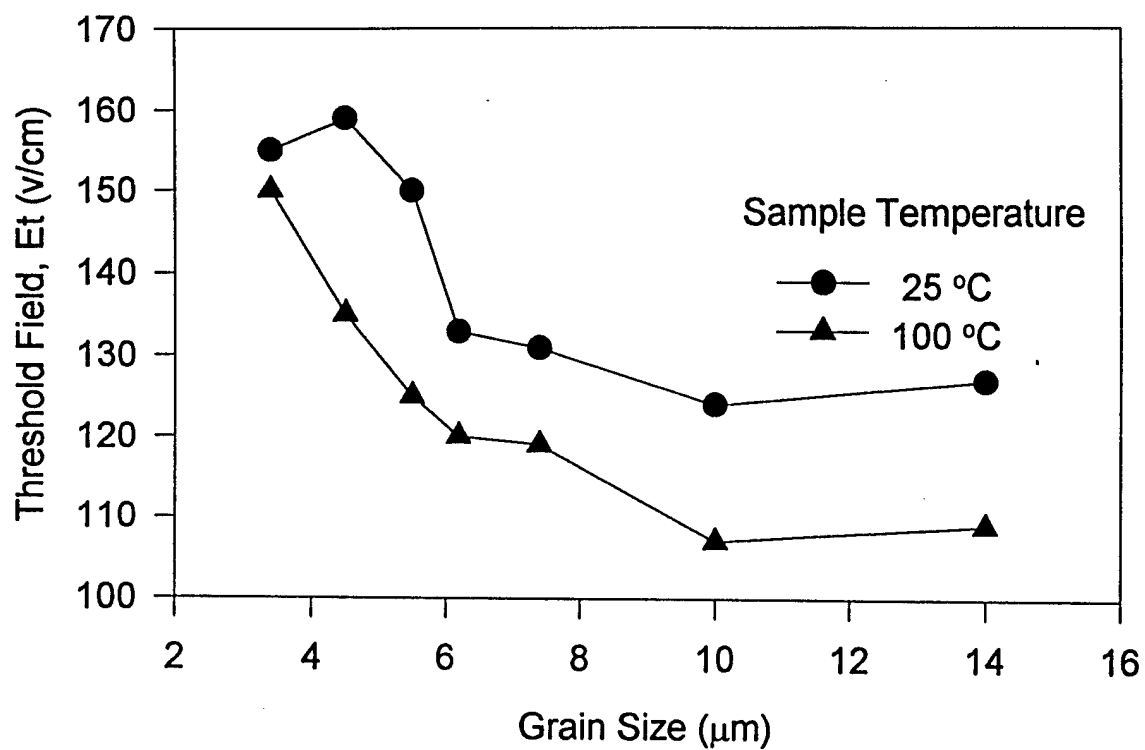


FIGURE 4 The threshold fields as a function of grain size obtained under different measuring conditions

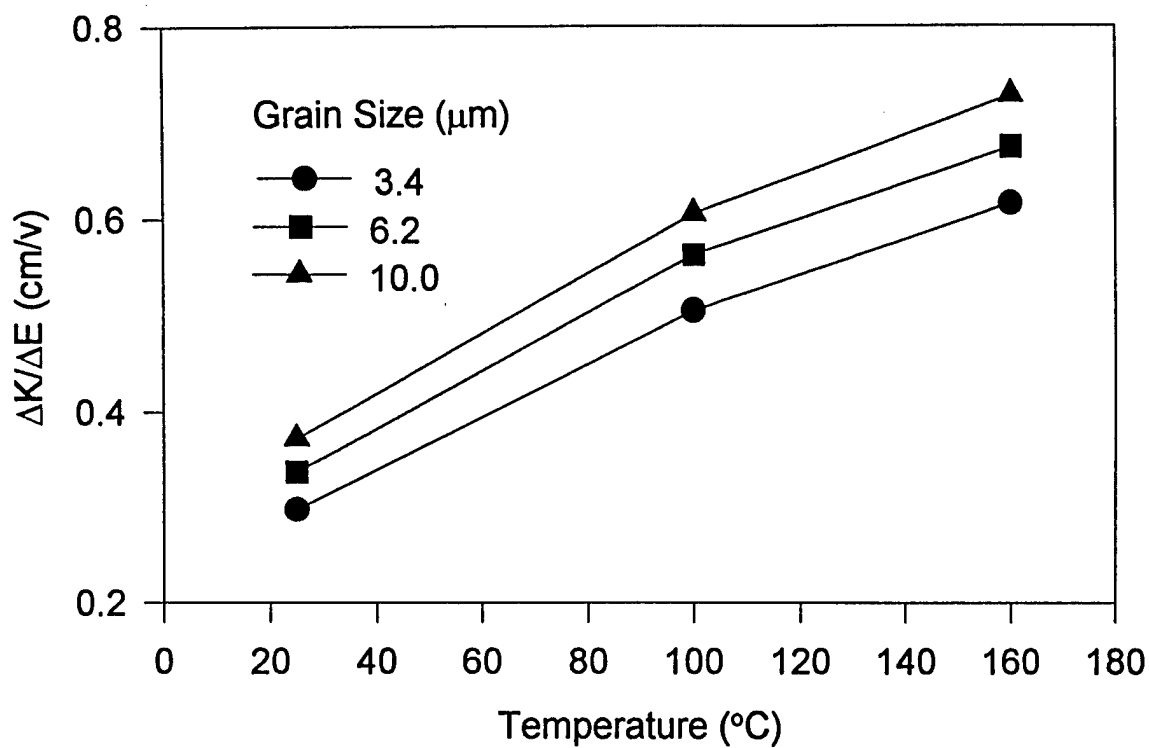


FIGURE 5 The  $\Delta K/\Delta E$  values measured at various temperatures on samples of different grain size

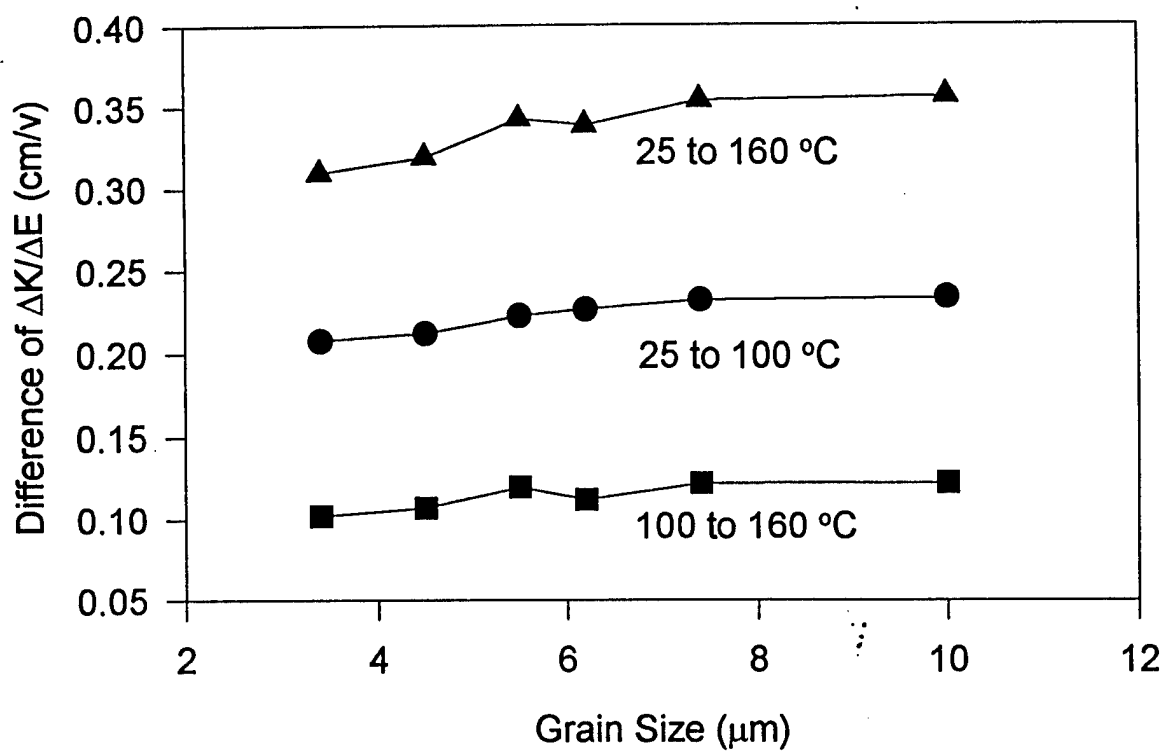


FIGURE 6 Difference of  $\Delta K/\Delta E$  caused by a variation of temperature ranges, obtained from samples having various grain sizes

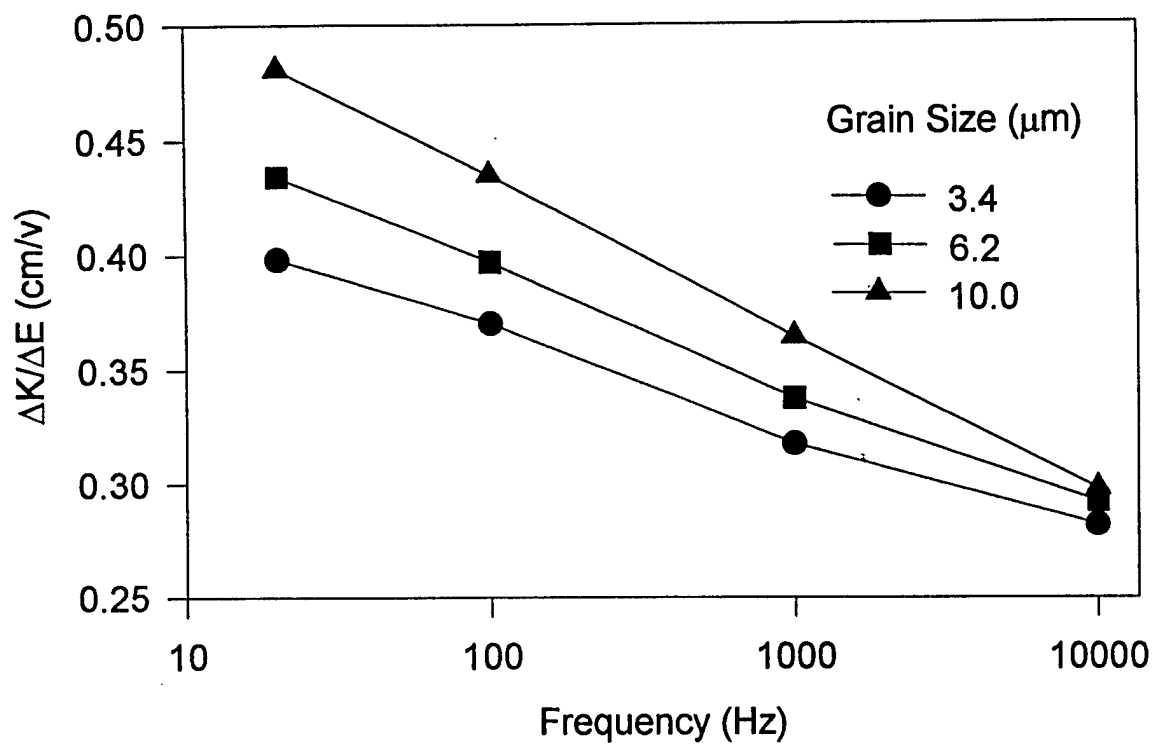


FIGURE 7 The  $\Delta K/\Delta E$  values measured at various frequencies for samples of different grain size

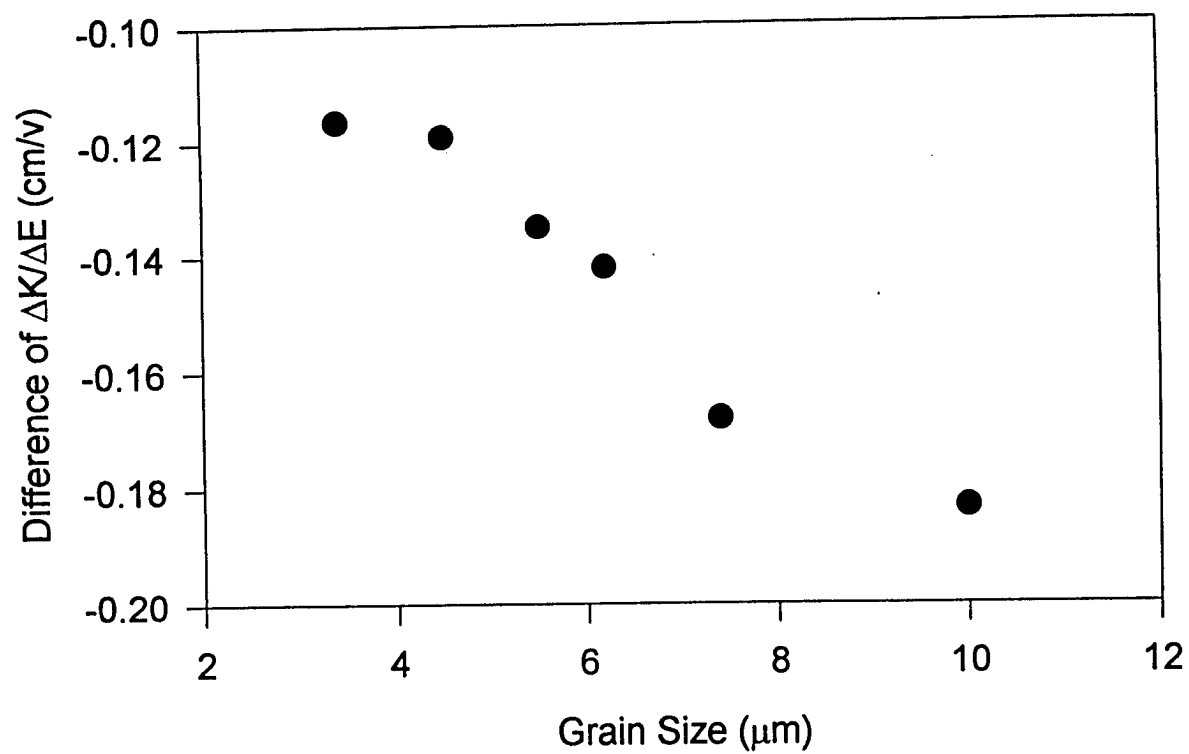


FIGURE 8 Difference of  $\Delta K/\Delta E$  caused by a frequency variation of an applied ac field, obtained from the samples having various grain size

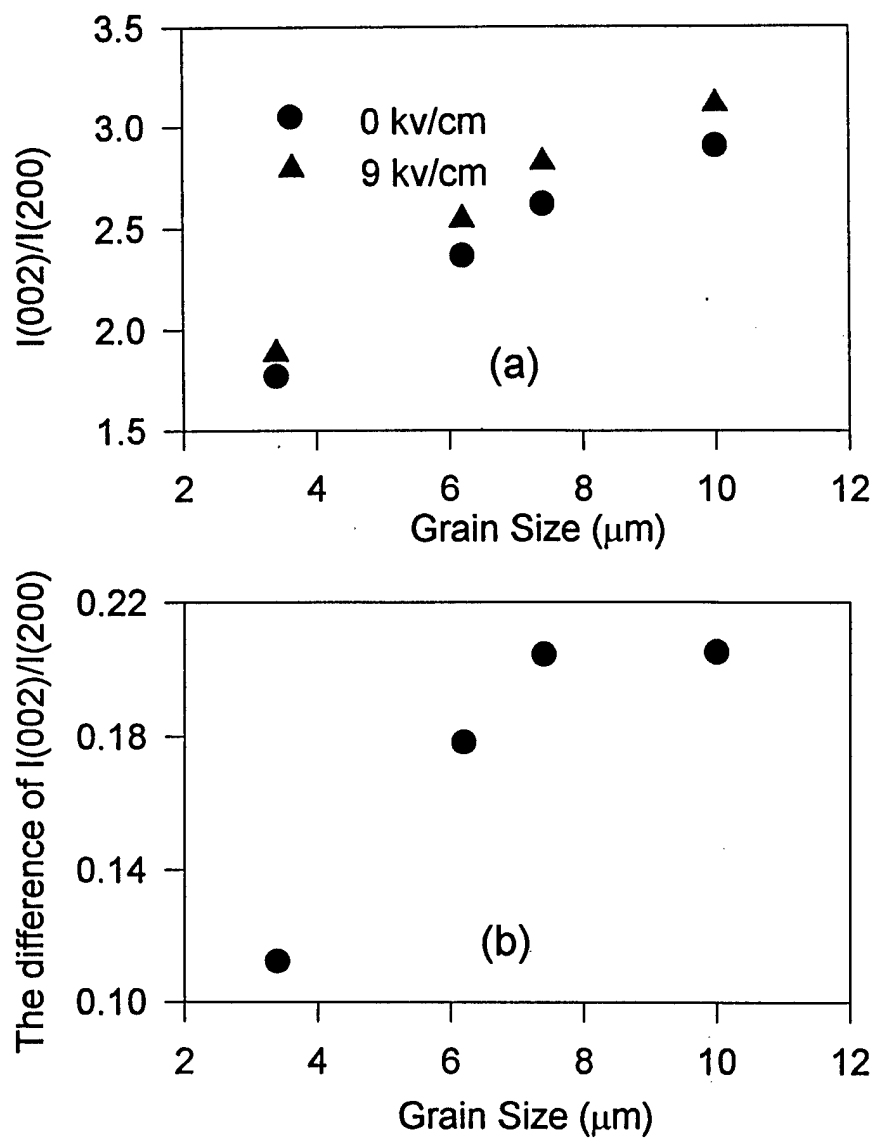


FIGURE 9 (a) X-ray peak intensity ratio of (002) to (200) plane  
(b) The difference of the peak intensity ratio obtained at bias free (0 kv/cm) and high bias field (9 kv/cm)

### **Part III.**

#### **Characterization of Nonlinear Piezoelectric Behavior of Rainbows**

**CHARACTERIZATION OF NONLINEAR PIEZOELECTRIC  
BEHAVIOR OF RAINBOW CERAMICS**

Submitted by : Youngwoo Moon  
Gene Haertling,

**The Gilbert C. Robinson Department of Ceramic Engineering  
Clemson University**



## 1. Introduction

Nonlinear behavior is commonly observed in ferroelectric ceramics when high electric field is applied. As a terminology, nonlinearity means that material properties such as dielectric and piezoelectric constants vary as a function of an applied electric field. In ferroelectric ceramics, linearity between components of stress and strain, dielectric field and displacement, and strain and electric field is limited to very low electric field. Most ferroelectric ceramics show significant nonlinearity with increasing electric field. In general, the dielectric and piezoelectric constants increase with increasing applied field. For the nonlinear behavior, the constitute equations are no longer valid. Considering that the piezoelectric devices are usually operated at high electric field, the nonlinear behavior becomes a limitation factor for proper design of ferroelectric devices.

It has been considered that the nonlinear behavior originates from response of the ferroelectric domains to an applied electric field. According to Arlt et. al, the domain switching which is induced by an applied field results in variations of the dielectric and piezoelectric constants. Based on a theoretical model, they expressed these variations as linear functions of the movement of  $90^\circ$  domain wall. Recently the domain structure was investigated using X-ray diffraction techniques. The results showed evidence for domain wall contributions to nonlinear behavior.

As is known, the Rainbow ceramic has a complicated internal stress pattern. The domain orientation of the oxide layer is critically affected by the nature of the internal stress. There are several papers published which refer to the formation of internal stress

and its contribution to the field-induced displacement of Rainbow ceramics. In general, the internal stress is related to the curvature which is determined as a function of thickness ratio between the oxide and reduced layers. The piezoelectric performance also varies as a function of the thickness ratio so that is associated with the internal stress.

Being associated with the domain switching process, the nonlinear behavior is subjected to stress applied to the piezoelectric samples. This study is concerned with the piezoelectric nonlinearity of the Rainbow ceramics. Owing to the high displacement with good load bearing capacity, the Rainbow ceramics are considered as promising piezoelectric devices for actuators and transducers. As pointed out in previous paragraphs, nonlinear phenomena are expected at the high electric fields where this device are usually operated. Therefore, an understanding of the nonlinearity is necessary to develop the Rainbow ceramics for proper applications. It is the main purpose of this research to investigate the variation of the piezoelectric nonlinear behavior for the Rainbow ceramics having various levels of internal stress. For analysis of the contribution of  $90^\circ$  domain switching, the intensities of (002) and (200) planes were observed from the X-ray diffraction patterns.

## **2. Experimental Procedure**

### **2.1 Fabrication of the Rainbow Samples**

Selection of the experimental material was primarily concerned with ferroelectric ceramics which are easy to fabricate the Rainbow ceramics. As a proper material, 1/53/47 PLZT ceramic was selected. This composition was used to fabricate the Rainbow

ceramics with a good reliability in several researches. As reported, the Rainbow ceramics were fabricated employing the one side chemical reduction process using a graphite block. The reduction temperature was performed at 950 °C. Based on the fact that the internal stress is related to the curvature of the Rainbow samples, the curvature was controlled to obtain various condition of internal stress. The various curvature of the Rainbow samples were achieved by controlling the thickness ratio which was determined as a function of the reduction time. In this study, the thickness ratio was defined as the thickness of the reduced layer divided by the total thickness of Rainbow sample.

## **2.2 Investigation of the Curvature Formation**

The curvature of the Rainbow ceramics is considered to depend on the dimensional changes which could occur during chemical reduction and cooling. For analysis of the curvature formation, the thermal expansion coefficients were measured for the PLZT ceramics and the reduced counterparts. The variation of dome height was directly measured as a function of temperature.

Dilatometer was used for measurement of the thermal expansion coefficients of both phases. The PLZT ceramics were prepared in bar types (length: 2.5cm, width: 0.6cm, thickness: 0.6cm). For the measurement of the reduced counterpart, the oxide sample was fully reduced. The measurements were performed with increasing temperature from room temperature to 950 °C, the temperature at which the Rainbow samples were fabricated. For accuracy, the rate of temperature increase was limited to 2 °C/minute.

Variations of the dome heights were directly measured. Fig. 1 illustrates the set up for the dome height measurement. After the reduction at 950 °C, the whole assembly was pulled out from the reduction furnace and placed on the dome height measurement system. During the cooling, dimensional changes occurred not only the dome height of the Rainbow samples but also the supporting system including graphite block and zirconia plates. To obtain variation of the dome height, the shrinkage of the supporting system was measured simultaneously with the measurement of the total variation. By compensating the total variation of shrinkage with the shrinkage of the supporting system, the variation of the dome height was obtained as a function of temperature. To obtain the true dome height plot as a function of temperature, the sample dome height was measured at room temperature and employed as a starting point of the plot of the dome height variation.

### **2.3 Piezoelectric nonlinear behavior**

In Rainbow ceramics, the major displacement occurs in the axial direction for a given applied field. The axial displacement is the largest and most interesting for applications of the Rainbow ceramics. Hence, the piezoelectric nonlinear behavior was investigated for axial displacement. From poled Rainbow ceramics, the uniaxial displacements were measured with increasing electric field. As illustrated in Fig. 2, dc electric field was applied in the thickness direction. The response of the axial displacement was measured using an LVDT (Linear Variable Differential Transformation) made by Lucas Schaeritz Co. For analysis of the piezoelectric nonlinear behavior of the Rainbow ceramics, a newly defined parameter called "normalized

displacement” was used. Fig. 3 shows the schematic diagram for the normalized displacement. As illustrated in Fig. 3, this parameter implies an average uniaxial displacement per unit applied field. This parameter can be expressed as

$$D_{\text{Norm}} = \frac{\text{Uniaxial Displacement}}{\text{Applied ElectricField}} \quad (1)$$

where  $D_{\text{norm}}$  represents the normalized displacement. The normalized displacement obtained from the Rainbow samples having various dome heights was plotted as a function of electric field.

The contribution of  $90^\circ$  domain wall motion to the nonlinear behavior was investigated employing X-ray diffraction. These experiments were carried out using an X-ray diffractometer (Sintag XDS 2000<sup>TM</sup>) with Ni-filtered Cu  $K\alpha$  radiation. The oxide side, which was exposed to x-ray, was electroded with aluminum for penetration of the x-ray beam. The intensity ratios of the (002) and (200) planes were measured for the samples at various electric fields applied in the thickness direction. To prevent electric discharge, a thin layer of silicon oil was spread over the sample surface. For accuracy of the measurement, the raw X-ray diffraction was fitted using statistical functions. In this experiment, the peak intensities were determined from the X-ray diffraction peaks fitted to a Gaussian function.

### 3. Results and Discussion

#### 3.1 Curvature Formation

The Rainbow fabrication process consists of two steps: the chemical reduction at high temperature and the cooling. During this process, the PLZT oxide experiences chemical decomposition and physical changes. As a result of chemical reduction, the reduced layer has quite different phases including several metal oxides ( $\text{TiO}_2$ ,  $\text{ZrO}_2$ ,  $\text{La}_2\text{O}_3$ , etc.) and metallic lead. A dimensional change was accompanied the chemical decomposition. It was observed that the PLZT samples were dimensionally smaller after reduction. Table 1 shows shrinkages observed from several compositions of reduced PLZT samples. Depending on the composition, the observed shrinkages were different. They ranged from -0.2 to -0.5%.

When the reduced samples were cooled down after the reduction, both the reduced and remaining oxide layer experienced thermal shrinkage. In addition, the oxide layer may have changed dimensionally during the ferroelectric phase transition at the Curie temperature. Based on measurements of thermal expansion, the dimensional change during cooling was investigated. Fig. 4 shows the linear thermal expansion plotted as a function of temperature for 1/53/47 PLZT oxide and its reduced sample. For the reduced sample, the thermal expansion was relatively linear from room temperature to the reducing temperature. The observed linear thermal expansion coefficient was about  $9.0 \times 10^{-6} / ^\circ\text{C}$ . However, the thermal expansion of the oxide sample varied significantly at the ferroelectric phase transition Curie point. Above the Curie point, the linear thermal expansion coefficient was  $9.2 \times 10^{-6} / ^\circ\text{C}$ . In contrast, much less thermal expansion was observed from the ferroelectric phase below the Curie point. Due to the contribution of volume expansion which generally accompanied the phase transition, slight change of

thermal expansion was observed just below the Curie point. For 1/53/47 PLZT ceramics, the average thermal expansion from room temperature to the Curie point was  $4.3 \times 10^{-6}$  /°C.

Table 2 lists the linear thermal expansion coefficients measured from several compositions of the PLZT ceramics and their counterpart reduced samples. All of the investigated oxide samples were ferroelectrics, and thus they exhibited thermal behavior similar to the 1/53/47 sample. When the temperature decreased lower than the Curie point, the thermal expansion coefficients of the all oxide samples reduced significantly. As was known, the Curie temperature was dependent upon the composition of the PLZT samples. For the reduced samples, the thermal expansions were relatively linear in the whole temperature range. In Table 2, it should be noticed that below the Curie point the thermal expansion coefficients of the reduced samples were much higher than those of the oxide samples. Above the Curie point, the difference between both samples were observed not to be very appreciable. This results implies that the dimensional mismatch between the oxide layer and the reduced layer of a Rainbow ceramic is caused mostly below the Curie point.

As discussed, several factors are considered to contribute to the occurrence of the dimensional differences. To investigate the contribution of each factor, variation of the dome heights were directly measured as a function of temperature. Fig. 5 shows the dome height of 1/53/47 PLZT Rainbow ceramics plotted as a function of temperature. The data were obtained from several Rainbow samples having different dome heights. In Fig. 5, it was found that a certain amount of dome height was created as a result of the chemical

reduction. The created amounts were different according to the samples. Based on the reduction shrinkage listed in Table 1, these results are understandable. As expected from the thermal expansion measurements, the dome heights were constant until the samples were cooled down to the Curie point. Below the Curie point, an appreciable increase of the dome heights has observed. The obtained plots show good agreement with the results of the thermal expansion behavior.

Similar experimental agreement was observed from the other compositions of PLZT ceramics. Fig. 6 illustrates variation of the dome height obtained from several different compositions. In the 5.5/56/44 PLZT Rainbow sample, a significant amount of dome height was created as a result of the high temperature reduction. This result may be associated with the relatively large reduction shrinkage of this composition shown in Table. 1. It can be observed that the temperature for initiation of the dome height increase gradually decreased with increasing La amount. This can be explained based on the variation of the Curie point as a function of the La amount which was used to describe the thermal expansion behavior in Table 2.

The dome height of a Rainbow ceramic is a function of the thickness ratio of the two layers. Fig. 7 illustrates the variation of the dome height as a function of the thickness ratio obtained from 1/53/47 PLZT Rainbow samples. As illustrated in Fig. 4, the dome height generally increases with an increase of the thickness ratio and then reaches a maximum at a certain ratio. It is known that the shape of this curve (dome height vs. thickness ratio) is influenced by the material properties of both layers. Similar to the thermal properties, the mechanical properties also play an important role in



determining the dome height. The mechanical properties obtained from the PLZT ceramics and the reduced samples are listed Table 3.

### **3.2 Uniaxial Displacement of the Rainbow ceramics**

Associated with piezoelectric applications such as actuator and transducer devices, the axial displacement of the Rainbow ceramic is the most interesting one. The uniaxial displacement obtained from several Rainbow samples with different dome heights is plotted as a function of applied field in Fig. 8. The uniaxial displacements increased as a function of electric field. It was observed that the increasing displacement behavior depended on the dome height. Fig. 9 shows the variation of the dome height and uniaxial displacement as a function of thickness ratio. In the low thickness ratio region, the uniaxial displacements were observed to increase along with increasing dome height as a function of thickness ratio. However, a further increase of the thickness ratio caused a decrease of the uniaxial displacement despite an increase of dome height.

Deformation of the oxide layer of Rainbow ceramics was observed to be elastic deformation. For elastic deformation, the larger deformation indicates larger stress is applied. Therefore, it can be considered that the Rainbow sample having higher dome height has larger deformation and thus possesses larger internal stress. Based on this consideration, at low thickness ratio, the uniaxial displacement of Rainbow ceramics is considered to increase with increasing internal stress. However, as shown in Fig. 9, there was an optimum internal stress at which the uniaxial displacement reached a maximum.

The oxide layer usually has two different stress regions. Fig. 10 illustrates the distribution of the internal stresses and the preferred domain orientation. As shown in Fig.

10, The top side is under tension and the bottom near the reduced layer is under compression. The boundary between the two stress regions is called the neutral axis where the internal stress is zero. The position of the neutral axis is a function of the curvature. When the dome height is low, the neutral axis occurs near the bottom of the oxide layer, thus the tension area becomes wide. With increasing dome height, the neutral axis moves toward the top side of the oxide layer. Consequently, the tension area becomes smaller and finally disappears. It is evident that not only the magnitude but also the distribution of the internal stress is related to the curvature of the Rainbow ceramics.

It is known that the field-induced displacement of piezoelectric ceramics is influenced by domain orientation. In Rainbow ceramics, the contribution of the internal stress on the field-induced displacement is associated with the distribution of reoriented domains. For the Rainbow ceramics, domain orientation is parallel to the surface in the tension area but perpendicular in the compression area as illustrated in Fig. 10. Depending on the magnitude and distribution of the internal stress, the curvature will be changed. As a consequence, the domain structure of the Rainbow ceramics will be changed with variation of the internal stress and thus the piezoelectric performance will be affected. Because the distribution of the reoriented domains also play an important role, it is considered that there is an optimum curvature at which the uniaxial displacement becomes a maximum. Experimentally, the optimum poled dome height for maximum uniaxial displacement was approximately 240  $\mu\text{m}$ . For the sample having a thickness ratio higher than 0.4, the uniaxial displacement decreased while the dome height increased.

### **3.3 Nonlinear Behavior of the Uniaxial Displacement**

Based on the uniaxial displacement discussed in previous paragraphs, the piezoelectric nonlinear behavior was investigated. Using Eq. 1, the normalized displacement ( $D_{\text{norm}}$ ) was calculated from the measured uniaxial displacement. The normalized displacements obtained from the Rainbow samples having different dome heights were plotted as a function of applied field in Fig. 11. The  $D_{\text{norm}}$  generally increased with increasing electric field and reached maximum. For higher electric field, the  $D_{\text{norm}}$  tended to decrease. The electric field for the maximum was observed to be about 10 - 15 kv/cm. Physically, the normalized displacement ( $D_{\text{norm}}$ ) means the displacement induced by a unit applied electric field. Hence the observed variation of the normalized displacement indicated the nonlinear behavior of the Rainbow ceramics.

In Fig. 11, it is noticed that the nonlinearity of the Rainbow samples was strongly influenced by the dome height. The sample having a 240  $\mu\text{m}$  dome height showed the highest normalized displacement. For numerical comparison of the nonlinear behavior, the difference between the  $D_{\text{norm}}$  measured at low electric field and maximum  $D_{\text{norm}}$  was calculated. This difference can be considered as a parameter indicating the magnitude of piezoelectric nonlinearity. Table 4 listed the difference along with the  $D_{\text{norm}}$  measured at low electric field and maximum  $D_{\text{norm}}$  and for the Rainbow ceramics having various dome heights. From Table 4, it was observed that the difference increases with increasing dome height. This result implies that the piezoelectric nonlinearity becomes significant with increasing internal stress. However, the sample having 282  $\mu\text{m}$  dome height showed

reduced nonlinearity despite increasing dome height. This is also considered to be related to the distribution of the internal stress which is described in previous paragraph.

In Rainbow ceramics associated with the internal stress, the domain structure and its response to an applied electric field is considered to be critical for the piezoelectric performance. The domain structure and  $90^\circ$  domain switching was investigated employing X-ray diffraction techniques. The X-ray peak intensity of (002) and (200) was measured at various electric fields for analysis of nonlinearity using the Rainbow samples. Fig 12 shows the variation of the intensity ratio of (002)/(200) peak obtained from the Rainbow samples having different dome heights. For comparison, the data obtained from normal 1/53/47 PLZT was plotted together using dotted line.

The intensity ratios of the Rainbow samples which is measured under zero electric field was lower than that of normal PLZT. This result indicates that the surface of the oxide layer is under tension. As a result of  $90^\circ$  domain switching, the intensity ratios increased with increasing electric field. It was found that the variation was greater in the Rainbow samples than normal PLZT. As shown in Fig. 12, variation of the intensity ratio was observed to be influenced by the dome height. Comparing the piezoelectric nonlinearity illustrated in Fig. 11 and Table 4, the variation of the intensity ratio was greater when the sample showed higher piezoelectric nonlinearity. For instance, the sample having  $240\text{ }\mu\text{m}$  dome height exhibited the largest variation of the intensity. For the sample having  $282\text{ }\mu\text{m}$ , the intensity increase was observed to decrease. In addition, the (002)/(200) at zero electric field was found to increase. As explained, this result is considered to originate from the distribution of the internal stress.

#### 4. Summary

The piezoelectric nonlinear behavior of 1/53/47 PLZT Rainbows was investigated phenomenologically. It was observed that the uniaxial displacement of Rainbow ceramics show significant nonlinear behavior for electric fields under 15 kv/cm. The nonlinear behavior was associated with the domain structure which is determined by the internal stress. The results are summarized as follows :

1. The piezoelectric nonlinear behavior of the 1/53/47 PLZT Rainbow ceramics has investigated. It was found that the Rainbow ceramics showed significant nonlinear behavior.
2. It was observed that the dome heights were mainly formed below the ferroelectric Curie temperature. The amount of dome height varied as a function of thickness ratio.
3. The uniaxial displacement of Rainbow ceramics increased as a function of applied electric field. Furthermore, the increased amount was significantly influenced by the dome height of the Rainbow samples.
4. For the analysis of nonlinear behavior, normalized displacements were calculated. It was found that the normalized displacement increased with an increase of applied electric field and reached a maximum when the electric field reached about 10 - 15 kv/cm.
5. In general, the piezoelectric nonlinearity of Rainbow ceramics increased with increasing dome height. However, the sample having maximum dome height did not

show maximum nonlinearity. This was considered to be related to the distribution of internal stress.

6. The variation of X-ray peak intensity ratio of (002) to (200) supported the fact that the nonlinear behavior was related to  $90^\circ$  domain switching. In Rainbow ceramics, this variation induced by electric field was greater than that of normal PLZT ceramics. It was considered that the internal stress affected the domain orientation and thus contributed to the nonlinearity of the Rainbow ceramics.

Table 1 Variation of diameter of PLZT ceramic wafers after reduction

Sample	before	after	ratio
1/53/47	945.5 mil	942.5 mil	- 0.32%
5.5/56/44	938.5 mil	934.0 mil	- 0.48%
8/65/35	906.0 mil	904.0 mil	- 0.22%

Table 2 Linear Thermal expansion Coefficients of normal PLZT and their Reduced Counterpart

Sample	25 - T <sub>c</sub> °C (10 <sup>-6</sup> /°C)	T <sub>c</sub> - 950 °C (10 <sup>-6</sup> /°C)
1/53/47	4.34	9.18
1/53/47R	8.97	9.09
5.5/56/44	2.79	8.05
5.5/56/44R	6.57	6.57
8/65/35	3.57	8.02
8/65/35R		

Table 3 Mechanical Properties of Normal PLZT and their Reduced Counterparts  
(reduced at 975°C)

Sample	Density r (*10 <sup>3</sup> kg/m <sup>3</sup> )	Shear Modulus G (*10 <sup>10</sup> N/m <sup>2</sup> )	Poisson's ratio s	Young's Modulus E (*10 <sup>10</sup> N/m <sup>2</sup> )
1/53/47	7.41	2.2615	0.390	6.2870
1/53/47R	6.90	1.6343	0.363	4.4551
5.5/56/44	7.54	2.7019	0.374	7.4248
5.5/56/44R	7.13	2.3204	0.348	6.2558
8/65/35	7.51	2.9412	0.362	8.0118
8/65/35R	6.61	2.2598	0.342	6.0653

Table 4 Normalized displacements of the Rainbow ceramics having various dome heights

Dome Height	D <sub>norm</sub> (μm/(kv/cm))		Difference
	at Low E	at High E	
45 μm	0.20	1.14	0.94
144 μm	0.70	3.03	2.93
240 μm	1.30	6.11	4.81
282 μm	1.10	4.89	3.8



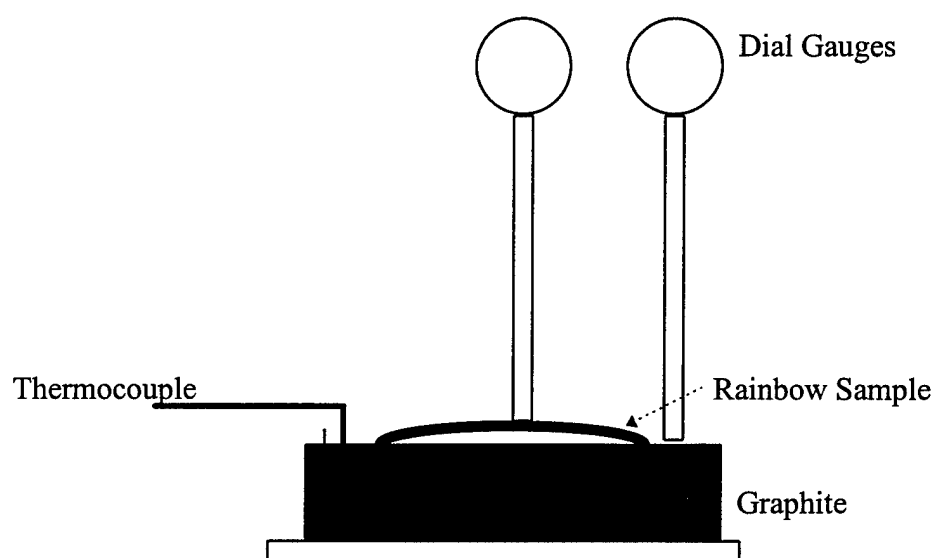


Fig. 1 Set up for measurement of dome height as a function of temperature

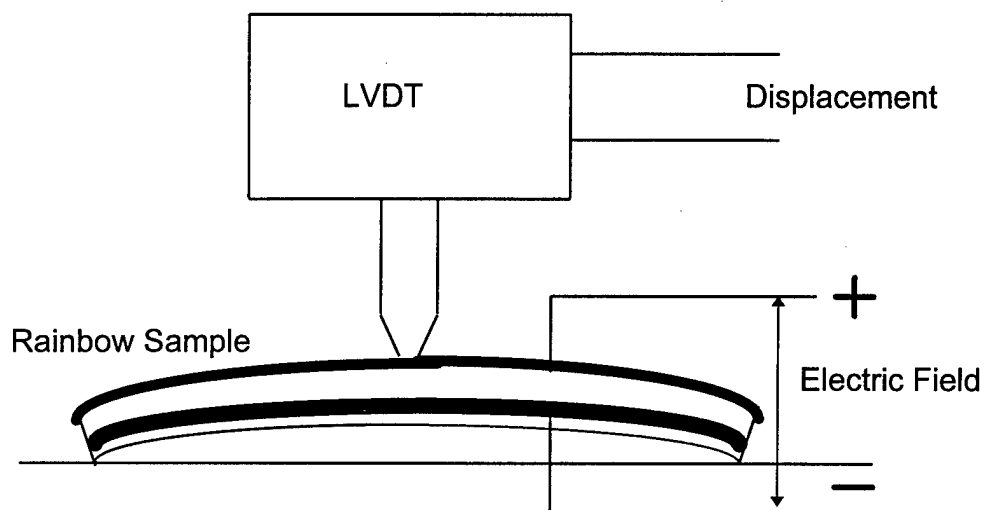
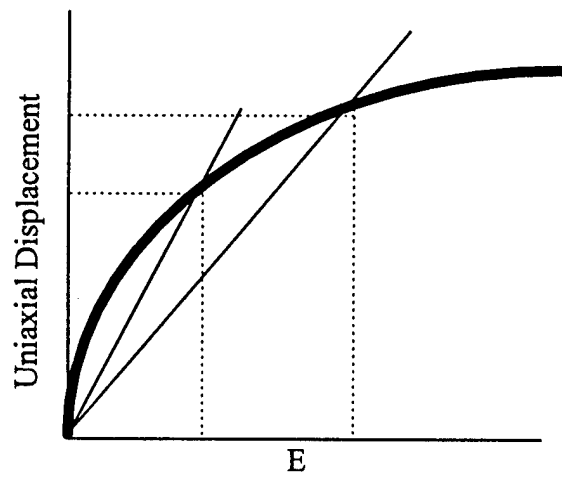


Fig. 2 Setup for displacement measurements



$$D_{\text{Norm}} = \frac{\text{Uniaxial Displacement}}{\text{Applied Electric Field}}$$

Fig. 3. Schematic diagram for definition of normalized displacement

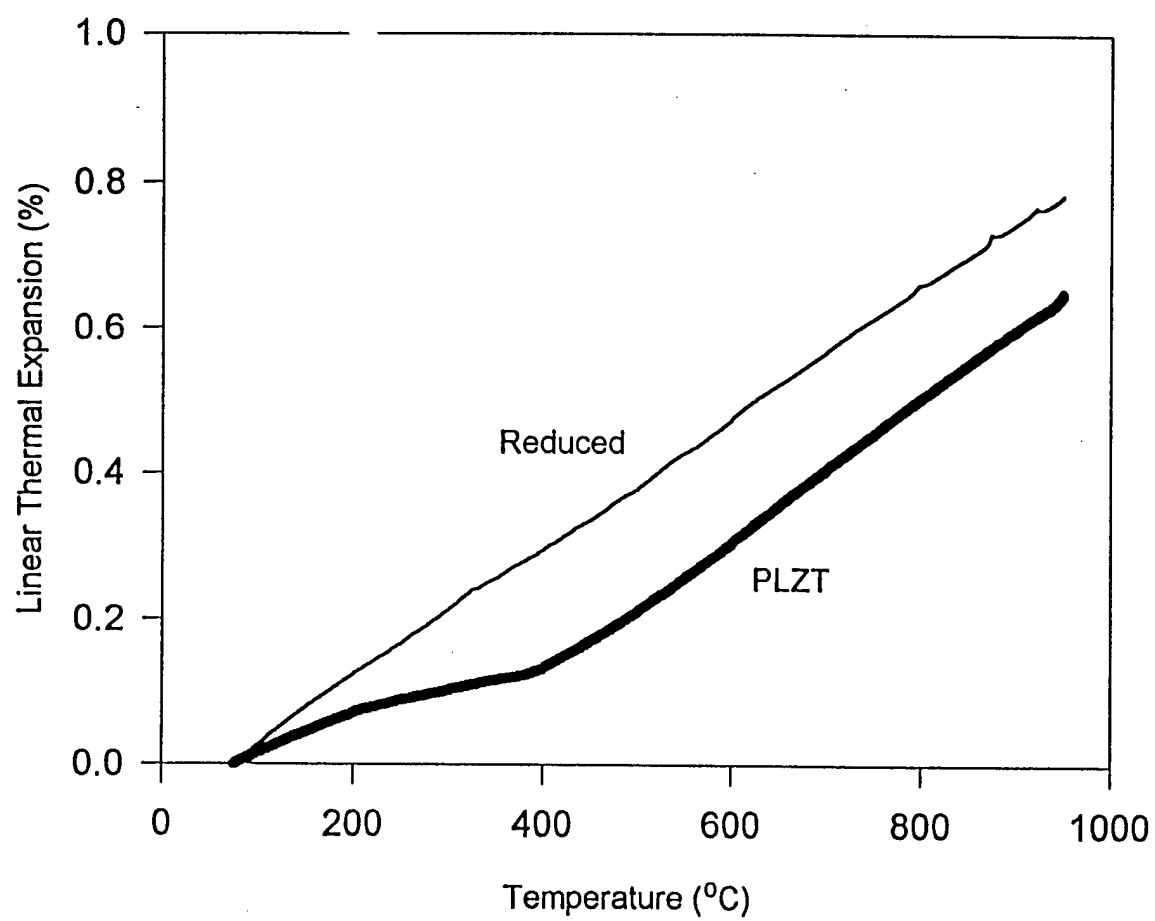


Fig. 4 Thermal expansion of reduced and oxide layers obtained from 1/53/47 PLZT ceramics

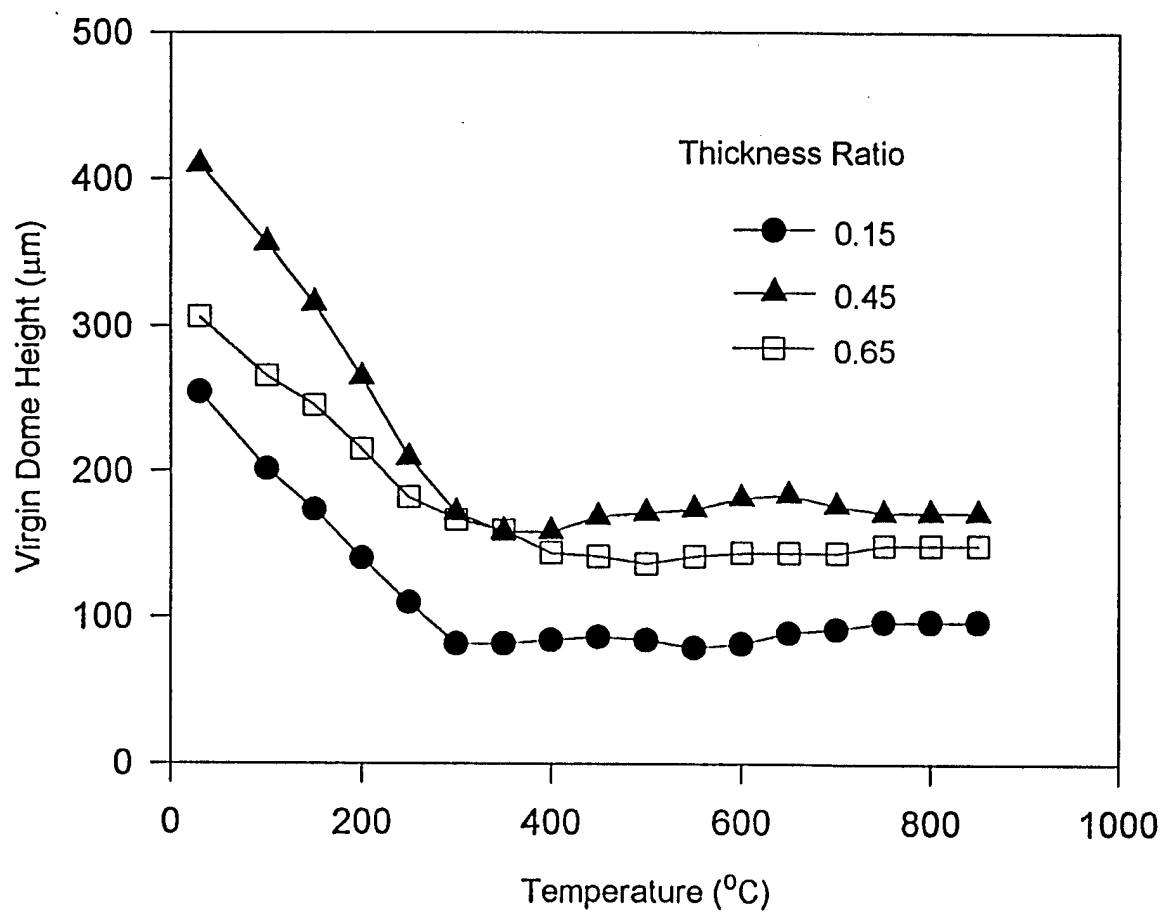


Fig. 5 Variation of virgin dome height of 1/53/47 PLZT Rainbow ceramics

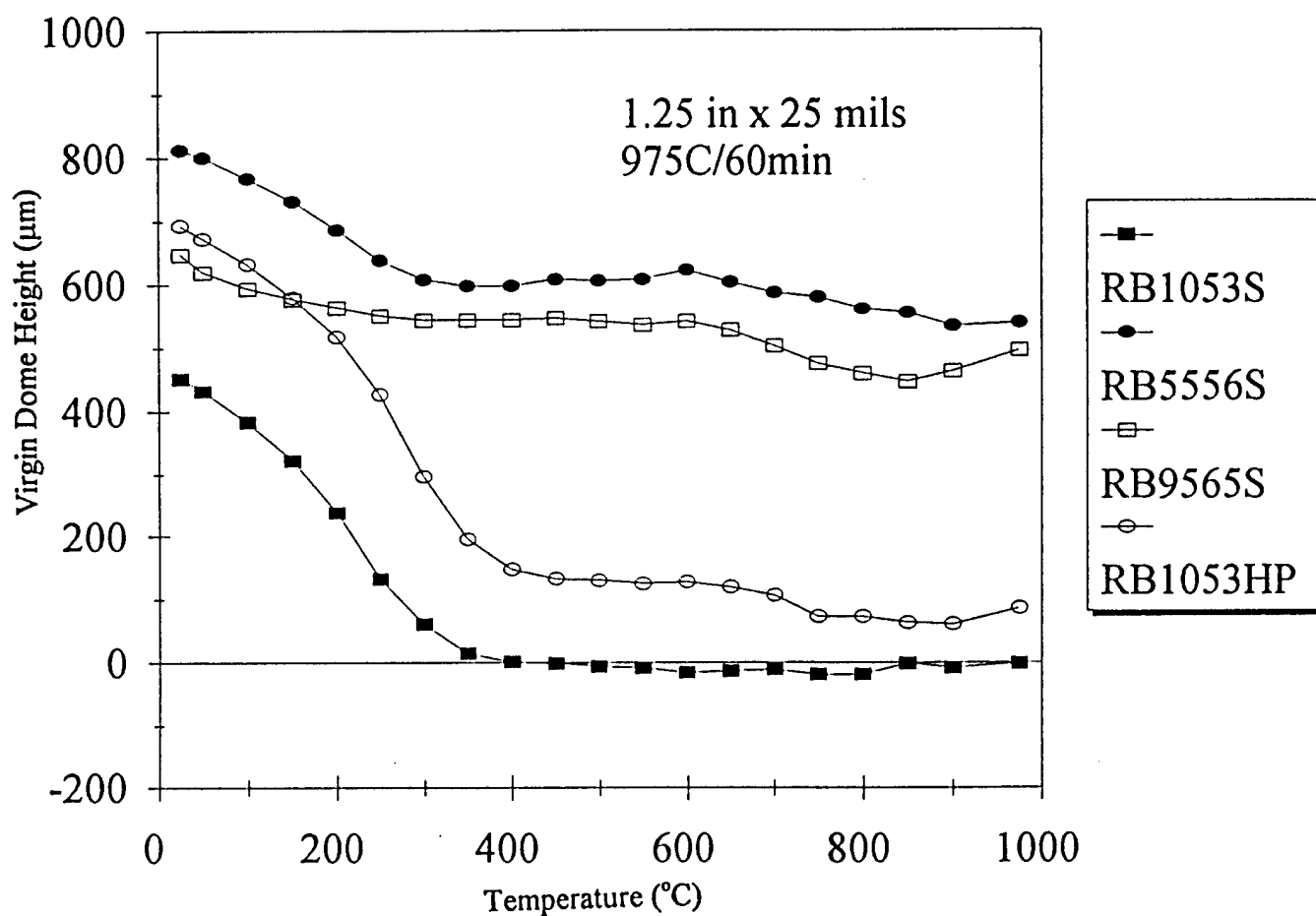


Fig. 6 Variation of virgin dome height observed for Rainbow samples fabricated from various PLZT ceramics  
 RB1053S : 1/53/47 sintered PLZT, RB5556S : 5.5/56/44 sintered PLZT,  
 RB9565S : 9/65/35 sintered PLZT, RB1053HP : 1/53/47 hot pressed PLZT

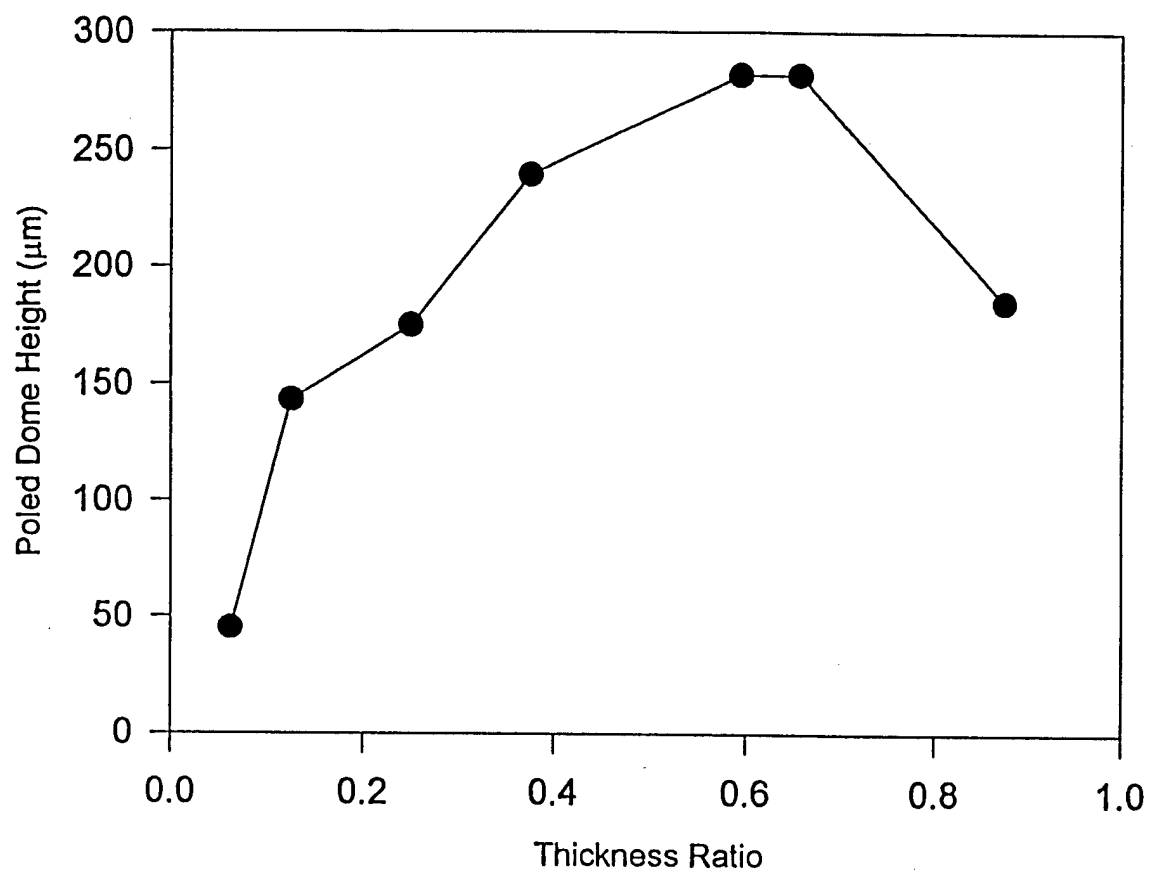


Fig. 7 Variation of poled dome height as a function of thickness ratio

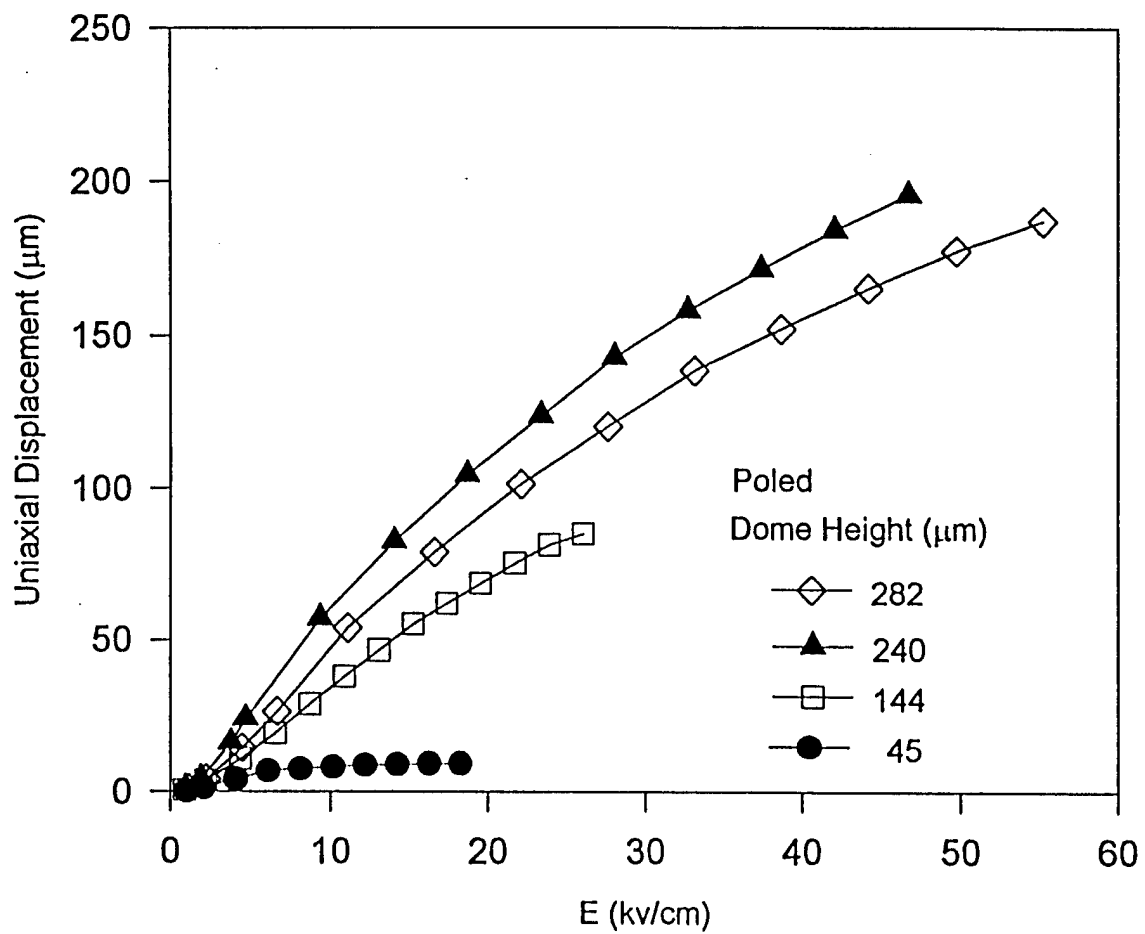


Fig. 8 Uniaxial displacement of Rainbow ceramics as a function of electric field



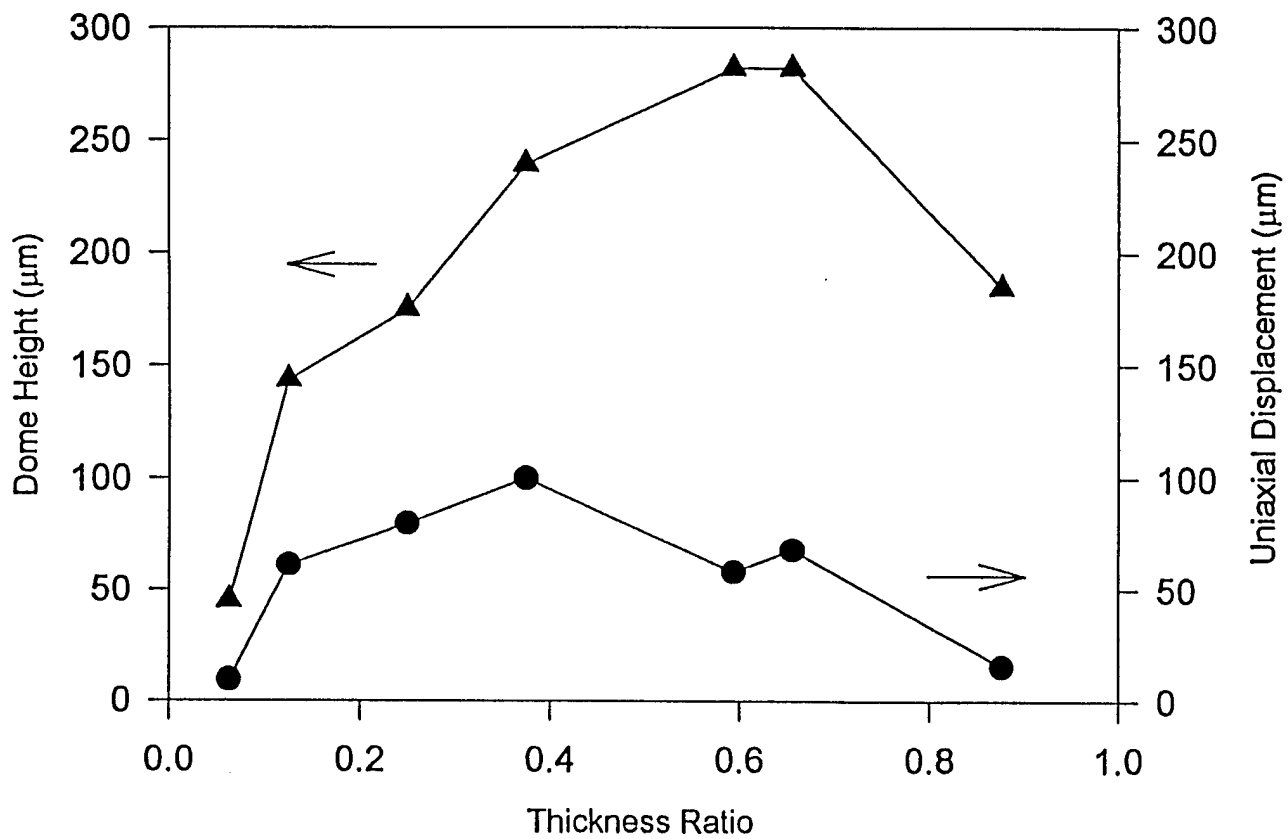


Fig. 9 Variation of dome height and uniaxial displacement of Rainbow samples as a function of thickness ratio

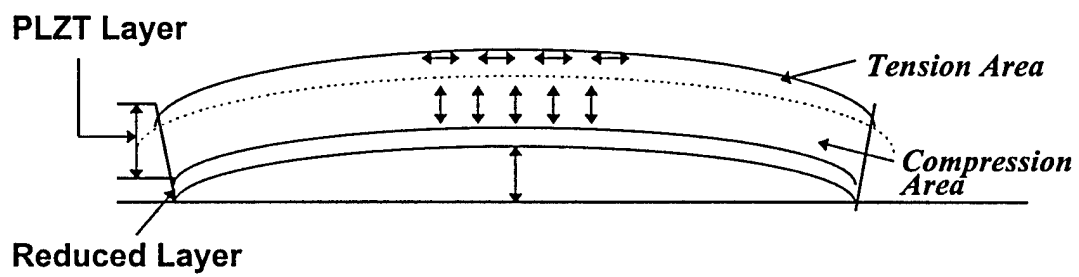


Fig. 10 Structure and internal stress distribution in a Rainbow ceramic

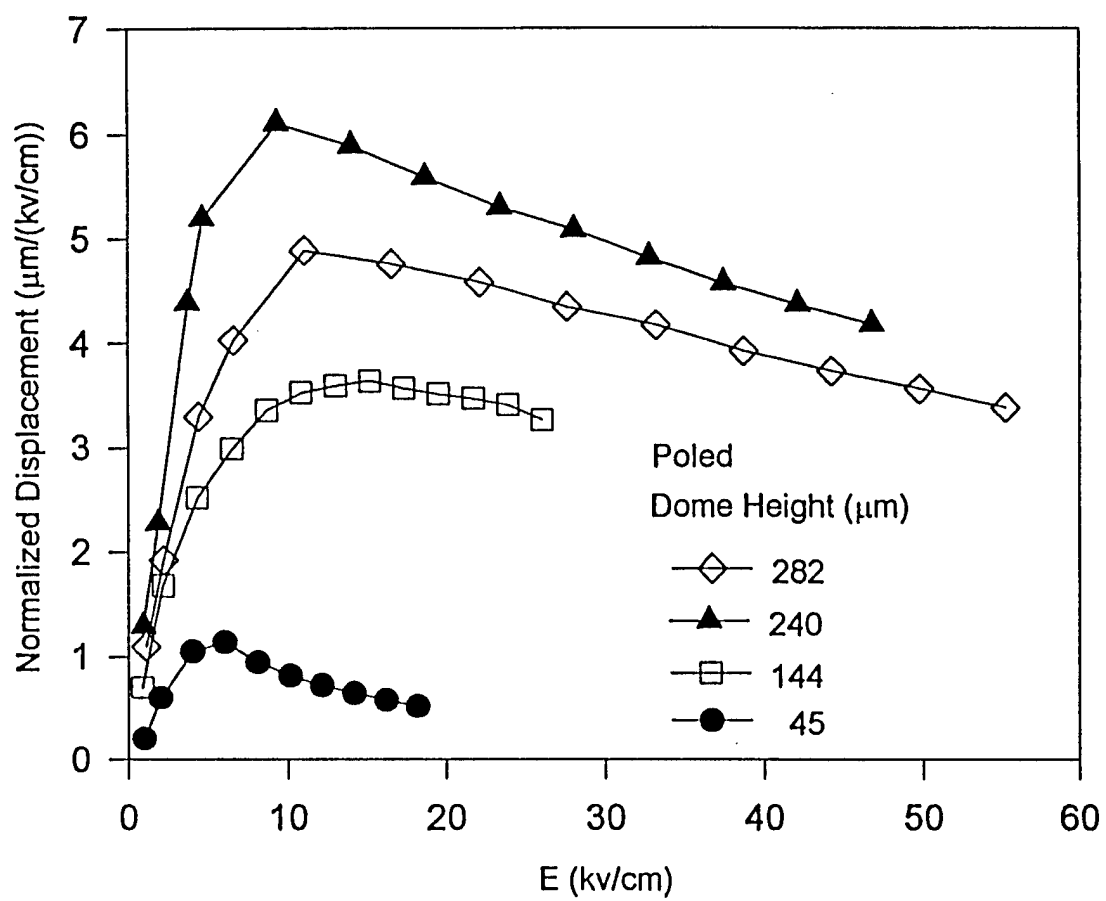


Fig. 11 Normalized displacement of Rainbow ceramics as a function of electric field

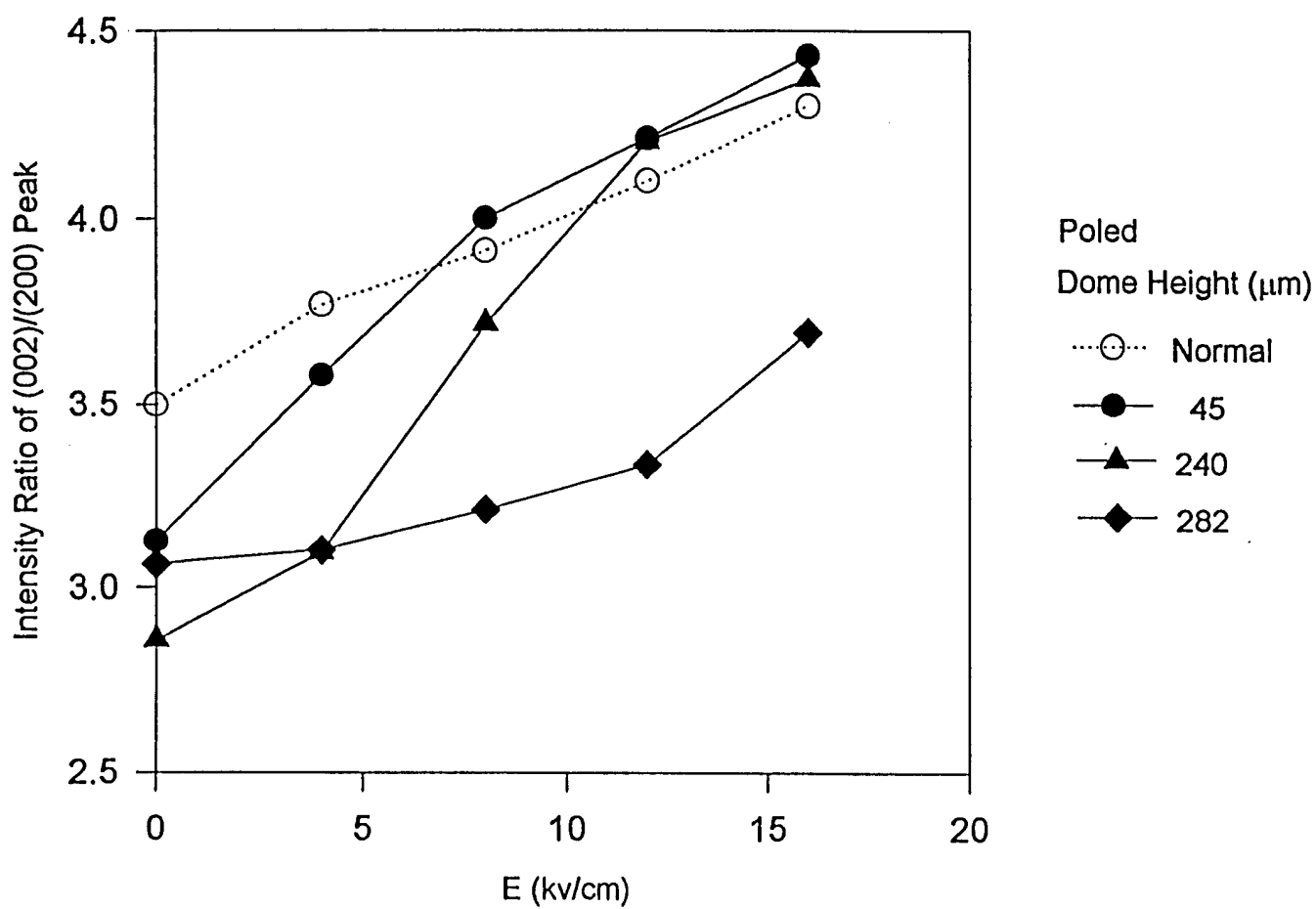


Fig. 12 Variation of X-ray peak intensity of (002) to (200) planes as a function of electric field

## **Part IV.**

### **Quantitative Characterization of Electrostrictive Butterfly Loops**

# **Quantitative Characterization of Electrostrictive Butterfly Loops**

Eugene Furman and Gene H. Haertling

*Gilbert C. Robinson Department of Ceramic Engineering, Clemson University,  
Clemson, South Carolina 29634-0907*

## **ABSTRACT:**

A new approach for the quantitative characterization of the electrostrictive butterfly loops is presented. Displacement phase angle and internal bias voltage can be determined with this technique. The model agrees well with the experimental butterfly loops for PLZT 8.4/70/30 benders. Of the possible contributors to the displacement phase angle the most important is the dielectric phase angle. The internal voltage, in addition to shifting the butterfly loop along the voltage axis, is shown to influence the magnitude of the displacement. An experimentally observed reduction of the displacement amplitude with increasing frequency was shown to be in part caused by the reduction of the internal voltage.

## I. INTRODUCTION

Considerable progress has been made in characterizing piezoelectric coefficients as complex quantities. The approaches based on piezoelectric resonance<sup>1</sup>, optical dilatometry<sup>2</sup>, and modified Berlincourt piezo  $d_{33}$  meter<sup>3</sup> have been successfully applied to determine complex piezoelectric coefficients of piezoelectric ceramics and polymers. The determination of complex piezoelectric constants is more straightforward than that of complex electrostrictive constants since the angle between the driving field and the induced strain for piezoelectric materials is independent of time. For electrostrictive materials, however, the induced strain is proportional to the square of the driving field, and the angle between the field and strain is not constant. Any model of electrostrictive response has to agree with the experimentally obtained phase information over the complete cycle of a periodic waveform.

The electrostrictive coefficients,  $M_{ijkl}$  and  $Q_{ijkl}$ , are defined as follows:

$$s_{ij} = M_{ijkl} E_k E_l \quad (1a)$$

$$s_{ij} = Q_{ijkl} P_k P_l \quad (1b)$$

where  $s$  is strain,  $E$  is the electric field, and  $P$  is the polarization. For practical applications the electrical field rather than polarization is more commonly used to control the strain. In many applications it would be advantageous to have a one-to-one correspondence between the field and strain, but the electrostrictive materials used in practice are characterized by the hysteretic butterfly loops. Hysteresis, in addition to energy dissipation, complicates the control of the sample position. A quantitative characterization and eventual control of the butterfly loops would enhance the use of electrostrictive ceramics in practical applications.

In this paper a technique to characterize butterfly loops of electrostrictive materials is described. In addition to the phase information, the technique is used to obtain the magnitude and sign of the internal voltage. For this study, the measurements were performed on RAINBOW (Reduced and Internally Biased Oxide Wafers) actuators based on lead lanthanum zirconate titanate (PLZT) ceramics. Rainbow actuators are novel devices capable of orders of magnitude larger displacements compared to the bulk ceramics for the same level of driving field, and as such are well suited for this study<sup>4-8</sup>.

In a number of ferroelectrics, including both soft and hard PZT ceramics, the hysteresis loop can be shifted along the field axis by a number of methods. The shift is characterized by an internal bias field,  $E_{int}$ . The internal bias field usually is caused by reorientable dipolar defects<sup>9-12</sup>. Defects are assumed to gradually orient in a direction corresponding to the minimization of the free energy. With benders such as Rainbows it is more appropriate to specify internal voltages rather than internal fields since the electric field inside a bender is not uniform.

## II. MODELING APPROACH

### A. Displacement Model

The relationship between the polarization and strain for the electrostrictive materials is often anhysteretic at low frequency<sup>13,14</sup>, implying that the electrostrictive coefficient  $Q$  is real. In contrast, the strain lags the driving field resulting in the butterfly loops, implying that the electrostrictive coefficient  $M$  is complex. The difference in response for the polarization and field-controlled strain is due to the phase lag between the polarization and driving field. For an applied sinusoidal field of  $E = E_0 \sin(\omega t)$  the polarization response is<sup>15</sup>:

$$P = P_0 \sin(\omega t + \delta) = f(\omega) E_0 \sin(\omega t + \delta). \quad (2)$$

(Note: In Eq. (2) and all further equations, the indices are omitted for clarity, but the tensor properties are implied.)

The modeling technique is applicable only when  $P_0$  is linearly proportional to  $E_0$ , i.e., when the factor  $f(\omega)$  is not a function of  $E_0$ , only of frequency. The dielectric phase angle,  $\delta$ , is related to the imaginary and real parts,  $\epsilon''(\omega)$  and  $\epsilon'(\omega)$ , respectively, of the dielectric constant,  $\epsilon$ , by:

$$\tan(\delta) = \epsilon''(\omega)/\epsilon'(\omega). \quad (3)$$

Assuming that there is no phase shift between the polarization and strain we can now rewrite Eq. (1b) as

$$s = Q(f(\omega) E_0 \sin(\omega t + \delta))^2 \quad (4)$$

indicating that with respect to the electric field, both the polarization and strain experience hysteresis defined by the same phase shift constant,  $\delta$ . For ferroelectric materials,  $\epsilon'(\omega)$  is orders of magnitude greater than  $\epsilon_0$ , in which case the relationship  $f(\omega) = \epsilon'(\omega)/\cos(\delta)$  is applicable<sup>15</sup>. Eq. (4) in the final form becomes:

$$s = Q(\epsilon'(\omega) E_0 \sin(\omega t + \delta)/\cos(\delta))^2 = \beta \sin(\omega t + \delta)^2 \quad (5)$$

where  $\beta = Q(\epsilon'(\omega) E_0 / \cos(\delta))^2$  is a constant at a particular frequency.

For a Rainbow actuator the observed displacement is a function of the effective electrostrictive coefficients (primarily  $M_{12}$ , which may be affected by internal stress compared to the stress-free constant), and the sample geometry. For the periodic electric field,  $E = E_0 \sin(\omega t)$ , the displacement lags the driving field, and since the electrostrictive coefficient  $M_{12}$  is negative, the simplest expression for the displacement consistent with Eq. (5) is



$$D = -D_0(\sin(\omega t + \theta))^2. \quad (6)$$

A non-zero displacement phase angle,  $\theta$ , is required for hysteresis to occur when the displacement is plotted versus the electric field. In general,  $\theta$  is a function of three variables:

$$\theta = f(\delta, \theta_p, \theta_e) \quad (7)$$

where  $\delta$  is the dielectric phase angle defined in Eq. (3),  $\theta_p$  is the phase angle between the polarization and displacement, and  $\theta_e$  is the phase delay introduced by the measurement circuitry. The functional relationship between the three components is unknown. Nevertheless, should  $\theta$  be approximately equal to  $\delta$ , it would imply that the displacement phase angle,  $\theta$ , is controlled by the dielectric phase angle,  $\delta$ .

In order for the range of data from the model to correspond to the range of the experimental data, Eq. (6) was modified as follows:

$$D = D_0(1 - (\sin(\omega t + \theta))^2) \quad (8)$$

which results in the range of displacements being between zero and the maximum experimental displacement,  $D_0$ . In the case of Rainbow samples, the interpretation of the displacement curves requires taking into account the effect of an internal voltage which shifts the butterfly loop. To incorporate the effect of the internal voltage, Eq. (8) is modified to include additional terms, A and B:

$$D = D_0 - (A \sin(\omega t + \theta) + B)^2. \quad (9)$$

This expression implies that the internal bias field,  $E_{int}$ , and the displacement phase angle,  $\theta$ , throughout the oxide portion of the sample were treated as uniform. The internal bias voltage is then equal to the product of the internal field and the oxide layer thickness.

Expanding Eq. (9) further by making  $\theta$  and B voltage-dependent did not result in an appreciable improvement in fit to the experimental data and made solution convergence more problematic. Therefore, Eq. (9) was used to fit the experimental displacement data.

Since the maximum displacement,  $D_0$ , is known from the experimental data, there are only three constants, A,  $\theta$ , and B, which have to be determined for the model. The Marquart-Levenberg algorithm was used to find the values that give the best fit between the model and the data over a complete period.

Since  $B/A$  and  $V_{\text{int}}/V_{\text{apl}}$  both define the relative shift of the butterfly loop, the internal voltage was calculated from the expression:

$$V_{\text{int}} = (B/A)V_{\text{apl}}. \quad (10)$$

It is preferable to characterize Rainbow devices in terms of internal voltages rather than internal fields because (1) the electric field in a Rainbow device may not be uniform due to the nonuniform stress distribution, and (2) the oxide and reduced layer thicknesses may not be known precisely.

## B. Polarization Model

To model the polarization loops the applied voltage waveform was first fit with the Marquart-Levenberg algorithm using the expression:

$$V_{\text{apl}} = V_1 \sin(\omega t + \theta_1) \quad (11)$$

where  $\theta_1$  is determined by the trigger level of the oscilloscope. The voltage proportional to the polarization was fit to the expression:

$$V_p = V_2 \sin(\omega t + \theta_2). \quad (12)$$

The dielectric phase angle,  $\delta$ , between the polarization and driving voltage is calculated using the following expression:

$$\delta = \theta_2 - \theta_1. \quad (13)$$

## III. EXPERIMENTAL PROCEDURE

Rainbow ceramics chosen for this study had the composition PLZT 8.4/70/30 (with respect to the  $\text{ABO}_3$  perovskite structure, 8.4 mol. % La replaces Pb on the A site, and 70 mol. % Zr and 30 mol. % Ti occupy the B site). Samples of this composition exhibit the electrostrictive strain response.

Rainbow sample preparation and properties were reported previously<sup>4-8</sup>. PLZT 8.4/70/30 samples were hot-pressed at 1200 °C for 6 hours at 14 MPa. A Rainbow was produced from the lapped wafer by placing the wafer on a graphite block and introducing the assembly into a preheated furnace. Reduction times at 975 °C were 90 and 120 minutes for samples 1 and 2, respectively. The reduction conditions were such that the samples were reduced on one side only. The epoxy silver electrodes used for measurements were cured at 200 °C. Both Rainbow samples had diameters of 32 mm and thicknesses of 0.51 mm. A diagram of a Rainbow sample is shown in Fig. 1.

The principle of operation of a Rainbow actuator is similar to that of a unimorph<sup>16</sup>. The reduced layer does not change its dimensions when electrical field is present and is a good electrical conductor. The oxide layer retains PLZT properties and changes its dimensions when electric field is across it. To satisfy boundary conditions at the interface between the oxide and reduced layers, the sample flexes when voltage is applied.

Field-induced displacements were determined using an LVDT (Linear Variable Differential Transformer)-based apparatus at room temperature. Unless otherwise specified, the displacements were measured by placing the extension rod at the center of the sample's oxide surface. The displacement and applied voltage data were collected by a computer for data analysis.

Dielectric measurements were performed using a Sawyer and Tower circuit. Data was collected using an HP 54504A digital storage oscilloscope, then transferred to a computer where hysteresis loops were modeled. In addition, an EG&G 5302 lock-in amplifier was used to measure the phase difference between the applied voltage and the voltage across the reference capacitor.

## IV. RESULTS AND DISCUSSION

### A. Modeling

Butterfly loops with no internal bias voltage were calculated for displacement phase angles,  $\theta$ , of  $0^\circ$ ,  $-10^\circ$ , and  $-20^\circ$  using Eq. (9), and the results are shown in Fig. 2. Two consequences of increased phase angle magnitude are: (1) a more pronounced hysteresis corresponding to a greater energy dissipation, and (2) a depression of the zero field point. However, the phase angle has no effect on predicted displacement magnitude. The sample with a zero phase angle displays a one-to-one correspondence between the driving voltage and the displacement.

Three butterfly loops with the internal bias voltage magnitudes,  $|V_{int}|$ , of 0 %, 10 %, and 30 % of the applied voltage magnitude,  $|V_{apl}|$ , were calculated and are shown in Fig. 3. For each of the loops the displacement phase angle,  $\theta$ , was kept constant at  $-10^\circ$ . The displacement loops were normalized to make the maximum displacement,  $D_0$ , equal to one for the loop with zero internal bias voltage. The results of increasing internal voltage include an increase in the magnitude of the displacement and a shift of the loop horizontally. The increasing range of displacements with increasing internal voltage is a consequence of the quadratic dependence of the displacement on a total local field which includes both the applied and internal fields. This effect could be significant in samples with large internal voltage. For example, in the case of  $|V_{int}| = 30\%$  of  $|V_{apl}|$ ,  $D_0$  is increased by 69 %. In contrast, for piezoelectric materials the internal field would have no effect on the magnitude of displacement unless the internal field is sufficiently large to introduce a nonlinear response.

## B. Comparison of Model to Measurements

The comparisons between the experimental butterfly loops and the model are shown in Fig. 4. The samples were tested with  $\pm 200$  V, 1 Hz sinusoidal waveforms. Excellent agreement between the experimental and modeling loops over the complete range of measurements for both samples supports the validity of the model. The internal voltages,  $-4.6$  V and  $-5.5$  V, and the phase angles,  $-12.1^\circ$  and  $-11.8^\circ$ , for samples 1 and 2, respectively, are quite similar. Although the internal voltages are small compared to the driving voltage, they increase the displacement by 4.6 % and 5.5 % for samples 1 and 2, respectively, compared to the hypothetical samples with no internal voltage. The signs of the internal voltages are negative, which is consistent with the easy switching direction being towards the oxide-reduced layer interface.

Both samples were well aged. To test the effects of aging on the displacement characteristics, sample 1 was thermally depoled and remeasured within 1 hour. The results were similar to the well-aged sample: an internal bias voltage of  $-6.1$  V and a displacement phase angle of  $-11.9^\circ$  were obtained from the model, indicating that the butterfly loop parameters do not change appreciably with aging.

The curvature of a Rainbow and its internal stresses vary as a function of distance from the center of the sample, with the largest tensile stress on the oxide surface near the edges of the sample predicted by Finite Element Modeling and characterized by x-ray diffraction<sup>6</sup>. Stress-optic measurements gave direct evidence of nonuniform stresses near the sample edges in the bulk of the oxide layer<sup>17</sup>. Since internal stresses are likely to contribute to internal voltages in Rainbow samples, the butterfly loops were measured for samples 1 and 2, with the data obtained along the sample surface starting at the center and moving toward the edge. Good agreement between the experimental data and the model was obtained for all of the loops.

Experimental field-induced displacements,  $D$ , and modeled displacement phase angles,  $\theta$ , and internal bias voltages,  $V_{\text{int}}$ , are shown for both samples in Fig. 5 ( $\theta$  and  $V_{\text{int}}$  are negative values, but graphed as positive). The maximum displacement was observed at the center of the samples, reducing gradually towards edge. For sample 1 the internal voltage showed a gradual reduction from the center towards the edge of the sample. For sample 2 the internal voltage was fairly constant across the sample. The phase angles were fairly constant for both samples except near the edge of sample 2.

The frequency dependence of the butterfly loop parameters for sample 1 is shown in Fig. 6. The largest reduction of displacement amplitude occurred between 1 and 10 Hz. Interestingly, the internal voltages also showed a large drop off in the same frequency range. Of the 21 % reduction in displacement from 1 to 10 Hz, approximately 6 % was due to the change in the internal voltage. It is likely that the internal voltage is nonuniform throughout the oxide layer. With increasing frequency, the regions in which polarization reorientation with applied field are hardest to achieve will not switch, causing the reduction in both the displacement magnitude and observed internal voltage.

The calculated phase angle was in a narrow range for all the measurements except at the highest frequency. An increase in the phase angle at 10 Hz is partly due to increased dielectric losses with increasing frequency and to the phase angle introduced by the LVDT's signal conditioner circuitry at higher frequencies.

The displacement versus polarization curve at 1 Hz is shown in Fig. 7. Unlike the displacement versus applied voltage, the displacement versus polarization has a one-to-one dependence. A plot of displacement versus polarization squared resulted in a straight line implying the electrostrictive response – a behavior similar to that of bulk PLZT 9.5/65/35 samples<sup>13,14</sup>. Since the displacement follows the polarization without the phase delay, the contribution of the experimental setup to the measurement of the phase angle at 1 Hz and below is negligible. However, at 10 Hz a slight hysteresis was observed.

Because the displacement follows the polarization with essentially no phase delay at frequencies of 1 Hz and below, the displacement phase delay is likely to have the origin in the dielectric phase delay between the driving electric field and the induced polarization in the same frequency range. The  $\theta_p$  and  $\theta_e$  contributions to  $\theta$  are negligible and  $\theta \approx \delta$ . To quantify the relationship between the dielectric and the displacement phase angles, the dielectric and displacement measurements were performed one after the other using identical experimental conditions. The dielectric phase angle,  $\delta$ , was determined from the phase lock measurement and the polarization loop curve fitting at 1 Hz. The observed and modeled polarization hysteresis loops are in good agreement (Fig. 8). A comparison of the dielectric and displacement phase angles in Table 1 indicates that they are almost identical, supporting the hypotheses that the electrostrictive losses are controlled by the dielectric response of the material.

## V. CONCLUSIONS

A technique for modeling butterfly loops for electrostrictive ceramics was presented. The displacement phase angle and internal voltages were determined from the curve fitting of the experimental displacement data to a characteristic function. The technique was successfully applied to PLZT 8.4/70/30 Rainbow ceramics. The internal voltages cause the asymmetry of the butterfly loops and increase the magnitude of the displacements. An observed reduction of displacement with increasing frequency is partly accounted for by a reduction of the internal voltages.

The phase angles and internal voltages did not change appreciably with the location on the sample at which the measurements were taken. The dielectric and displacement phase angles were found from modeling to be almost identical implying a close tie between the dielectric and the displacement responses. Absence of hysteresis in the dependence of displacement on polarization further supports the primary role of the dielectric response in determining the displacement phase angle of the electrostrictive Rainbow devices.

## VI. ACKNOWLEDGMENTS

The authors are grateful to Prof. C. L. Cox and Dr. G. Li for useful discussions. The work was sponsored by the U. S. Office of Naval Research under contract No. N00014-91-J508 and by NASA under contract No. NAG-1-1301.

- <sup>1</sup>J. Smits, IEEE Trans. Son. Ultrason. SU-23, 393 (1976).
- <sup>2</sup>T. Yamaguchi and K. Hamano, Jpn. J. Appl. Phys. 18, 927 (1979).
- <sup>3</sup>H. Wang, Q. Zhang, and L. E. Cross, Jpn. J. Appl. Phys. 32, L1281 (1993).
- <sup>4</sup>G. H. Haertling, Am. Ceram. Soc. Bull. 73, 93 (1994).
- <sup>5</sup>E. Furman, G. Li, and G. H. Haertling, Ferroelectrics 160, 357 (1994).
- <sup>6</sup>G. Li, Doctoral thesis, Clemson University, Clemson, South Carolina, 1995.
- <sup>7</sup>G. Haertling, in *Proceedings of the 9th IEEE Symposium on Applications of Ferroelectrics*, University Park, PA, edited by Pandey (IEEE, New York, 1994), pp.313-318.
- <sup>8</sup>C. Elissalde and L. E. Cross, J. Am. Ceram. Soc. 78, 2233 (1995).
- <sup>9</sup>K. Carl and K. H. Härdtl, Ferroelectrics 17, 473 (1978).
- <sup>10</sup>P. V. Lambeck and G. H. Jonker, J. Phys. Chem. Solids 47, 453 (1986).
- <sup>11</sup>G. Arlt and H. Neumann, Ferroelectrics 87, 109 (1988).
- <sup>12</sup>U. Robels, J. H. Calderwood, and G. Arlt, J. Appl. Phys. 77, 4002 (1995).
- <sup>13</sup>Z. Y. Meng, U. Kumar, and L. E. Cross, J. Am. Ceram. Soc. 68, 459 (1985).
- <sup>14</sup>Q. Zhang, W. Pan, A. Bhalla, and L. E. Cross, J. Am. Ceram. Soc. 72, 599 (1989).
- <sup>15</sup>H. Fröhlich, *Theory of Dielectrics* (Clarendon Press, Oxford, 1958).
- <sup>16</sup>K. Uchino, *et. al.*, J. Appl. Phys. 26, 1046 (1987).
- <sup>17</sup>G. Haertling, in *Annual Report to NASA, Part III*. (Contract No. NAG-1-1301, 1995-1996).

Table 1. Dielectric and displacement phase angles measured at 1 Hz

<u>Type of Phase Delay</u>	<u>Measurement</u>	<u>Phase Angle</u>
dielectric	lock-in amplifier	-12.2°
dielectric	Sawer-Tower and curve fitting	-12.2°
displacement	LVDT and curve fitting	-12.4°

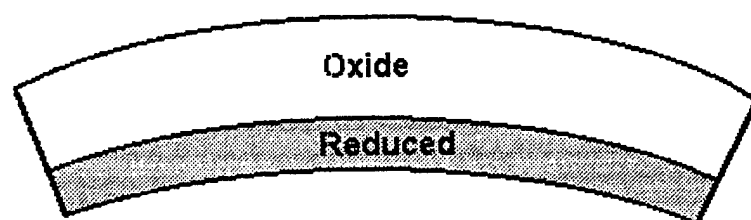


Figure 1. Diagram of Rainbow sample



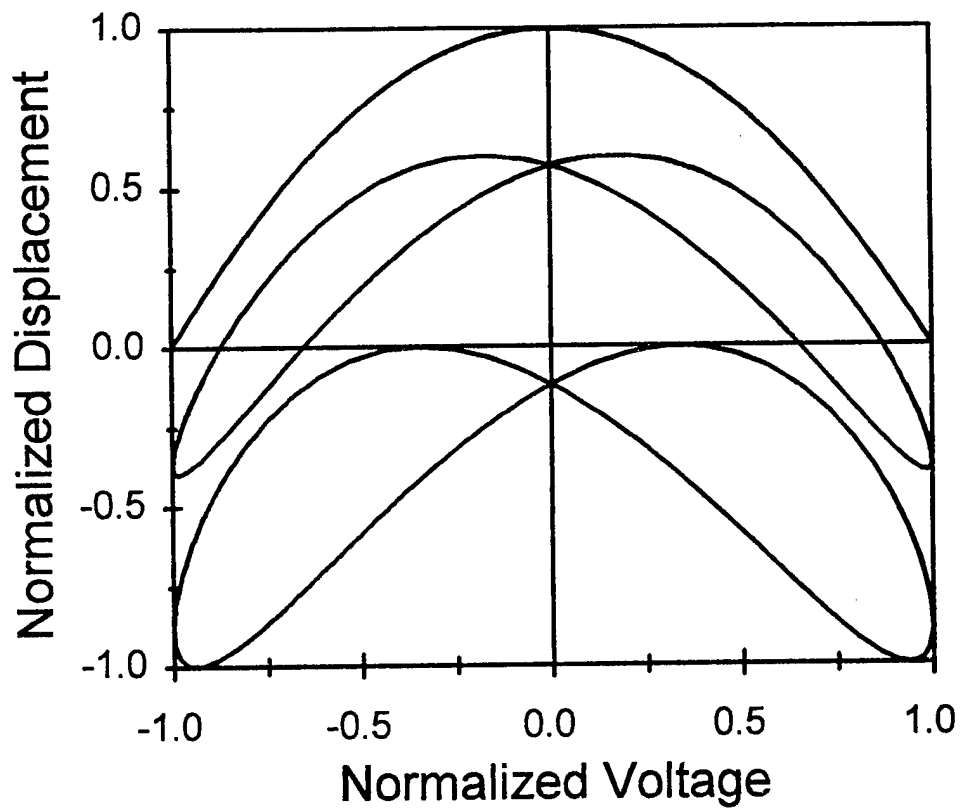


Figure 2. Butterfly loops calculated for different displacement phase angles. Top:  $0^\circ$ , Middle:  $-10^\circ$ , Bottom:  $-20^\circ$ . The internal bias voltage is 0 V for all loops.

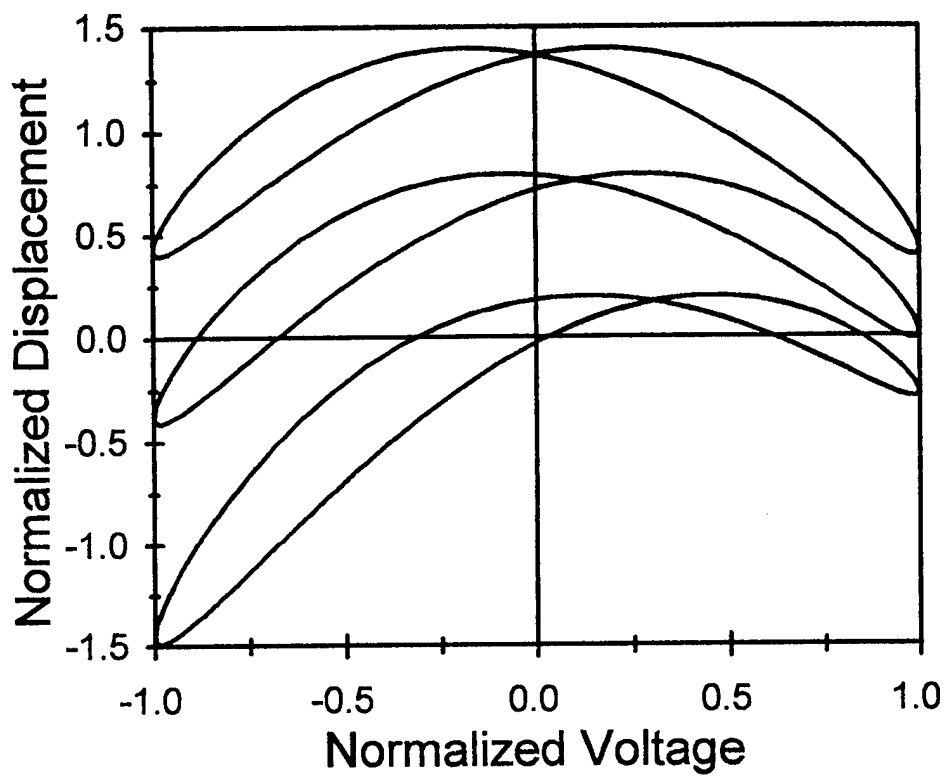


Figure 3. Butterfly loops calculated for different internal bias voltage magnitudes. Top: 0 %, Middle: 10 %, Bottom: 30 %. The displacement phase angle is  $-10^\circ$  for all loops.

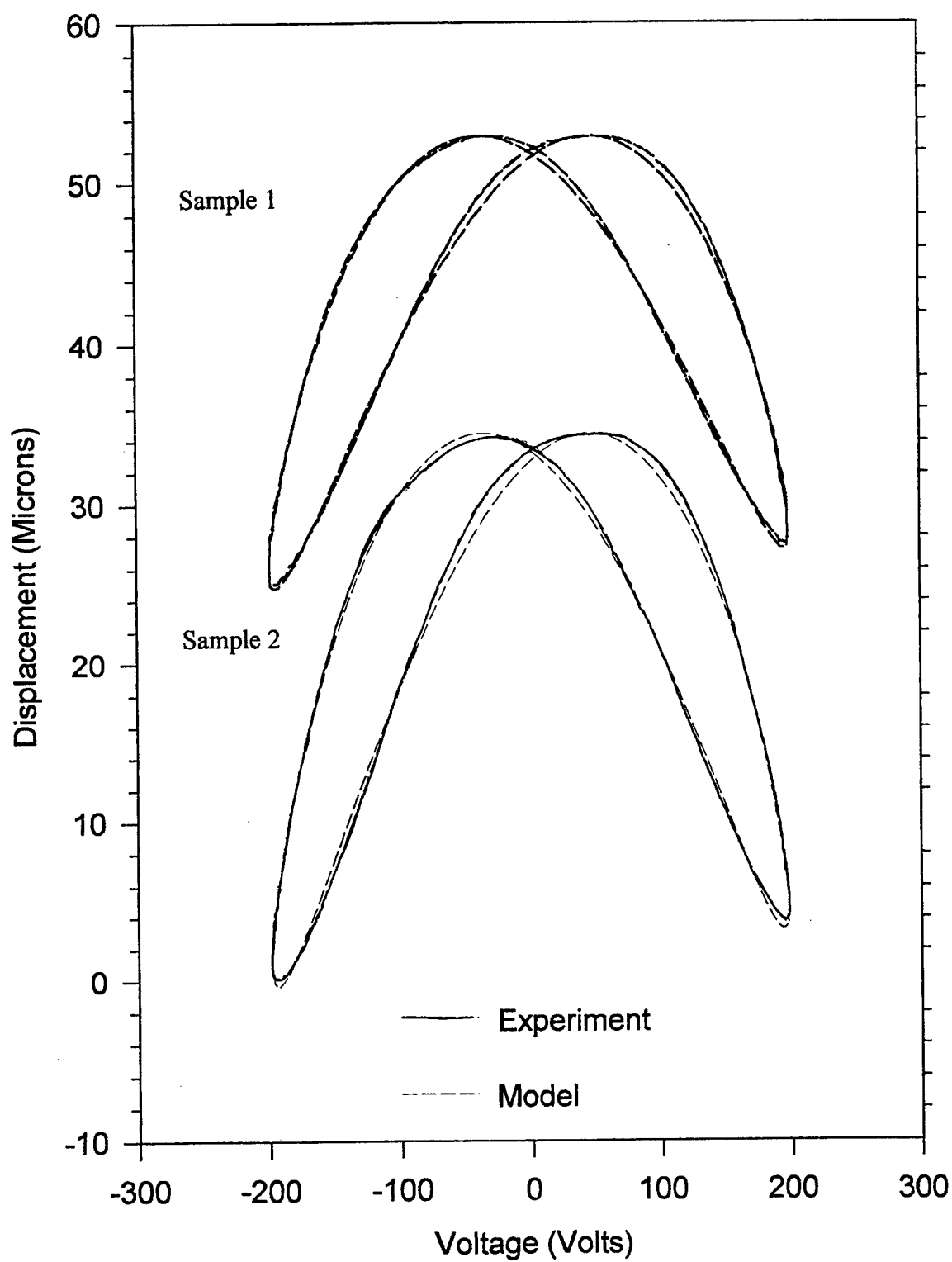


Figure 4. Experimental and modeled butterfly loops for samples 1 and 2.

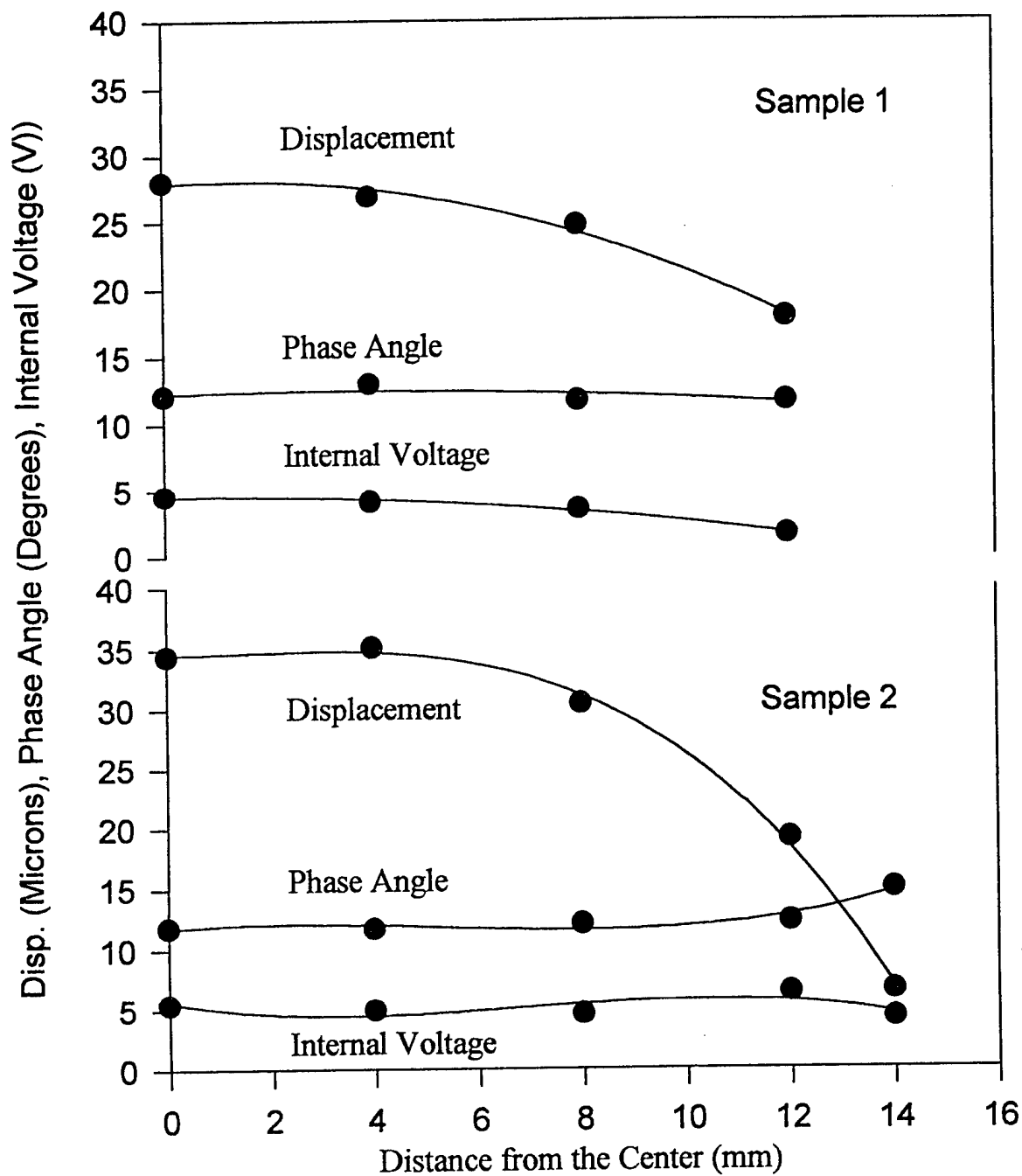


Figure 5. The characteristic parameters of the butterfly loop for samples 1 and 2 as a function of distance from the center. Phase angles and internal voltages are negative values, graphed here as positives.

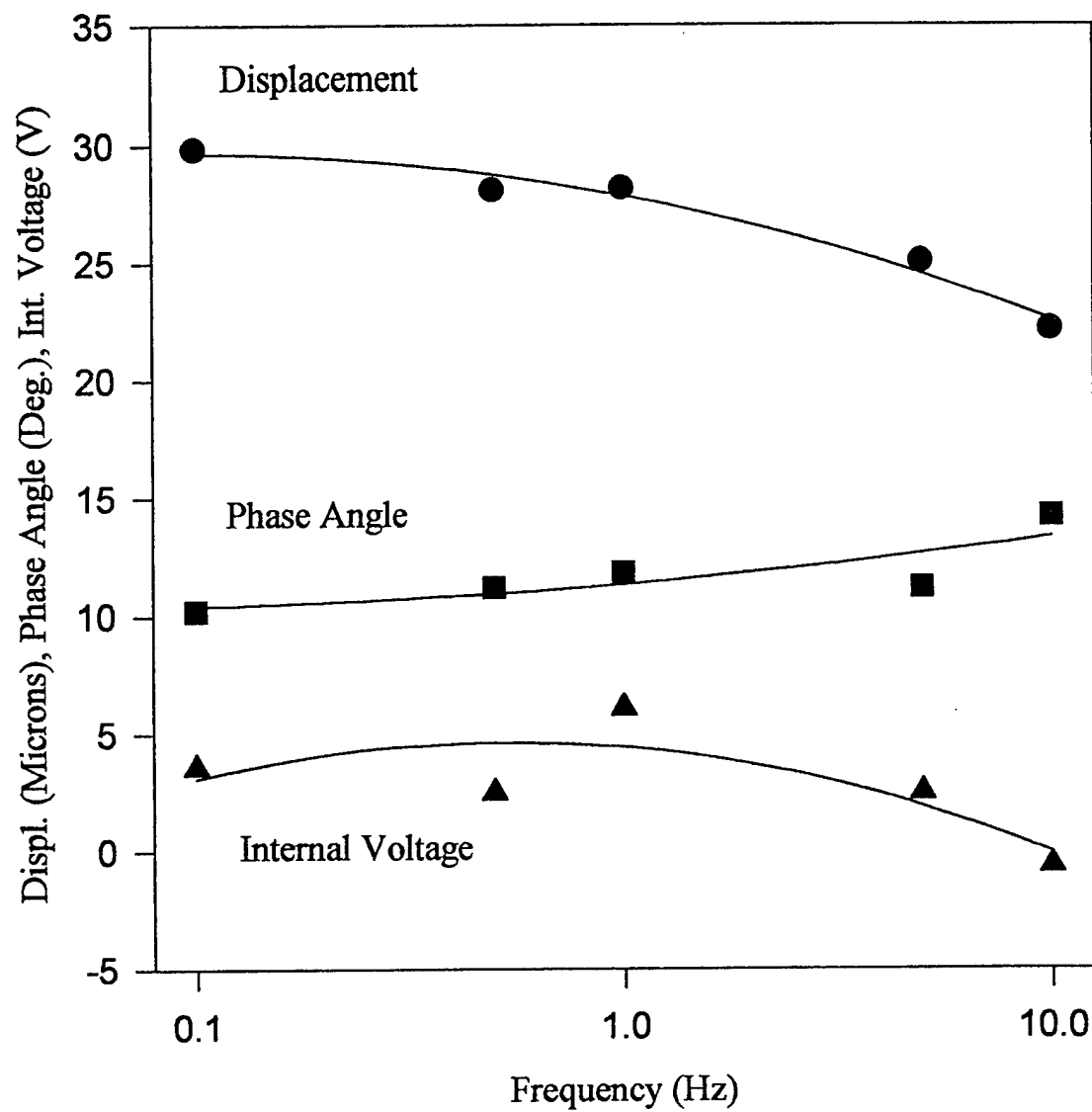


Figure 6. The characteristic parameters of the butterfly loop for sample 1 as a function of frequency. Phase angles and internal voltages are negative values, graphed here as positive.

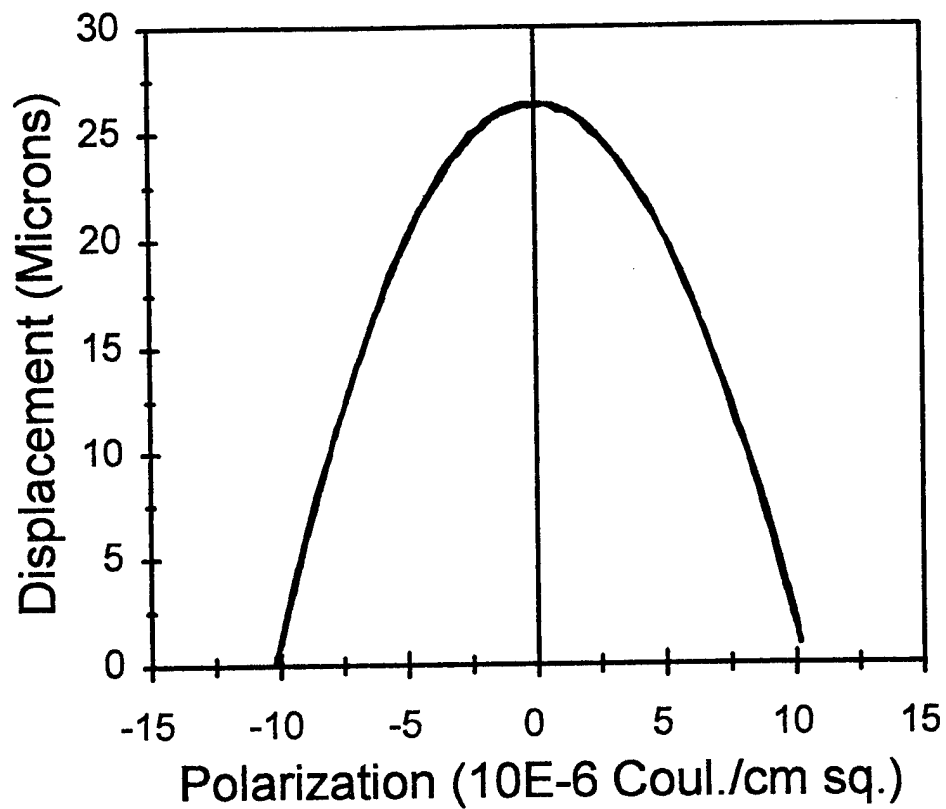


Figure 7. The displacement versus polarization loop at 1 Hz for sample 1.

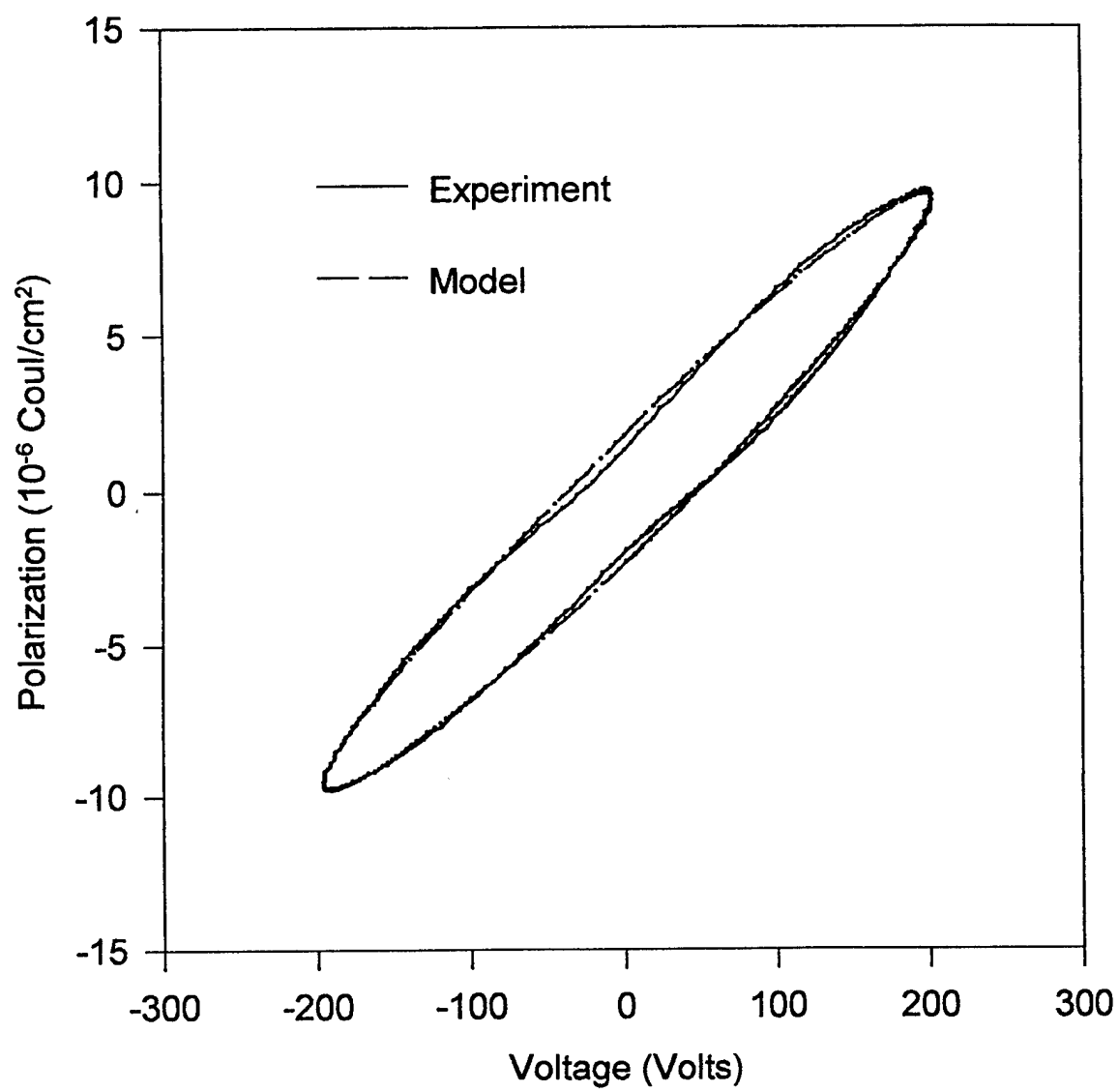


Figure 8. Experimental and modeled polarization loops for sample 1.

**Part V.**

**Characterization of Rainbow Ceramics for Active Vibration Control**

Submitted by :

Guang Li

Gene Haertling



# **Characterization of Rainbow Ceramics for Active Vibration Control and Noise Suppression Applications**

**Abstract:** With a combined merit of high stress-sensing response and high field-induced displacement, Rainbow ceramics appear very promising for such newer applications as active vibration control and noise suppression in advanced mechanical systems. The properties pertinent to this aspect of application, including the frequency dependence of field-induced displacement, electromechanical coupling, and stress-sensing response, were investigated using samples made from PLZT compositions. A method for mounting a Rainbow on a mechanical structure was developed that allows the Rainbow to deliver maximum stresses and achieve optimal stress sensing at the same time. The stress-sensing and stress-generating characteristics of Rainbows mounted on an aluminum cantilevered beam were determined and the results were compared with those obtained using normal PLZT elements on the same structure. Aging behavior in the presence of bias stresses, which is associated with this mounting technique, was measured and evaluated. Some results of finite element analysis and theoretical calculation are also presented.

## **1. Introduction**

Rainbow ceramics have been considered for a wide range of actuation applications due to their high field-induced displacement and moderate load-bearing capability [1]. More recent studies revealed that this new device possesses good stress-sensing characteristics as well when

operated in the dome mode [2]. The combined merit of high stress-sensing response and large field-induced displacement renders the Rainbow ceramic a very promising candidate for newer applications such as active vibration control and noise suppression in a variety of advanced mechanical structures and systems. This report presents results of an investigation on the properties of Rainbow ceramics which are pertinent to the applications in this respect. The properties investigated include the frequency dependence of field-induced displacement, electromechanical coupling and stress-sensing response. Some results of finite element analysis and theoretical calculation are given in conjunction with the experimental data. A special approach for mounting a Rainbow on a mechanical structure is introduced for which the stress-sensing and stress-generating characteristics were determined and compared with those obtained from normal ceramic elements of the same dimensions. Finally, the aging behavior of Rainbow properties associated with this mounting technique is discussed. It is hoped that the information given in this report can provide useful guidelines to further exploration of the Rainbow ceramic for active vibration control and noise suppression in the future. These results should also be of value for use of Rainbow ceramics in other fields of application.

## **2. Sample Preparation**

A number of different compositions from the PLZT system were chosen to prepare the ceramic wafers for the production of the Rainbow samples. These compositions, located in the vicinity of the morphotropic phase boundary separating the tetragonal and rhombohedral phases, include PLZT 1.0/53/47(La/Zr/Ti), 5.5/56/44, and 5.5/59/41. Fabrication procedures for the ceramic wafers and Rainbow samples are available elsewhere [3]. The Rainbow samples had dimensions ranging from 15-25 mils in thickness and 0.5-1.30 inches in diameter. Different

values of the thickness ratio, which is defined as the ratio of the reduced layer thickness to the total thickness, were achieved by using different reduction times during processing. As usual, the Rainbow samples are identified in terms of the composition and processing conditions of the original, unreduced ceramic wafers. For instance, RB1053 represents a Rainbow made from a PLZT 1.0/53/47 ceramic.

### **3. Results and Discussion**

#### *3.1 Frequency Dependence and Electromechanical Coupling*

Figure 1 shows the dependence of the field-induced displacement on the frequency of the driving electric field determined using an optical interferometry system made by Zygo Inc. A sample with its concave side facing downwards was placed on a flat metal plate and secured around its edge to the plate with three small pieces of Scotch tape that formed a triangle pattern. A sinusoidal unipolar voltage was applied to the sample. The magnitude of the applied voltage, which was in the same direction as the poling field, was between 20 and 75 V which corresponds to an electric field of 1.5 to 2.5 kV/cm depending on the thickness ratio of the sample (note that all the samples shown in Figure 1 had the same total thickness). Usually the displacement signal followed a sinusoidal trace analogous to the input voltage, except in the vicinity of a resonance where overtones of significant magnitude were observed in addition to the fundamental frequency. The peak-to-peak values in the displacement were recorded at each frequency increment.

As is indicated in Figure 1, all of the Rainbow samples exhibited a progressive decrease in the displacement with increasing frequency. Marked variations in the neighborhood of 900 Hz were caused by the mechanical resonance of the samples in this frequency region. It was found

that the displacement drop depended considerably on sample's thickness ratio. The percentage decrease from 0.1 Hz to 100 Hz was estimated to be 13%, 38% and 36% for RB5556-51, RB5556-43 and RB5556-59, respectively, whose thickness ratios are indicated in the figure.

The reduction of the displacement with increasing frequency was considered to be likely associated with the interaction of the internal stress with domain switching under applied field. With increase of the driving field frequency, the domains responsible for the stress-enhanced effect in the Rainbow ceramic [4] are expected to undergo enhanced relaxations originating from the internal friction due to the presence of the high internal stress, and eventually become locked. As a results, the field-induced displacement is reduced progressively. This argument appears to be well justified by the fact that a Rainbow behaves more like a conventional unimorph in terms of its field-induced displacement characteristics when the frequency is increased. Figure 1 also compares the Rainbow samples with a unimorph and a Cerambow. The unimorph sample was made by bonding a PLZT ceramic wafer to a fully reduced wafer at room temperature with a commercial epoxy. The Cerambow was produced on the basis of a stress-biasing technique analogous to the Rainbow technology, but the internal stress level in a Cerambow is considerably lower [5]. It can be seen that the displacement from the unimorph was nearly frequency independent throughout the frequency range studied. Similarly, there was only an approximately 8% drop in the displacement from 0.1 Hz to 100 Hz for the Cerambow sample, as compared to a 38% drop in the Rainbow of the same thickness ratio. This observation is consistent with the aforementioned stress-related mechanism for the frequency dependence of the Rainbow ceramic, because the internal stress in the unimorph is negligible and that in the Cerambow is much lower. It is worthwhile mentioning that in a study on Rainbows by Elissalde *et al* [6], it was found that in the regions near the reduced/unreduced layer interface the PLZT properties were slightly

altered due to changes in microstructure resulting from the chemical reduction process. These regions may play an increasingly important role in affecting the frequency-dependent characteristics as the unreduced layer becomes very thin.

The change of the effective coupling coefficient and mechanical quality factor for the dome mode with thickness ratio was given in Figures 2 and 3. The data in the figures were calculated according to equations  $k_{eff} = (f_p^2 - f_s^2)^{1/2} / f_p$  and  $Q_m = R / (\omega L)$  whose parameters were determined by curve-fitting the impedance spectrum of the sample using a standard equivalent circuit. A typical example of such curvefit is displayed in Figure 4. As is shown in Figure 2, the electromechanical coupling exhibited a maximum at a thickness ratio around 0.4. The mechanical  $Q_m$  in Figure 3 dropped drastically with increasing thickness ratio after peaking at the thickness ratio of approximately 0.2. This drastic reduction in  $Q_m$  suggests that additional relaxation mechanisms may have been introduced as the thickness of the unreduced layer diminishes.

The change of the effective coupling coefficient with thickness ratio was evaluated via the finite element method (FEM). For verification purposes the same relationship was also determined through analytical calculations. Due to unavailability of analytical equations for the disk-shaped bender structure the verification was performed based on strip-shaped structures. The modeling results obtained are given in Figure 5. It is surprising to note that the analytical models developed by different authors, although they all are able to produce consistent values for the field-induced displacements, provide totally different solutions to the dependence of the coupling coefficient on thickness ratio. Among these models Smits' model does not even give a correct answer for the fact the a finite value exists at the thickness ratio of unity, instead of

obviously a zero value. On the other hand, Ikeda's results nicely match the FEM curve (FEM-1) over the entire range of the thickness ratio. As is also shown in Figure 5, a disk-shaped structure (FEM-2) possesses a higher electromechanical coupling than does the strip-shaped structure (FEM-1) for a given thickness ratio.

The above modeling analyses have not taken into account the influence of either the internal stress or the domed configuration. When the effect of the curvature was included, the coupling coefficient values at lower thickness ratios were found to be improved, as is shown in Figure 5 (FEM-3). This implies that a curved structure is capable of conversing more energy than a flat structure. By comparing Figure 5 with Figure 2, it can be seen that the experimental values on the coupling coefficient are significantly lower than the theoretical predictions, particularly at higher thickness ratios (more than 50% lower in most cases). This difference between experiment and modeling was considered to be another indication of the frequency dependence of Rainbow properties since the coupling coefficient data were determined at the resonant frequencies. In other words, the difference between experiment and modeling may improve under steady state conditions.

Electromechanical coupling as a function of sample's diameter was determined for both the dome mode and the radial mode. A sample was measured starting at the largest diameter and then sanded down to a smaller diameter value for the next measurement. The results of these measurements are given in Figure 6 for two Rainbow samples of different compositions. As can be seen, the value for the radial mode is nearly independent of diameter from 1.3 inches down to 0.35 inches. As for the dome mode, there seems to be an optimum value at a diameter somewhere between 0.8 and 1.0. The corresponding relationship of the resonant frequency

versus diameter for the dome mode is displayed in Figure 7. As anticipated, the frequency values decreased inversely with diameter.

### *3.2 Stress-sensing and stress-generating characteristics of Rainbow on mechanical structure*

Conventional approaches for mounting a piezoelectric element to a structure to be controlled, such as surface mount and embedding, are not applicable to the Rainbow ceramic because of the domed configuration. When used on Rainbow ceramics, these approaches would be very inefficient in terms of energy transfer between the Rainbow and the structure. Deriving a suitable mounting method is, therefore, crucial for use of these devices for active vibration control and noise suppression. In this work, a special means was developed which is able to effectively deliver mechanical energy to the structure and, at the same time, sense the stresses in the structure. A schematic of this mounting technique with a Rainbow on a cantilevered structure is demonstrated in Figure 8. A Rainbow with a hole drilled through in the center is bolt held to the structure under prestress. When a voltage is applied across the Rainbow, the change of the curvature results in transfer of mechanical energy from the Rainbow to the structure through the variation of the bending moment and stretching force at the Rainbow's edge. This process is similar to the case of a piezoelectric element on a structure with a surface mount, as is also shown in the figure. Conversely, any vibrations of the structure cause changes in the Rainbow curvature which transform into electric signals via the piezoelectric effect of the Rainbow. In the following discussions, the Rainbow samples, and the piezoelectric elements used for comparison, were located at the positions  $\frac{1}{4}$  and/or  $\frac{1}{2}$  measured from the free end of an aluminum cantilevered beam having dimensions of 120×25×1.5 mm (length×width×thickness).

The piezoelectric elements had the same composition (PLZT 5.5/56/44) and dimensions as the Rainbow samples which were 22.4×0.5 mm (diameter×thickness).

Figure 9 illustrates the stress-sensing characteristics of a Rainbow on the aforementioned structure driven by another Rainbow nearby which was operated under three different levels of applied voltage. The stress-sensing Rainbow in this case was situated at the position  $\frac{1}{4}$  from the free end. Output signals were collected directly from the sample electrodes and fed to a lock-in amplifier controlled by a computer. The resonant characteristics of the structure can be clearly seen from Figure 9 along with the variation of the signal amplitude with frequency. It is evident that a higher driving voltage produced a higher level of stress which was approximately linearly proportional to the applied voltage.

The stress-sensing Rainbow sample in the above measurement was replaced by a piezoelectric element and similar measurements were carried out. The results obtained are displayed in Figure 10 together with the corresponding curve appearing in Figure 9 for comparison. As can be seen, the two curves exhibited very similar characteristics, with the Rainbow sample possessing a slightly higher sensing sensitivity in the low-frequency regions.

Likewise, the Rainbow sample used for the stress generation was substituted by a piezoelectric element. In this way the stress-generating characteristics of the Rainbow and the piezoelectric element could be compared. The measured results are presented in Figure 11. As indicated, the resonant behavior of the structure was slightly altered after replacement of the Rainbow sample by the piezoelectric element, but overall, the two curves look very similar. Based on the signal amplitude, it seems that the Rainbow sample was able to generate a higher level of stress as compared to the piezoelectric element. However, it should be mentioned that



the electric field on the Rainbow was also higher because the same amplitude of voltage was employed for the Rainbow and the piezoelectric element.

### *3.3 Rainbow Properties under Static Bias Stress*

As indicated previously, this mounting technique involves prestressing of the Rainbow on the structure. It is desirable, as also for other similar applications, to have some basic understanding of any effects of persistent external stresses on the Rainbow properties. In this study, selected Rainbow samples were subjected to static external stresses of various magnitudes by placing weights normal to the major surface of the samples. Changes in the properties such as dome height, field-induced displacement, coupling coefficient, capacitance and piezoelectric constant were recorded as a function of time. In one case two strip-shaped samples with identical dimensions and thickness ratio were tested under different levels of stress. In the other case disk-shaped samples having different thickness ratios were investigated under the same stress level.

Figure 12 displays the change of the dome height (curvature) with time for the samples indicated. RB5556-1 and RB5556-2 were strip-type samples of 20 mm long, 5 mm wide and 0.5 mm thick with a thickness ratio of approximately 0.3. Samples RB1053-1 and RB1053-2 had a circular geometry of 31.8 mm diameter and 0.675 mm thick, and their thickness ratios were approximately 0.3 and 0.6, respectively. As seen in Figure 12, the dome height of all the samples underwent a drastic reduction within 10 days after the stress was applied. Thereafter, the changes became leveled off for RB5556-1 and RB5556-2. However, for the RB1053 samples the decrease of the dome height progressed continuously, though less drastically, which is probably attributed to a much larger applied stress and a ferroelastically softer structure as

compared to the case of the RB5556 samples. The sample RB1053-1 was almost flattened out after approximately 100 days.

The change of the field-induced displacement under bias stress presents quite different characteristics among these samples, which is shown in Figure 13. For RB1053-2 the displacement first increased and then dropped progressively. On the contrary, the displacement of RB1053-1 decreased at the beginning but slightly recovered after about 70 days. The variations of the displacements for the RB5556 samples were relatively gradual. These characteristics of the field-induced displacement under external stress are believed to be a combined consequence of a number of influences whose details remain to be understood. However, the behavior of RB1053-1 seems to be explainable from the curvature change under stress. Two processes with opposite consequences are considered to occur as the curvature is reduced. On one hand, the stress-enhanced effect for the field-induced displacement diminishes with reducing dome curvature. On the other hand, the reduction in the dome curvature results in a decrease of the geometrical stiffness and consequently an increase in the displacement. As the sample becomes flat under the influence of stress, the effect of the stiffness reduction becomes dominant. As a result, an increase of the displacement is expected to occur. It is also recognized that intrinsic degradation of the properties under stress, for example due to internal microcracks, would eventually play a significant role.

The change of the coupling coefficient for the dome mode is displayed in Figure 14. The coupling coefficient values for the RB5556 samples were not significantly affected by external stressing. As for the RB1053 samples, the coupling coefficient showed a trend of increase with time. Such a result appears to be also associated with the reduction in the curvature, because it was found experimentally that a circular sample with smaller curvature corresponds to a higher

coupling coefficient value. This, however, is contradictory to the finite element analyses given previously, which, again, could be ascribed to the frequency-dependent characteristics of the Rainbow samples.

Figures 15-16 show the piezoelectric coefficient  $d_{33}$  and capacitance as a function of time, respectively. Statistically both the parameters increased with time, but at various degrees.

From the above results, it was recognized that the change of the Rainbow properties under external bias stress is very complex. It is dependent on the extrinsic factors such as the geometry and thickness ratio of the sample as well as the intrinsic properties like the composition and microstructure. Further work is needed for a better understanding of this subject.

#### **4. Summary and Conclusions**

The properties of Rainbow ceramics relevant to vibration control and noise suppression applications, such as the frequency dependence of field-induced displacement and electromechanical coupling, were investigated using samples made from PLZT compositions. It was found that the field-induced displacement decreased progressively with increasing frequency. The extent of the decrease depends strongly on the thickness ratio of the sample, among other factors. The coupling coefficient of the dome mode was considerably lower than the theoretical predictions for all samples having different dimensions and thickness ratios. This may be attributed to the frequency-dependent characteristics of Rainbow ceramics, because the experimental values were determined at the resonant frequencies, which could be quite different than the values at lower frequencies.

A method for mounting a Rainbow on a mechanical structure was developed. The results for Rainbows mounted on an aluminum cantilevered beam show that their stress-sensing and

stress-generating characteristics are similar to or better than those obtained using normal PLZT elements on the same structure. The aging behavior of Rainbow properties in the presence of bias stresses, which is associated with this mounting technique, was evaluated. Generally, the changes of the Rainbow properties with time under external stresses are quite complex, as they are strongly dependent on both intrinsic and extrinsic influences. The trend of property variation with time is usually different from property to property, and the magnitude of the variation at a given time period is also very different for different properties.

## 5. References

- [1] G. H. Haertling, "Rainbow Ceramics - A New Type of Ultra-High-Displacement Actuator," *Am. Ceram. Soc. Bull.*, **73**, 93-96 (1994).
- [2] G. Li and G. H. Haertling, "Stress-Sensing Characteristics of PLZT-Based Rainbow Ceramics," accepted for publication in *Smart Materials and Structures* (1997).
- [3] G. Li, E. Furman and G. H. Haertling, "Fabrication and Properties of PSZT Antiferroelectric Rainbow Actuators," *Ferroelectrics*, **188**, 223-236 (1996).
- [4] G. Li, E. Furman and G. H. Haertling, "Stress-Enhanced Displacements in PLZT Rainbow Ceramics," accepted for publication in the *Journal of the American Ceramic Society* (1997).
- [5] B. Barron, G. Li and G. H. Haertling, "Temperature Dependent Characteristics of Cerambow Actuators," in the *Proceedings of the Tenth IEEE International Symposium on Applications of Ferroelectrics*, Rugster, New Jersey, 1996 (to be published).
- [6] K. Elissalde, L. E. Cross and C. A. Randall, "Structure-Properties Relations in Reduced and Internally Biased (Rainbow) Actuators," *J. Am. Ceram. Soc.*, **79**, 2041-48 (1996).

- [7] Jan G. Smits and Wai-shing Choi, "The Constituent Equations of Piezoelectric Heterogeneous Bimorphs," *IEEE Trans. Ultrasonics, Frequencies, Frequency Control*. **38**(3), 256-270 (1991).
- [8] M. R. Steel, F. Harrison and P. G. Harper, "The Piezoelectric Bimorph: an Experimental and Theoretical Study of its Quasistatic Response," *J. Phys. D: Appl. Phys.*, **11**, 979-989 (1978).
- [9] Ikeda, T. 1994. *Fundamentals of Piezoelectricity*, Oxford University Press, Oxford, Chap. 4.

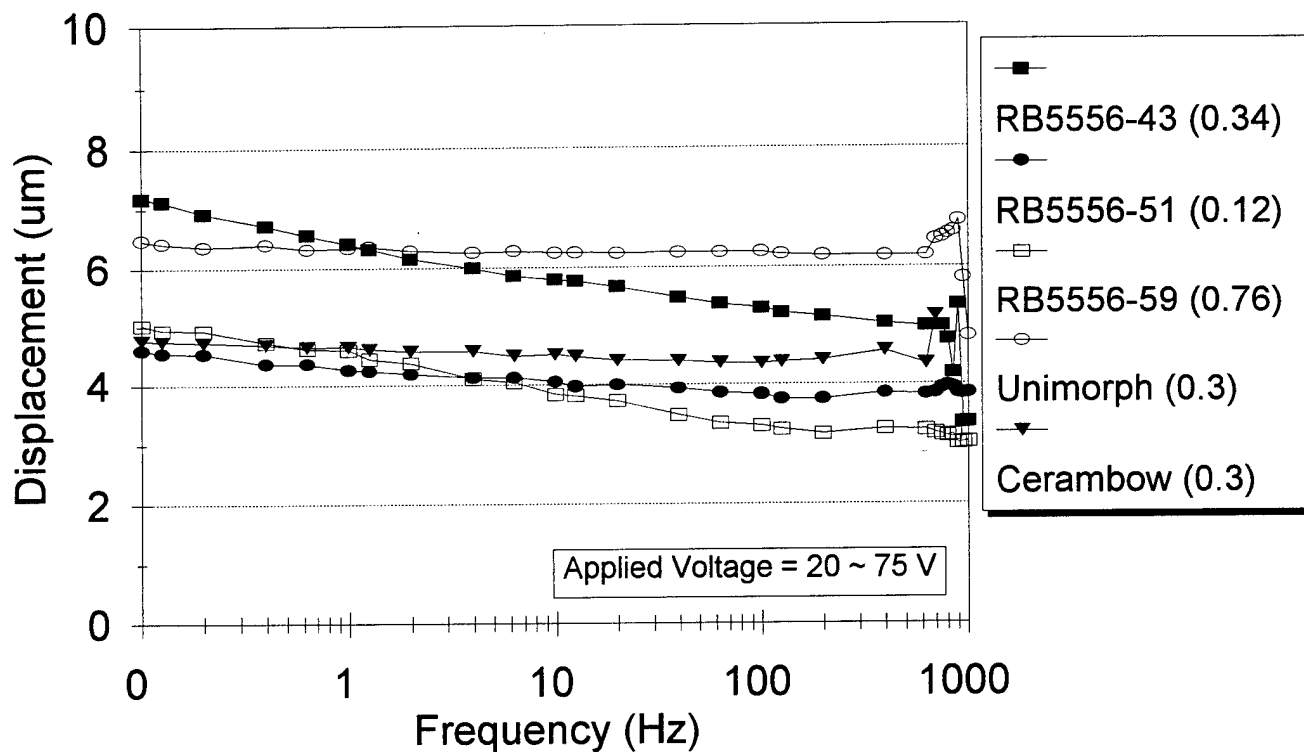


Figure 1. Frequency dependence of field-induced displacement. The numbers given within the parenthesis in the legend denote the thickness ratios of the corresponding sample.

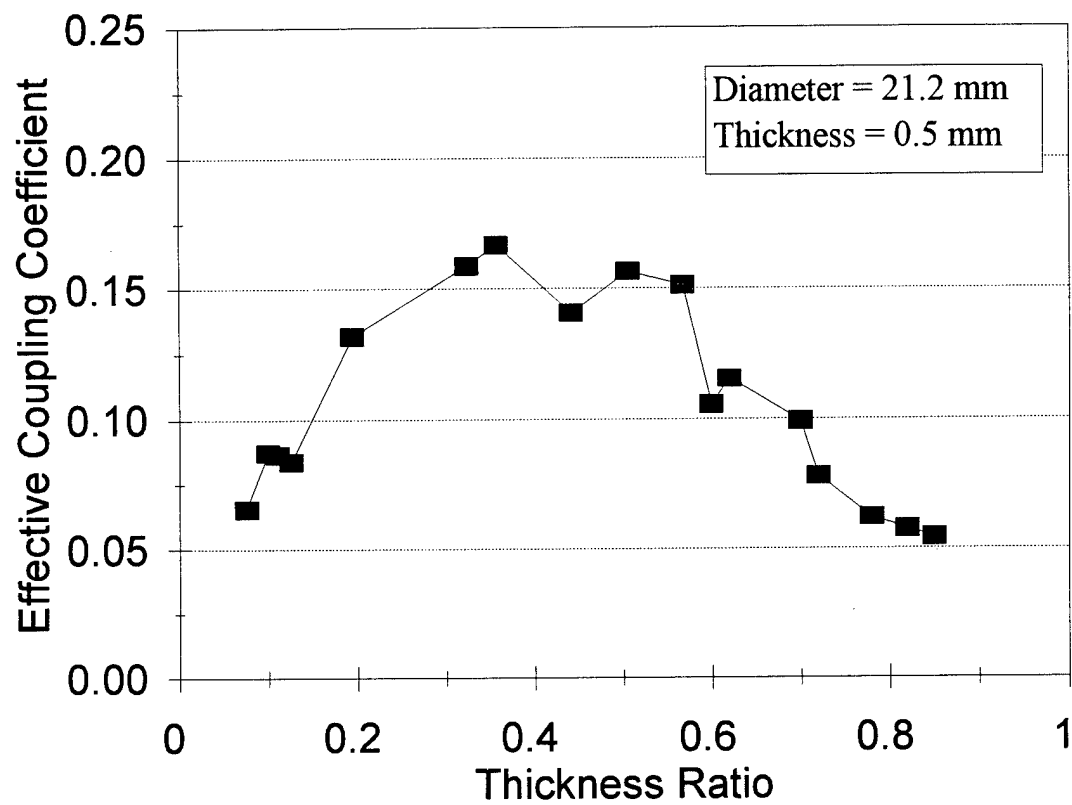


Figure 2. Variation of dome mode coupling coefficient as a function of thickness ratio for RB5556 samples.

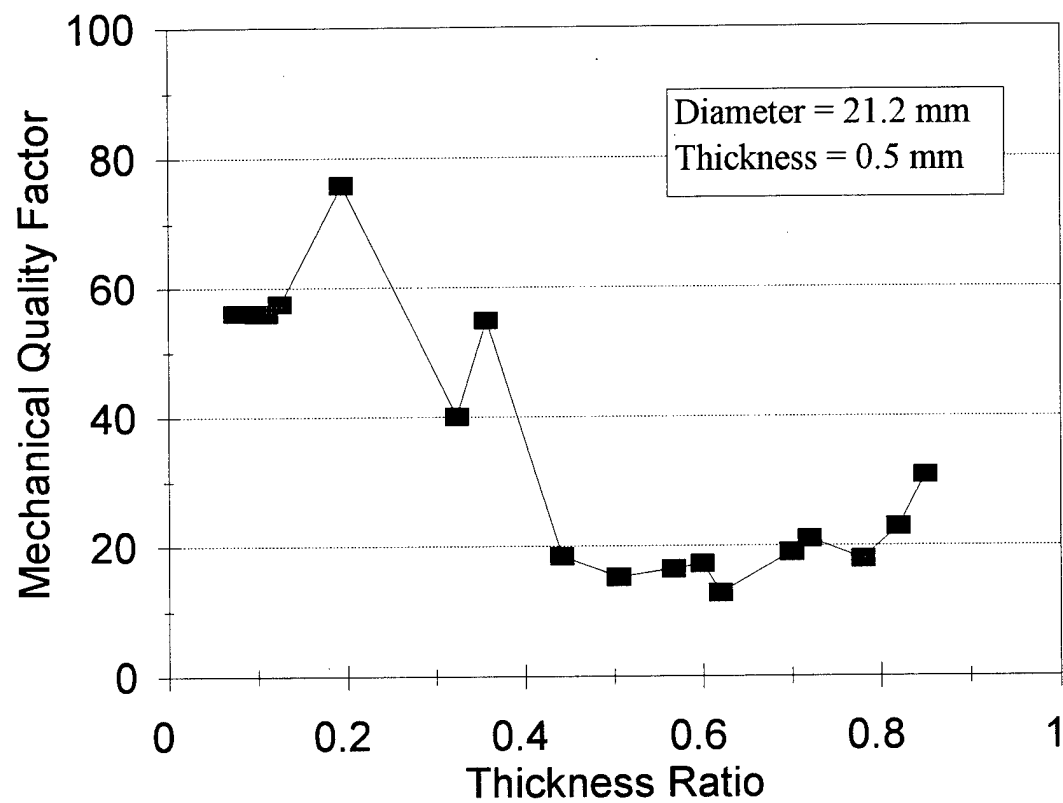


Figure 3. Variation of mechanical quality factor of the dome mode as a function of thickness ratio for RB5556 samples.



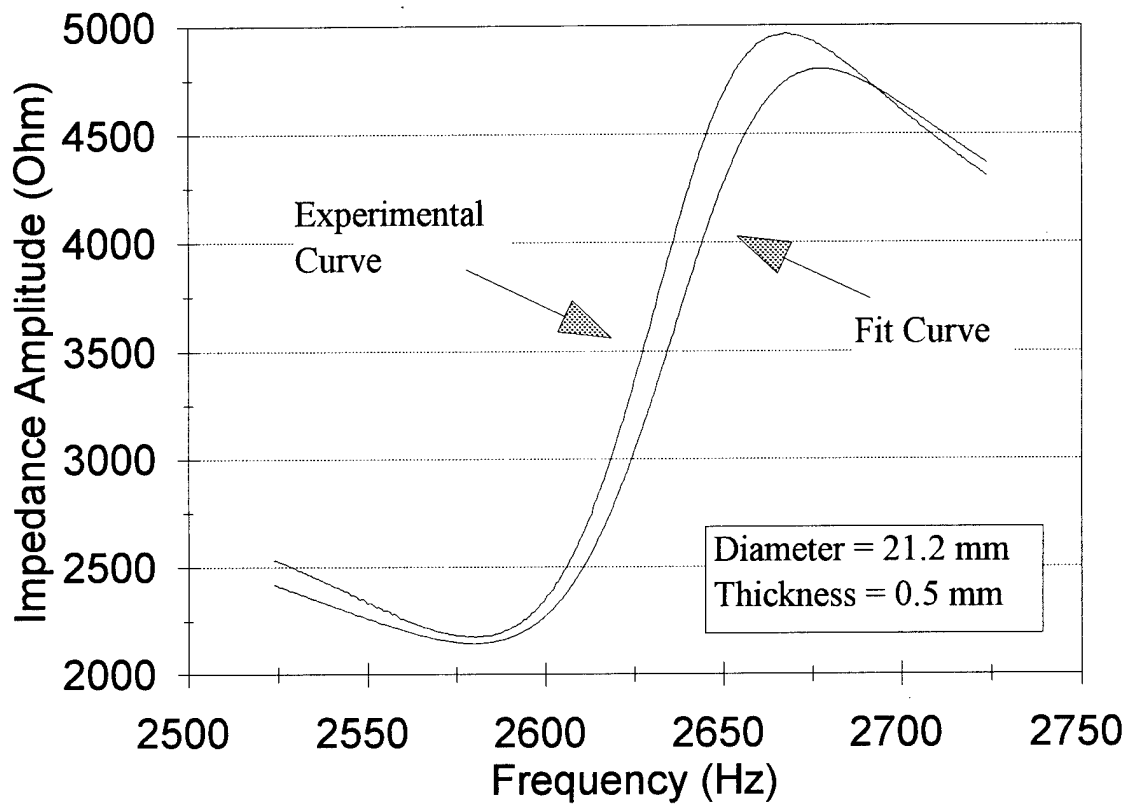


Figure 4. Change of impedance amplitude as a function of frequency near the dome mode resonance of a RB5556 sample.

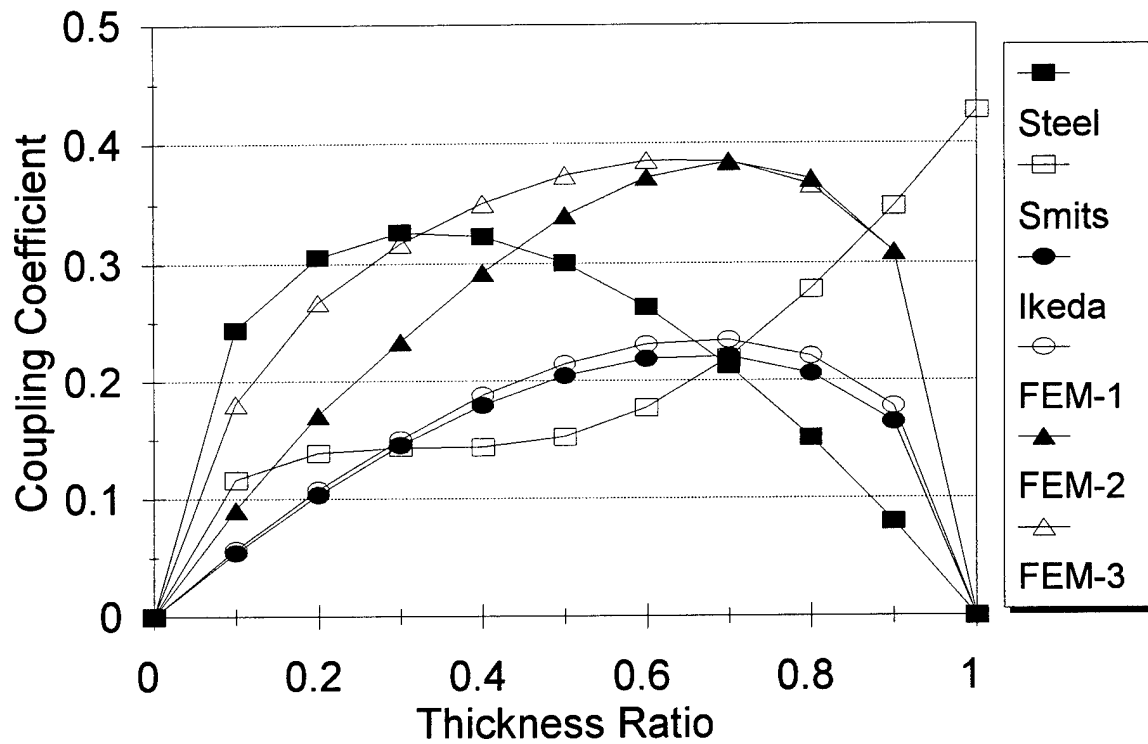


Figure 5. Relationships between bending (dome) mode coupling coefficient and thickness ratio derived from different analytical models and finite element analyses. FEM-1 represents results for strip-shaped samples, FEM-2 for disk-shaped samples, and FEM-3 for disk-shaped samples with curvature.

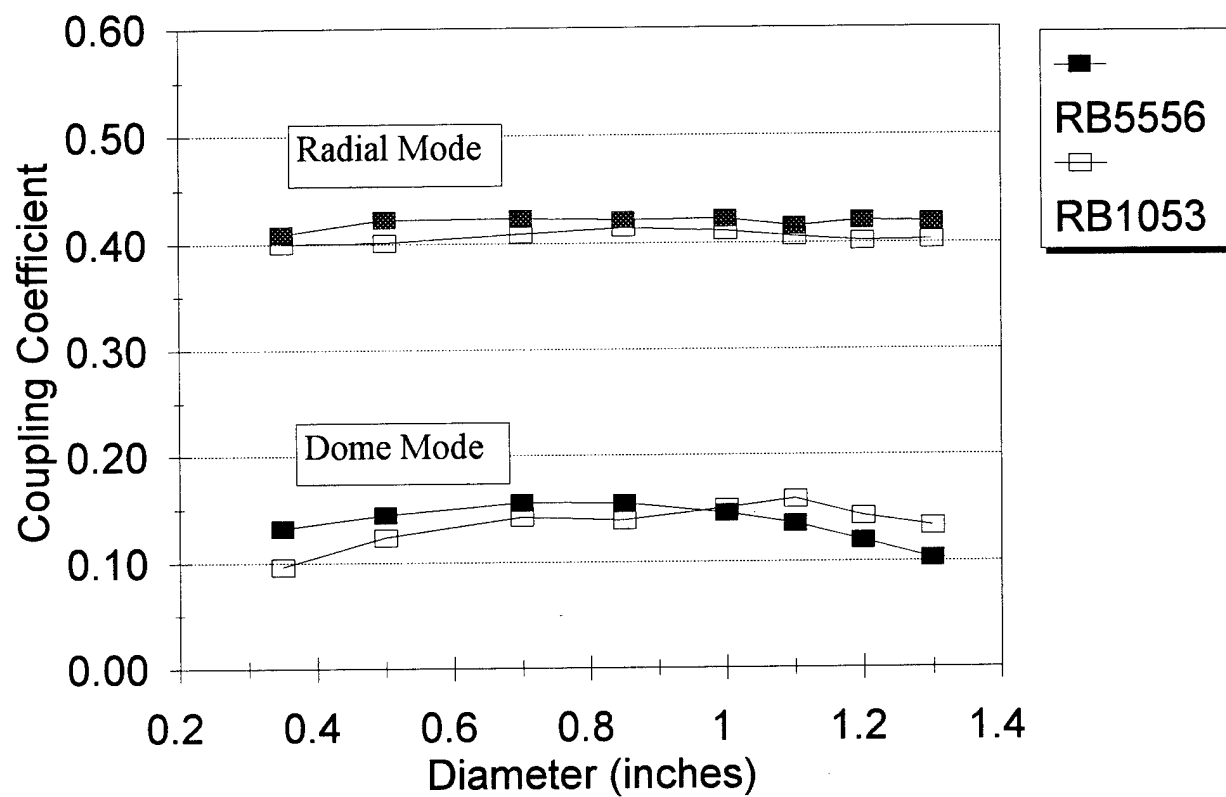


Figure 6. Change of effective coupling coefficients with sample diameter for RB5556 and RB1053 samples.

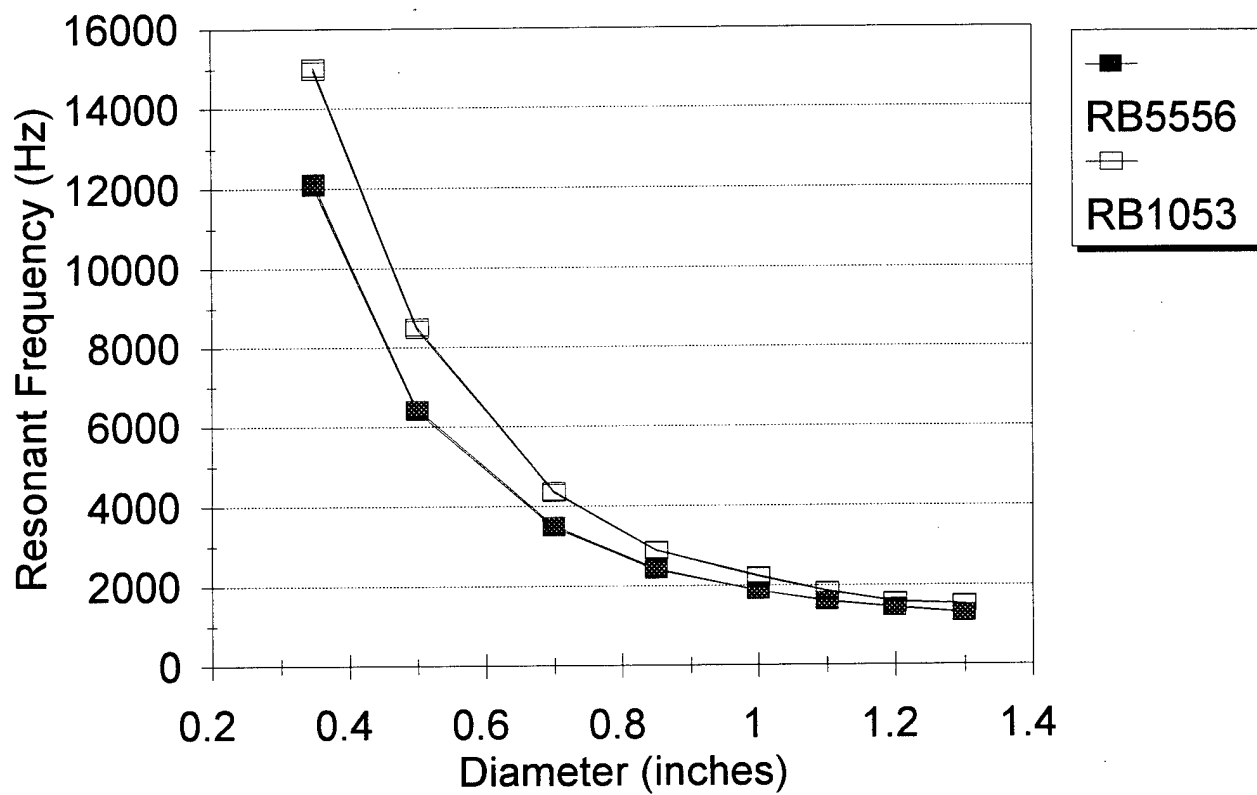
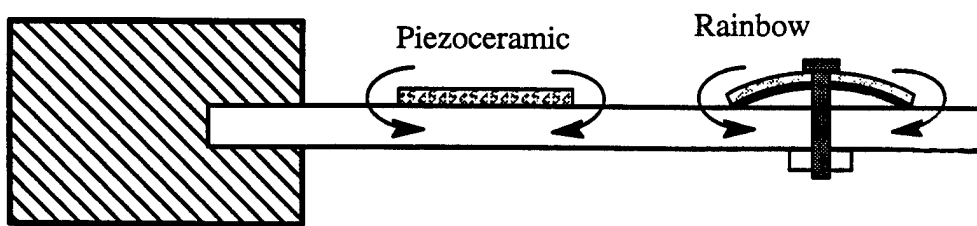


Figure 7. Change of resonant frequency of the dome mode with sample diameter.

Side View



Top View

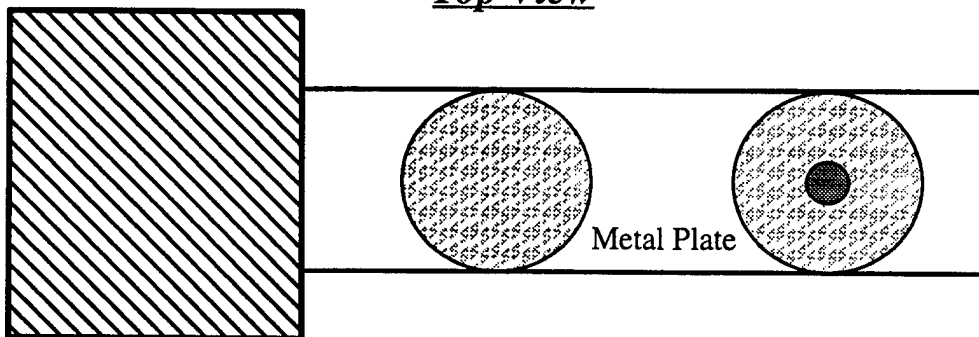


Figure 8. Schematics of Rainbow and piezoelectric wafer on cantilevered beam for stress sensing and stress generation.

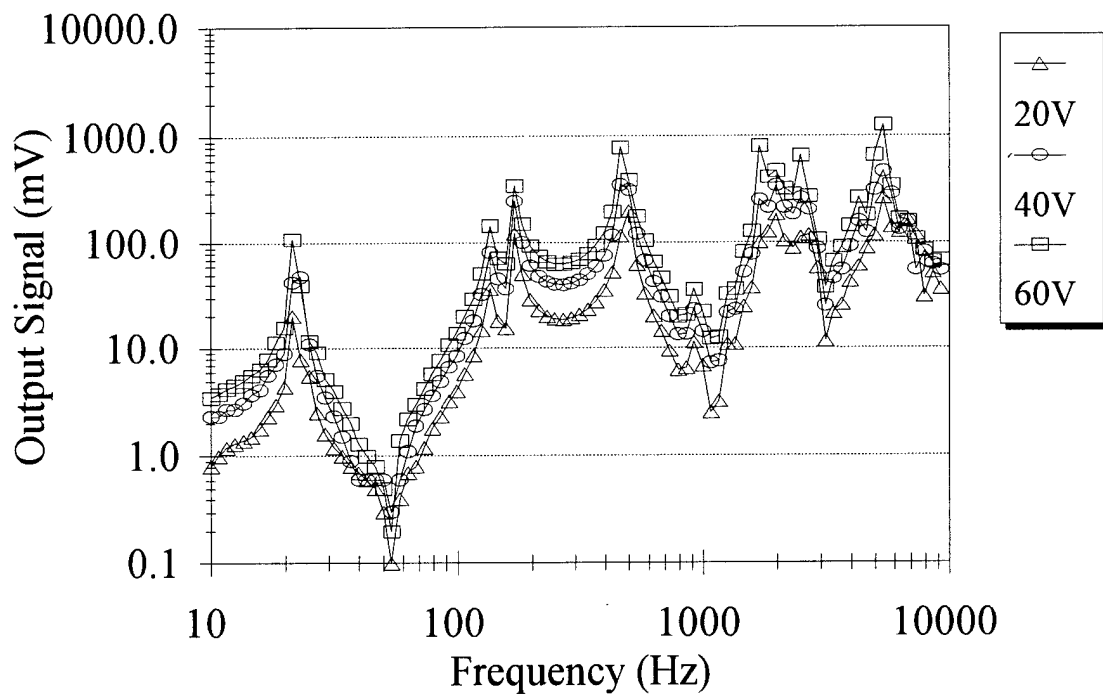


Figure 9. Voltage signals as a function of frequency from a Rainbow stress sensor on a cantilevered structure driven by a Rainbow under different applied voltages.

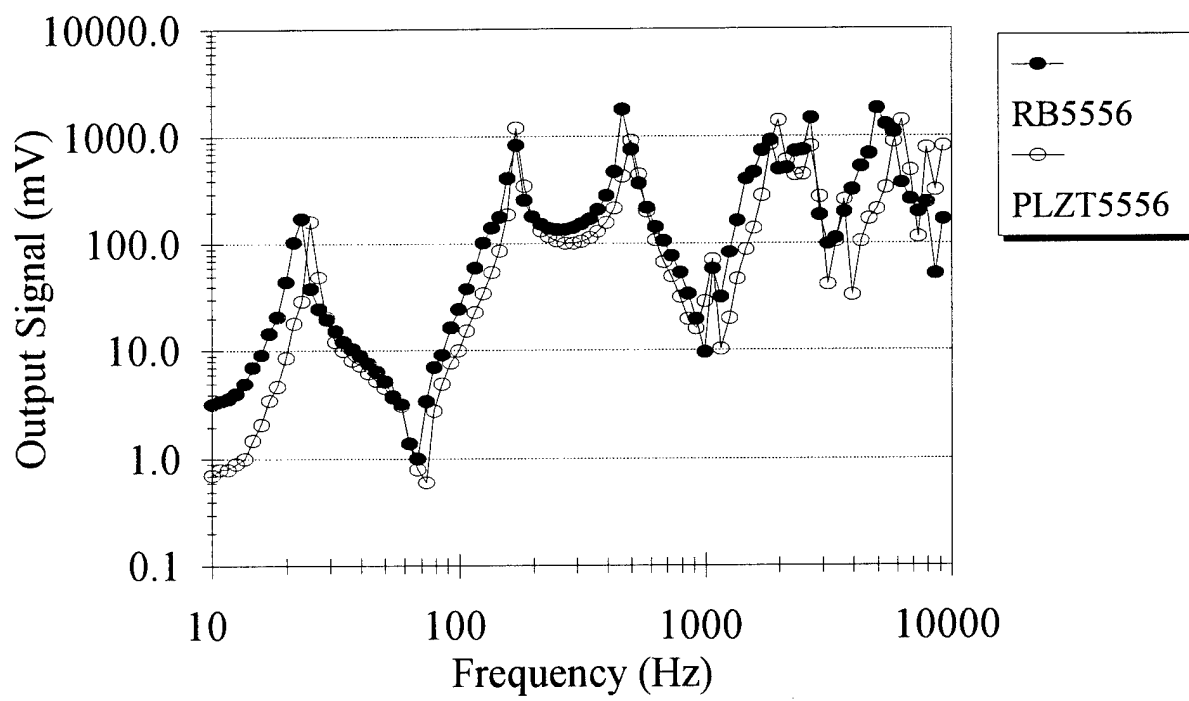


Figure 10. Voltage output signals as a function of frequency from a Rainbow and a PLZT stress sensor on a cantilevered structure.

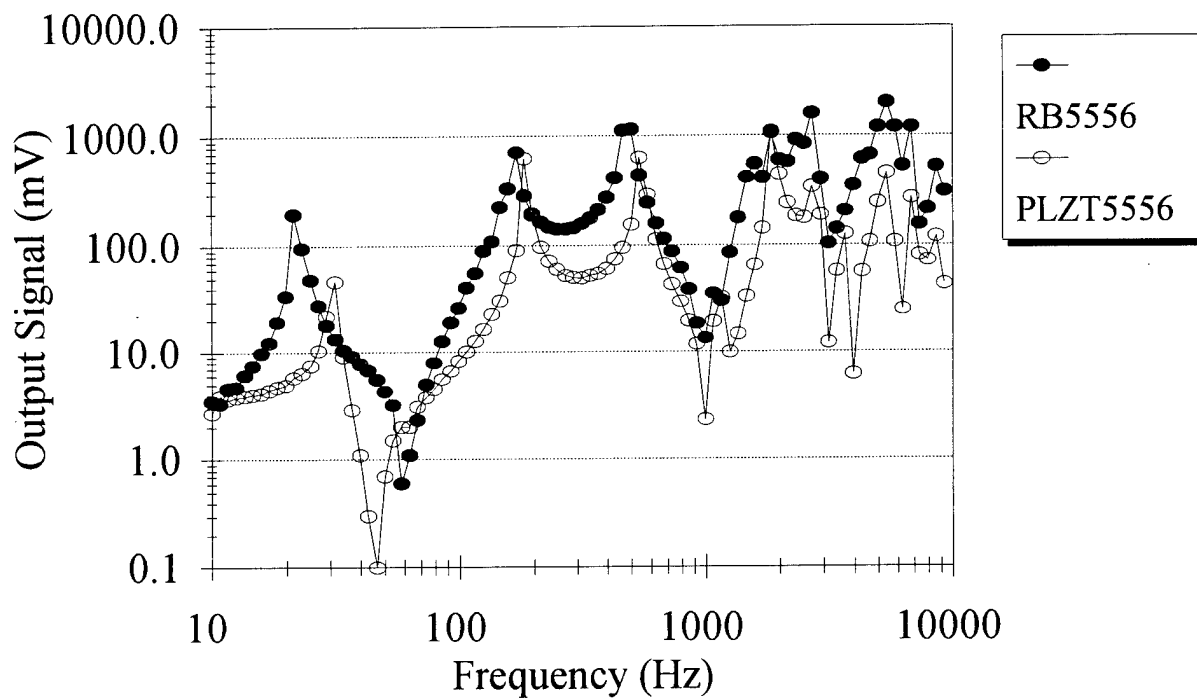


Figure 11. Voltage signals as a function of frequency from a Rainbow stress sensor on a cantilevered structure driven by a Rainbow and a PLZT stress generator.



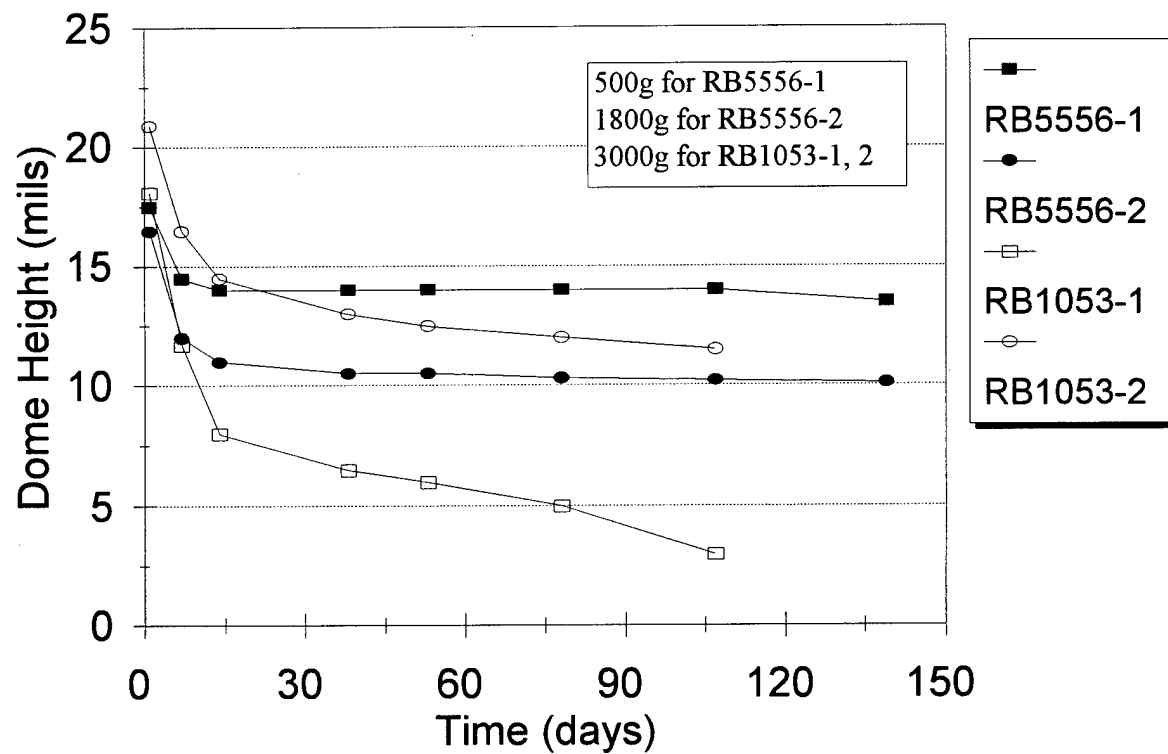


Figure 12. Change of dome height with time in the presence of applied stresses.

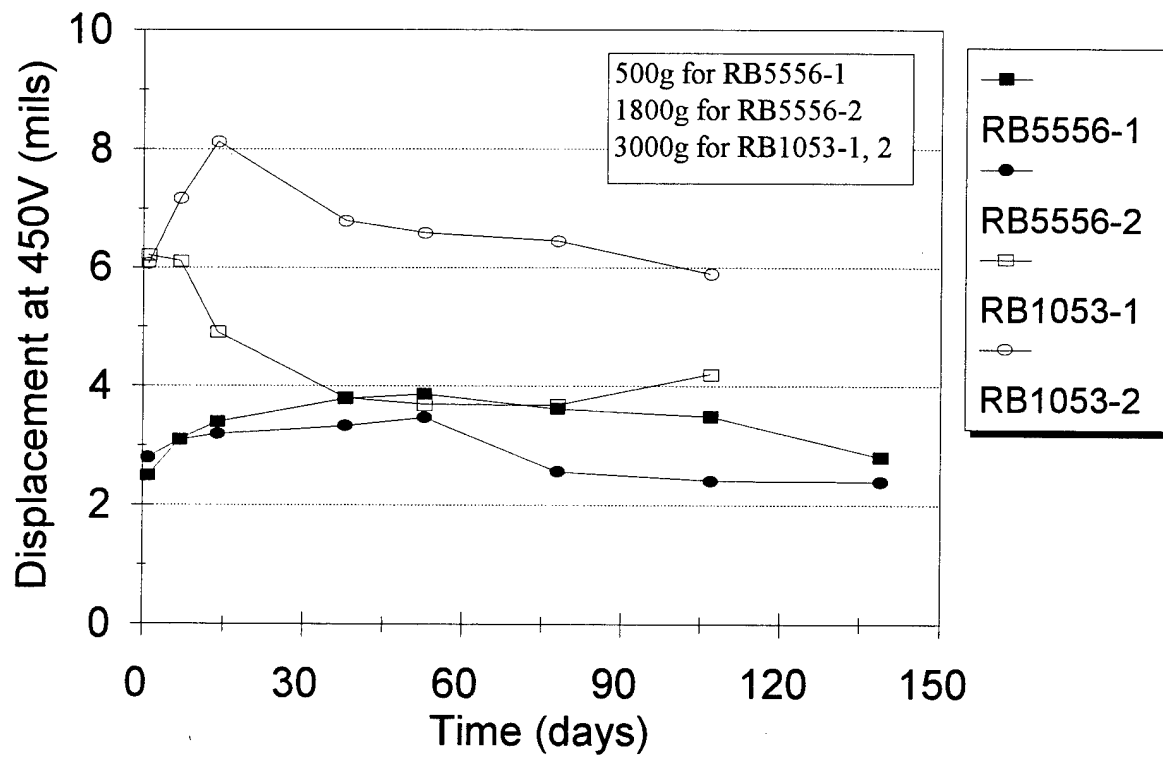


Figure 13. Change of field-induced displacement with time in the presence of applied stresses.

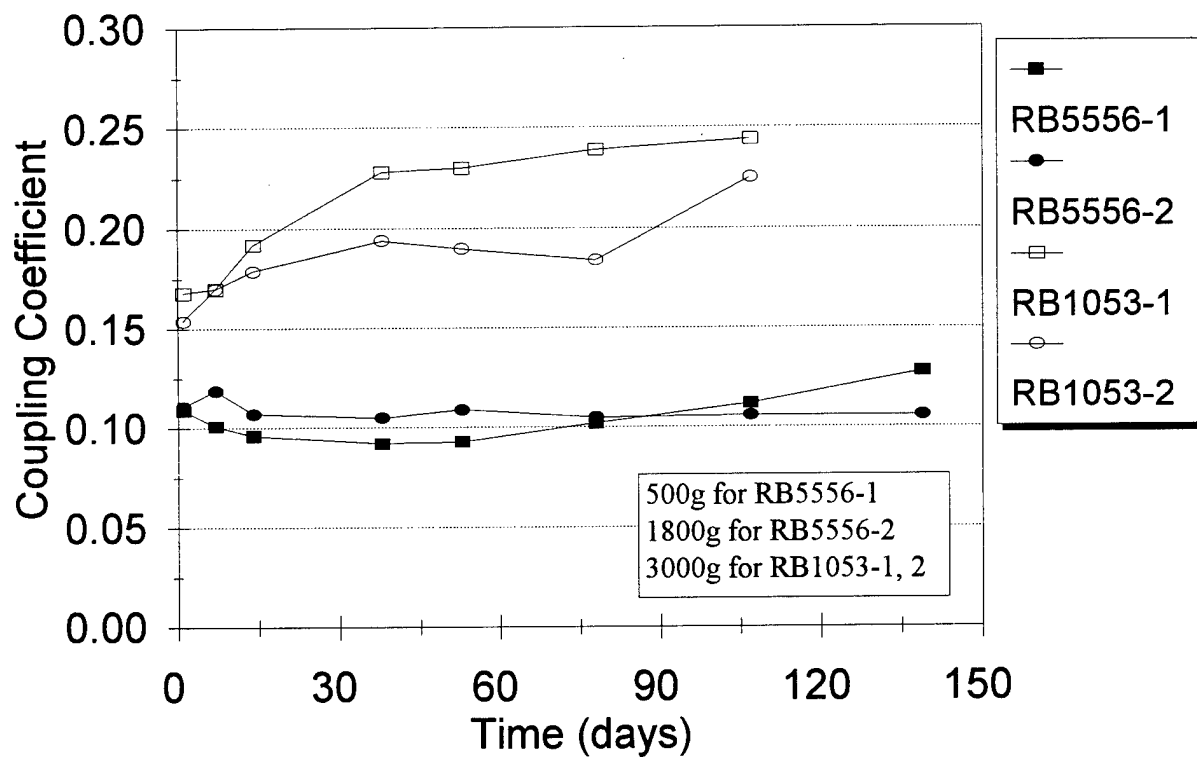


Figure 14. Change of effective coupling coefficient of the dome mode with time in the presence of applied stresses.

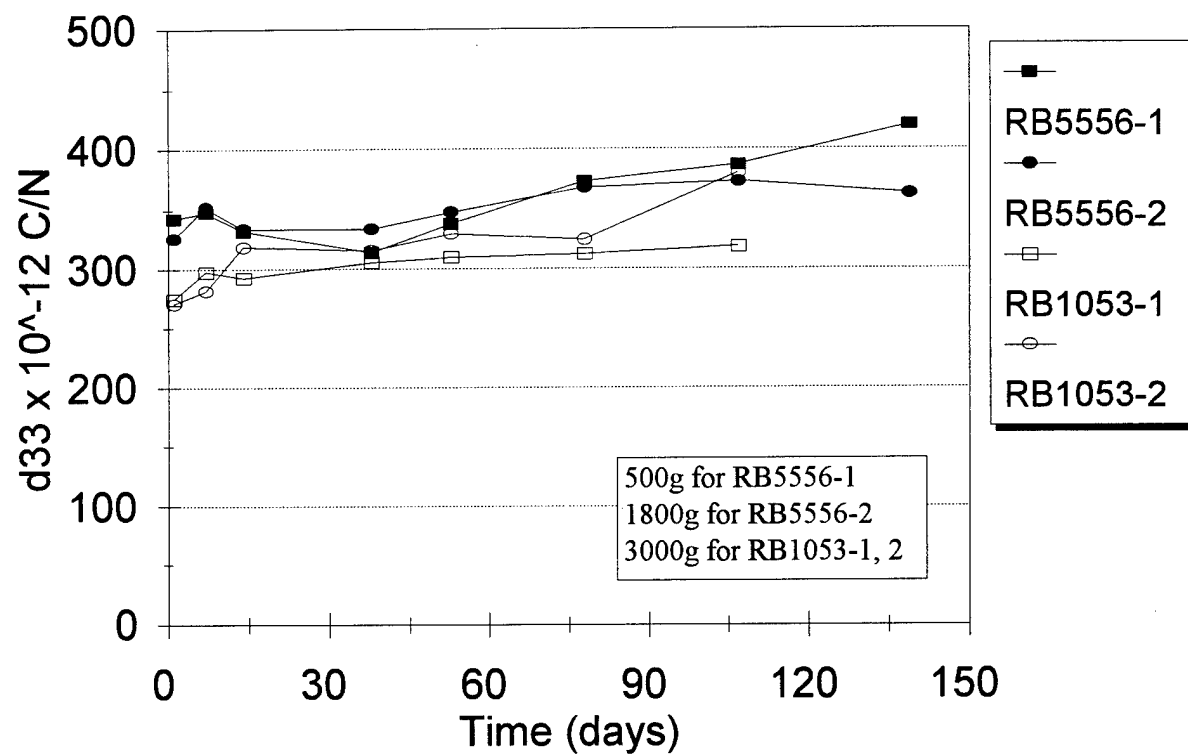


Figure 15. Change of piezoelectric coefficient with time in the presence of applied stresses.

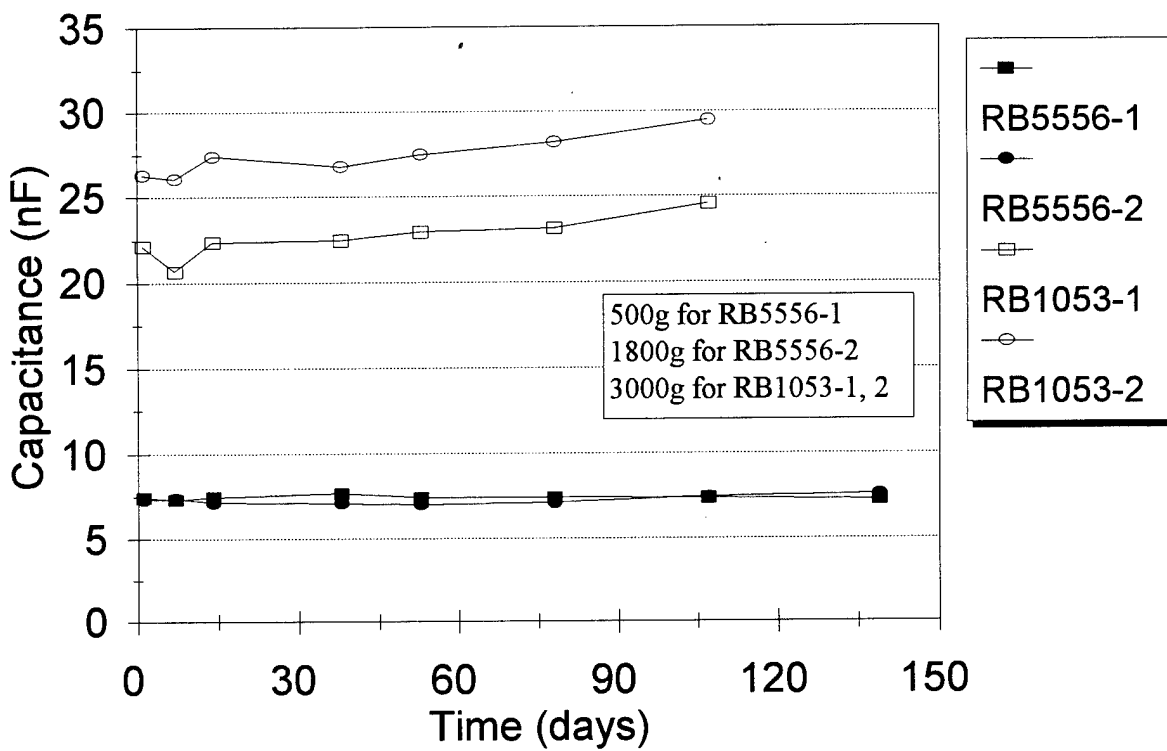


Figure 16. Change of capacitance with time in the presence of applied stresses.

**Part VI.**

**Stress Effects in Cerambow Actuators**

Submitted by :

Bret Barron  
Gene Haertling

## **Stress Effects in Cerambow Actuators**

### **I. Abstract**

The purpose of this report is to present the most recent findings concerning the Cerambow(CERAMic Biased Oxide Wafer) actuator at Clemson University. X-ray diffraction patterns containing the (200) and (002) peaks from selected thickness ratio Cerambow samples were obtained to better understand the state of stress in the ceramic layer. Frequency dependent displacement behavior of the Cerambow was studied from 0.1 to 400 Hz using a laser interferometer. Cerambow samples having a 0.3 thickness ratio were seen to exhibit a more pronounced stress-enhanced effect compared to those with a 0.5 thickness ratio based on the x-ray diffraction data. The displacement of the Cerambows used in this investigation decreased as frequency was increased up to approximately 100 Hz. From 200-400 Hz the displacement increased and was considered to be caused by the existence of a resonant dome mode at these frequencies.

### **II. Introduction**

In the field of electronic ceramics, there has been an ongoing effort to produce actuation devices from ferroelectric materials.<sup>1</sup> Ferroelectric ceramic actuators have been considered to be more advantageous than other actuator types for many reasons including low cost, high induced stress, compact size and quick response. The capabilities of bulk ferroelectric (piezoelectric and electrostrictive) materials has been vigorously studied. The greatest displacements achieved by bulk materials have been determined to be insufficient

for many practical applications, which include linear motors, pumps, speakers, variable focus lenses, and medical detection devices. For this reason, strain-amplifying techniques have been studied and developed, and serious improvement to the maximum displacement achievable by ferroelectric ceramics has been achieved.<sup>2,3</sup>

One of the most promising revelations in the area of ceramic actuation devices is the Rainbow (Reduced And Internally Biased Oxide Wafer) actuator. A Rainbow is formed by chemically reducing one side of a high lead containing ceramic wafer at an elevated temperature. Upon cooling to room temperature, stress is imparted to the oxide ceramic layer by the reduced layer resulting in a domed or saddle shaped structure. Rainbow ceramics have shown to yield ultra-high displacements when subjected to an electric field when compared to any other bulk ceramic actuators.<sup>4</sup> It has been proven that a high internal stress field is responsible for the performance of Rainbows.<sup>5</sup>

The Cerambow actuator is based on the same stress-bending technology as the Rainbow. Bonding a high thermal expansion substrate to a PLZT ceramic wafer at a moderate temperature forms a Cerambow. The Cerambows for this investigation were made by solder bonding electroded piezoelectric or electrostrictive ceramics to brass substrates with a thermal expansion coefficient approximately four times greater than the ceramic. While the Cerambow is basically a unimorph bender, the Rainbow is a monomorph consisting of a piezoelectrically active oxide layer and an inactive reduced layer.

It is known that of the two types of domain reorientation,  $180^\circ$  and non- $180^\circ$ , which take place in ferroelectric ceramics upon the application of an electric field, only non- $180^\circ$  rotations are responsible for dimensional changes in the material. By this theory,



increasing the population of non-180° domains in a ferroelectric ceramic should lead to an increase in the displacement achievable by the material. In terms of unit cell geometry, 180° domains would be oriented parallel to each other, and non-180° domains at an angle to each other. In tetragonal phase ceramics, this angle is 90° and in rhombohedral phase ceramics it can be either 71° or 109°. Figure 1 shows a diagram of the orientation for 180° and 90° domains. Domains which reside in the regions of compressive stresses are more likely to undergo 180° switching under the application of an electric field normal to the stress, while those in a region of tensile stresses are more likely to undergo a non-180° reorientation.

The high internal stress fields in the Rainbow were characterized by a compressive stress at the intermediate layer between the reduced and oxide layers which decreases toward the top of the oxide layer. For certain thickness ratio Rainbows, a region of tensile stress was discovered near the surface that was maximized at a thickness ratio of ~0.3.<sup>6</sup> A diagram of the relationship between the (200)/(002) intensity ratio and the domain structure is located in Figure 2. The intensities of the (200) and (002) x-ray diffraction peaks are determined by the amount of domains that are oriented parallel and perpendicular to the sample surface respectively.

This investigation aims to show the presence of stress-enhanced mechanisms in the Cerambow which contribute to the displacement as in the Rainbow. A study of the frequency-dependent displacement properties of Cerambows is also included.

### **III. Experimental Procedure**

#### **1. Sample Preparation**

Conventional mixed oxide techniques were used to prepare PLZT 1.0/53/47, 5.5/56/44, and 9.0/65/35 powders according to the B-site vacancy formula for the PLZT system. Raw materials were batched and ball mixed for 30 minutes in distilled water. After drying, the powders were calcined at 925°C for two hours and then milled with distilled water in a high alumina containing ball mill for one hour. Slugs were pressed from the dried material and sintered in an oxygen atmosphere at 1250°C for four hours.

A diamond saw was used to slice the sintered samples into disks, which were ground to a diameter of 31.75 mm and lapped to the appropriate thickness. Silver electrodes were applied to each side of the ceramic disk and dried at 200°C for 20 minutes and then fired at 550°C. A non-electroded ring approximately 1 mm in width was left around the circumference of one side of the wafer to prevent any excess solder from bonding to it during Cerambowing.

A disk was cut to the appropriate diameter from a sheet of brass foil having a thickness of 0.127 mm. The ceramic and brass disks were placed in a sonicator filled with acetone for one minute to insure a clean surface prior to bonding. The brass disk was placed on a piece of sheet metal on a hot plate preheated to approximately 250°C. The brass was allowed to heat up to maximum expansion, and was tinned with 60/40 Sn/Pb solder. The ceramic disk was placed on top the solder with the non-electroded side faced up, and a preheated weight was lowered onto the device to hold it together while it was removed from the hot plate.

Pressure was applied normal to the surface of the Cerambow by hand for approximately 20 seconds after removal from the hot plate, and then it was allowed to cool to room temperature. The edge of the Cerambow was sanded with 400-grit sandpaper to remove any excess solder and decrease the chance of electrical breakdown during testing. The samples were then poled at twice the coercive field for the respective composition for one minute.

The samples that were used to obtain x-ray diffraction data were prepared slightly different than a regular Cerambow. Before electroding, these disks were placed in a box furnace at 700°C for one hour to relieve any stress in the ceramic generated due to slicing, grinding, and lapping. Only one side of the ceramic was coated with silver electrode before bonding. An aluminum electrode was evaporated onto the top surface of each sample that was to be used to evaluate the change in the (200)/(002) peak intensity ratio as a function of electric field. Silicon oil was spread onto each Cerambow before a voltage was applied for insulation purposes. The voltage was applied to the samples through pieces of aluminum foil which were taped to their electrodes.

## **2. Measurements**

X-ray diffraction patterns of the (200) and (002) peak intensities were obtained with a Scintag 2000 XDS x-ray diffractometer using Ni-filtered copper  $K\alpha$  radiation. Scans of each sample were taken at a rate of 1 degree per minute between 42 and 46 degrees of  $2\theta$ . The (200) and (002) peaks were fitted using a Gaussian fitting function.

Frequency versus displacements was recorded for selected Cerambow samples from 0.1-400 Hz. All displacement measurements were taken using a 200 volt unipolar voltage. A Zygo ZMI 1000 laser interferometer interfaced with a computer was used to

obtain these measurements. Figure 3 contains a diagram of the interferometer setup.

A laser beam comprised of two orthogonally polarized beams with different frequencies was generated by the laser head and aimed at the optical probe. When the incoming beam entered the optical probe it was divided into two perpendicular beams with different polarizations. One beam was deflected immediately into the detector, while the other was sent to the sample. The second beam deflected off of a piece of reflective silicon tape located on the sample and back into the detector. Movement of the sample resulted in an optical path change between the two beams. The detector converted the optical interference into an electrical signal that was sent to the computer. The peak to peak displacement shown on the computer was reported as the displacement at that frequency.

#### **IV. Results and Discussion**

Figures 4 and 5 are plots of the (200)/(002) peak intensity ratios of selected 1/53/47 and 5.5/56/44 samples as a function of electric field. The 1.0/53/47 and 5.5/56/44 samples having a 0.3 thickness ratio in both graphs showed a much greater slope than the other samples, 1.5 and 0.6 times respectively. The sample having a 0.0 thickness ratio is bulk PLZT and in Figure 1 it is shown to have a similar (200)/(002) peak intensity ratio change as a function of electric field. as the sample having a 0.5 thickness ratio.

As stated before, domains that undergo non-180° reorientation with the application of a poling voltage give an additional contribution to displacement.

Piezoelectric ceramic materials which are placed under tension are known to possess

preferred orientation in the direction of stress. The application of an electric field perpendicular to the direction of this preferred orientation would result in an increase in the amount of  $90^\circ$  rotations, and hence displacement, compared to a stress-free ceramic. For this reason, greater changes in the (200)/(002) peak intensity ratio with electric field are expected from Cerambows that have the largest region of tensile stress. Due to their much larger slope, it is believed that the 0.3 thickness ratio samples in Figures 4 and 5 benefit from some type of stress enhanced effect. These results agree with previous finite element models, which underestimated the performance of Cerambows having a thickness ratio below 0.4 up to 78 %.<sup>7</sup> This underestimation was considered to be due to stress enhanced mechanisms that were not incorporated into the model.

Figures 6 and 7 are plots of the displacement of Cerambows having different thickness ratios as a function of frequency. A decrease in the displacement was observed from frequencies from 0.1 to 100 Hz. The PLZT 1/53/47 samples showed about the same amount of decrease, 30 and 23 %, for the 0.3 and 0.5 thickness ratio samples respectively. The 9.0/65/35 samples showed a similar response, decreasing approximately 15 % each.

Not only was the frequency-dependent displacement of Cerambows thought to be due to stress-enhanced effects, nonlinear and hysteresis effects, which were known to be more pronounced at higher fields, were thought to be responsible for their behavior also. All samples were exposed to the same voltage for these measurements, so the 0.5 thickness ratio samples were exposed to a higher field. Therefore, any nonlinear effect would be much more pronounced for the 0.5 thickness ratio samples.

As frequency was increased, some domains that lie in regions of tensile stress which are necessary for large displacements may not have enough time to switch.

Because any nonlinear or hysteresis effect should have been less evident in the 0.3 thickness ratio Cerambows and they decreased approximately the same amount as the thinner samples, the frequency data may also show the presence of a stress-enhanced effect in these samples. Therefore both the x-ray diffraction and frequency dependent displacement data show that a stress enhanced effect may play a role in the behavior of 0.3 thickness ratio Cerambow actuators.

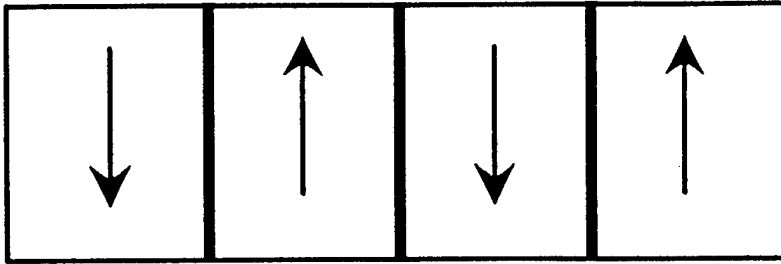
## **V. Summary**

Cerambows having a 0.3 thickness ratio experienced a much greater change in their (200/(002) peak intensity ratios as a function of electric field compared to the other samples tested in this study. Based on this fact, Cerambow devices possessing a 0.3 thickness ratio were found to benefit from a stress enhanced effect.

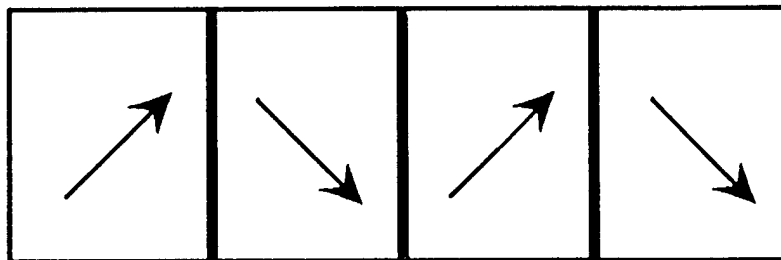
Cerambows with thickness ratios of 0.3 and 0.44 showed similar frequency dependent displacement characteristics from 0.1 to 400 Hz. From 0.1 to 100 Hz, the displacement of the Cerambows decreased up to 30 % depending on thickness ratio and composition. The samples having a 0.3 thickness ratio were believed to exhibit a stress enhanced effect because they consistently showed approximately the same amount of decrease as the 0.44 thickness ratio samples, although they were less influenced by nonlinear effects. Increasing the frequency further resulted in an increase in displacement up to 400 Hz. This behavior was explained by the existence of a resonant dome mode at these frequencies.

## VI. References

1. Kenji Uchino, "Electrostrictive Actuators: Materials and Applications," *Ceramic Bulletin*, **65**, No. 4, pp. 647-652, 1986.
2. G. H. Haertling, "A New Type of Ultra-High Displacement Actuator," *Bull. Am. Ceram. Soc.*, **73**, No. 1, pp. 93-96, 1994.
3. Y. Sugawara, K. Onitsuka, S. Yoshikawa, Q. Xu, R.E. Newnham, and K. Uchino, "Metal-Ceramic Composite Actuators," *J. Am. Ceram. Soc.*, **75**, No. 4, pp. 996-998, 1992.
4. G. H. Haertling, "Chemically Reduced PLZT Ceramics for Ultra-High Displacement Actuators," *Ferroelectrics*, **154**, pp. 101-106, 1994.
5. G. Li, "Stress-Enhanced Displacements in PLZT Rainbow Actuators," to be published.
6. G. Li, "Influence of Internal Stress on the Electromechanical Properties of PLZT Stress-Biased (Rainbow) Ceramic Actuators," Ph. D. Thesis, Gilbert C. Robinson Department of Ceramic Engineering, Clemson University, 1995.
7. Bret Barron, "Characterization of Ceramobw Actuators," Part I of Annual Report to the Office of Naval Research, Grant No. N00014-94-1-0563, "Stress-Enhanced Ferroelectric Materials and Structures," July 1996.



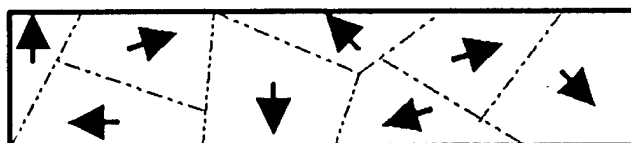
$180^{\circ}$  Domains and Domain Walls



$90^{\circ}$  Domains and Domain Walls

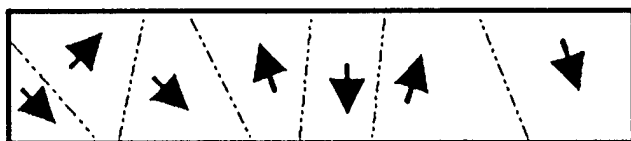
Figure 1. Diagram of the two different domain types in a tetragonal ferroelectric. The bold face lines represent domain walls for the particular domain type.





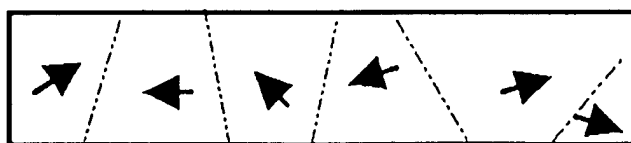
$$\frac{I_{200}}{I_{002}} = x$$

Randomly Oriented Stress-Free Ceramic



$$\frac{I_{200}}{I_{002}} < x$$

Ceramic Under Compression



$$\frac{I_{200}}{I_{002}} > x$$

Ceramic In Tension

Figure 2. Diagram of the domain orientation in a ferroelectric ceramic under various stress conditions.

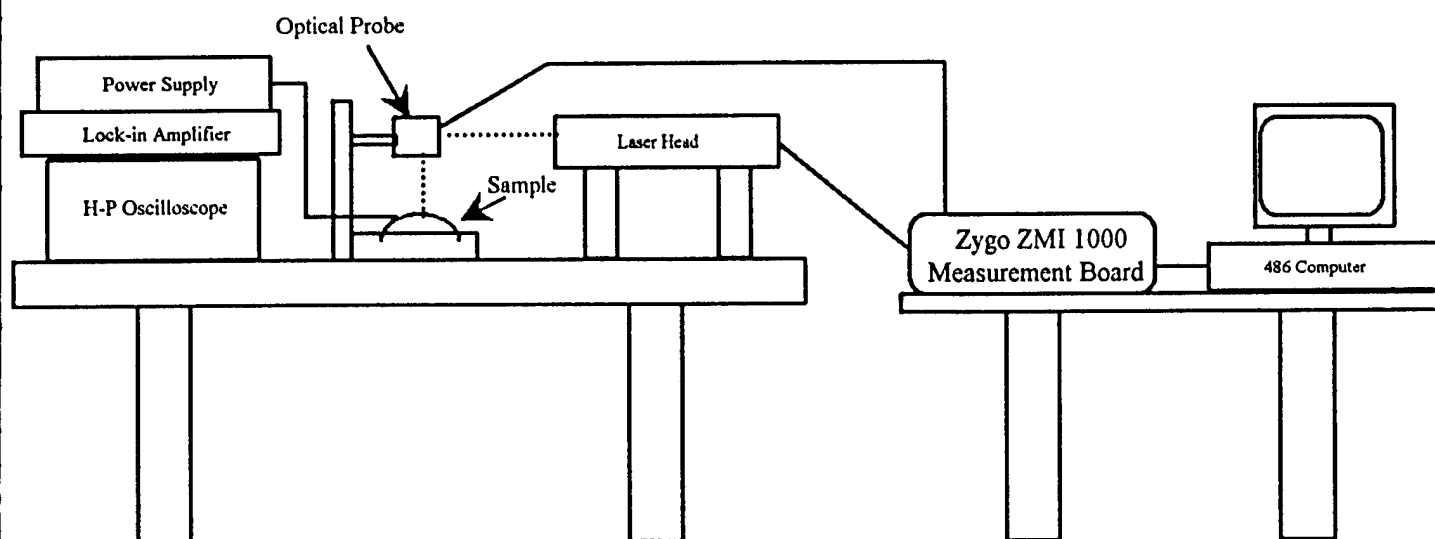


Figure 3. Schematic diagram of the experimental setup used to measure the frequency-dependent displacement properties of Cerambow actuators from 0.1 to 400 Hz.

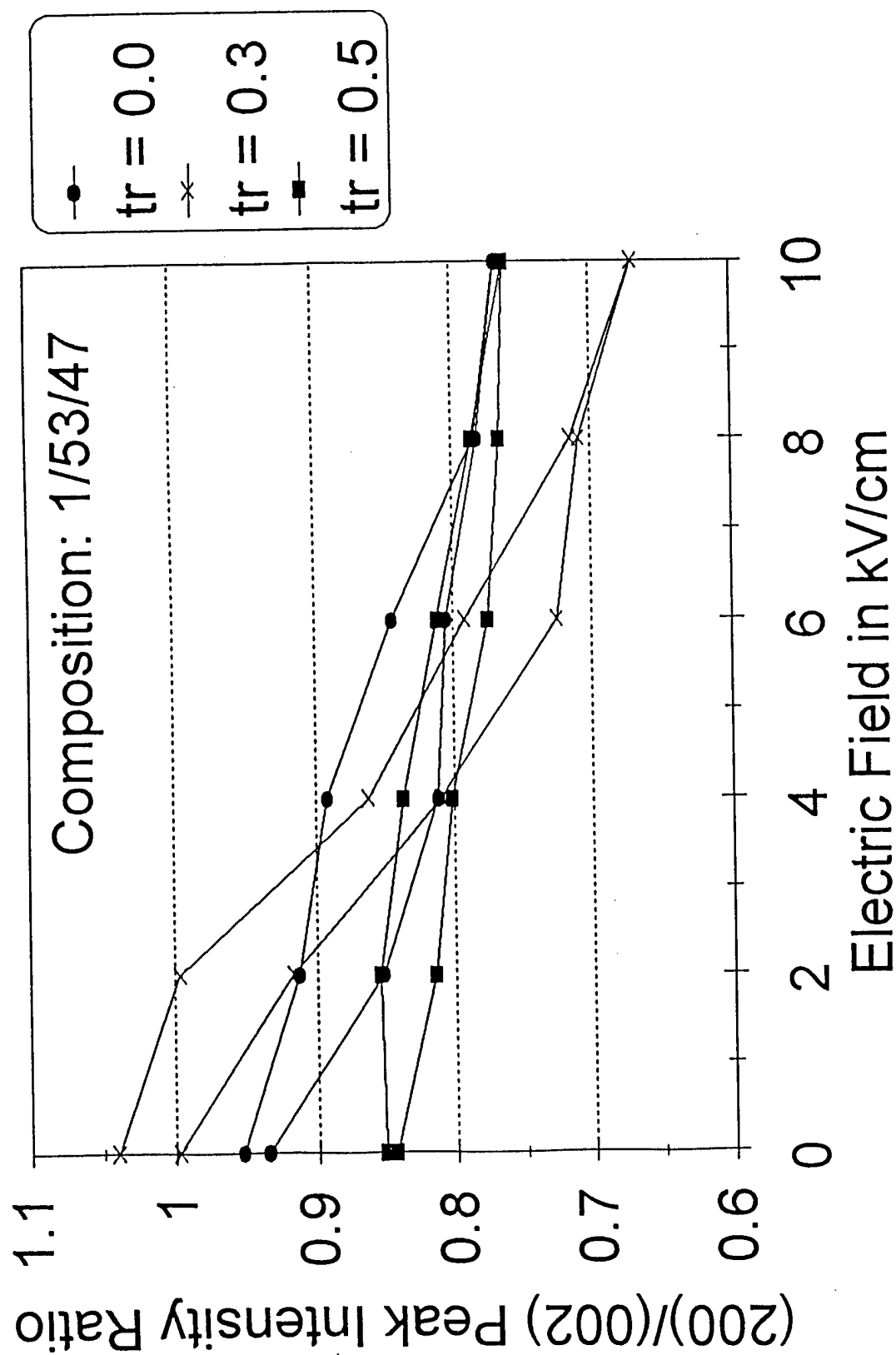


Figure 4. Variation of the (200)/(002) peak intensity ratio with the application of an electric field for PLZT 1/53/47 Cerambow samples.

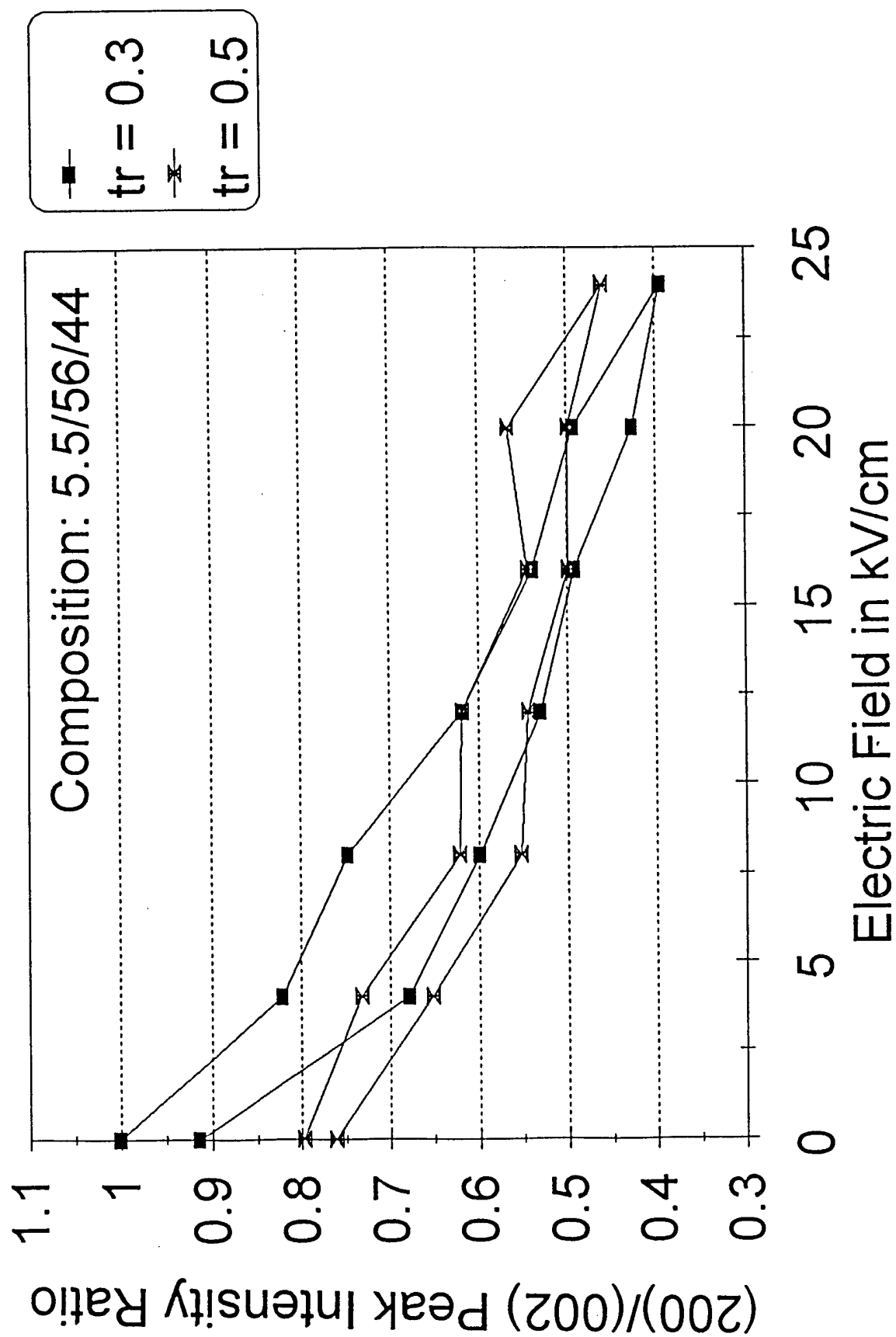


Figure 5. Variation of the (200)/(002) peak intensity ratio with the application of an electric field for PLZT 5.5/56/44 Cerambow.

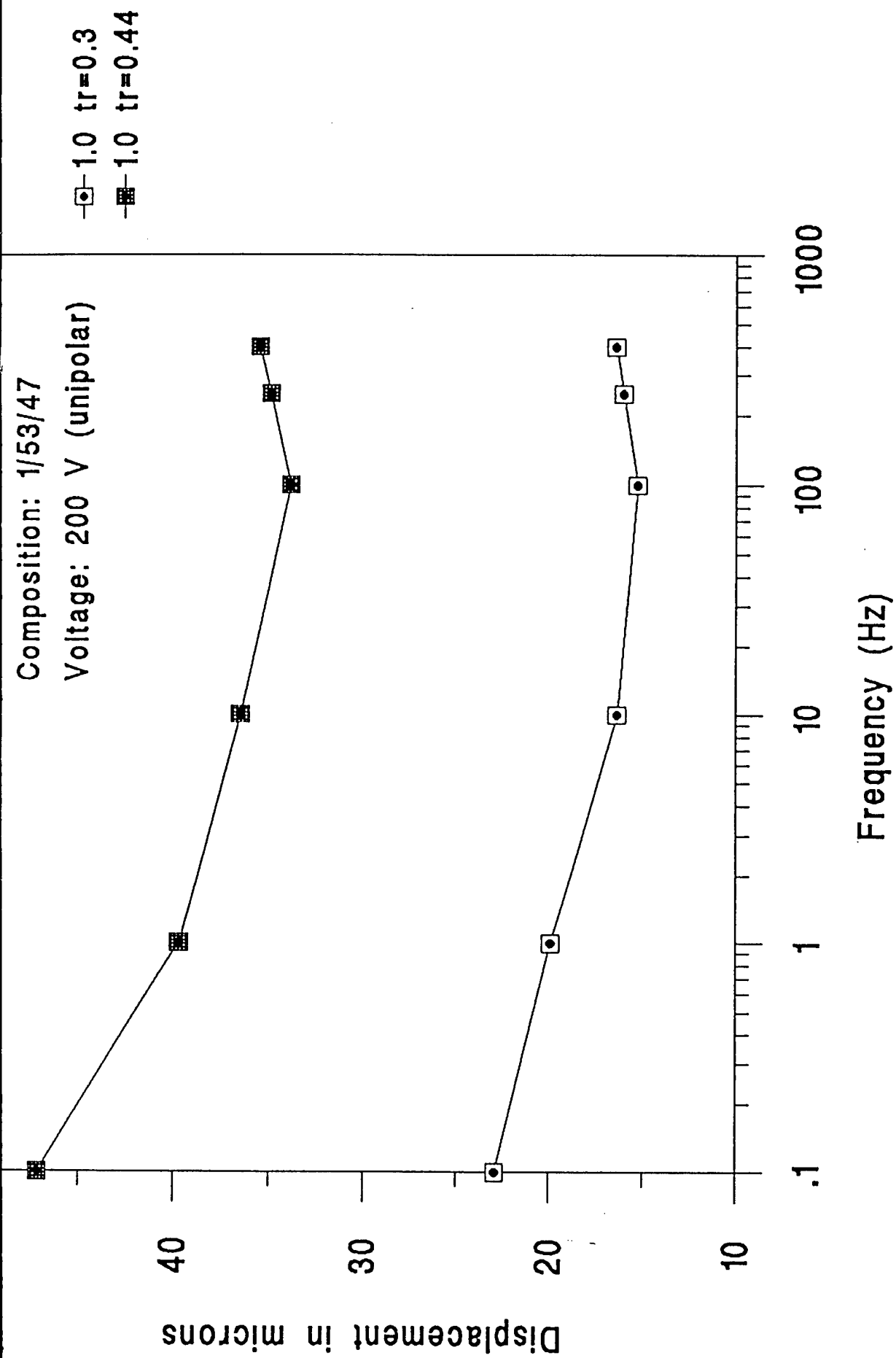


Figure 6. Displacement of 1/53/47 PLZT Cerambows at 200 volts as a function of frequency.

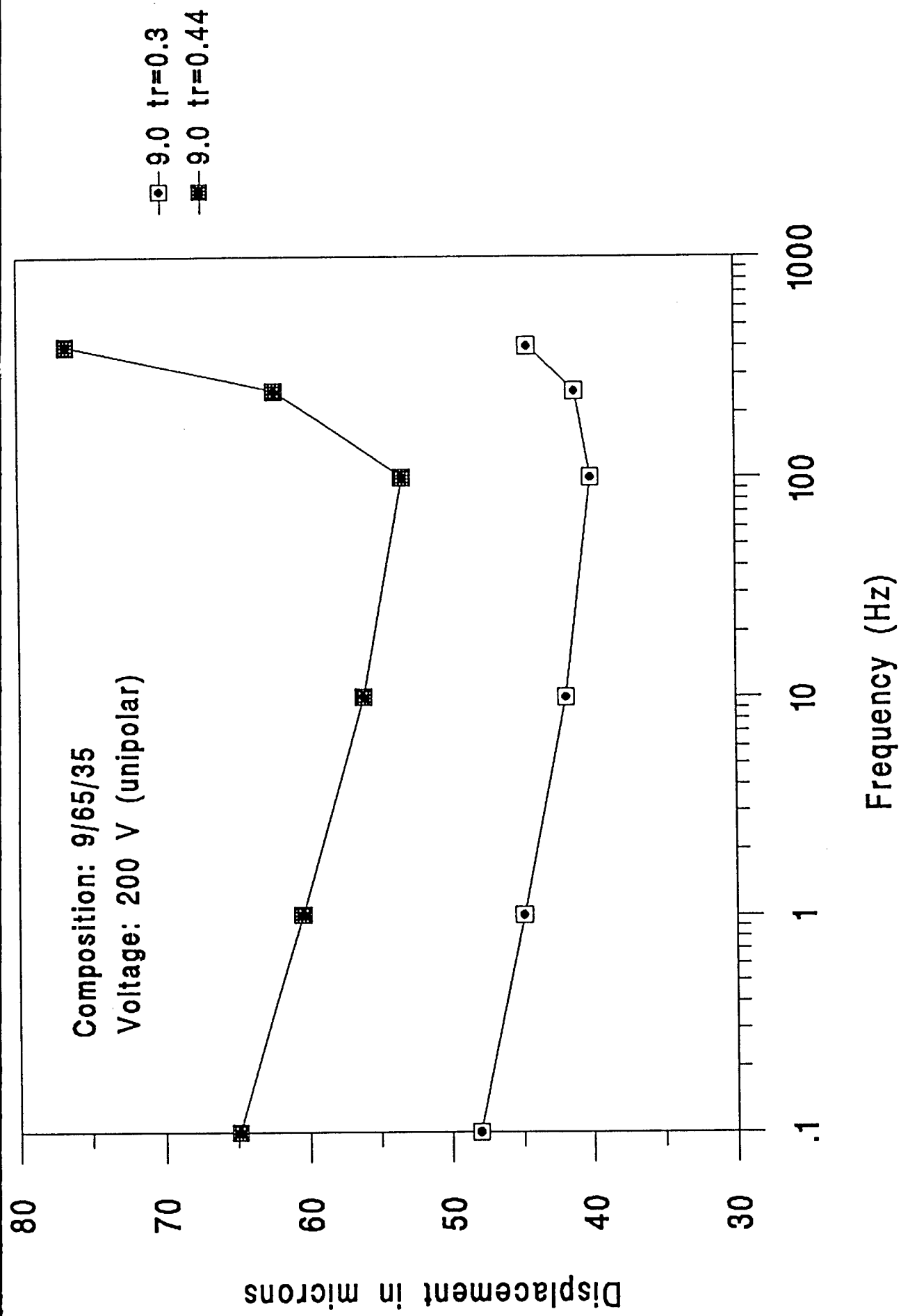


Figure 7. Displacement of 9.0/65/35 PLZT Cerambows at 200 volts as a function of frequency.

**Part VII.**

**Voltage-Induced Displacement Properties of Cerambow Actuators**

Submitted by :

Bret Barron  
Gene Haertling

## Voltage-Induced Displacement Properties of Cerambow Actuators

Bret W. Barron, Guang Li, and Gene H. Haertling  
Gilbert C. Robinson Department of Ceramic and Materials Engineering  
Clemson University  
Clemson, SC, 29634-0907

**Abstract** A new type of ceramic actuator has been developed called the CERAMBOW (CERAMic Biased Oxide Wafer). In this technology, bonding two layers with mismatched thermal expansion coefficients results in a structure that is a purposely stress-biased unimorph actuator. The voltage-induced displacement properties of Cerambows having varying PLZT 1/53/47, 5.5/56/44, and 9/65/35 layer thicknesses were evaluated and compared to Rainbow actuators. The temperature dependent displacement properties of Cerambows were studied from 25 to 150°C. Cerambow actuators with dimensions of 31.75 mm x 0.5 mm (diameter x thickness) achieved displacements as high as 135  $\mu\text{m}$  at 450 volts. In addition, the displacements of 1/53/47 and 5.5/56/44 Cerambows showed good temperature stability up to 110°C

**Introduction** Over the last ten years, there has been an ongoing effort to produce piezoelectric and electrostrictive actuator configurations which produce strains that meet the requirements of today's applications which include linear motors, pumps, speakers, deformable mirrors, and micropositioners.<sup>1,2</sup> Presently, the most common types of composite actuator configurations are unimorph and bimorph benders in addition to flextensional devices. It is known that each of these technologies has limitations in regard to size, weight, maximum displacement, or load bearing capability.<sup>3</sup>



The Cerambow was developed in the shadow of one of the most promising strain-amplification techniques to this day known as the Rainbow (Reduced And Internally Biased Oxide Wafer) actuator. A Rainbow actuator is produced by chemically reducing one side of a high lead-containing ceramic wafer at an elevated temperature, resulting in a dome or saddle shaped 2-layer composite structure. The mechanisms responsible for the unique geometry of the Rainbow have been previously reported.<sup>4</sup> The stresses which are imparted to the ceramic via the Rainbow process create a state of tension toward the top, and compression toward the bottom of the unreduced, oxide layer. The ultra-high displacements achievable by Rainbow ceramics can be attributed to this stress-biased condition.

The Cerambow is considered a relative of the Rainbow because they are both based on similar stress-bending technologies. However, temperatures of fabrication are much lower for the Cerambow, and the bonding mechanism is significantly different; i.e. a discrete, physical bond for the Cerambow and an intragranular, chemical bond for the Rainbow. Bonding a high expansion substrate to an electroded piezoelectric disk at a moderate temperature forms a Cerambow. The resulting domed or saddle-shaped configuration in the Cerambow is due entirely to the difference in thermal expansion coefficients between the ceramic and substrate layer.

While the Rainbow is a monomorph consisting of a piezoelectrically active oxide and an inactive reduced layer, the Cerambow is essentially a typical unimorph. In both devices, the inactive layer (consisting of the substrate, bonding layer, and bottom electrode in the Cerambow) laterally constrains the active piezoelectric or electrostrictive layer. Applying an electric field to either actuator causes a dimensional change in the

lateral direction by the active layer. To accommodate this strain, the total composite (active and inactive layers) must bend, resulting in a buckling motion perpendicular to the radial direction of the device. This axial displacement is maximized at the dome center.

In the past there have been many attempts to quantify and alleviate the stresses produced when metals and ceramics are joined. In Cerambow technology, the stresses generated during bonding and subsequent cool down are believed to be responsible for the above average performance of the device. It is believed that the stress gradients present in the ceramic layer of a Cerambow, like the Rainbow, enable it to produce greater displacements at a given voltage than the average unimorph bender. This effect has been studied in the Rainbow and was identified as a stress-enhanced effect.<sup>5</sup>

This paper reports on the process by which Cerambow actuators are fabricated and presents a characterization of their voltage-induced displacement properties under various conditions. In addition, a direct comparison between Cerambows and Rainbows was obtained for the 1/53/47 composition.

## **Experimental Procedure**

**(1) Sample Preparation** Many material properties are optimized for electromechanical transducer applications at the morphotropic phase boundary (MPB) between the ferroelectric rhombohedral and tetragonal phases of the PLZT system.<sup>6</sup> The ferroelectric PLZT compositions used in this investigation were chosen because they lie on or near the MPB. Conventional mixed-oxide techniques were used to prepare PLZT 1/53/47 (La/Zr/Ti), 5.5/56/44, and 9/65/35 powders. Raw materials were batched according to the traditional B-site vacancy formula for the PLZT system. The batched oxide powders were

thoroughly mixed in a ball mill using a 1:1 weight ratio of powder to distilled water.

After drying, the powder was placed in an alumina crucible and calcined at 925°C for two hours. Milling of the calcined powder was carried out using a high alumina ball mill and distilled water.

PLZT slugs were dry pressed using a pressure of approximately 20 MPa and sintered for 4 hours at 1250°C in an oxygen atmosphere. The sintered slugs were then sliced with a diamond saw, ground to a diameter of 31.75 mm and lapped to the appropriate thickness, which ranged from 0.18 - 0.43 mm for each actuator in this study. The disks were coated with silver electrodes (DuPont 7095) on each side, dried at 200°C for 20 minutes and then fired at 550°C for 30 minutes. A non-electroded ring approximately 1 mm wide was left around the outer circumference of one side of the wafer to prevent any excess solder from bonding to the top electrode.

Cerambows could be fabricated from a wide array of materials. In this study, a brass substrate having a thermal expansion coefficient approximately four times greater than that of the ceramic was used. A disk was cut to the appropriate diameter from a sheet of brass foil having a thickness of 0.127 mm. Both the brass disk and the electroded ceramic sample were placed in a sonicator in acetone for one minute to insure a clean surface prior to bonding. The brass disk was placed on a piece of sheet metal on a hot plate preheated to approximately 250°C. The brass was allowed to heat up to maximum expansion, and was tinned using 60/40 Sn/Pb solder. This solder composition was chosen because it possesses the highest joint strength of the tin/lead solders (43.8 MPa).

The electroded PLZT wafer was then placed on top of the solder with the unelectroded-ring side faced up. A preheated steel weight was lowered onto the device to hold it together while it was removed from the hot plate. Pressure was applied normal to the surface of the Cerambow by hand for approximately 20 seconds after removal from the hot plate, and the setup was allowed to cool to room temperature. The edge of the Cerambow was sanded with 400-grit sandpaper to remove any excess solder and decrease the chance of electrical breakdown during testing.

For Rainbow ceramics, the ratio of the reduced layer thickness to the total thickness of the device is most important for maximizing field-induced displacement. This parameter is defined as the thickness ratio. In addition, to properly compare Cerambow and Rainbow actuators the thickness ratio must be kept constant between them. In the Cerambow, the combined thickness of the substrate, solder, and bottom electrode was considered to be equivalent to the reduced layer of the Rainbow. The Cerambow samples made for this investigation were generally found to have an inactive layer thickness of 0.18 mm. Therefore each Rainbow sample was reduced for the proper time and temperature to obtain a 0.18 mm reduced layer. Consequently, the PLZT 1/53/47 disks required a reduction temperature of 950°C for 35 minutes. Since the edges of a Rainbow tended to be more reduced than the remainder of the structure, samples were ground to the appropriate diameter after processing, thus eliminating the region of nonuniform reduction. Silver epoxy electrodes (DuPont 5504) were then applied to both sides and cured at 200°C for 30 minutes.

**(2) Measurements** The density of each fired PLZT slug was determined by the immersion method. All densities were found to be greater than 95 % of theoretical for their respective compositions. The grain sizes of PLZT 1/53/47 and 5.5/56/44 were determined by the linear intercept method and were 7  $\mu\text{m}$  and 3  $\mu\text{m}$ , respectively. Each piezoelectric actuator sample was poled for one minute using an electric field greater than twice the coercive field. This poling field was determined to be 16 kV/cm for 1/53/47 and 25 kV/cm for 5.5/56/44. Three samples were fabricated for each testing condition and the average displacements were reported.

A linear variable differential transformer (LVDT) setup was used to record the voltage-induced displacements of each actuator. The displacement as a function of voltage up to 600 volts was recorded for each sample. The same samples were also tested under a point loading varying from 10 to 1000 grams applied at the dome center under an applied voltage of 450 volts. In order to measure the temperature dependency of the displacement in the Cerambow, the samples were submerged in mineral oil during heating on a hot plate. Displacements were recorded for increasing and decreasing temperature. A diagram of this setup is given in Figure 1.

**Results and Discussion:** The voltage-induced displacements for a series of Cerambow 5.5/56/44 samples with varying thickness are shown in Figure 2. All samples exhibited nearly linear behavior as a function of voltage. The maximum displacement observed at 450 volts was approximately 175  $\mu\text{m}$ , and was achieved by the thinnest Cerambow. A comparison between Cerambows and Rainbows having a thickness ratio of 0.32 is

displayed in Figure 3. For all 1/53/47 Cerambow samples, displacements between 50-75 % of the Rainbows were achieved. A fundamental structural difference between both actuators was most likely responsible for this behavior. In the Rainbow, the interfacial layer between the reduced and oxide layers is extremely thin and essentially nonexistent, whereas the Cerambow possesses a bonding layer that is approximately 50  $\mu\text{m}$  in thickness. It has been reported that in the bimorph and unimorph structures, increasing the thickness of the bonding layer leads to a decrease in the achievable displacement at a given field.<sup>7</sup>

In Rainbows and Cerambows with thinner oxide layers, sometimes the stress induced by the inactive layer during cooling can act to bend the structure into a shape similar to that of a saddle as opposed to the more common dome configuration. From this investigation it was seen that most samples having a total thickness less than approximately 0.45 mm adopted the saddle configuration, while those with a total thickness greater than 0.45 mm adopted the dome configuration. Actuators operating in the saddle mode were known to give greater displacements than those operating in the dome mode. The point must also be made that thinner actuators were exposed to a higher electric field, which would lead to greater displacements. The displacements of the two thinnest samples in Figure 2 were believed to be slightly greater than the remaining samples due to a combination of these factors.

Figure 4 shows a graph of the change in displacement at 450 volts for Cerambows with varying thicknesses under a point loading applied at the dome center. As the loading increased, the thicker samples showed a more slight decrease in displacement

than the thinner samples for each composition. The underlying reason for this behavior was that thicker samples were known to possess greater stiffness, allowing them to maintain more of their curvature under the point loading.

Cerambow samples gave more similar displacements compared to the Rainbow under point loaded conditions. The data from samples having a 0.5 thickness ratio is reported in Figure 5. When these measurements were recorded, each sample was placed on top of a metal washer. It is known that Rainbow samples can give displacements only as large as their dome heights, meaning they cannot reverse their curvature to accommodate an increasing point load or electric field without failure. Cerambows have shown the ability to reverse their curvature without breaking, most likely due to their thicker, more ductile bonding layer, which explains why they showed displacements more comparable to the Rainbow under these conditions.

Figure 6 contains a plot of the displacements of Cerambows with a thickness ratio of 0.29 as a function of temperature. As the temperature was increased, the displacement gradually increased up to approximately 100-115 °C. Past this temperature range, a significant decrease in the displacement was observed, becoming more pronounced up to the maximum temperature. Upon cooling the samples, a similar trend was observed.

The ferroelectric compositions used in this study were known to have piezoelectric properties similar to those of PZT-5. Berlincourt, et al, reported a plot of the change of the  $d_{31}$  coefficient versus temperature.<sup>8</sup> A rise in temperature is accompanied by an increase in the  $d_{31}$  coefficient for PZT-5A up to 115 °C and beyond. It was assumed that the ferroelectric materials used to make the Cerambows in this showed similar behavior. The increase in this material property directly influences the

performance of Cerambows because, as stated previously, the lateral dimensional change perpendicular to the direction of the applied electric field is responsible for the bending motion in these actuators. This factor was considered to be the major contributor to the behavior of the ferroelectric Cerambow actuators up to approximately 115 °C.

From 115-150°C, the displacement of the piezoelectric Cerambows decreased significantly. At these temperatures, the rapid softening of the solder bonding layer allowed the metal and ceramic layers to begin to move relative to each other. When voltage was applied, the deformation in the piezoelectric layer was not entirely transformed into bending motion, leading to a decrease in the observed displacement. As temperature was increased further, the bonding layer became more ductile, transforming even less of the piezoelectric strains into bending.

As for the electrostrictive 9/65/35 Cerambows, the displacement at 450 Volts decreased as the temperature was increased from room temperature to 150 °C. This type of behavior was expected from this material because it was known to have a Curie temperature that lies at approximately room temperature. As the temperature of this material was increased, the amount of obtainable polarization within it decreases, hence the net displacement decreases. Likewise, the softening of the bonding layer surely contributed to the decrease in performance.

**Summary** The Cerambow has proven to be a viable strain-amplification technique for motor piezoelectric applications, producing displacements between 50-75 % of Rainbow samples having the same dimensions. The range of samples made for this investigation all showed fairly linear voltage dependence up to 600 volts. Cerambows made from



1/53/47 PLZT produced strains which were equivalent to those of Rainbows under point loaded conditions.

The temperature dependent displacement capabilities of PLZT 1/53/47 and 5.5/56/44 Cerambow actuators was evaluated and found to be fairly constant up to temperatures of approximately 100°C. Past this temperature range, there was a sharp decrease in the displacement. The softening of the bonding layer was considered to be the major contributing factor to this behavior. The 9/65/35 samples showed a decrease in their displacement as a function of temperature, which was expected due to the nature of electrostriction under these conditions.

## References

1. Gene H. Haertling, "Chemically Reduced PLZT Ceramics for Ultra-High Displacement Actuators," *Ferroelectrics*, **154** 101-106 (1994).
2. Y. Sugawara, K. Onitsuka, S. Yoshikawa, Q. Xu, R. E. Newnham, and K. Uchino, "Metal-Ceramic Composite Actuators," *J. Am. Ceram. Soc.*, **75** [4] 996-998, (1992).
3. Gene H. Haertling, "Rainbow Ceramics- A New Type of Ultra-High Displacement Actuator," *Bull. Am. Ceram. Soc.*, **73** [1] 93-96 (1994).
4. Guang Li, "Influence of Internal Stress on the Electromechanical Properties of PLZT stress-biased (Rainbow) Ceramic Actuators," Ph. D. Thesis, Gilbert C. Robinson Department of Ceramic Engineering, Clemson University (1995).
5. Guang Li, "Stress-Enhanced Displacements in PLZT Rainbow Actuators," to be published, (1997).

6. Gene H. Haertling, "Compositional Study of PLZT Rainbow Ceramics for Piezo Actuators," Proceedings of the Ninth International Symposium of on the Applications of Ferroelectrics, Pennsylvania State University, University Park, PA, 1994.
7. Michael A. Marcus, "Performance Characteristics of Piezoelectric Polymer Flexure Mode Devices", *Ferroelectrics*, **57**, 203-220 (1984).
8. D. A. Berlincourt, D. R. Curran, and H. Jaffe, "Piezoelectric and Piezomagnetic Materials and Their Function in Transducers," Physical Acoustics, p. 206 (1964).

### Figure Titles

- Fig. 1. Schematic diagram of the experimental setup used to measure the temerature-dependent displacements of Cerambows.
- Fig. 2. Comparison of the voltage-induced displacements of Cerambows with varying oxide layer thickness.
- Fig. 3. Voltage-induced displacement of Cerambow and Rainbow samples having a 0.32 thickness ratio.
- Fig. 4. Displacement at 450 volts of 9/65/35 Cerambow samples under a point loading at the dome center.
- Fig. 5. Cerambow/Rainbow voltage-induced displacement comparison under an increasing point loading.
- Fig. 6. Temperature-dependent displacement properties of Cerambow actuators having a 0.29 thickness ratio.

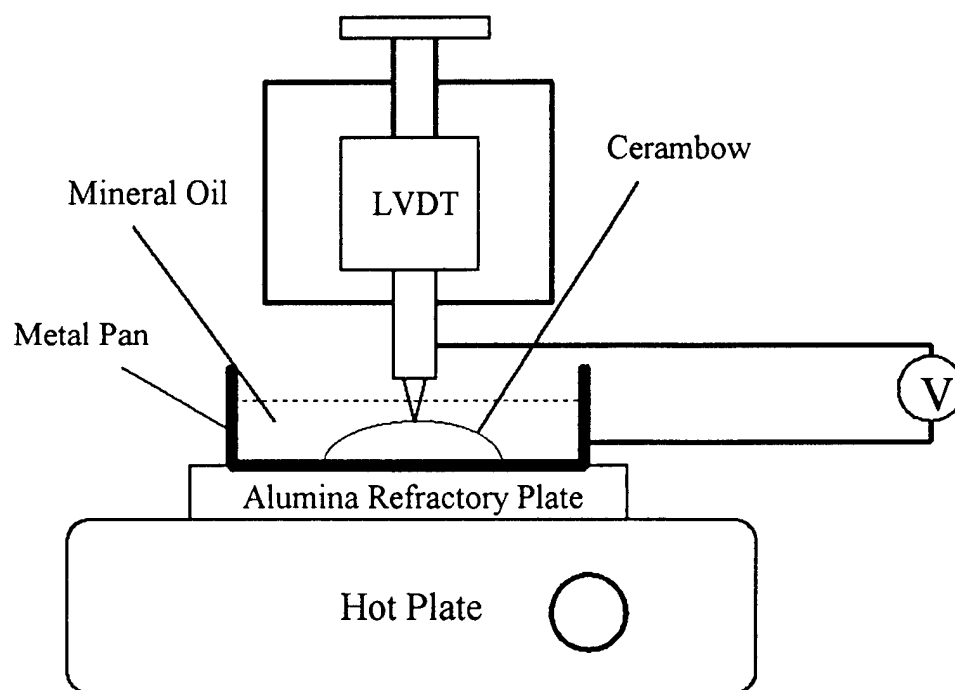


**Fig. 1.** Schematic diagram of the experimental setup used to measure the temperature-dependent displacements of Cerambows.

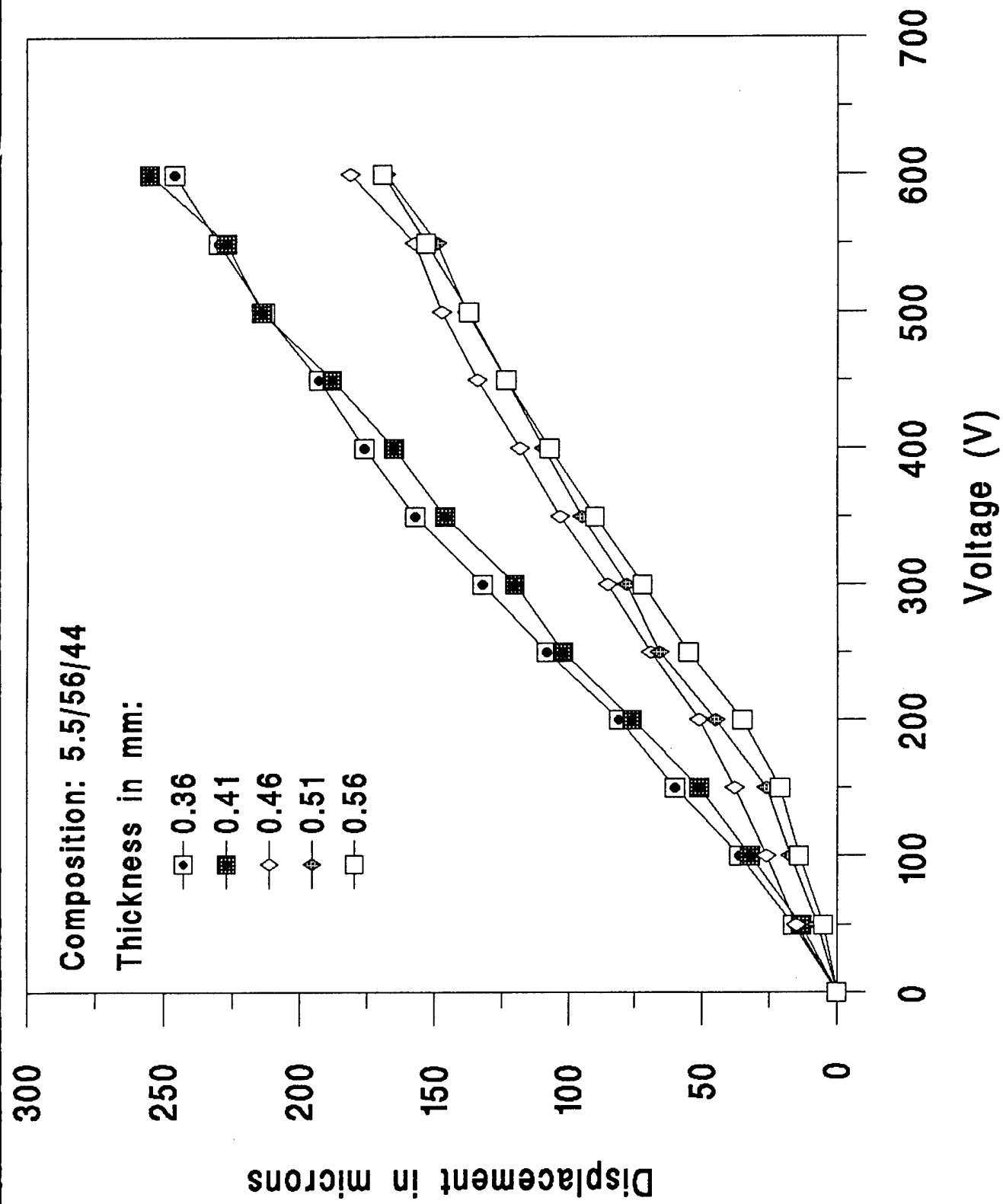


Fig. 2. Comparison of the voltage-induced displacements of Cerambows with varying oxide layer thickness.

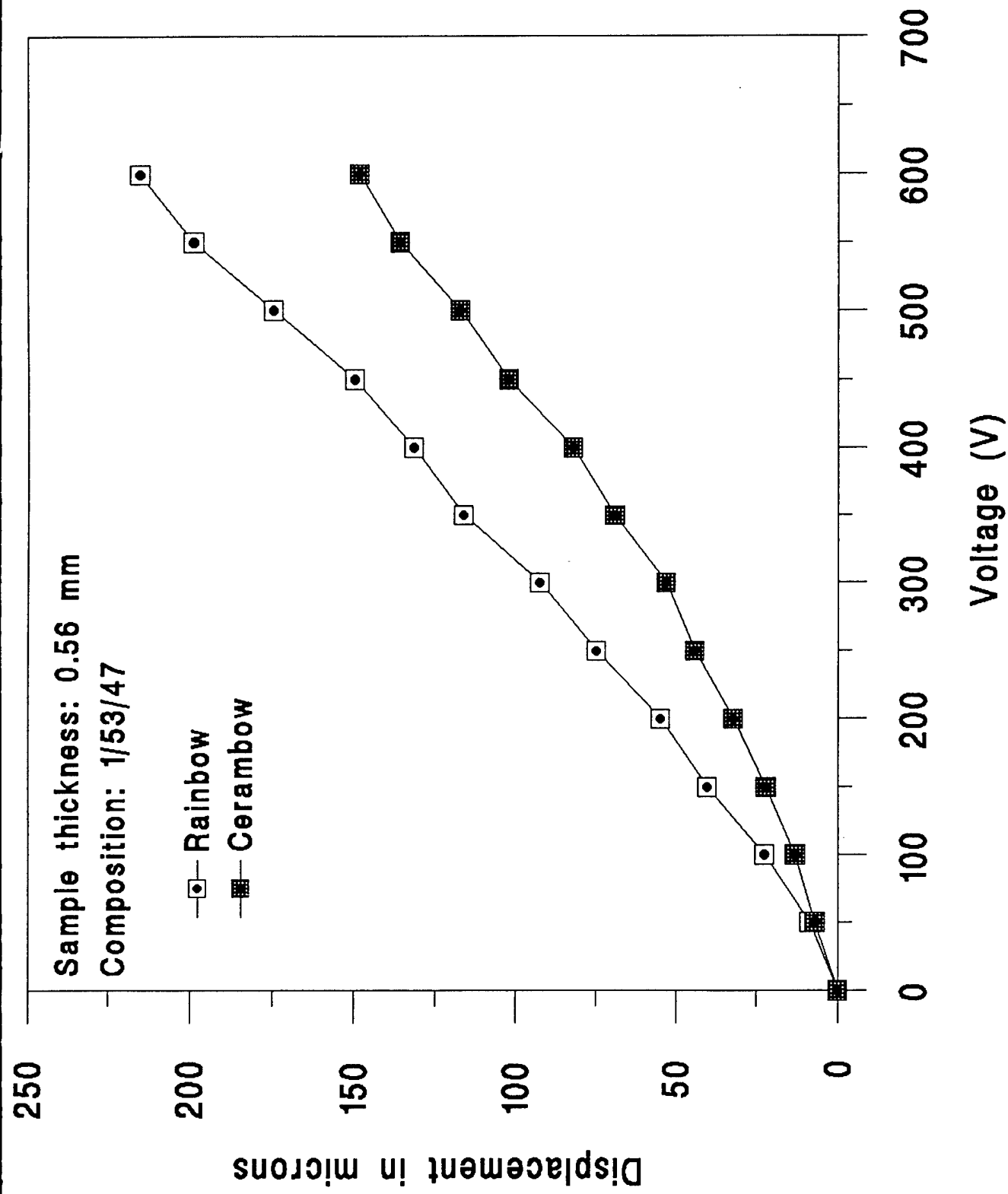


Fig. 3. Voltage-induced displacement of Cerambow and Rainbow samples having a 0.32 thickness ratio.

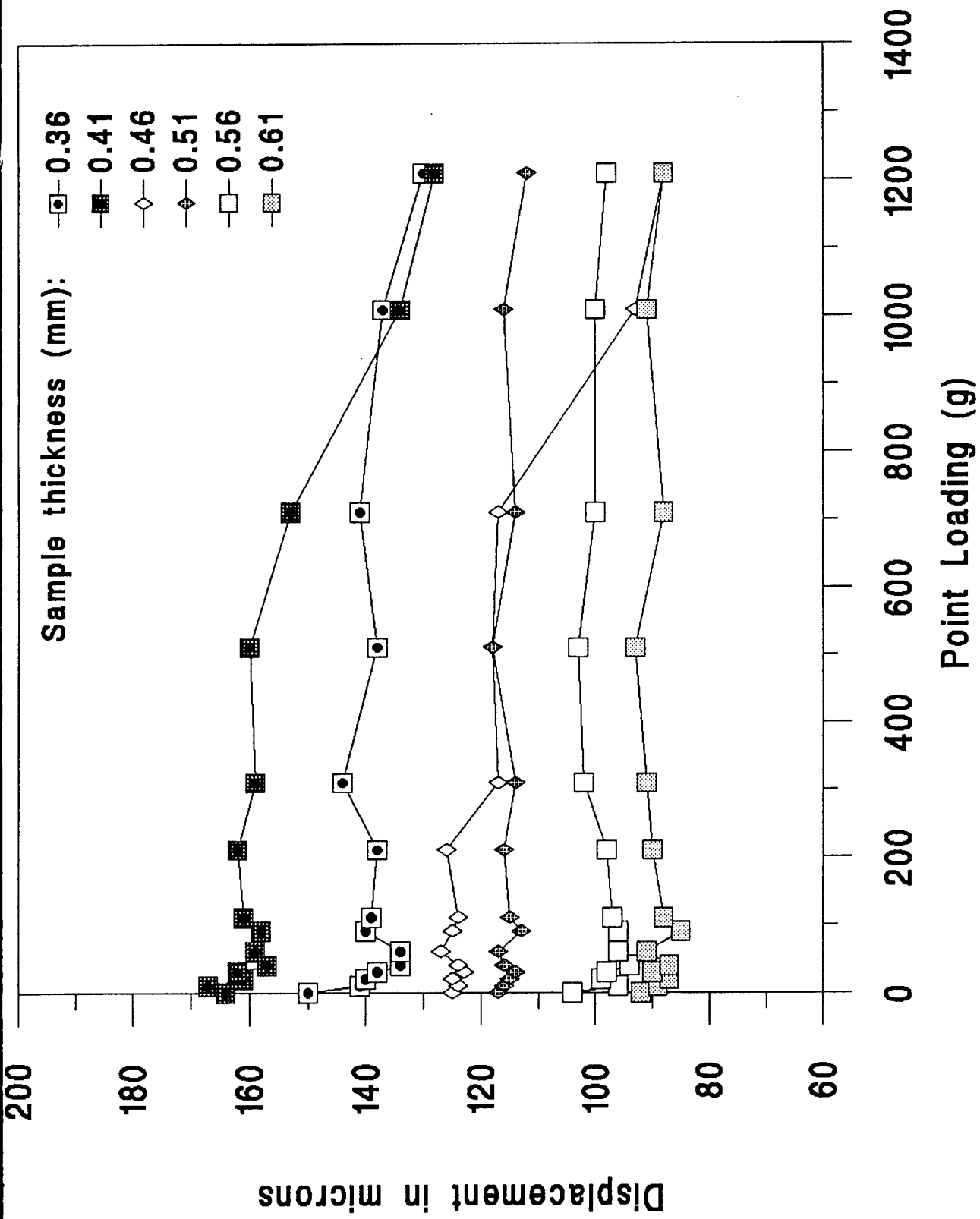


Fig. 4. Displacement at 450 volts of 9/65/35 Cerambow samples under a point loading at the dome center.

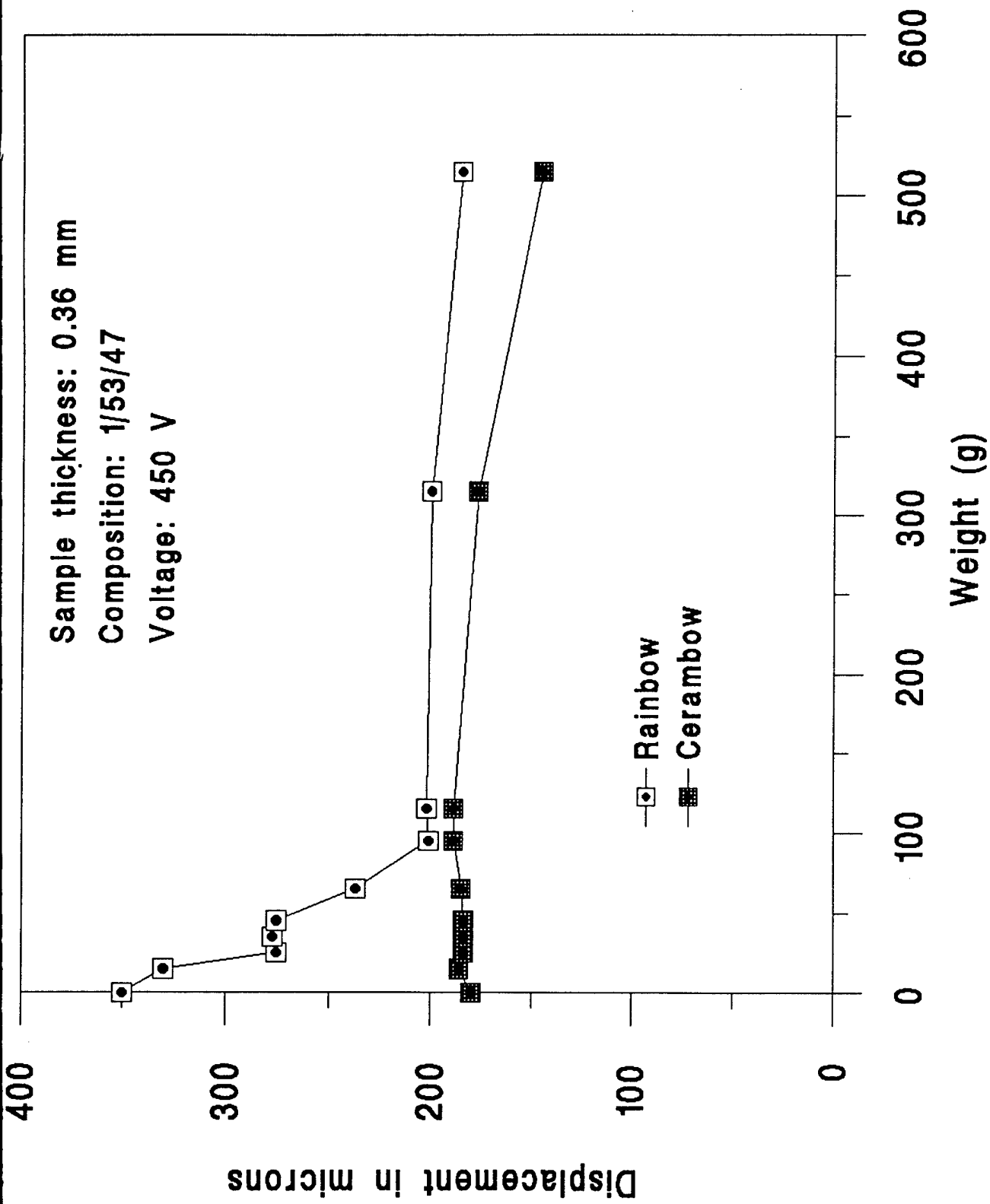
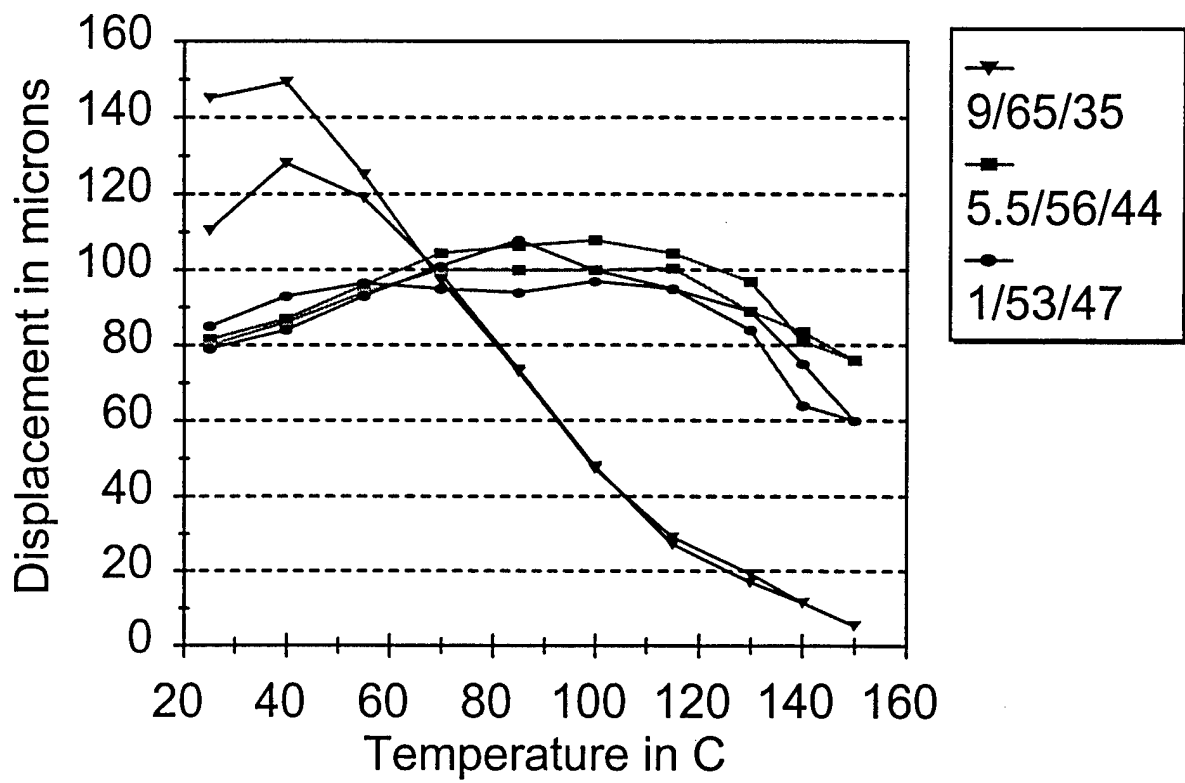


Fig. 5. Cerambow/Rainbow voltage-induced displacement comparison under an increasing point loading.



**Fig. 6.** Temperature-dependent displacement properties of Cerambow actuators having a 0.29 thickness ratio.



**Part VIII.**

**Intelligent Processing and Stressing of Electrooptic Thin Films**

# **INTELLIGENT PROCESSING OF ELECTROOPTIC THIN FILMS**

## **Annual Report**

### **Electrooptic Ceramics**

Submitted by: William E. Paradise  
Gene Haertling

**The Gilbert C. Robinson Department of Ceramic Engineering  
Clemson University**

## SUMMARY

Electrooptic ceramics have properties that can vary widely due to thickness, shape and processing method. These materials have conventionally been produced by a variety of deposition processes. These processes include the bulk ceramic techniques (sintering, hot pressing and tape casting) along with chemical (sol-gel, CVD and MOD) and physical (evaporation, sputtering and laser ablation) processes used in producing thin films. The goals of the ONR program on "Intelligent Processing of Electrooptic Thin Films" are to determine the similarities and differences in material properties produced by various processes. Producing electrooptic thin films and bulk ceramics from the same acetate precursors and then characterizing the chemical, electrical, physical and electrooptic properties of these materials carried out parts of these goals. It is desirable that processing methods used be compatible with both thin films and bulk ceramics in order to better compare their respective properties. An acetate precursor system was employed to produce both acetate solutions for spin and dip coated thin films as well as coprecipitated powders for bulk ceramics.

In another study, the dielectric and electrooptic properties of the thin films were manipulated by varying the stresses placed upon the films. Selected thin films in the lanthanum-modified lead zirconate titanate system (PLZT) were produced by both the dip-coating and spin-coating process. Varying magnitudes of strains ( $\pm 2 \times 10^{-3}$ ) were applied using a three-point bending setup. Properties measured were dielectric constant, saturation polarization, remanent polarization, coercive field, crossover birefringence, total birefringence, optical coercive field and d-spacing. The effects of the applied stresses on the physical and electrical properties of the films are discussed. Comparisons were made among thin films under mechanically applied stresses of different magnitude. Finally theoretical modeling is designed for understanding the effects of applied stresses on the dielectric and electrooptic properties of PLZT thin films.

## INTRODUCTION

The perovskite lanthanum-modified lead zirconate titanate system (PLZT), because of its combined dielectric, pyroelectric, piezoelectric and electrooptic properties, has created new possibilities for their use in electronic and photonic devices. Electrooptic ceramics in general have been a topic of interest due to the desirable properties they possess. The importance of electrooptic thin films is evident in their many applications ranging from sensors to light modulators.[1] These thin film uses come from the electrooptic bulk ceramics developed over the years. Thin films possess some advantages over bulk ceramics such as easier integration with silicon technology, lower operating voltage, higher speed and lower cost which make them more desirable for many devices. The research for new materials with unique and improved properties has continued as new modifications and compositions of the PLZT system are constantly developed.

Electrooptic thin films have properties that can vary widely due to their differences in thickness, processing method and substrate type.[2] The effects of applying mechanical stress to electrooptic ceramics, known as strain-biasing, has been used in image storage and display applications.[3] It has also been shown that under compressive stress a transition in ceramics from a rhombohedral to a tetragonal symmetry can occur.[4] It is believed that through the study of these materials, an optimization of their properties can be achieved. In order to understand and optimize thin film electrooptic behavior, a comparison is necessary between the thin film and bulk ceramics properties. The understanding of the correlation between stresses and the changes within thin film properties is also needed.

Direct correlation between the bulk and thin film materials is difficult since typically the precursors and processing techniques of each are different. This problem was eliminated by using the same acetate precursor solutions in the manufacturing of the PLZT bulk ceramics and thin films within this research. It is believed that this process allows for a close comparison of PLZT bulk and thin film electrooptics by minimizing or eliminating differences in the processing of these materials induced by precursor impurities, batching variations and differences in mixing of the precursor materials. This

allows us to characterize similarities and differences in the properties of bulk ceramics produced from chemically coprecipitated powders and dip coated thin films produced by a metallorganic decomposition process without having variations in starting materials as a factor.

Research on quenched PLZT 9.5/65/35 ceramics showed that internal stresses induced in samples can enhance polar region ordering which would produce a more ferroelectric-like response by the material.[5] This response would produce higher remanent polarizations in quenched samples than in annealed samples. A compressive stress in the thin films will align the domains parallel with the applied electric field, enhancing the ferroelectric properties of the thin films. Tensile stresses will align the domains perpendicular to the applied field and the effect will be a decrease in the remanent polarization, shown in Figure 1.[6] Watanabe et al. [7] proposed that differences in lattice constant between bulk and thin film PZT ceramics can be caused by the mechanical stress present within the thin films. When a polycrystalline ceramic is deformed in such a way that the strain is uniform over a relatively large distance, the lattice plane spacing in the constituent grains changes from a stress-free value to some new value corresponding to the magnitude of the applied stress. The new spacing is essentially constant from one grain to another for any particular set of planes that are similarly oriented with respect to the stress.

It has been shown that mechanical stresses altered the properties of several electrooptic bulk devices and resulted in materials for new applications. Wang et al. [8] described a thin film light modulator that utilizes the interference of multiple reflections of light between the bottom and the top electrode to obtain a high contrast ratio. The primary role of electrooptic thin film materials in integrated optical and electrooptic devices is to modulate light waves. Since the materials are electrooptic, such modulations can be achieved by electrically controlling the indices of refraction in the thin film materials. The characterization of the electrooptic properties of the thin film materials is of obvious importance. While several investigations on the effects of stress on the properties of bulk electrooptic ceramics have been reported, it is believed that systematic investigation of stress effects on electrooptic thin films has not been

conducted.

By producing electrooptic thin films from acetate precursors and characterizing the electrical and electrooptic properties of these materials an optimization of the thin films properties may be reached. The principal interests now under examination are the understanding and modeling of the manner in which stresses acting on and within these films can effect their properties.

## **EXPERIMENTAL PROCEDURE**

### *Processing*

PLZT bulk ceramics and dip coated thin films were produced using a water soluble acetate precursor method.[9] The chemical coprecipitation process which was used to produce PLZT powder from acetate precursors is shown in Figure 2.[10] This processing method produces bulk and thin film samples from the same batches. This allowed for a unique comparison of properties between bulk ceramics and thin films since it reduced or removed any variations between batches and precursor histories. All the elements needed to produce PLZT were placed into an acetate form and mixed together. The acetate precursors were chosen primarily for their low cost, insensitivity to moisture, and chemical stability. The starting precursors were titanium acetyl acetate, zirconium acetate, lanthanum acetate and lead subacetate powder. The lead subacetate was mixed into solution by the addition of acetic acid and methanol so that all of the acetate precursors were in a liquid form in order to promote a more homogeneous and intimate mixing. Incomplete mixing would produce compositional fluctuations between bulk and thin film solutions. A portion of this solution was then taken off to be used for the thin film productions.

The bulk portion of the solution was coprecipitated in a high-speed blender by adding oxalic acid and methanol during blending in order to bring about precipitation of the PLZT powder. As stated earlier, this process produces a more homogeneous mixture of precursors and therefore produces a more intimately mixed PLZT powder with a

smaller particle size than the mixed oxide process. This powder was then vacuum dried at 70°C to produce a solid cake. The cake was crushed, calcined at 500°C for 8 hours and milled in trichloroethylene for 6 hours to produce a PLZT oxide powder. The powder was then either pressed into disks at 21 MPa and sintered at 1250°C in a lead-rich atmosphere for 4-6 hours or hot pressed for 4-6 hours at 1250°C and 14 MPa. Typically, 110g of powder was produced for hot pressing. The sintered and hot pressed parts were sliced on a diamond saw and lapped to 20 mils thickness. Electroless nickel electrodes were plated onto the ceramics through a series of chemical baths. The samples were electroded for measurement of their dielectric and hysteresis loop properties.

Thin films were produced by the automatic dip coating process shown in Figure 3.[6] These films were produced to determine if the firing temperature could be reduced without affecting the film's properties. For thin film production, the small portion (usually 5g) of the decanted acetate solution was diluted with methanol at a 4:1 ratio by weight. This improves solution stability and reduces cracking during heat treatments. The films were dipped onto silver foil substrates, allowed to dry for 30 seconds and pyrolyzed at 500°C or 700°C for 3 minutes. Some of the films had their firing temperature changed after the first and/or before the last layer was applied. Therefore, a "575" film had the first layer fired on at 500°C, the middle 22 layers fired on at 700°C and the remaining layer fired on at 500°C. All of the films had 24 layers and were approximately 1  $\mu\text{m}$  thick. The films were electroded by vacuum evaporation of copper and measured for dielectric constant, electrical resistivity and hysteresis loop characteristics. Electrooptic measurements could not be made on these films due to the rough surface of the silver substrate.

In another experiment the chemical coprecipitation process was used again to produce PLZT acetate precursors. Incomplete mixing would produce compositional fluctuations within the thin film's structure. Both an automatic dip coating and an automatic spin coating process were used to produce thin films. The dip coated films were dipped onto silver foil substrates, allowed to dry for a minute and then pyrolyzed at 700°C for three minutes. Three compositions (2/55/45, 9/65/35 and 28/0/100) were used, and of each of these compositions, three film thicknesses were produced. The three films

of each composition had 24, 48 and 72 layers and were approximately 1, 2 and 3 microns thick respectively. The films were then electroded with evaporated copper for measurement of their dielectric and hysteresis loop properties.

The spin coated films were spun onto 2" diameter ultra thin (~50  $\mu\text{m}$ ) platinum coated silicon wafers. The ultra thin Pt/Si wafers were used due to the substrates flexibility and smooth reflective surface. Three compositions were produced, each consisting of 20 layers and were approximately 2 microns thick. Films were spun at 2000 rpm for 30 seconds and allowed to dry for a minute before heating. Rapid thermal processing was used to pyrolyze the film at 700°C for one minute per layer before cooling to room temperature between layers. The films were electroded with evaporated copper for measurement of the dielectric and hysteresis loop properties, while indium tin oxide electrodes were used in the electrooptic measurements, as shown in Figure 4. A 2 micron thin film of composition 11/65/35 was also produced on an Ag foil substrate by dip coating so that a direct comparison could be made between the films produced on the ultra thin Pt/Si with that of the films produced on Ag.

#### *Automatic Spin Coater*

Thin films were produced by an automatic spin coat reactor/analyzer, which is shown in Figure 5.[11] The automatic spin coat reactor/analyzer, produced by Digital Controls, Inc. in Rolla, MO, is controlled by an IBM compatible, 80386DX computer with software to operate the ellipsometer and set parameters for atmospheric gas control, deposition, spinning, heating and cooling. It was utilized for spin coating and rapid thermal processing of electrooptic thin films from liquid acetate precursors. Computer control provided hands-off fabrication and flexibility in processing of the films. Samples may be prepared without exposure to the outside environment.

The fluid dispense system has the capability of depositing one of three precursor solutions onto 1/2" to 4" diameter substrates. A nitrogen dusting step can also be inserted through the dispense arm before fluid deposition. Spinning is executed with an ac brushless servomotor and controller with programmable time, speed and acceleration.



Six water-cooled parabolic strip heaters with infrared quartz lamps containing tungsten filaments comprise the rapid thermal processing unit. This RTP unit allows the sample to be heated to 700°C within 5 to 10 seconds. Variable atmospheric gases (N<sub>2</sub>, O<sub>2</sub>, Ar) and low pressures as well as vacuum capability are possible in the atmosphere control system. In-situ thickness measurements may be taken before and after heating by a Gaertner Scientific laser ellipsometer. A typical run would proceed as follows:

1. Chamber was pumped down to vacuum pressures
2. Chamber was vented with set gas mixture and pressure
3. Dispense arm moved over substrate, blew off surface with nitrogen gas and fluid injected onto substrate
4. Sample stage spin initiated
5. Dispense arm moved back and heater (water cooled quartz infrared lamps) moved forward over sample stage
6. Heater ramped and soaked at set parameters using a rapid thermal annealing process
7. Heater moved back and laser ellipsometer used to measure film thickness

This cycle can be repeated for any number of layers or with a change in composition between layers. A cooling stage was placed in between layers to allow the film to cool before the next deposit of solution.

### *Stressing*

To induce a stress within the thin films, the films were placed within a three-point bender and flexed as shown in Figure 6. The applied stress in the films was correlated to the curvature of the films. The electrical properties were measured at various stress levels by measuring them at different film curvatures. Simply taking measurements at concave versus convex curvatures compared compressive versus tensile stress effects on properties.

## MEASUREMENTS

Bulk and thin film samples were measured for dielectric constants, electrical resistivities and hysteresis loops. The capacitance and dissipation factor were measured on bulk and thin film samples using a Leader LCR meter at a measuring frequency of 1 kHz. Resistance was measured using a Keithley electrometer. Hysteresis loops were also measured for both materials to determine their polarization versus an electric field. The bulk samples were measured using a Sawyer-Tower circuit with a dc applied voltage of  $\pm 1400$  V, and the hysteresis loops were plotted with a Goerz Metrawatt X-Y plotter. Hysteresis loops of the thin film samples were measured at 1 kHz using a Sawyer-Tower circuit with oscilloscope readout shown in Figure 7. The coercive fields, remanent and saturated polarizations were measured for all of the samples from their hysteresis loops as demonstrated in Figure 8. Electrooptic properties of the thin films on opaque substrates were measured with reflective differential ellipsometry, as shown in Figure 9.[12] The measurement involves the detection of a phase shift in a probing light beam reflected from the film. The changes in the extraordinary and ordinary indexes were then determined by measuring the phase shift at various incident angles, since the extraordinary and ordinary index calibration coefficients are dependent on the angle. Properties measured were crossover birefringence, total birefringence and optical coercive field as demonstrated in Figure 10.

The films were flexed to induce a stress. The applied stress in the films was determined by two techniques:

- (a) The strain induced within the thin films was calculated by measuring the radius of curvature the film exhibits while being stressed.
- (b) Film strain measured in a direction normal to the film plane was also calculated based on the interplanar d-spacings obtained from X-ray diffraction data.

The strain induced within the thin films was calculated by Equation 1

$$\text{Strain} = \frac{(t/2)}{R} \quad (1)$$

where  $t$  is the total thickness of the film and substrate, and  $R$  is the radius of curvature of the film.[13] Some assumptions need to be made before this equation can be used though. First, it is assumed that the axes of symmetry lie through the center of the film. Second, the film must have a constant radius of curvature. And third, the substrate must be rigid enough not to plastically deform so as not to relieve any of the stress applied to the film. Radius of curvature can be found by using the following equation

$$(2R-d)*d = L^2 \quad (2)$$

where  $d$  is the deflection of the substrate and film, and  $L$  is the length of the deflection from the center as shown in Figure 11.[14] The stress is obtained by multiplying the strain value with the Young's modulus of the material. The sign agrees with the convention that it is positive for tension and negative for compression. The X-ray diffraction analysis for measuring the strain applied on the thin films used a Scintag XDS 2000 diffractometer with Cu K $\alpha$  radiation at a scan rate of 2 $^\circ$ /min. Comparisons were made between the calculated and measured values of the applied strain.

A film residing on a rigid substrate of much greater thickness is unable to move freely. Therefore, after the fabrication process, the film is usually strained in a way corresponding to the induced tensile or compressive stress imposed by the substrate. The substrate should also experience an opposite stress exerted by the film and deform accordingly, which may lead to a distribution or a relaxation of the induced stresses within the film.[15] This effect is neglected for the dip coating process since the two sides of the substrate are evenly coated and the bending moments from the films on the opposite sides are thus expected to cancel each other.

Should there exist any difference in the thermal expansion behavior between the thin film and the substrate, development of intrinsic stresses within the film during the cooling stage will occur. Since most ferroelectric materials possess large electromechanical coupling effects, the presence of an intrinsic stress in a ferroelectric film will affect its dielectric properties. This intrinsic stress tends to be compressive for PLZT thin films produced on silver substrates due to the PLZT's lower thermal expansion than that of the silver substrate. For PLZT thin films produced on Pt/Si substrates the intrinsic stress tends to be tensile due to the PLZT's higher thermal expansion. The effect of the total stress acting on the films produced within this paper was not analyzed, only the effects of the applied portion of the total stress within the films. It is believed that the magnitude of the applied stresses is significantly greater than any intrinsic stress which may be present within the film after processing. Therefore, it is the addition of the applied stresses to the thin films that was measured and any induced stress due to thermal expansion mismatch was not taken into account.

## RESULTS AND DISCUSSION

### *Bulk and Thin Film Comparison*

Hot pressed bulk ceramics and dip coated thin films on Ag foil substrates were fabricated, and a comparison of properties was established. Sintered and hot pressed ceramics along with dip coated thin films (on silver foil) for the 9/65/35 composition were compared as shown in Table 1. These values showed that the hot pressed ceramics had very little remanent polarization and reached a lower saturation level than the other two; while the thin films had a large amount of remanent polarization with a lower dielectric constant than either of the bulk ceramics. These effects have been reported to be due to differences between bulk and thin film configurations. The fact that the thin film dielectric constants were generally lower could be attributed to the small grain size of the thin films, mechanical clamping effects or, due to the high electric field applied to the thin films, the voltage sensitivity of the measurement. This could imply that the hot

pressed ceramics had better properties due to larger grain growth and fewer defects, which would be expected with hot pressed materials. These differences could also be seen when comparing the hysteresis loops as in Figure 12. Internal stresses induced in samples, as stated earlier, can enhance polar region ordering producing a more ferroelectric-like response by the material. This response would produce higher remanent polarizations. These findings could explain the memory behavior found in the thin films used in this experiment. Residual stresses may have caused these films to retain ferroelectric memory hysteresis loops that were not observed in the bulk materials.

The coercive fields and remanent polarizations were calculated for all the films in the temperature dependence test and are listed along with dielectric constants and dissipation factors in Table 2. The highest poled dielectric constants were found to be in the "777" thin film. In comparison to the "777" sample, the hysteresis loop of the "555" sample was more conductive and electrically shorted more readily. The ac loop of the "777" sample reached much better saturation and looked similar to a bulk hysteresis loop. The ac hysteresis loops are shown in Figure 13. The hysteresis loops also became slimmer as the temperature used increased. All this indicated that films fired at higher temperatures had better nucleation and grain growth. As anticipated, the properties of the thin films were found to be highly dependent on firing schedule. Graphs of the improvements in properties with firing temperatures are shown in Figures 14 and 15. These graphs clearly show the increase in dielectric constant and remanent polarization as the firing temperature is increased from 500°C to 700°C.

### *Stress Effects*

#### *Dielectric Constant*

Subtracting the value obtained from the film before a stress was induced normalized the values measured. This was done in order to compare the properties measured between the different substrates and between the different compositions. The composition 2/55/45 was chosen for study because it lies near the morphotropic phase

boundary in the PLZT system. This phase boundary composition regularly exhibits a ferroelectric memory behavior. The material exhibits both a rhombohedral and tetragonal symmetry since the 2/55/45 composition lies near this boundary. It was observed from the experiment that with an increasing tensile stress the dielectric constant for this composition increased for films on Ag and decreased for the films on Pt/Si, as shown in Figures 16 and 17. It is believed that upon stressing a transition in symmetry is taking place within the 2/55/45 thin film on Ag. This change in symmetry toward more rhombohedral symmetry would account for an increase in the dielectric constant. The decrease shown for the film on Pt/Si is believed to be due to the domain aligning caused by the induced stress. The difference shown between the films on Ag with that of the films on Pt/Si is thought to come about from the opposite intrinsic stresses placed within the films during processing which were due to thermal expansion mismatch. More X-ray analysis may be required to better understand any physical changes that may influence this property.

The 9/65/35 composition is near the paraelectric phase region and tends to have a slim-loop hysteresis with very little memory behavior. It was observed for this composition on Ag that the addition of either a compressive or tensile stress had very little affect on the dielectric constant. A decrease was observed for the film on Pt/Si from compression to tension, which was similar to the 2/55/45 on Pt/Si.

The 28/0/100 and 11/65/35 compositions lie within a cubic region and also tend to exhibit slim-loop properties. Their properties should not vary much under stress due to this pseudo-cubic nature and the limited number of domains present. The 11/65/35 composition on Ag showed a slight change in the dielectric constant under different stresses with a maximum being reached when a compressive stress was placed on the film as shown in Figure 16. The addition of a further compressive stress caused the dielectric constant to decrease. This decrease is also evident with the addition of a tensile stress. The 11/65/35 composition on Pt/Si followed the trend of the other films on Pt/Si by decreasing slightly from compression to tension.

### *Hysteresis Properties*

Compressive stresses within the thin films will align the domains parallel with the applied electric field. This type of ordering will increase the ferroelectric properties of the thin films. A tensile stress will align the domains perpendicular to the applied field, and the effect will be a decrease in the ferroelectric properties. For the films produced on Ag both the 9/65/35 and the 28/0/100 showed this effect to some degree, but the 2/55/45 thin films had a decrease in remanent and saturated polarization under a compressive stress, as shown in Figures 18, 19 and 21. This response for the 2/55/45 composition is not yet fully understood, especially since the films on Pt/Si only increased with compressive stress as shown in Figures 20 and 22. Most likely a combination of factors are affecting these properties under the stresses applied. The effects of having the sample clamped during measurement are now being investigated as a possible explanation along with understanding the thermodynamics involved.

The remanent polarizations and coercive fields of all the thin films tended to increase under a compressive stress and decreased under tensile, as shown in Figures 21-24. The 9/65/35 thin films tended to show a slight change within the properties measured, this can be related to the amount of domains present within the films. As the number of domains present within the films decreased from the memory material to the slip loop films the amount of change observed decreased. The pseudo-cubic thin films did not show much of a change within any of the properties measured. This can again be related to the composition's pseudo-cubic structure producing a very stable material with very few domains present.

### *Lattice Spacing*

X-ray diffraction patterns of the 2 $\mu$ m 2/55/45 thin film were taken at different stress levels. In analyzing the lattice spacings of the different levels of applied stress, it was observed that the compressive stress produced slightly larger d-spacings than in the tensile stress. As shown previously, mechanical stress present in PLZT thin films can

cause differences in the lattice constant between bulk and thin film materials. When a polycrystalline ceramic is deformed in such a way that the strain is uniform over a relatively large distance, the lattice plane spacing in the grains change to a new value corresponding to the magnitude of the applied stress, as shown in Figure 25. A uniform strain over the thin film will cause a shift of the diffraction lines to new  $2\theta$  positions. The new spacing is essentially constant from one grain to another for any particular set of planes that are similarly oriented with respect to the stress. A smaller lattice constant perpendicular to the film corresponds to a tensile stress. A graph of the (200) d-spacings at the various stress levels is shown in Figure 26. From this figure it can be seen that the d-spacing does decrease from compressive to tensile stress as expected. The change in the d-spacings can be used to calculate the amount of induced stress. Comparing this to the calculated stress from the radius of curvature measurements shows good agreement between the two techniques as shown in Figure 27.

### *Birefringence*

The birefringence of a material is dependent on the material's structure. Stresses placed upon PLZT thin films will change the electrooptic properties measured in the same way that the stresses effect the dielectric properties of the PLZT thin films. Only the films on Pt/Si could be measured because the surface of the silver substrate used for the other films was too rough to properly reflect the laser beam used in the measuring process. It was seen that compressive stresses induced within PLZT thin films on Pt/Si caused a broadening of their hysteresis loops. This change toward a more ferroelectric memory material is also seen in the electrooptic properties. An increase in all three of the properties measured for each composition was observed when a compressive stress was applied to the PLZT thin films on ultra thin Pt/Si, Figures 28, 29 and 30. The amount of the change within the properties decreased as the compositions moved away from the 2/55/45 memory composition. The 11/65/35 compositions pseudo-cubic structure is very stable under applied stresses and therefore it was no surprise to see only a slight change in the electrooptic properties measured for these thin films.



## SUMMARY AND CONCLUSIONS

Sintered and hot pressed ceramics along with dip coated thin films (on silver foil) for the 9/65/35 composition were compared. PLZT bulk ceramics and thin films were fabricated from the same acetate precursor solutions in order to minimize batching variations and accurately compare properties between bulk and thin film samples of the same compositions. The bulk materials produced slim hysteresis loops, but this was never completely achieved in the thin films. It has been suggested that these differences may be attributed to the induced stresses built up within the thin films. This comparison of bulk and thin film electrooptics is believed to be accurate since both used the same starting precursors. It is thought that the complete mixing of precursors and accurate batching of materials which was used for both bulk and thin film production provided a minimization of differences that could cause serious variations in their composition and properties. . It is believed this process provided a true correlation between these materials. The only variables between the bulk ceramics and the thin films were their differences in processing, which may have caused physical differences

The properties of the thin films were found to be highly dependent on the firing schedule used. It is believed that at higher firing temperatures the films had better nucleation and grain growth, which would account for the increase in measured properties.

As anticipated, the properties of the thin films were found to be dependent on the type and amount of stress applied. A compressive stress on the thin films will align the domains. This aligning will produce slightly larger d-spacings within the material and, if parallel with the applied electric field, increases in the dielectric properties. It is also believed that the increase in dielectric constant within the 2/55/45 thin films produced on Ag, upon applying a tensile stress, may be caused by a change in symmetry. The 28/0/100 and 11/65/35 composition's properties did not vary much under stress, which may be due to their pseudo-cubic structure.

Only the films produced on the ultra thin Pt/Si substrates were used in the

electrooptic measurements due to the silver substrates of the other films being too rough for the reflected measuring technique used. The electrooptic properties followed the same trends as was observed for the dielectric properties of the thin films on ultra thin Pt/Si. As the induced stress went from compressive to tensile the measured electrooptic properties decreased. It was also shown that the amount of change observed decreased as the composition moved toward a more cubic, and therefore stable, structure.

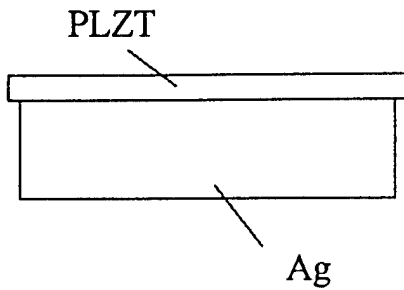
## REFERENCES

- [1] G. H. Haertling, Engineered Materials Handbook, 1124-1130 vol. 4 Ceramics and Glasses), ASM International, (1991).
- [2] K. D. Preston and G. H. Haertling, "Comparison of Electro-Optic Lead-Lanthanum Zirconate Titanate Films on Crystalline and Glass Substrates," *Appl. Phys. Lett.* 60 [23], 2831-33 (1992).
- [3] Juan R. Maldonado and Allen H. Meitzler, "Strain-Biased Ferroelectric-Photoconductor Image Storage and Display Devices," Proc. IEEE 59 [3], 368 (1971).
- [4] A. H. Meitzler and A. H. O'Bryan, Jr., "Ferroelectric Behavior of PLZT Ceramics When Subjected to large Tensile Strains," *Appl. Phys. Lett.* 19 [4], 107 (1971).
- [5] W. Y. Gu, E. Furman, A. Bhalla and L. E. Cross, *Ferroelectrics* 89, 221 (1989).

- [6] K. K. Li, "A Study of PLZT Ferroelectric Thin Films Chemically Derived From Acetate Precursors," Ph.D. Thesis, Clemson University, Clemson, SC (1993).
  
- [7] H. Watanabe, T. Mihara and C. A. Paz De Araujo, "Device Effects of Various Zr/Ti Ratios of PZT Thin-Films Prepared by Sol-Gel Method," Proceeding of the 3<sup>rd</sup> International Symposium on Integrated Ferroelectrics 139-50 (1991).
  
- [8] F. Wang and G. H. Haertling, "Thin Film Ferroelectric Reflection Spatial Light Modulator with Fabry-Perot Etalon," Intelligent Processing of Ferroelectric Thin Films, Annual Report, submitted to The Office of Naval Research, (1994).
  
- [9] G. H. Haertling, "PLZT Thin Films Prepared From Acetate Precursors," *Ferroelectrics* 116, 51 (1991).
  
- [10] D. Dausch, "An Investigation of the Dielectric and Hysteresis Properties of PLZT Ferroelectric and Multilayer Composite Thin Films," Ph.D. Thesis, Clemson University, Clemson, SC (1995).
  
- [11] D. Dausch and G. H. Haertling, "Spin Coated Thin Films and Bulk Ceramics," Intelligent Processing of Ferroelectric Thin Films, Annual Report, presented to The Office of Naval Research, (1994).
  
- [12] F. Wang, K. K. Li, E. Furman and G. H. Haertling, "Discrete Electro-Optic Response in Lead Zirconate Thin Films from a Field-Induced Phase Transition," *Opt. Lett.* vol. 18, 1615-17 (1993).

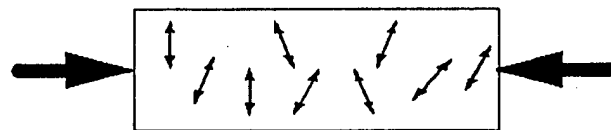
- [13] C. H. Hsueh and A. G. Evans, "Residual Stresses in Metal/Ceramic Bonded Strips," *J. Am. Ceram. Soc.* [3], 241-8 (1985).
- [14] S. Timoshenko, "Analysis of Bi-Metal Thermostats," *J. Optical Soc. Am.* [11], 233-56 (1925).
- [15] R. W. Hoffman, Physics of Nonmetallic Thin Films, ed. by C. H. S. Dupuy and A. Cachard, 273-353, Plenum Press, New York (1976).
- [16] H. Beige and G. Schmidt, "Electromechanical Resonances for Investigating Linear and Nonlinear Properties of Dielectrics," *Ferroelectrics* 41, 39-49 (1982).

Film in  
Compression



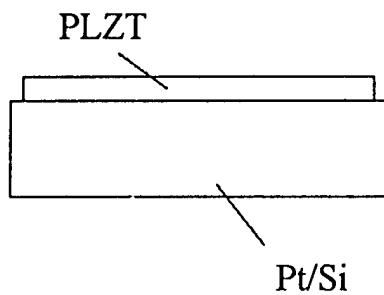
$$\alpha_S > \alpha_F$$

Domain Aligning

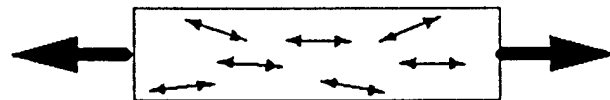


Parallel to Field

Film in  
Tension



$$\alpha_S < \alpha_F$$



Perpendicular to Field

**Figure 1.** Effects of compressive and tensile stresses on domain orientation.

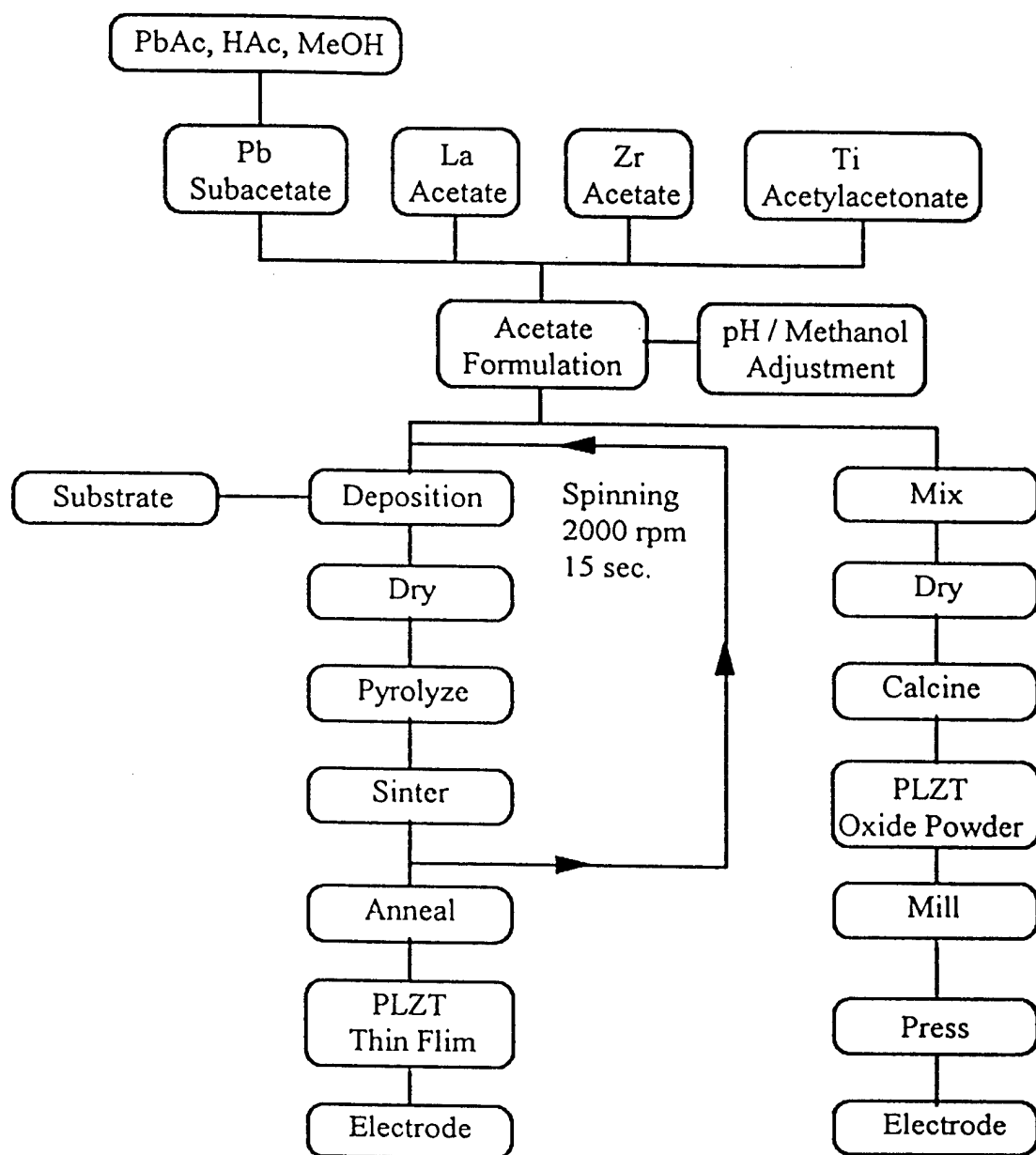


**Figure 2.** Acetate precursor coprecipitation process for producing PLZT thin film solutions and bulk powders.

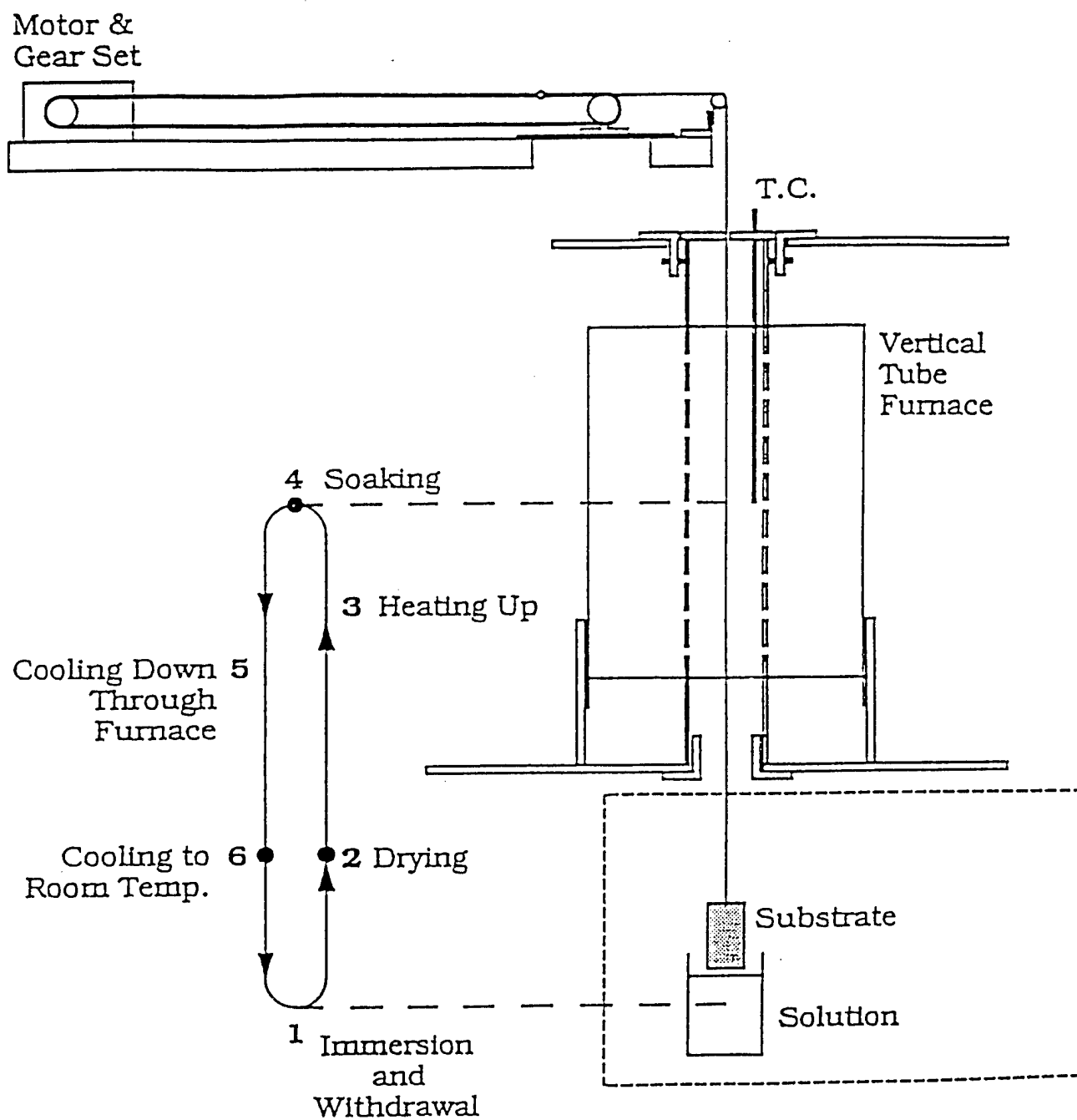


**Figure 3.** Automatic dip coating apparatus (designed by Kewen Li, Clemson University).

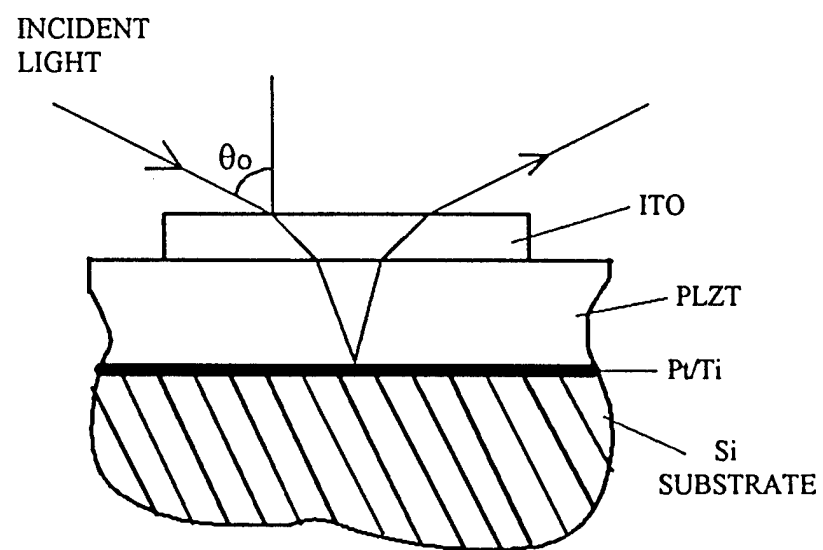
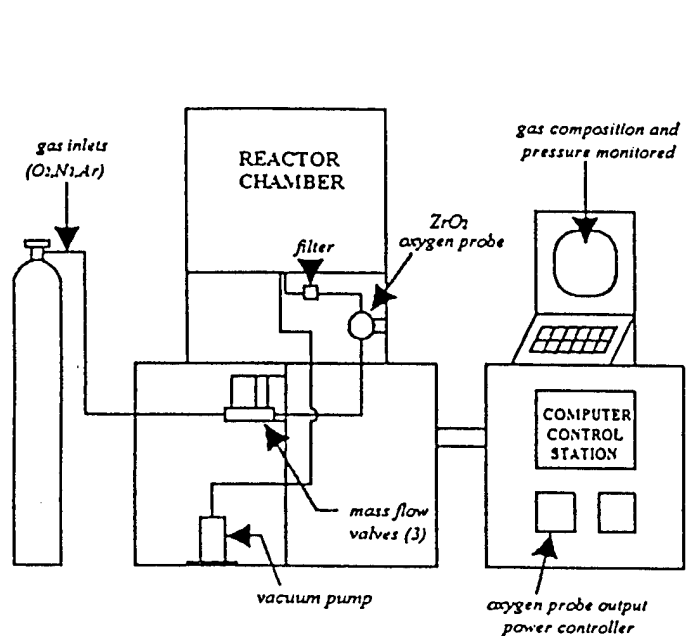
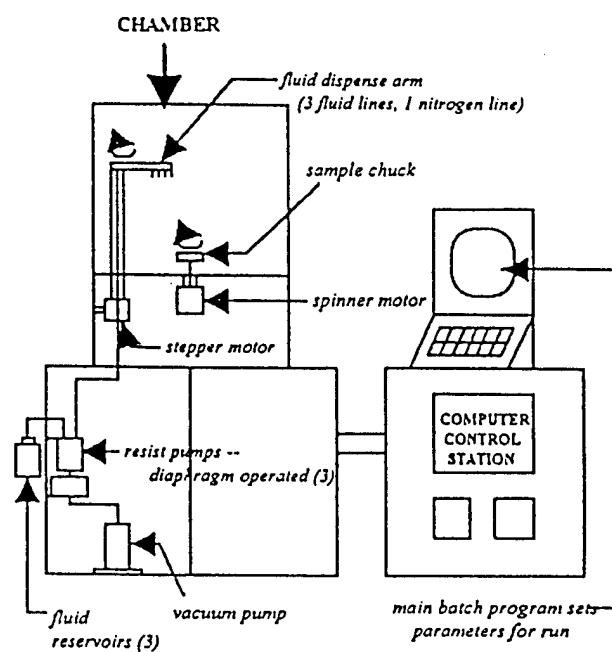


**Figure 4.** Electrode set-up used for reflective birefringence testing.

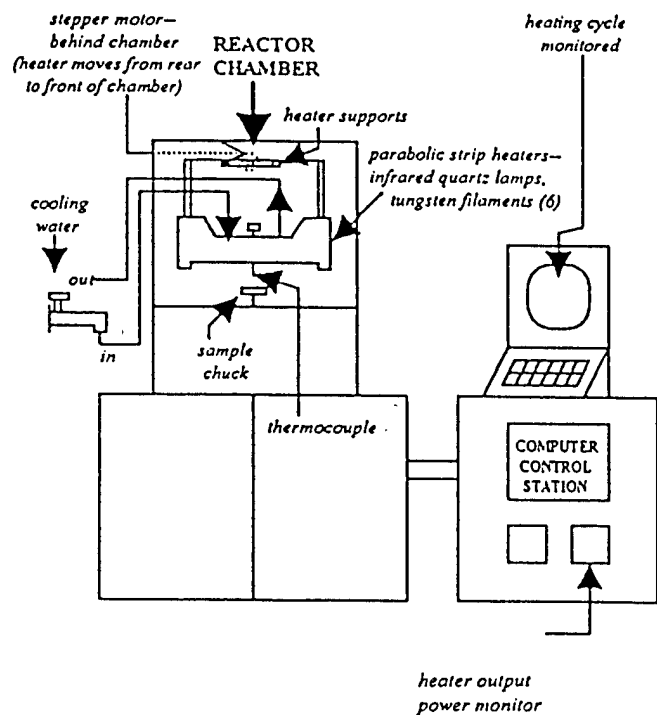




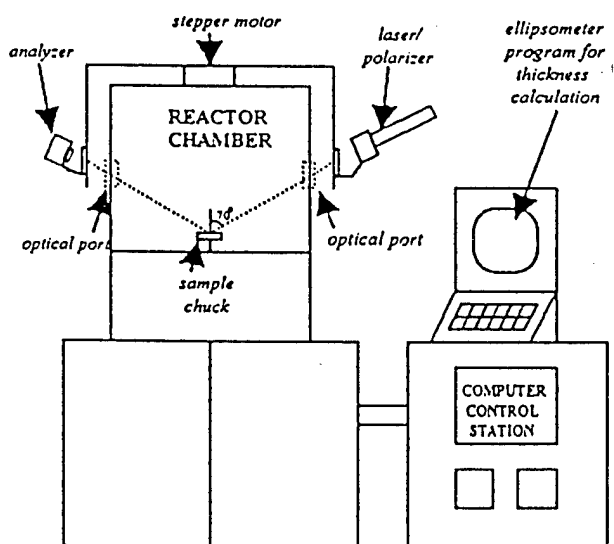
ATMOSPHERE CONTROL SYSTEM



FLUID DISPENSE SYSTEM



RAPID THERMAL PROCESSING UNIT



IN SITU LASER ELLIPSO METER

Figure 5. Automatic spin coat reactor/analyzer.

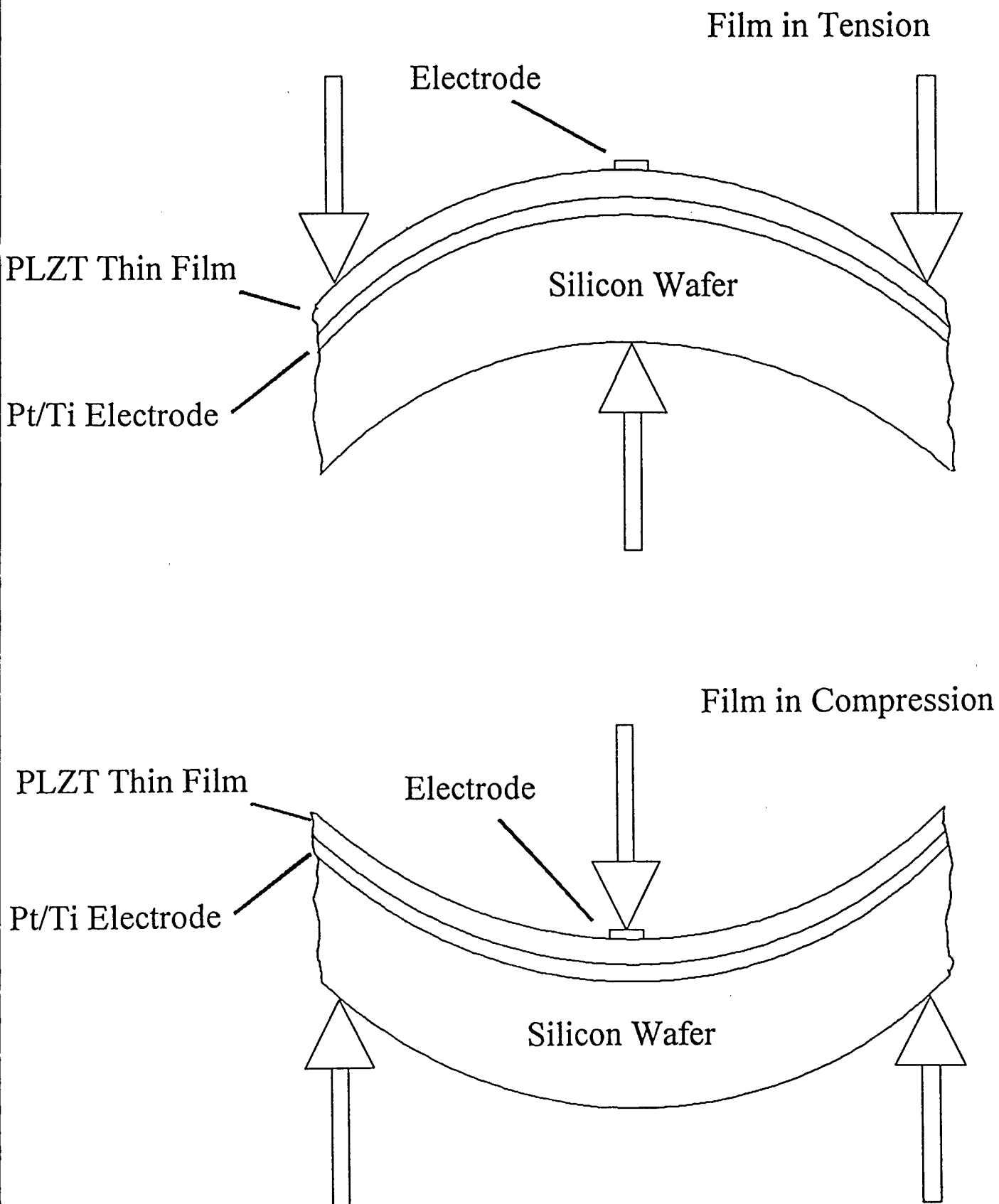


**Figure 6.** Stresses induced within the thin film from bending of substrate.

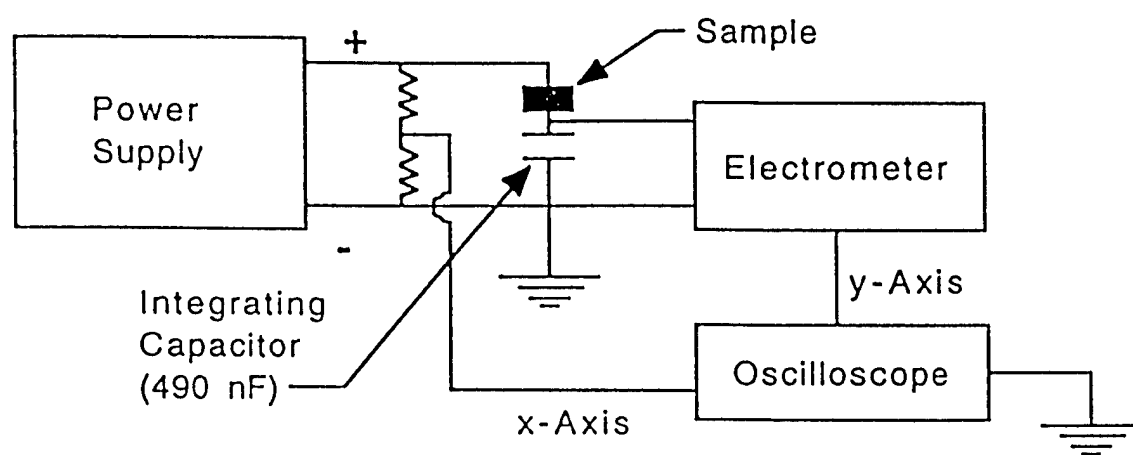


**Figure 7.** Sawyer-Tower circuit used in hysteresis loop set-up.

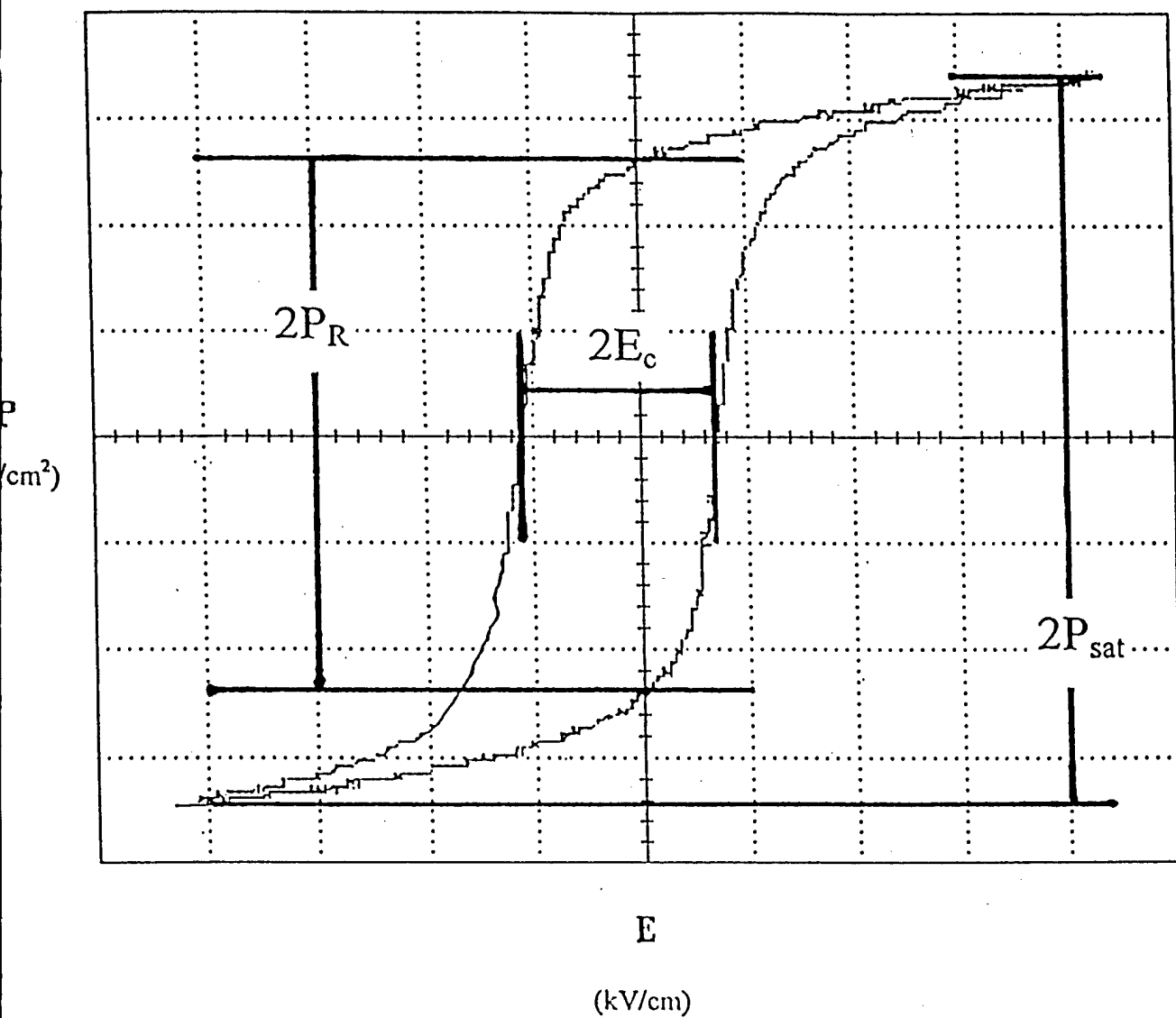
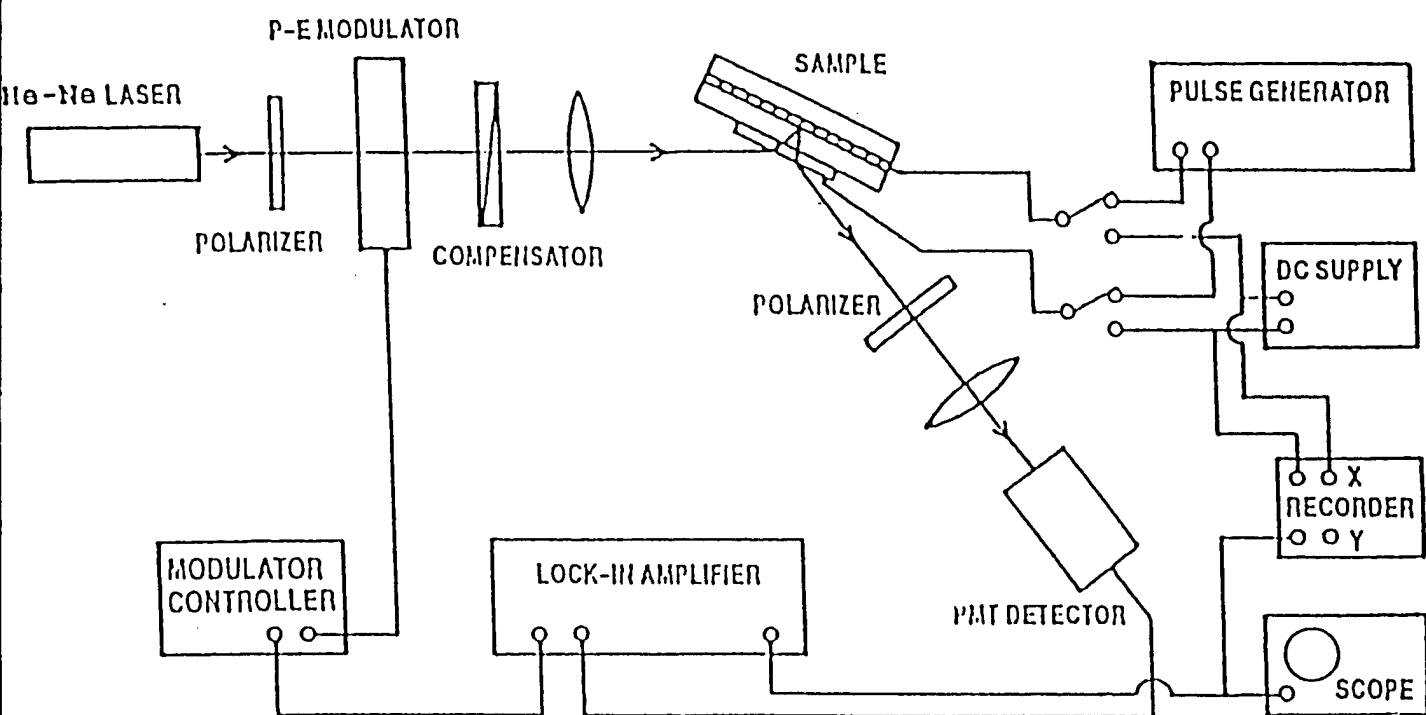
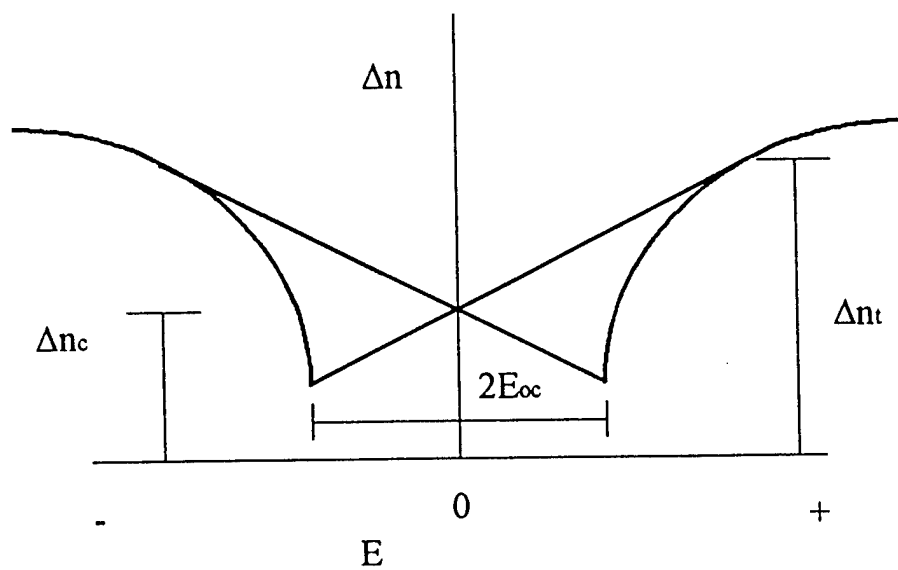


Figure 8. Measured values from hysteresis loops.



**Figure 9.** Instrumental set-up for Electrooptic measurements in the reflection mode.



**Figure 10.** Electrooptic behavior of a ferroelectric ceramic.

Fine pitch screws

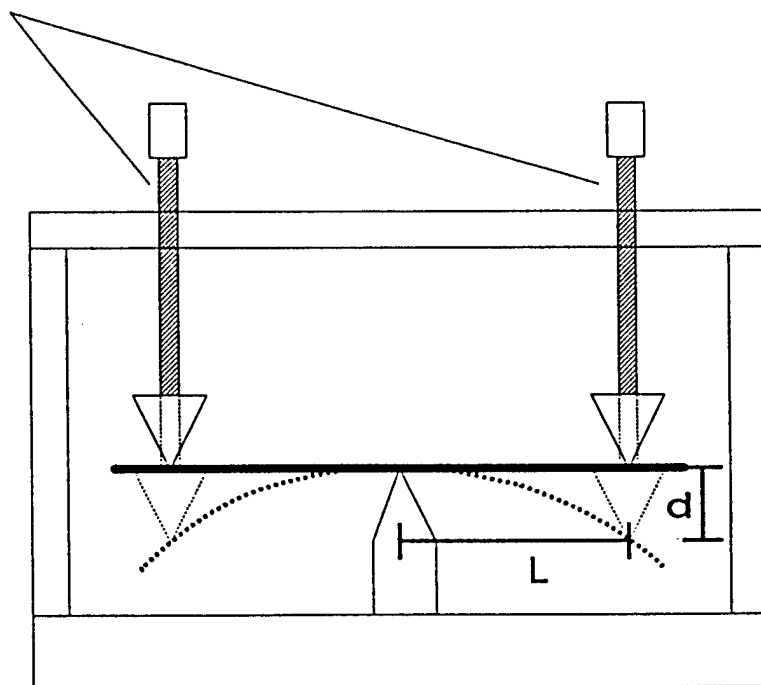


**Figure 11.** Diagram of the bending apparatus used in stressing thin films, and the measurements needed to calculate strain.

**Table 1.** Electrical properties of sintered, hot pressed and dip coated PLZT (9/65/35) thin films.

	$\tan \delta$ (pol)	K (pol)	$E_C$ [kV/cm]	$P_R$ [ $\mu\text{C}/\text{cm}^2$ ]	P10 [ $\mu\text{C}/\text{cm}^2$ ]	P20 [ $\mu\text{C}/\text{cm}^2$ ]
<b>Sintered</b>	.035	4205	1.77	3.27	26.2	29.6
<b>Hot pressed</b>	.033	4317	.958	1.45	20.57	27.13
<b>Thin film</b>	.151	3194	23	19.7	-----	-----

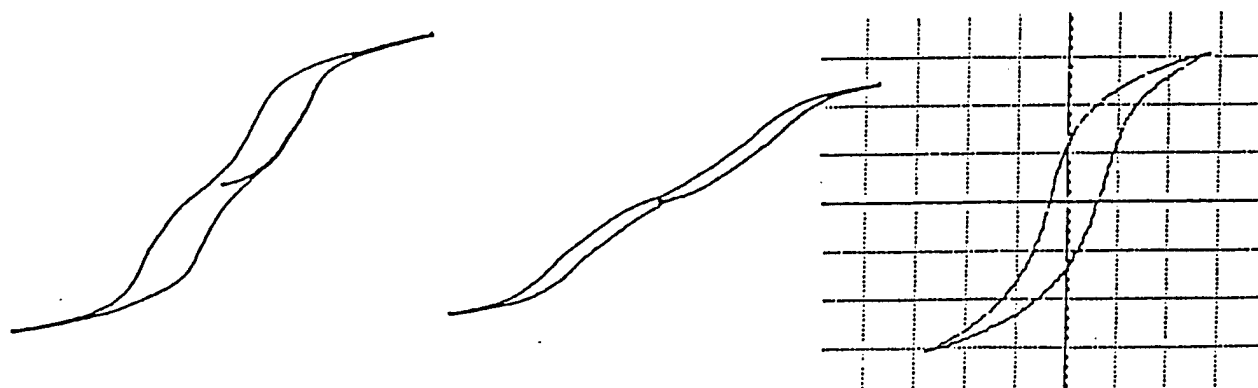


**Figure 12.** Hysteresis loops for sintered and hot pressed bulk materials and dip coated thin films (PLZT 9/65/35).

**Table 2.** Electrical properties of PLZT (9/65/35) thin films with various firing schedules.

	$P_R$ [ $\mu\text{C}/\text{cm}^2$ ]	$E_C$ [kV/cm]	$\tan \delta$ (pol)	K (pol)
555	----	----	.035	----
755	----	----	.034	----
575	14.1	38	.094	1174
775	15.4	24	.116	2014
557	9	19	.119	1833
757	14.1	21	.162	2414
577	11.8	23	.138	1901
777	19.7	23	.151	3194

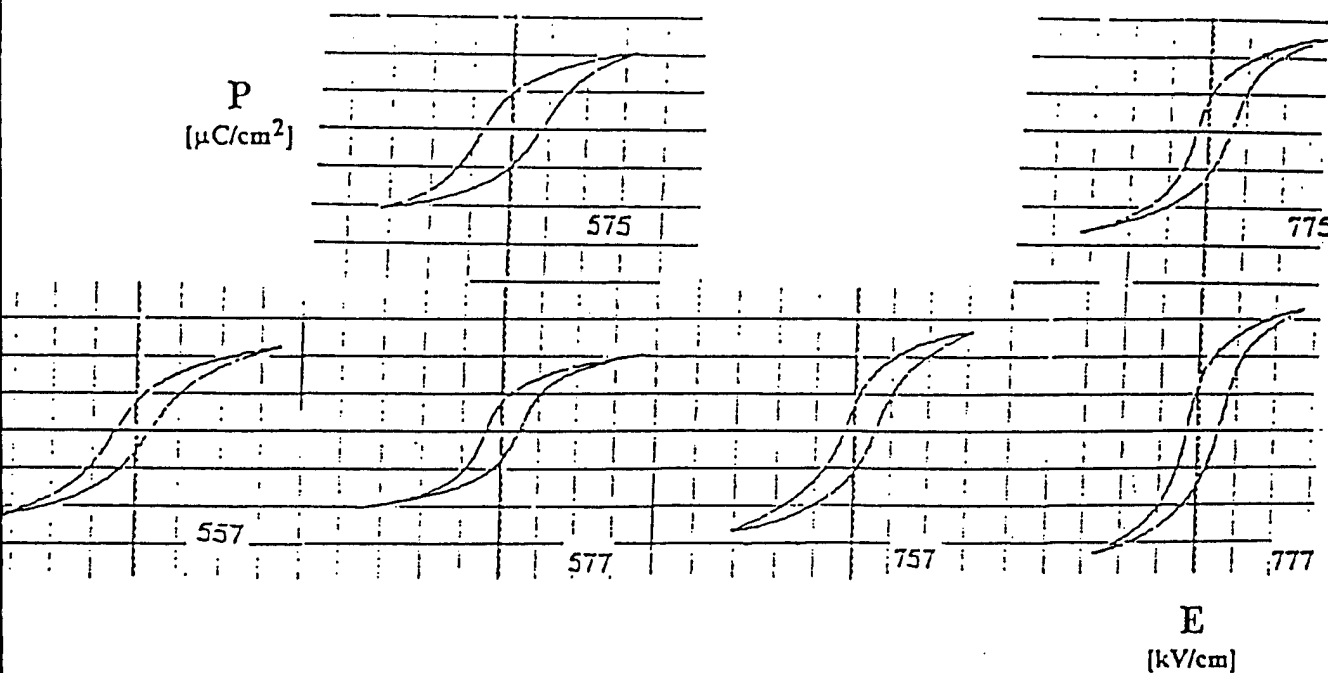


**Figure 13.** Ac hysteresis loops of PLZT 9/65/35 thin films with various firing schedules. Vertical scale =  $15 \mu\text{C}/\text{cm}^2$  per div. Horizontal scale =  $50 \text{kV}/\text{cm}$  per div.



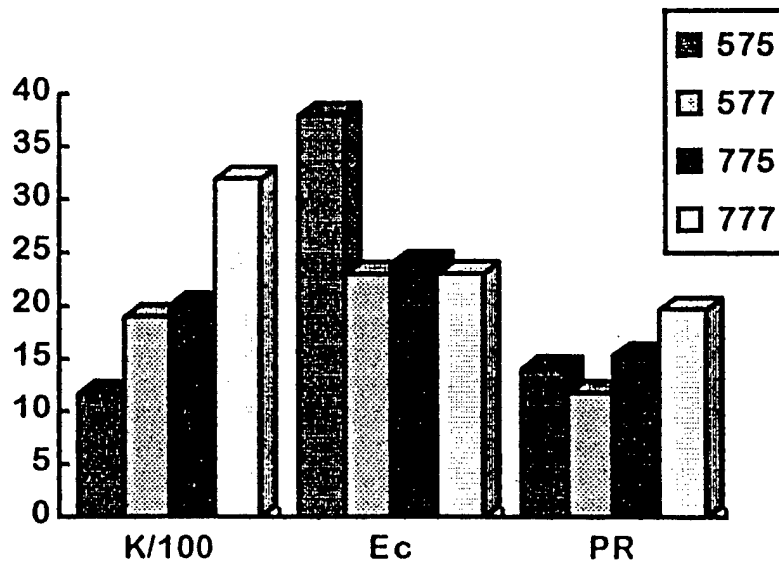


**Figure 14.** Thin film electrical measurements arranged according to increasing temperature within firing schedule.

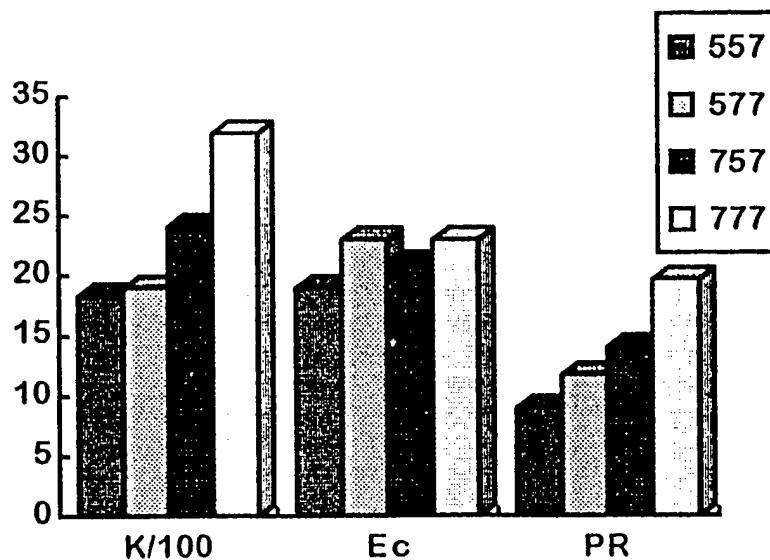


**Figure 15.** Thin film electrical measurements arranged according to increasing temperature within firing schedule.

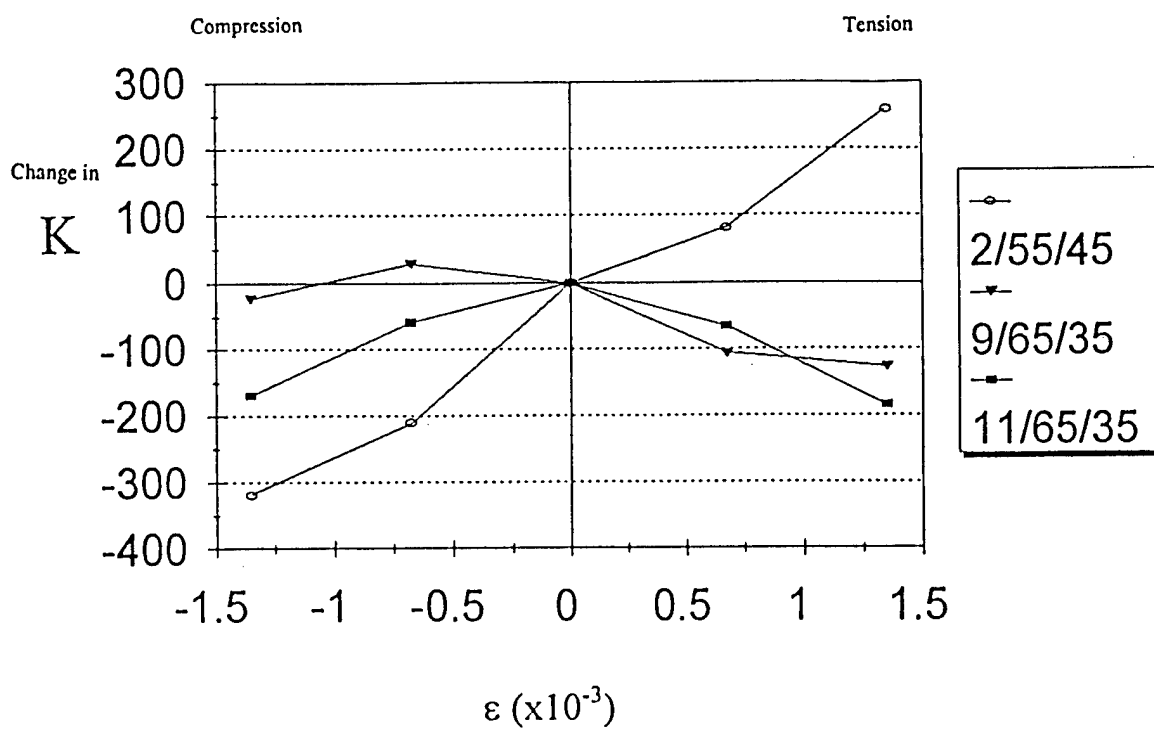


**Figure 16.** Change in dielectric constant for 2 $\mu$ m PLZT thin films on silver substrates.

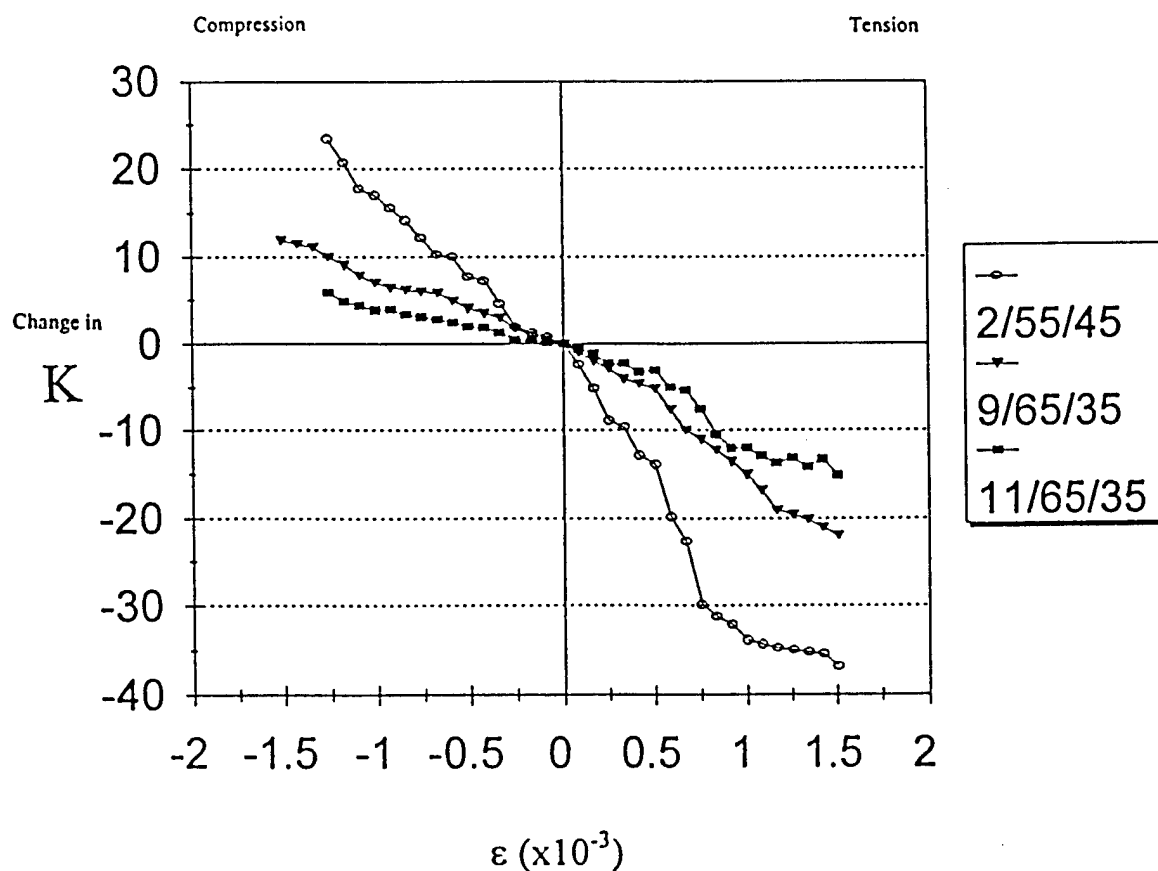


**Figure 17.** Change in dielectric constant for 2 $\mu$ m PLZT thin films on ultra thin Pt/Si substrates.

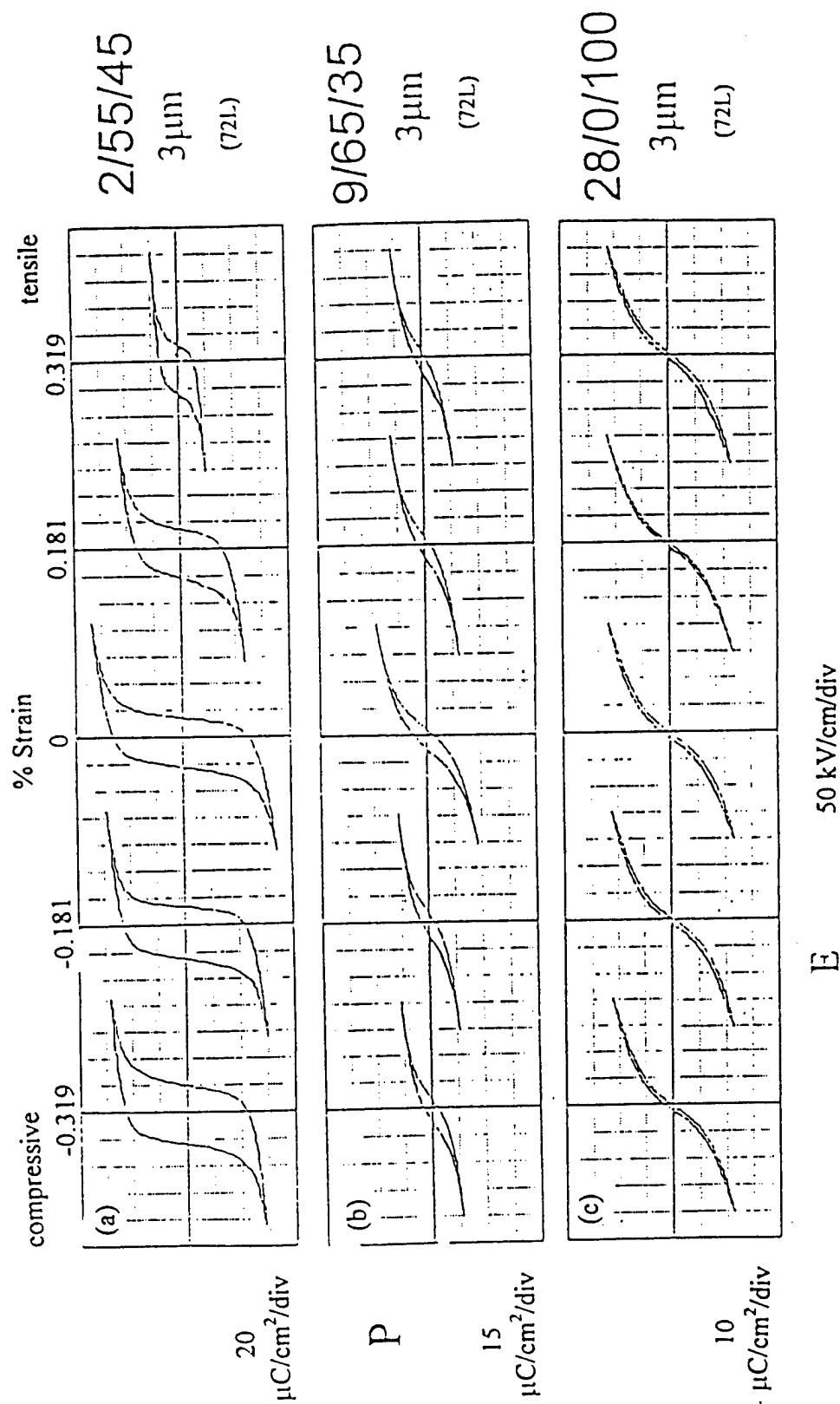


**Figure 18.** Hysteresis loops for 3 $\mu$ m thin films of different compositions on Ag foil measured at various stress levels.

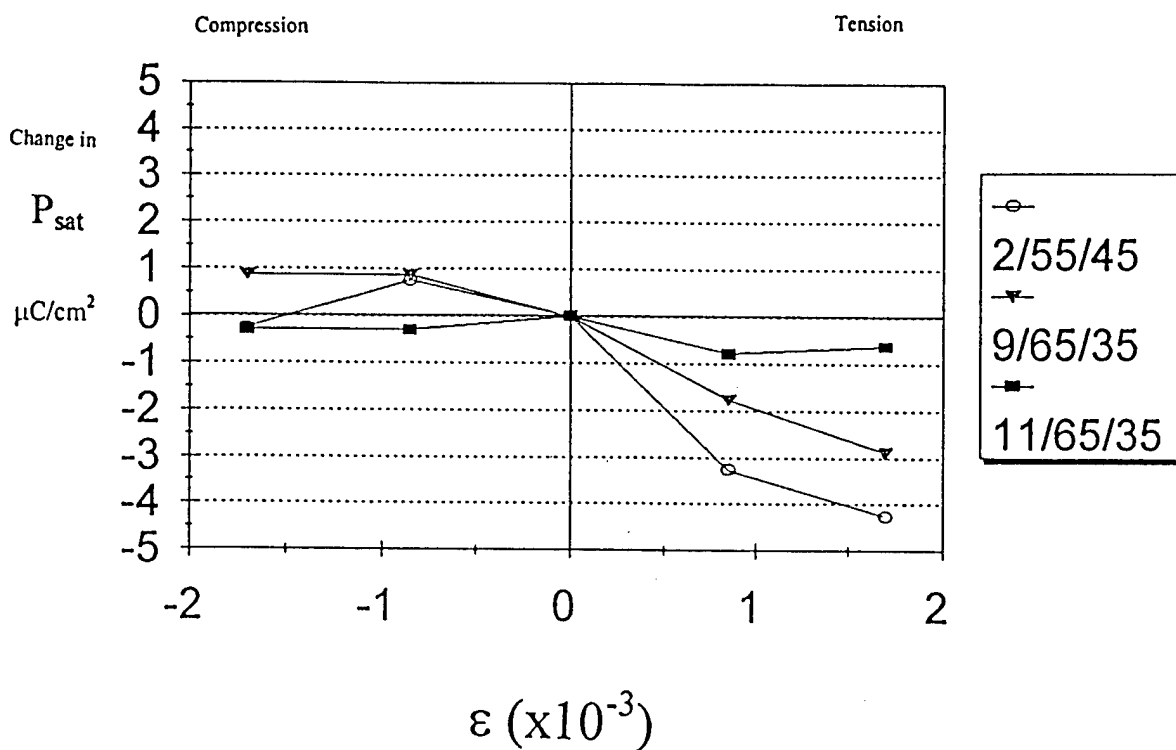


**Figure 19.** Change in saturated polarization for  $2\mu\text{m}$  PLZT thin films on silver substrates.

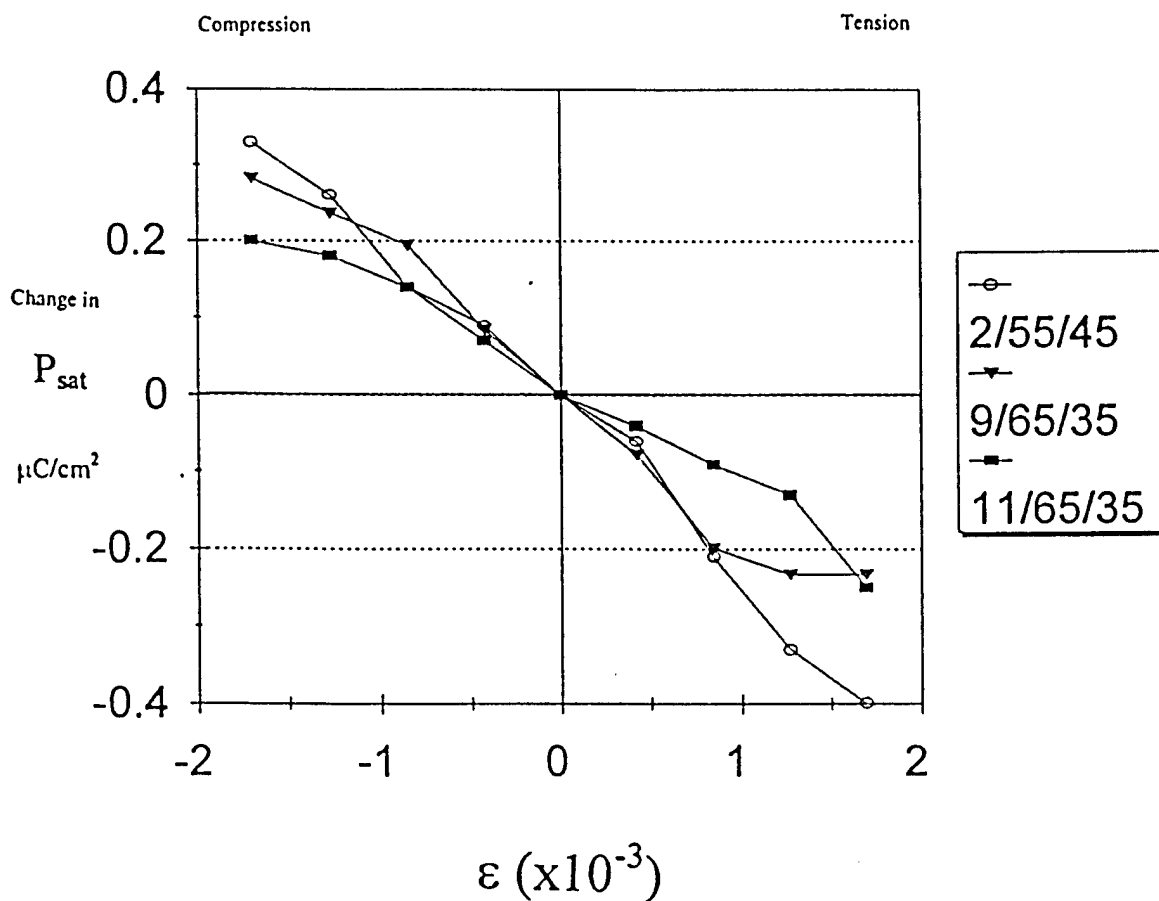


**Figure 20.** Change in saturated polarization for  $2\mu\text{m}$  PLZT thin films on ultra thin Pt/Si substrates.

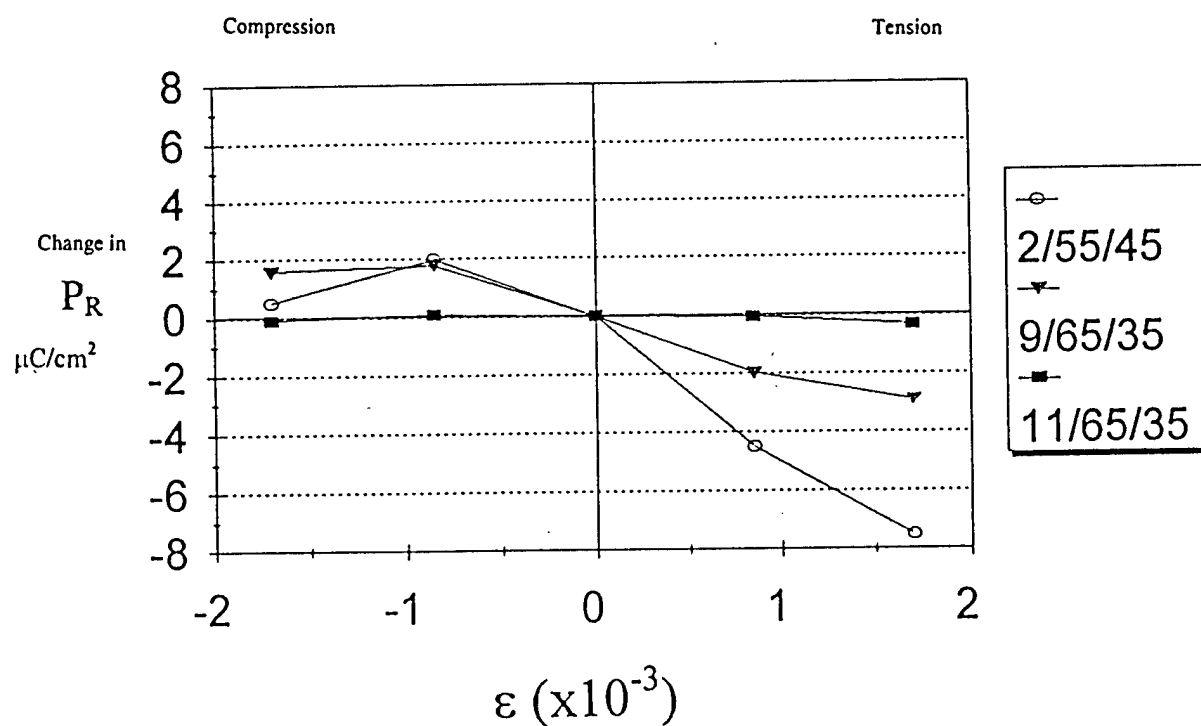


**Figure 21.** Change in remanent polarization for 2  $\mu\text{m}$  PLZT thin films on silver substrates.

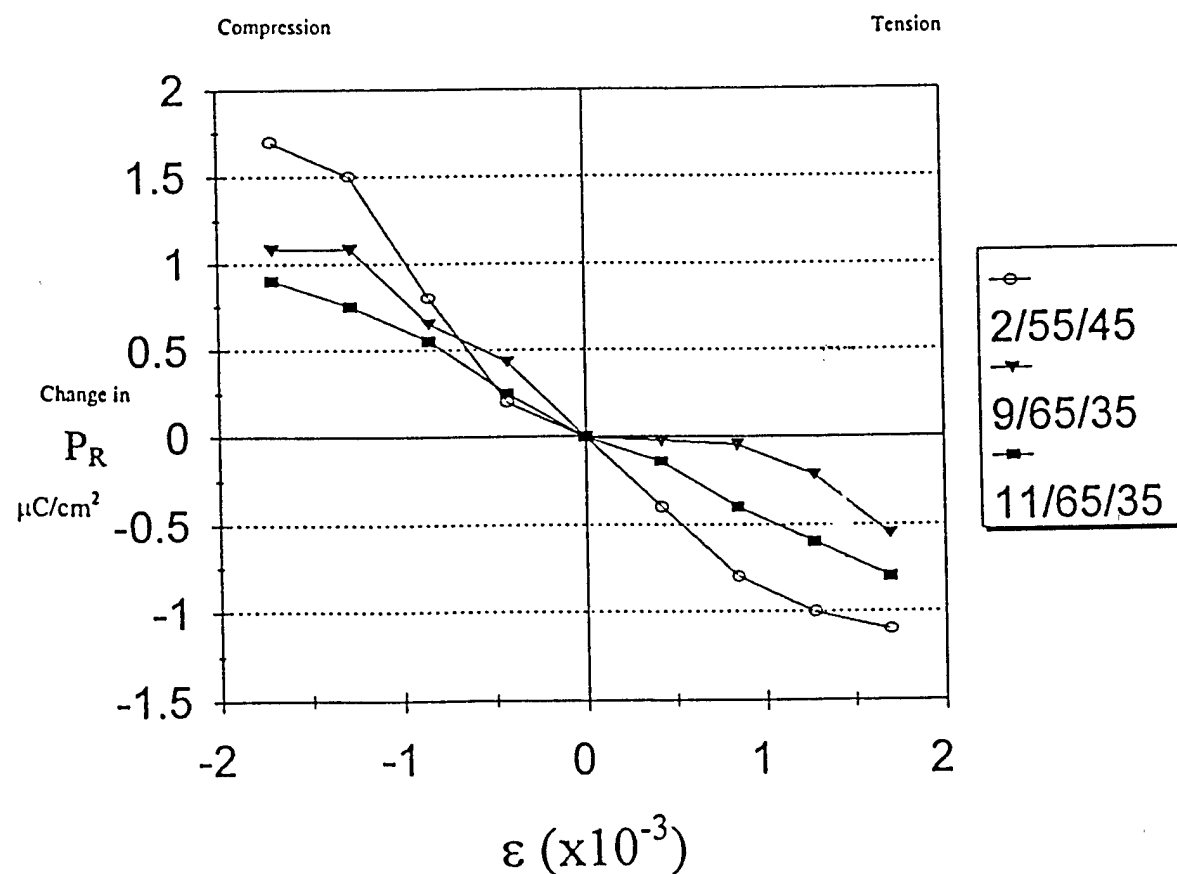


**Figure 22.** Change in remanent polarization for 2  $\mu\text{m}$  PLZT thin films on ultra thin Pt/Si substrates.

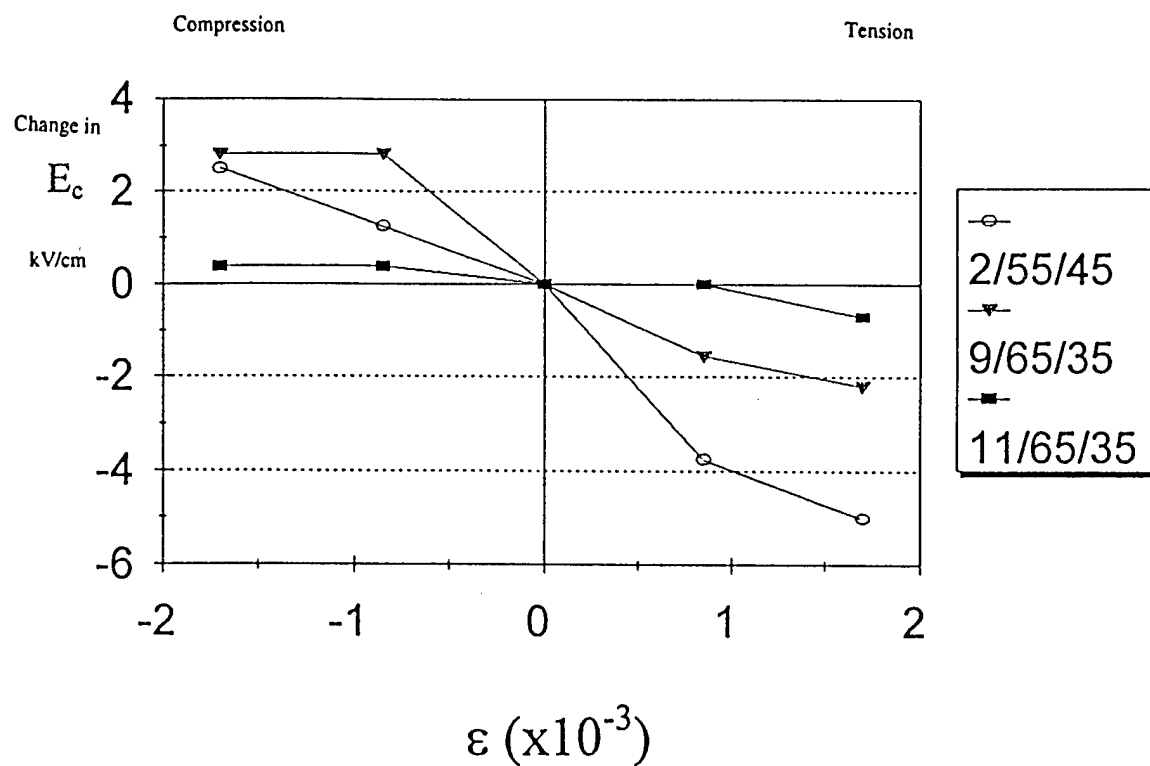


**Figure 23.** Change in coercive field for 2  $\mu$ m PLZT thin films on silver substrates.

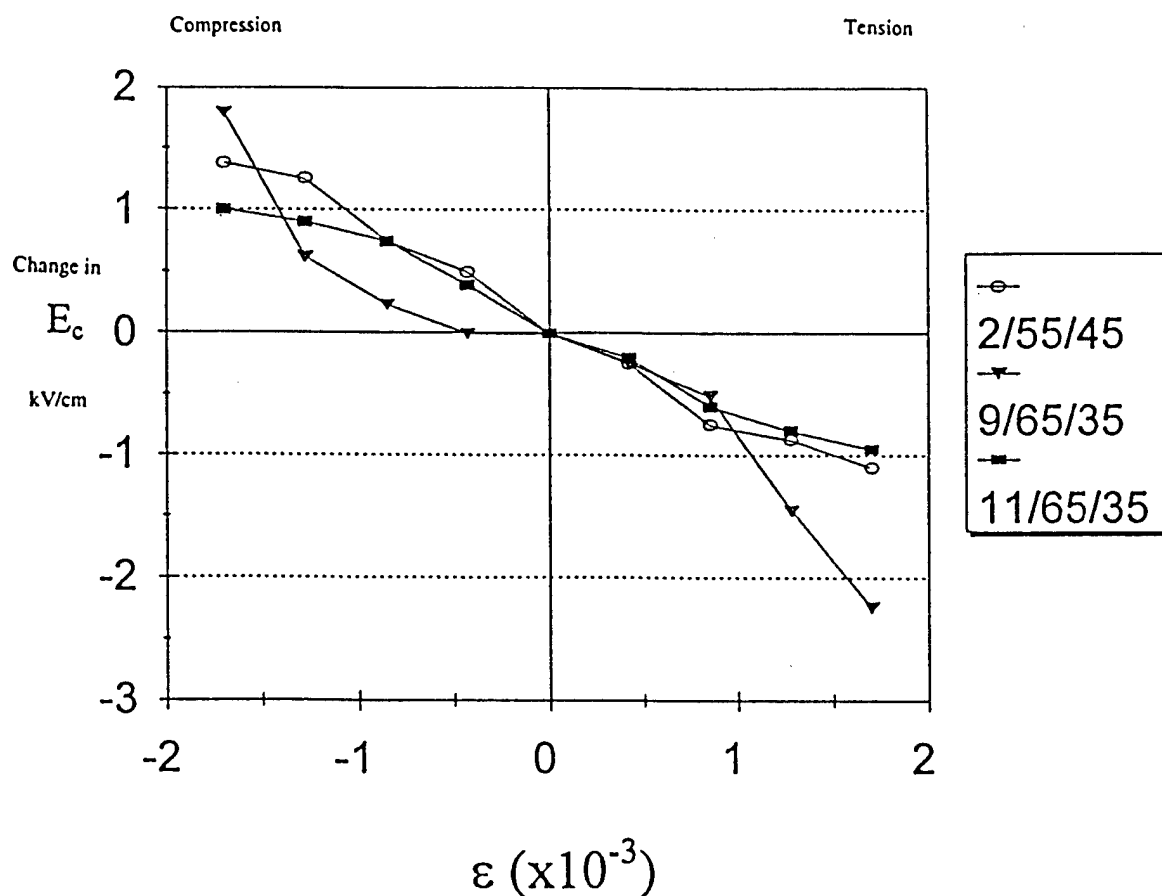


**Figure 24.** Change in coercive field for 2  $\mu$ m PLZT thin films on ultra thin Pt/Si substrates.

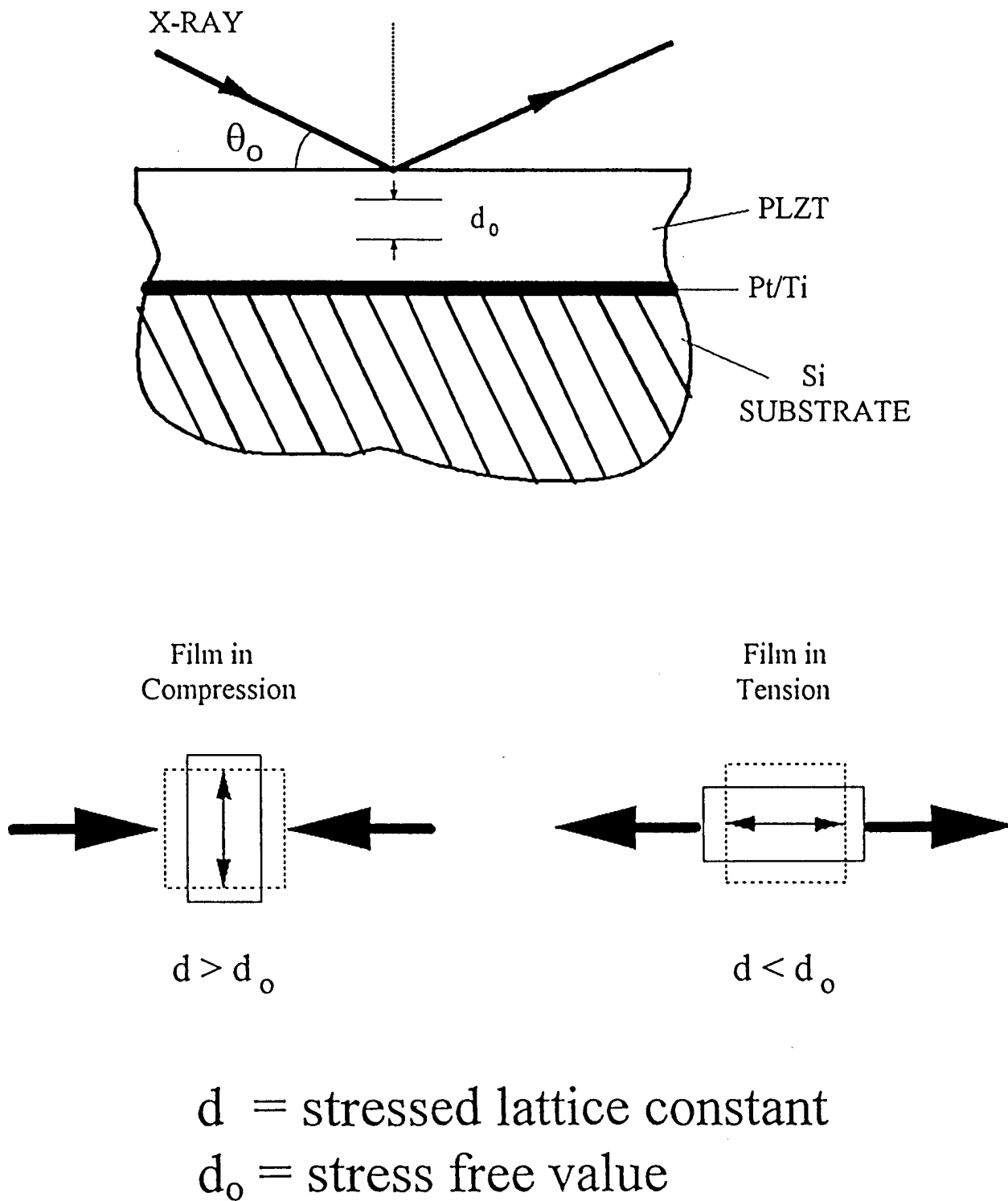
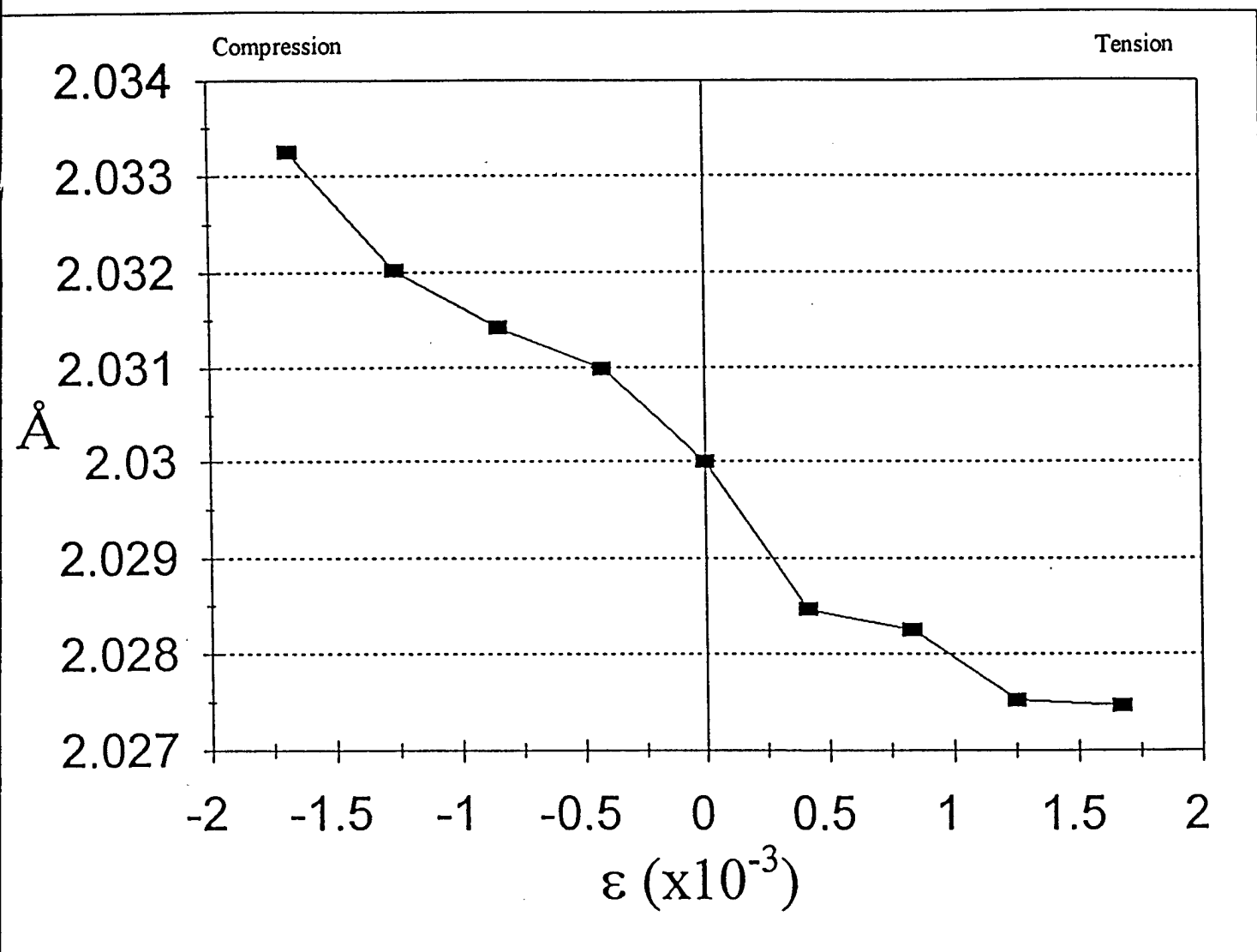
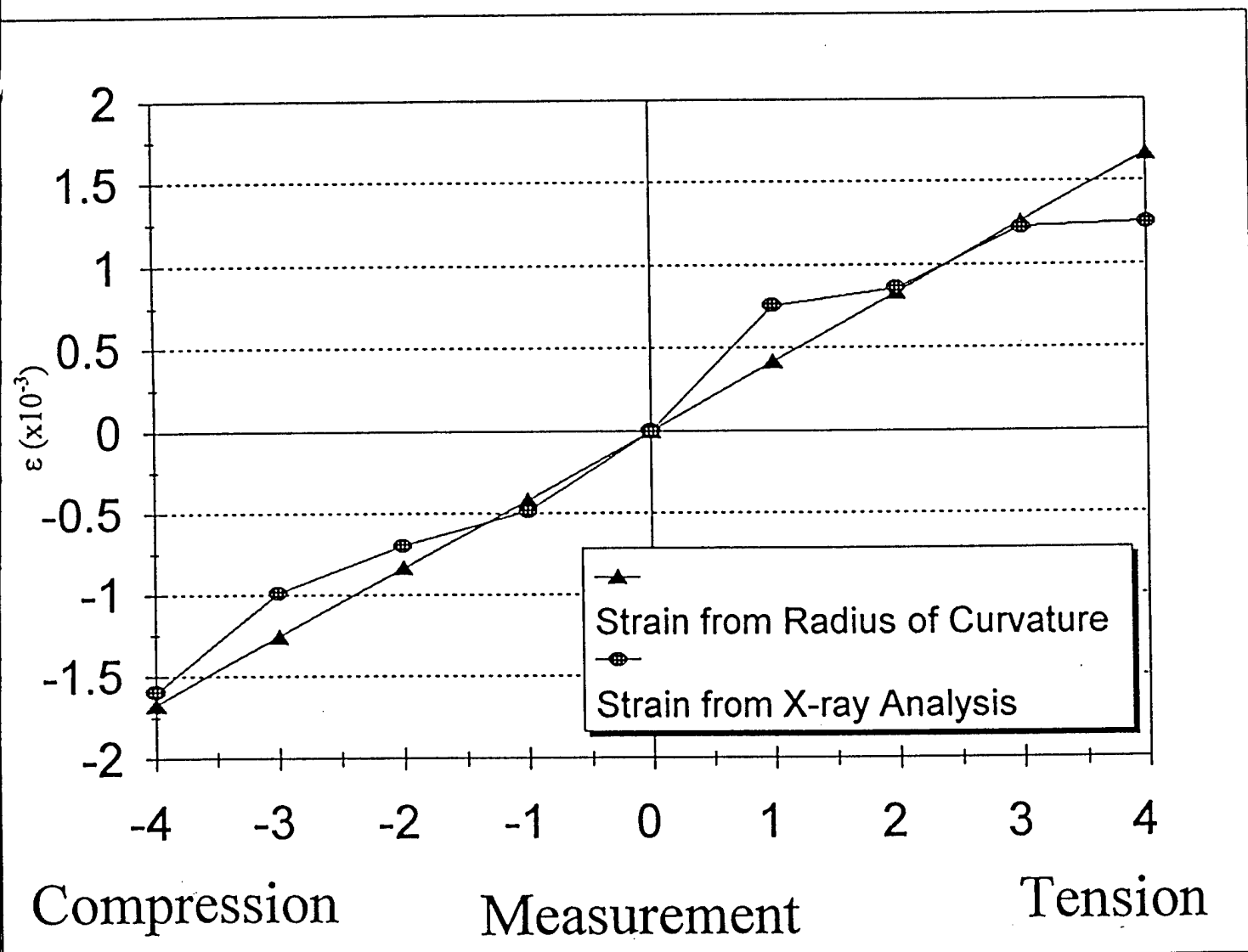


Figure 25. Determining stresses within thin films by use of X-ray analysis of d-spacings.



**Figure 26.** Change in d-spacing versus induced stress for (200) peak of 2 $\mu$ m PLZT 2/55/45 thin film on ultra thin Pt/Si.





**Figure 27.** Comparison of strains obtained from radius of curvature measurements and X-ray analysis.

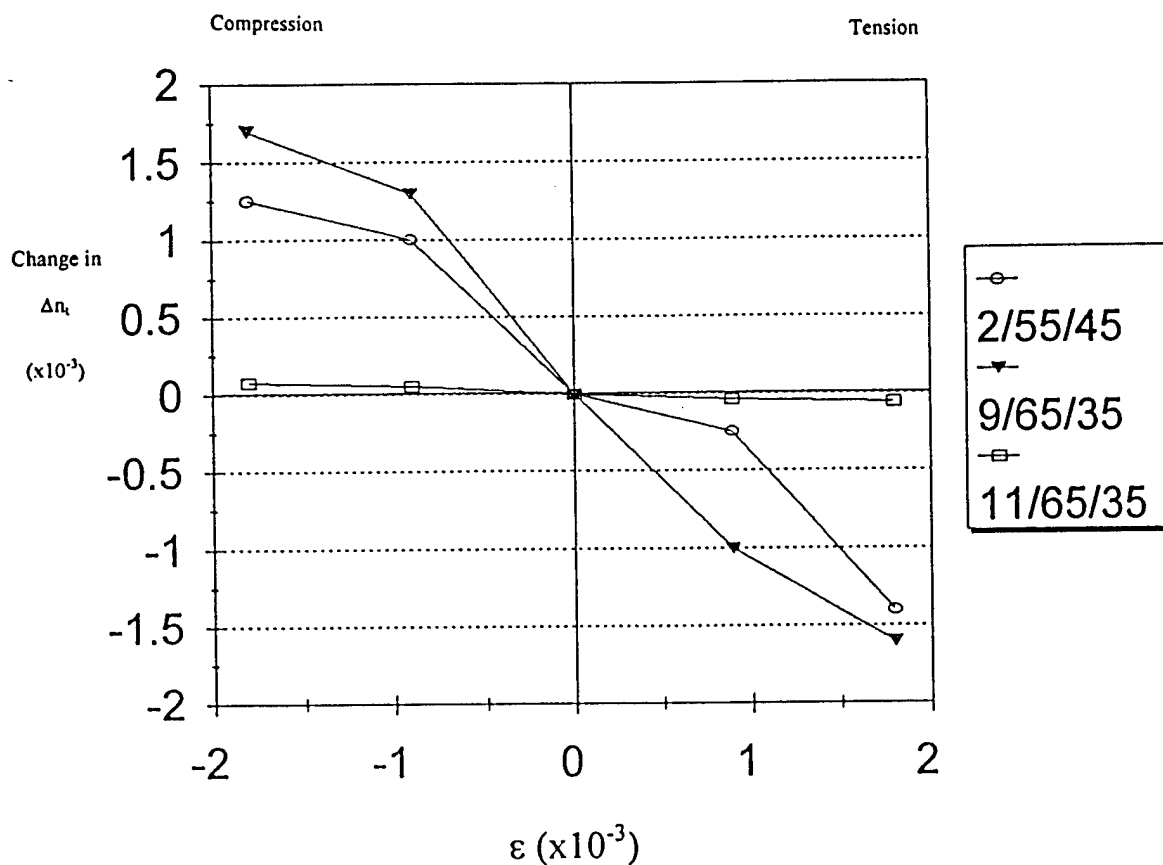


**Figure 28.** Change in total birefringence for 2 $\mu$ m PLZT thin films on ultra thin Pt/Si substrates.

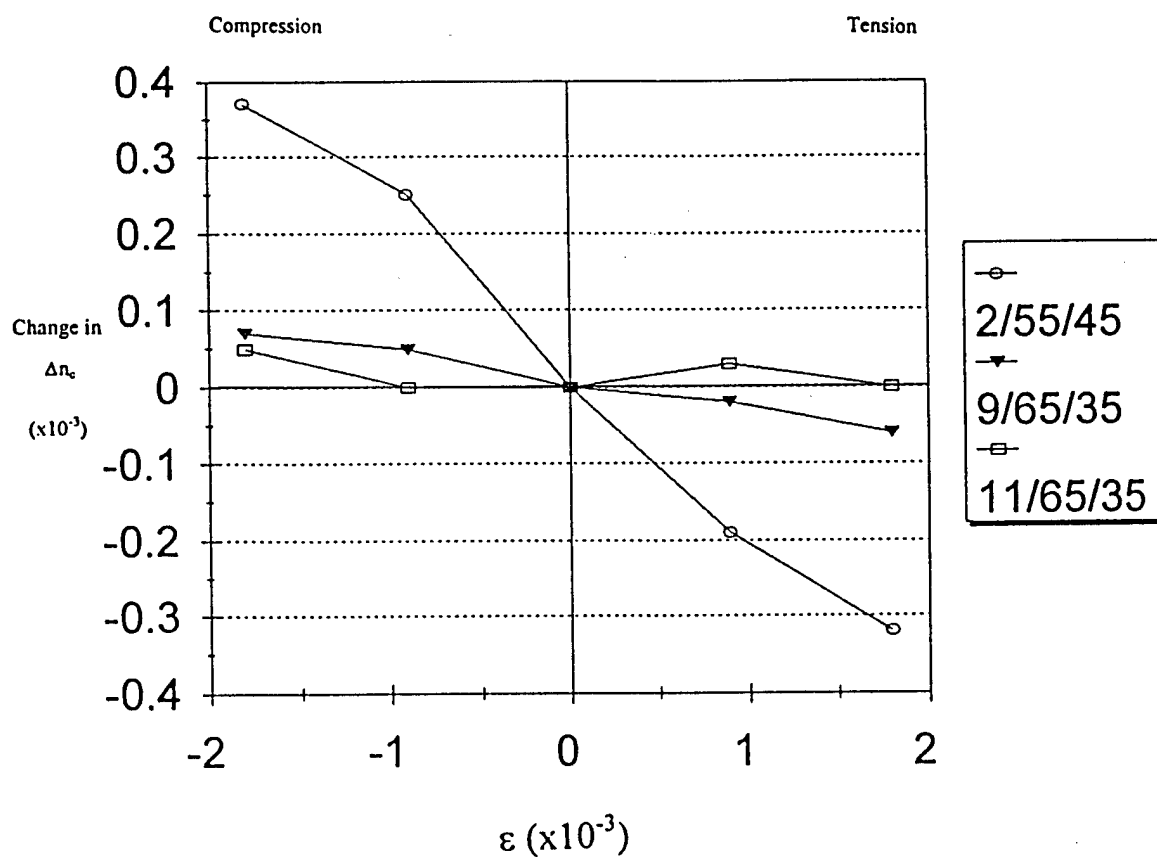


**Figure 29.** Change in crossover birefringence for 2 $\mu$ m PLZT thin films on ultra thin Pt/Si substrates.

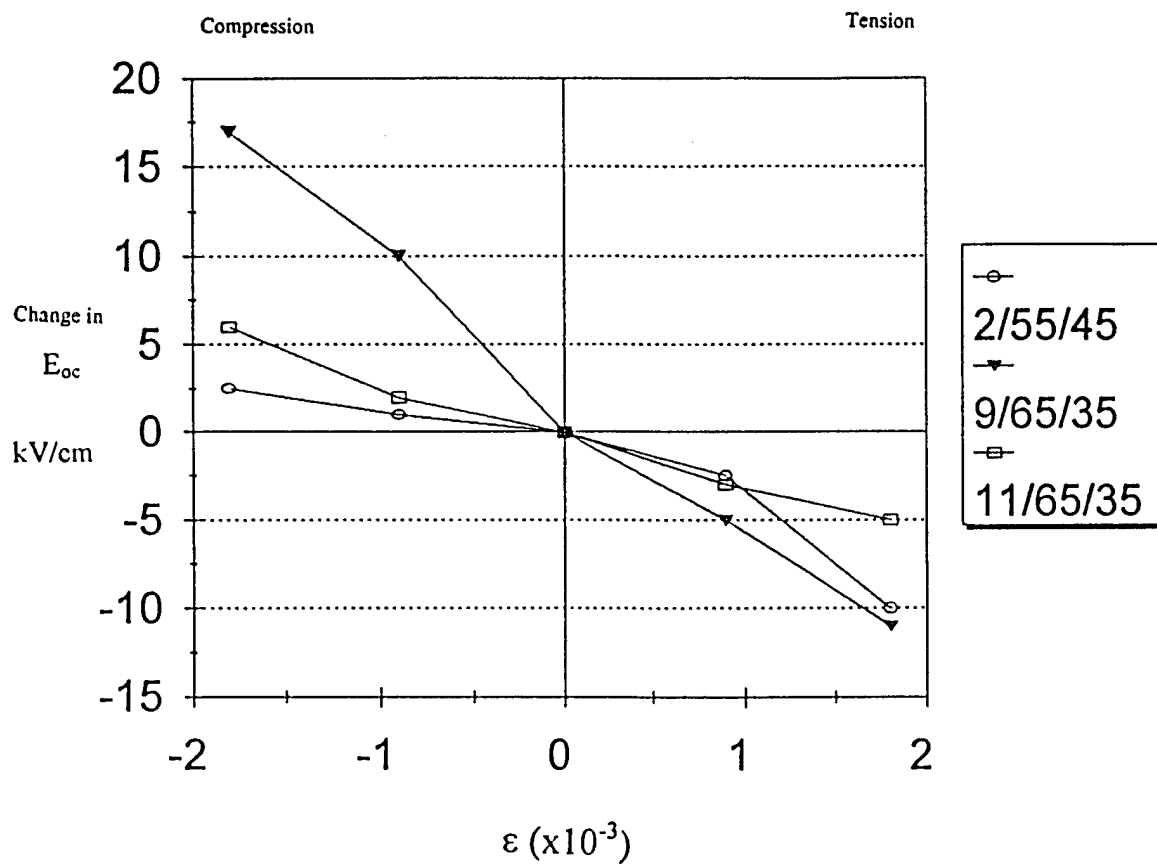


**Figure 30.** Change in optical coercive field for 2 $\mu$ m PLZT thin films on ultra thin Pt/Si substrates.

## **Part IX.**

### **Effects of Rapid Photothermal Annealing of PLZT**

# EFFECTS OF RAPID PHOTOTHERMAL ANNEALING ON THE PROPERTIES OF PLZT 2/55/45 THIN FILMS PRODUCED BY RF MAGNETRON SPUTTERING

G. Li<sup>1</sup>, Y. Chen<sup>2</sup>, R. Singh<sup>2</sup> and G. H. Haertling<sup>1</sup>

<sup>1</sup>Department of Ceramic Engineering

<sup>2</sup>Department of Electrical and Computer Engineering

Clemson University

Clemson, SC 29634

## ABSTRACT

Effects of rapid photothermal annealing on the properties of PLZT 2/55/45 thin films deposited on platinum-coated Si wafers by RF magnetron sputtering were investigated. The crystalline phase and microstructure of the thin film samples prepared under various processing conditions were examined and analyzed using XRD and AFM techniques. The ferroelectric, dielectric, fatigue and current-voltage characteristics of these films were determined and compared with those of the films obtained through conventional furnace annealing and rapid thermal annealing without UV illumination. Improvements of various degrees were observed in the properties of the samples processed via the rapid photothermal annealing. The role of UV irradiation in the thin film annealing process is discussed.

## INTRODUCTION

Over the past ten years ferroelectric thin film materials have been extensively investigated for DRAM and nonvolatile memory devices along with a number of other applications ranging from energy storage capacitors, infrared and optical sensors, to ultrasonic transducers and optical modulators.<sup>1-9</sup> Although marked advances have been made in these areas, there exist some problems that need to be resolved. For example, the presence of defects and imperfections has been related to the fatigue rate, leakage current density and imprint behavior of the ferroelectric thin films used in memory devices. For many applications, a highly uniform structure with minimal defects is not only desirable but critical.

Rapid thermal annealing coupled with UV illumination has recently emerged as a promising means to improve structural homogeneity and enhance electrical

performance of semiconductor and dielectric thin films derived by a number of deposition techniques.<sup>10-11</sup> This new annealing technique, also known as rapid photothermal annealing, involves irradiation of a thin film sample with high-energy ultraviolet photons while the sample is being processed by a conventional rapid thermal annealing scheme. It is generally believed that the UV illumination can help in reducing the activation energy of individual ions so that they have more chance to reach the lowest energy positions. As a result, the structural homogeneity and hence the overall performance of the thin film are improved.

In this paper, PLZT 2/55/45 thin films produced by RF magnetron sputtering were used to study the effects of the rapid photothermal annealing on the properties of ferroelectric thin film materials. The crystalline phase and microstructure were examined using X-ray diffraction (XRD) and atomic force microscopy (AFM) techniques. Properties of the thin films including the dielectric constant and loss, ferroelectric hysteresis loop, fatigue and leakage current density were determined and compared with those of the films prepared using conventional furnace annealing and rapid thermal annealing.

## EXPERIMENTAL

The PLZT thin films were prepared from powder targets using a RF-magnetron sputtering system manufactured by Kurt J. Lesker Inc. The substrates used were commercial platinum-coated silicon wafers. Traditional mixed-oxide processing methods were employed to obtain the PLZT target powders. Starting materials were reagents of PbO, La<sub>2</sub>O<sub>3</sub>, ZrO<sub>2</sub> and TiO<sub>2</sub>, which were wet mixed according to 2/55/45 (La/Zr/Ti) ratios plus 3 atm% excess PbO, dried overnight, calcined at 925°C for 2 hours followed by ball milling in a polyethylene bottle with trichloroethylene for six hours. The powders obtained were supplemented with 20 wt% PbO, well mixed, and then pressed into shallow, 4 inch diameter copper target dishes. Table I gives the typical deposition conditions employed in the PLZT sputtering.

Table I. Deposition parameters for PLZT thin film sputtering

Pre-sputtering	5 minutes
Base Pressure	<5×10 <sup>-6</sup> Torr
RF Power	50 Watts
Total Pressure	60 mTorr
Ar/O <sub>2</sub> Ratio	1:1
Substrate Temperature	310 °C
Deposition Rate	115 nm/hr

The thin film samples were post annealed using conventional furnace annealing (FA) and rapid thermal annealing (RTA) approaches in addition to the rapid photothermal annealing (RPTA). The RTA was performed in a cylindrical assembly equipped with six tungsten halogen lamps of 2 kW each that provided optical and thermal energy for the annealing process. The RPTA process used the same assembly as the RTA except that the PLZT layer was illuminated with additional UV energy provided by a 150 W deuterium lamp (Hamamastu, model L1385 ) with peak intensities at 125 and 160 nm. Unless otherwise stated, the processing conditions for both RPTA and RTA were 650°C for 5 min with a rise time of 1 minute. For the furnace annealing, a sample resting on a zirconia plate was placed into a preheated furnace at 690°C and heat treated for 40 min. The sample together with the zirconia plate was then removed from the furnace and allowed to cool down in air. After annealing, the samples were deposited with copper top electrode dots of 0.785 and 0.219 mm<sup>2</sup> using a vacuum evaporator. The thickness of the films was measured on a profile analyzer, which was typically 0.23  $\mu$ m.

The X-ray diffraction (XRD) analyses of the crystalline phase, orientation and crystallinity of the films were performed using a Scintag XDS 2000<sup>TM</sup> diffractometer. A Topomatrix Discoverer (V3.06) atomic force microscope (AFM) with an image resolution of 200 $\times$ 200 pixels was employed to examine the surface morphology. The scan rate and sample bias for the AFM were 10,000 nm/sec and 1 mV, respectively. Dielectric properties of the thin films were measured on a precision LCR meter (HP 4284A) at a frequency of 1 kHz. The values of the leakage current density were determined using a picoamper meter (HP4140B) controlled by a HP 9000 computer. Ferroelectric hysteresis loops and related parameters such as the coercive field and remanent polarization were obtained from a RT-66A tester produced by Radiant Technologies. Fatigue characteristics were determined using a Sawyer-Tower circuit with a sinusoidal applied voltage (10V<sub>p-p</sub>) cycling at a maximum frequency of 40 kHz.

## RESULTS AND DISCUSSION

Figure 1 shows the X-ray diffraction patterns of the samples prepared by RPTA under different temperatures from 500°C to 650°C. A major portion of the perovskite phase was found to have been formed at a temperature as low as 550°C. It is clear from the figure that the phase evolution from the pyrochlore to perovskite took place mostly between 500°C and 550°C. Full development of the perovskite structure occurred at a temperature somewhere between 550°C and 600°C. As showed in Figure 2, no appreciable difference in the X-ray diffraction

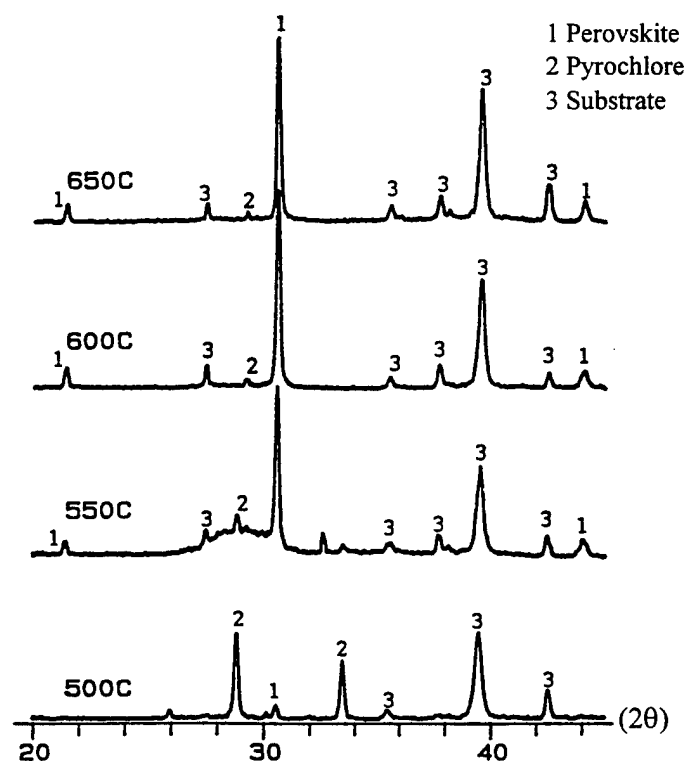


Figure 1. X-ray diffraction patterns of samples prepared with RPTA under different annealing temperatures.

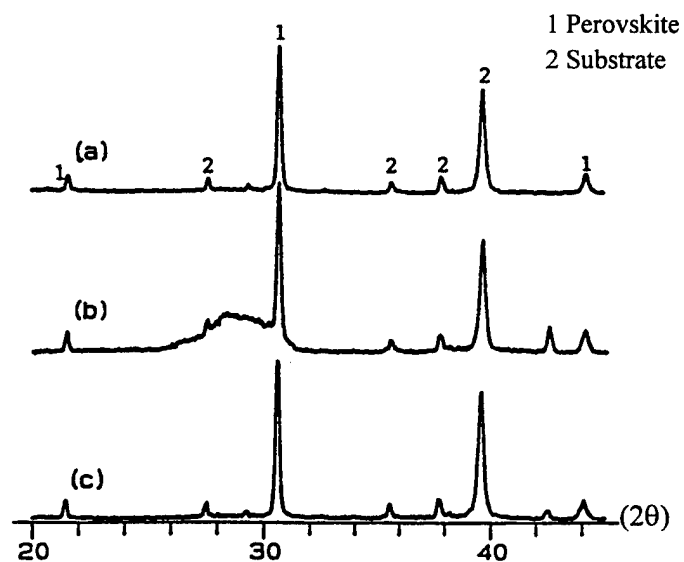


Figure 2. X-ray diffraction spectra of samples prepared with (a) RPTA, (b) RTA and (c) FA.



spectra was observed among the samples with RPTA, RTA and FA processes. These spectra correspond to a crystalline structure of randomly oriented domains.

The AFM micrographs in Figure 3 display the surface features of the thin film samples obtained from the three annealing approaches. The displayed regions were so chosen that some microcracks were visible. As can be seen, the surface roughness was in a similar range of variation for these pictures, but the sample made by RPTA appears to have less and finer microcracks in comparison with the other two cases.

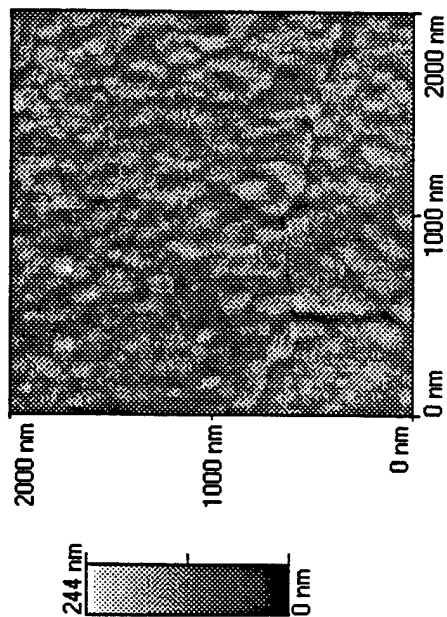
A series of thin film samples deposited under virtually the same conditions were measured for their dielectric properties and ferroelectric loop parameters. Table II gives the typical values of these properties for the samples processed using RPTA, RTA and FA. The dielectric loss was approximately 20% lower with RPTA than with RTA, and was generally also lower compared to the furnace annealing. However, the dielectric constant with the RPTA process was also lower relative to those of the other two processes. The values for the remanent polarizations  $+P_R$  and  $-P_R$  were very similar among these annealing methods, which was around  $31 \mu\text{C}/\text{cm}^2$  for this particular PLZT composition. It was found that the hysteresis loops of the samples prepared by RPTA were usually more symmetric with respect to the electric field axis, as manifested by the closeness of the  $+E_C$  and  $-E_C$  values for the RPTA against FA and RTA processes indicated in Table II. The distortion of the hysteresis loop was probably associated with mechanisms similar to those proposed by Pike *et al* who suggested that an asymmetric distribution of immobile defect-related charge was responsible for the voltage shift in the hysteresis loop of ferroelectric thin films.<sup>12</sup>

Table II. Dielectric and ferroelectric properties of PLZT 2/55/45 thin films prepared by different annealing approaches

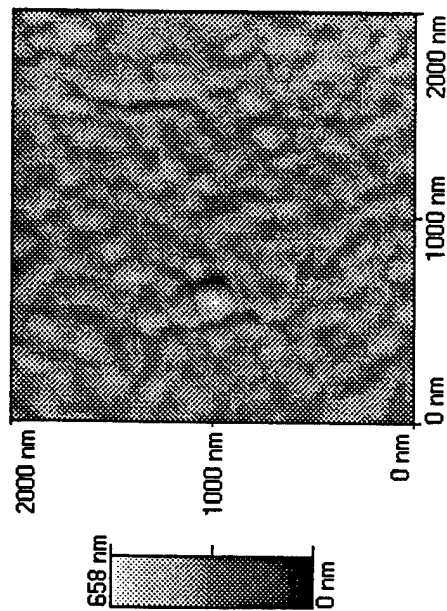
	<i>FA</i>	<i>RTA</i>	<i>RPTA</i>
<i>K</i>	960	849	611
$\text{tg}\delta$ (%)	17.8	13.4	10.6
$+P_R$ ( $\mu\text{C}/\text{cm}^2$ )	31	31	30
$-P_R$ ( $\mu\text{C}/\text{cm}^2$ )	34	34	31
$+E_C$ (kV/cm)	124	122	124
$-E_C$ (kV/cm)	105	114	123

FA = Furnace Annealing; RTA = Rapid Thermal Annealing; RPTA = Rapid Photothermal Annealing; *K* = dielectric constant;  $\text{tg}\delta$  = dielectric loss;  $P_R$  = remanent polarization;  $E_C$  = coercive field.

PLZT RTA



PLZT RPA



PLZT FA

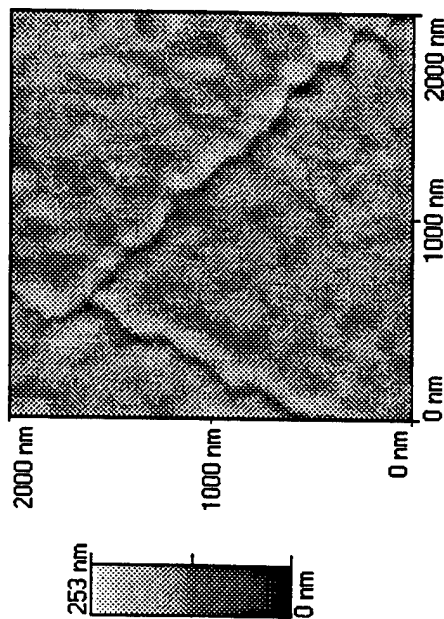


Figure 3. AFM micrographs of the samples prepared by RPTA (top right), RTA (top left), and FA (bottom).

Figure 4 displays the ferroelectric hysteresis loops of the samples obtained at different annealing temperatures. Consistent with the X-ray diffraction data, a fully developed hysteresis loop was observed at 600°C and 650°C. Since the temperature increment for this experiment was relatively large (50°C), it is not clear at what temperature a fully developed perovskite structure had been achieved. But, judging from the X-ray diffraction data, it is likely well below 600°C. This characteristic of low-temperature processing offers one of the more useful advantages of rapid thermal annealing over the furnace annealing. For the furnace annealing, the conversion of the pyrochlore to perovskite phase is incomplete until usually above 650°C. It is yet to be determined whether or not the UV irradiation plays a noticeable roll in achieving a mature structure at lower temperatures.

The fatigue characteristics of the thin film samples derived using RPTA, RTA and FA approaches are presented in Figures 5 through 8. As with other PZT-based thin films reported in the literature, the PLZT 2/55/45 materials (Figure 5) showed a progressive decrease in the remanent polarization with increasing number of voltage cycles. An appreciable reduction in the remanent polarization occurred after  $10^6$  voltage cycles. Improvements in the fatigue properties by rapid photothermal annealing over the other two approaches are clearly evident in Figure 5. There was little difference in the variation of the remanent polarization between RTA and FA.

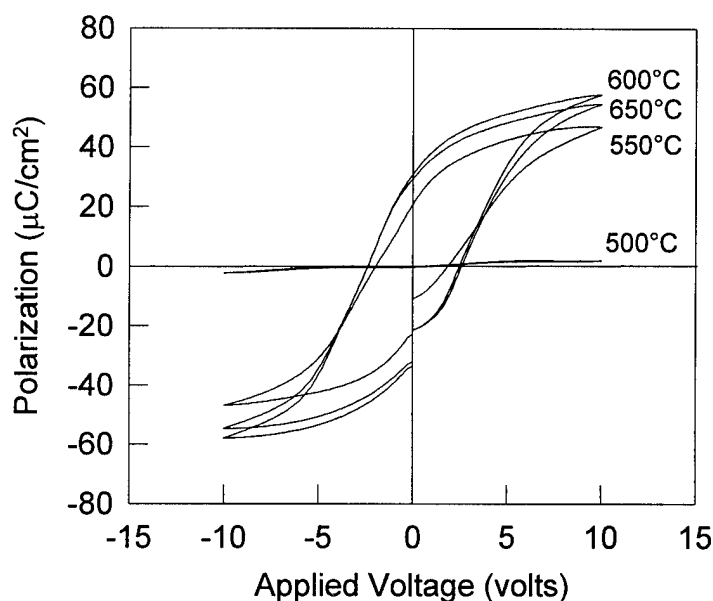


Figure 4. Polarization-voltage hysteresis loops of samples prepared under different annealing temperatures.

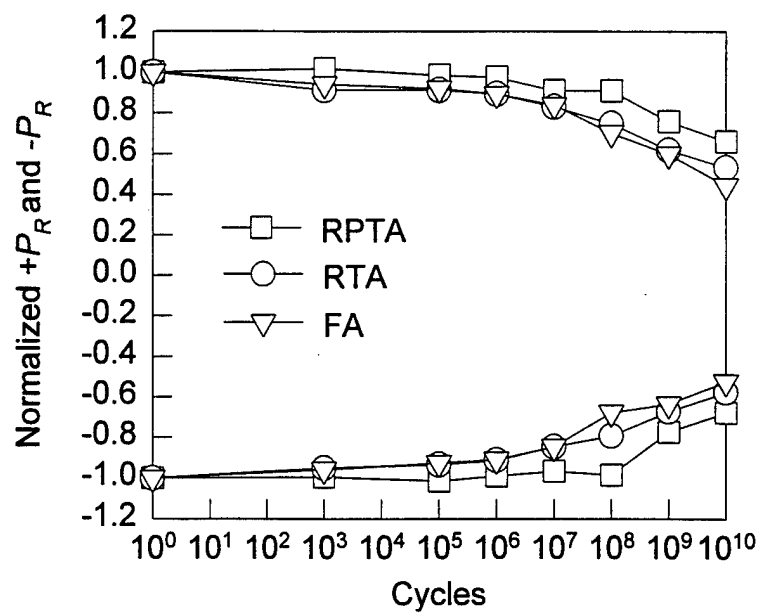


Figure 5. Variation of normalized remanent polarization with voltage cycles for samples processed with different annealing approaches.

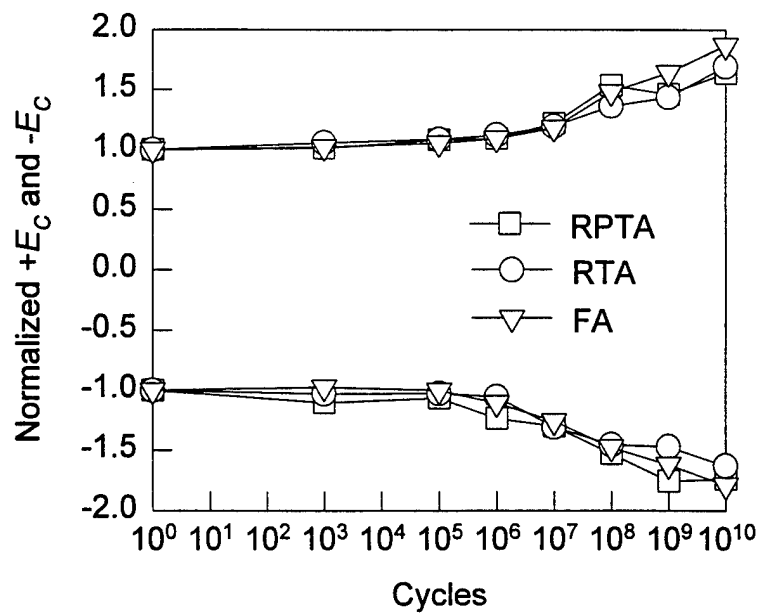


Figure 6. Variation of normalized coercive field with voltage cycles.

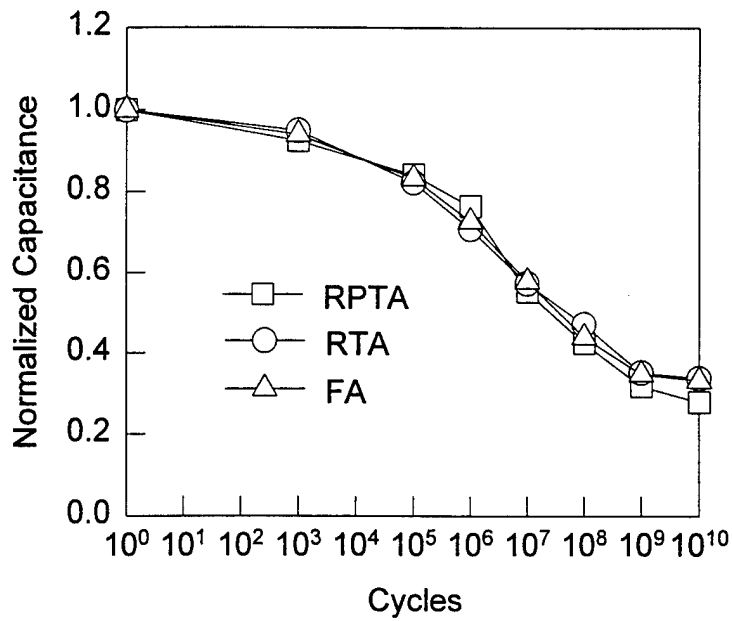


Figure 7. Variation of normalized capacitance with voltage cycles for samples processed with different annealing approaches.

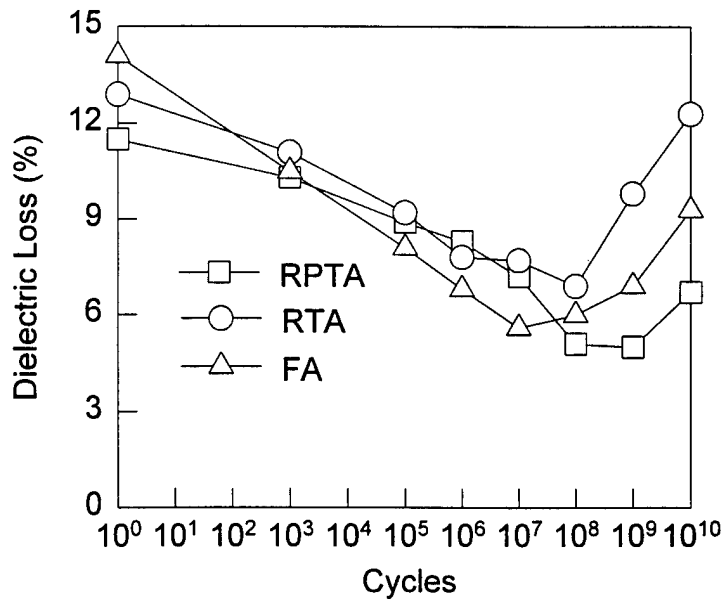


Figure 8. Variation of dielectric loss with voltage cycles.

The variation of the coercive field with cycle number was very similar for all the samples (Figure 6). The coercive field began to rise significantly after about  $10^6$  cycles. An average 50% increase was found after  $10^8$  cycles. Both the capacitance and dielectric loss of these samples decreased drastically with increasing voltage cycles (Figures 7 and 8). But the loss data recovered after around  $10^8$  cycles. This behavior can be attributed to the deterioration of sample resistivity, as will be shown later. It is commonly believed that after a certain number of voltage cycles the ferroelectric domains become locked by trapped space charges and/or defect ions.<sup>13-14</sup> In this situation, the contribution of domain switching to the dielectric response is diminished and consequently the dielectric constant is reduced.

A number of representative hysteresis loops measured at different voltage cycles are illustrated in Figure 9. The reduction of remanent polarization and the increase of coercive field with increasing cycles can be clearly seen. A significant increase in conductivity can be deduced from the roundup of the tips at polarization saturation of the loops after large numbers of cycles, which is responsible for the rebound of the dielectric loss values mentioned earlier.

The current-voltage characteristics of the samples are shown in Figure 10. The data with RPTA, RTA and FA exhibited very similar variations up to about 2.2 volts. Beyond this voltage value, the differences became noticeable among these annealing techniques. The leakage current density was observed to improve with the RPTA process at higher voltage levels over the RTA and FA processes.

It is well known that the interaction of photons with matter leads to quantum as well as thermal effects depending on the energy of the photons involved.<sup>15</sup> Most of the research work in the past did not pay sufficient attention to the quantum effects and focused mainly on the thermal effects. The quantum energy associated with the photons having wavelengths greater than approximately 800 nm is generally negligibly small for most practical purposes. However, with light sources of sufficient intensity in the UV and VUV wavelength regions, the quantum effects in the materials resulting from illumination of the light sources may be significant. It is expected that these quantum effects will reduce the activation energy involved in a material processing, thus minimizing microscopic defects and internal stresses. Indeed, it has been shown that by means of UV irradiation, diffusion coefficients were increased in silicon wafers<sup>10</sup> and the residual stress level was significantly reduced in the polymeric Teflon on Si/Al substrates and dielectric  $\text{Ta}_2\text{O}_5$  thin films on Si or Poly-Si substrates.<sup>10</sup>

At the present time the role of UV illumination in the annealing processing of the PLZT thin films presented in this paper has not been fully determined. It is, however, believed that by absorbing UV photons, individual ions consisting of the thin films gain extra opportunity in overcoming potential barriers and hence

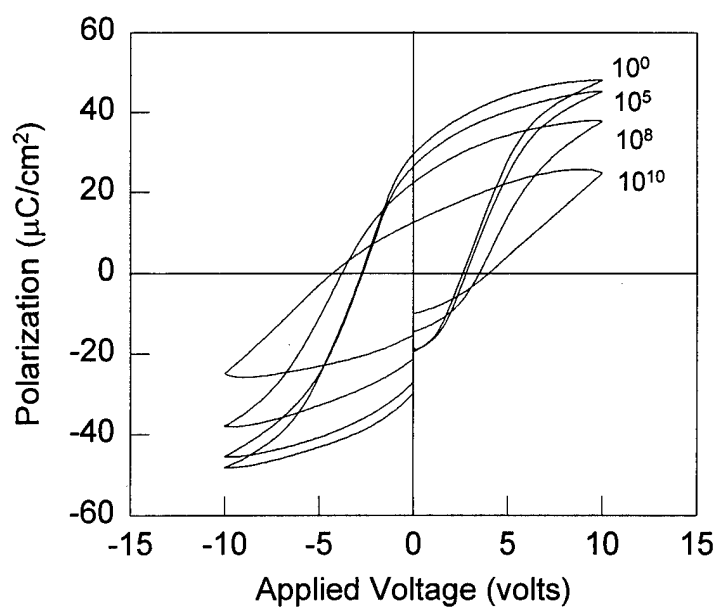


Figure 9. Polarization-voltage hysteresis loops for sample subjected to different numbers of voltage cycles.

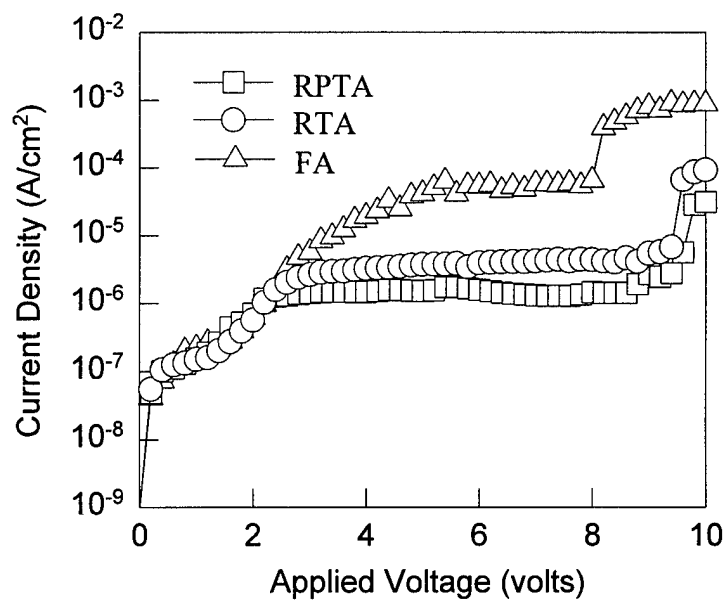


Figure 10. Current-voltage relationship of the samples annealed with different annealing approaches.

finding energetically more stable positions. The improvements found in the properties of the PLZT thin films by using the rapid photothermal annealing were considered to be primarily ascribed to the improvement of the structural uniformity and reduction of microscopic effects. Further work is underway with hope in achieving a deep insight into the effect of the rapid photothermal annealing on the properties of ferroelectric thin films and related mechanisms.

## CONCLUSIONS

PLZT 2/55/45 thin films on platinum-coated Si wafers deposited by RF magnetron sputtering were annealed using the newly emerging rapid photothermal annealing technique. A fully developed perovskite structure indicated by X-ray diffraction patterns was obtained with the RPTA below 600°C, a temperature considerably lower than used in the furnace annealing process. The AFM micrographs show that the samples with UV treatment generally have less and finer microcracks. The effects of the rapid photothermal annealing on the thin film properties were investigated with reference to those of the films prepared by conventional furnace annealing and rapid thermal annealing. Improvements of various degrees in the performance were observed for the samples processed by rapid photothermal annealing. Dielectric loss was typically reduced by 20% with UV irradiation versus without UV irradiation, with a concomitant decrease in dielectric permittivity. A more symmetric hysteresis loop with respect to the electric field axis was generally seen after UV illumination. The fatigue properties were slightly improved in the case of RPTA. In addition, a lower leakage current density was observed in the samples treated with the rapid photothermal annealing as compared with furnace annealing and rapid thermal annealing.

## ACKNOWLEDGMENT

This work was supported by NASA under grant No. NAG-1-1301 and ONR under grant No. N00014-94-1-0563.

## REFERENCES

- <sup>1</sup>W. Warren, D. Dimos, H. N. Al-Shareef, M. V. Raymond, B. A. Tuttle and G. E. Pike, "Links between Electrical and Optical Fatigue in  $\text{Pb}(\text{Zr,Ti})\text{O}_3$  Thin Films," *J. Am. Ceram. Soc.*, **79**[6] 1714-16 (1996).
- <sup>2</sup>K. Suu, A. Osawa, N. Tani, M. Ishikawa, K. Nakamura, T. Ozawa, K. Sameshima, A. Kamisawa and H. Takasu, "Preparation of  $(\text{Pb,Lu})(\text{Zr,Ti})\text{O}_3$  Ferroelectric Films by RF Sputtering on Large Substrate," *J. J. Appl. Phys.*, **35**[9B] 4967-71 (1996).



<sup>3</sup>O. Auciello, K. Gifford, D. Lichtenwalner, R. Dat, H. Al-Shareef, K. Bellur and A. Kingon, "A Review of Composition-Structure-Property Relationships for PZT-Based Heterostructure Capacitors," *Integrated Ferroelectrics*, **6** 173-187 (1995).

<sup>4</sup>E. M. Griswold, L. Weaver, D. S. McIntyre, M. Sayer and I. D. Calder, "Crystallization of Rapid Thermal Processed PZT:Platinum and Ruthenium Oxide Electrodes," *Integrated Ferroelectrics*, **10** 123-30 (1995).

<sup>5</sup>J. F. Scott and C. A. Paz de Araujo, "Ferroelectric Memories," *Science*, **246** 1400-11 (1989).

<sup>6</sup>T. Shiosaki, "Growth and Applications of Piezoelectric and Ferroelectric Thin Films," *IEEE Ultrasonics Symposium Proceedings*, **1** 537-46 (1990).

<sup>7</sup>A. Parel and J. S. Obhi, "Ferroelectric Thin Films for Integrated Sensor and Memory Devices," *GEC Journal of Research*, **12**[3], 141-52 (1995).

<sup>8</sup>R. Watton, "Ferroelectric Materials and IR Bolometer Arrays: from Hybrid Arrays towards Integration," *Integrated Ferroelectrics*, **4**(2), 175-86 (1994).

<sup>9</sup>F. Wang, E. Furman and G. H. Haertling, "Electro-optic Measurements of Thin-Film Materials by Means of Reflection Differential Ellipsometry," *J. Appl. Phys.*, **78**[1] 1-7 (1995).

<sup>10</sup>R. Singh, R. Sharangpani, K. C. Cherukuri, Y. Chen, D. M. Dawson, K. F. Poole, A. Rohatgi, S. Narayanan and R. P. S. Thakur, "How Rapid Isothermal Processing Can Be a Dominant Semiconductor Processing Technology in the 21st Century," *Mat. Res. Symp. Proc.*, **429**, 81-94 (1996).

<sup>11</sup>R. Singh, S. Alamgir and R. Sharangpani, "Deposition of High Dielectric Constant Materials by Dual Spectral Sources Assisted Metalorganic Chemical Vapor Deposition," *Appl. Phys. Lett.*, **67**, 3939-41 (1995).

<sup>12</sup>G. E. Pike, W. L. Warren, D. Dimos, B. A. Tuttle, R. Ramesh, J. Lee, V. G. Keramidas and J. T. Evans, "Voltage Offset in (Pb, La)(Zr, Ti)O<sub>3</sub> Thin Films," *Appl. Phys. Lett.*, **66**, 484-86 (1995).

<sup>13</sup>W. L. Warren, D. Dimos, B. A. Tuttle, G. E. Pike, R. W. Schwartz, P. J. Clews and D. C. McIntyre, "Polarization Suppression in Pb(Zr,Ti)O<sub>3</sub> Thin Films," *J. Appl. Phys.*, **77**[12], 6695-02 (1995).

<sup>14</sup>W. Pan, S. Sun and P. Fuierer, "Effects of Ferroelectric Switching on the Dielectric and Ferroelectric Properties in Lead Zirconate Titanate Ceramics and Their Modeling," *J. Appl. Phys.*, **74**[2], 1256-64 (1993).

<sup>15</sup>H. Kroemer, "Quantum Mechanics," *Printice Hall*, N.J., 5 (1994).

**Part X.**

**Publications**

# Temperature Dependent Characteristics of Cerambow Actuators

Bret W. Barron, Guang Li, and G. H. Haertling  
The Gilbert C. Robinson Department of Ceramic Engineering  
Clemson University  
Clemson, SC 29634-0907

**Abstract**--A new type of piezoelectric actuator has been developed called the Cerambow. Cerambow technology is based on a thermal contraction mismatch between two bonded layers which results in a stress-biased structure. For this investigation, brass substrates were solder-bonded to PLZT 1/53/47 and 5.5/56/44 disks at an elevated temperature. During cooling, stresses are imparted to the ceramic by the metal and a domed structure results. The displacements of Cerambows were recorded as a function of temperature under both loaded and non-loaded conditions. The results showed a fairly constant displacement up to approximately 100°C, followed by a rapid decrease to the maximum temperature of 160°C. After thermal cycling, the displacements were found to be close to the initial displacement values. Prior to and after thermal cycling, the mechanical quality factor and the effective coupling coefficient of the dome mode for each sample were calculated.

## I. INTRODUCTION

In recent years there has been a considerable amount of work done in the area of incorporating piezoelectric materials into structures which can produce strains that are greater than the bulk materials.<sup>1,2</sup> One such actuator configuration is the newly developed Cerambow (CERAMic Biased Oxide Wafer).

The Cerambow actuator was developed in the shadow of one of the most promising developments in the field of strain-amplified actuators known as the Rainbow. In the Rainbow, it was found that the unique geometry was a result of the reduction of volume in the reduced layer, the unit cell volume change at the paraelectric-ferroelectric phase transformation, and the thermal expansion coefficient mismatch between the reduced and unreduced layers.<sup>3</sup>

The Cerambow was based on the same stress-bending technology as the Rainbow, but the temperatures of fabrication were much lower, and the bonding mechanism was inherently different. The Cerambow relies solely on the thermal expansion mismatch between the substrate and ceramic layers to create a domed structure. The stress gradients which are present in the ceramic layer after cooling enable the Cerambow to produce greater displacements at a given voltage than the average unimorph bender. In the Rainbow this effect was described as the stress-enhanced effect.<sup>4</sup> Preliminary finite element modeling results suggest that the Cerambow may also benefit from this phenomenon. While the Rainbow is a monomorph

consisting of piezoelectrically active oxide and inactive reduced layers, the Cerambow is a typical unimorph.

The inactive layer in the Cerambow structure laterally constrains the active layer. When an electric field is applied to the device, the contraction in the lateral direction by the active layer results in a bending motion which is maximized at the dome center. The room temperature properties have shown the Cerambow to be a viable strain-enhancing technique, but an understanding of the temperature dependence of their displacement properties is essential for consideration as actuation devices.

## II. EXPERIMENTAL PROCEDURES

### A. Sample Preparation

Conventional mixed oxide techniques were used to prepare PLZT 1/53/47 and 5.5/56/44 powders for this investigation. Raw materials were batched according to the traditional B-site vacancy formula for the PLZT system and were mixed for 30 minutes in a ball mill. The mixed powder was placed in an alumina crucible and calcined using a ramp rate of 5°C/min. to 925°C for 2 hours. Milling was done for one hour at a 1:1 weight ratio of powder to distilled water.

Slugs were dry pressed and sintered for 4 hours at 1250°C in an oxygen atmosphere. The slugs were then cut using a diamond saw and lapped to a diameter of 3.175 cm and thickness of 0.0432 cm. Silver epoxy electrodes (DuPont 7095) were applied to each side of the ceramic disk and dried at 200°C for 20 minutes and then fired at 550°C for 30 minutes. A non-electroded ring about 1 mm in width was left around the outer radius of one side of the wafer to prevent any excess solder from bonding to it during Cerambowing.

### B. Cerambow Fabrication

A brass disk was then cut to the appropriate diameter from a sheet of foil having a thickness of 0.0127 cm. Both the electroded ceramic and the brass disk were placed in acetone and cleaned in a sonicator. The brass disk was placed on a piece of sheet metal located on a hot plate preheated to approximately 250°C. The brass was allowed to heat up to maximum expansion, and 60/40 Sn/Pb solder was uniformly applied to it. An electroded PLZT wafer was placed on top

of the solder with the fully electroded side down. A preheated steel weight was used to hold the device together while it was removed from the heat. Pressure was applied by hand for approximately 20 seconds after removal from the hot plate, and then the setup was allowed to cool to room temperature. The edge of each Cerambow was sanded to remove any excess solder and decrease the chance of electrical breakdown during testing.

### C. Measurements

The density of each sample was determined by the immersion method after sintering. All densities of the samples used in this experiment were > 95% of the theoretical. The grain sizes of the PLZT 1/53/47 and 5.5/56/44 prepared for this investigation were determined on a Ziess optical microscope by the linear intercept method and were found to be 7  $\mu\text{m}$  and 3  $\mu\text{m}$ , respectively. The samples were poled after Cerambowing at a field approximately twice the coercive field, 16 kV/cm for 1/53/47 and 25 kV/cm for 5.5/56/44, for one minute.

The equivalent circuit and the effective coupling coefficient parameters for the dome mode were obtained using a Hewlett-Packard 4194A Impedance / Gain-Phase Analyzer. The quality factor,  $Q_m$ , and the effective electromechanical coupling coefficient,  $k_{\text{eff}}$ , were then calculated by the following expressions:

$$Q_m = \frac{(L_1 / C_1)^{\frac{1}{2}}}{R_1} \quad (1)$$

$$k_{\text{eff}}^2 = \frac{(f_p^2 - f_s^2)}{f_p^2} \quad (2)$$

Where  $L_1$ ,  $C_1$ , and  $R_1$  were the equivalent inductance, resistance, and series capacitance of the equivalent circuit for each sample. In Equation 2,  $f_s$  and  $f_p$  were the series and parallel resonance frequencies of the resonant mode respectively.

All strain measurements were done using a Lucas-Schaevitz LVDT (Linear Variable Differential Transformer). The dome center of each sample was marked with a scribe to ensure greater consistency in the recorded data. Before and after temperature cycling, the dome height of each sample was recorded. The sample was immersed in mineral oil in a metal pan and placed onto an alumina refractory disk on a hot plate. Because a negative pressure would develop underneath the domed structure of the Cerambow during testing, each sample was placed onto three metal strips arranged in a triangular pattern. Without the metal spacers, the sample would stick to the bottom of the metal pan after

several applications of the electric field, resulting in no net motion.

The probe used to measure the displacements was built so that the part which was encompassed by the LVDT was separated from the metal tip by an insulating ceramic layer. This configuration allowed the application of the voltage to be carried out through the tip of the probe to the sample. A voltmeter was used to make sure that 450 volts was applied to the sample at each temperature. The temperature was varied from 25°C to 160°C and back to 25°C at a rate of approximately 0.5 °C/ min. The temperature was recorded by a Type K thermocouple placed into the mineral oil directly above the sample attached to a voltmeter. Up until 130°C, the displacement at 450 volts was recorded every 15°C. After that point, the amount of displacement was decreasing at a much faster rate and the measurements were taken every 5°C. Three samples were tested under each condition and the data were averaged to construct the appropriate diagrams. The experimental setup is shown in Figure 1.

### III. RESULTS AND DISCUSSION

The mechanical quality factor and effective coupling coefficient of the Cerambows used in this investigation are located in Table 1. The subscripts were meant to indicate when the measurements were obtained during the testing cycle. The subscripts b, a, and al, signify measurements taken before thermal treatment, after thermal treatment, and after thermal treatment under a point loading of 200 grams respectively.

The mechanical quality factor under both testing conditions showed a slight decrease after thermal cycling. It has previously been seen that prolonged exposure to high temperatures results in a poor bond between the metal and ceramic layers. This may be responsible for the decrease in this property that was observed. The samples which were tested under point-loaded testing conditions showed a slightly less decrease than the non-loaded specimens. This

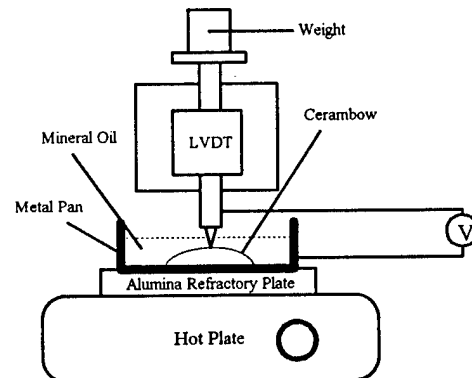


Fig. 1. Experimental setup used to calculate the bending displacement of Cerambow actuators as a function of temperature.

TABLE 1  
MECHANICAL QUALITY FACTOR AND EFFECTIVE COUPLING COEFFICIENT FOR  
CERAMBOW ACTUATORS BEFORE AND AFTER THERMAL CYCLING

Property	5.5/56/44	1.0/53/47
$Q_b$	67	87
$Q_a$	40	60
$Q_{al}$	54	84
$k_{eff_b}$	.164	.174
$k_{eff_a}$	.186	.180
$k_{eff_{al}}$	.183	.186

could be due to the fact that the pressure being exerted onto the sample aided in maintaining the bond between the ceramic and metal layers during thermal cycling.

The effective coupling coefficient of Cerambows showed an increase after thermal cycling under loaded conditions. This may be related to the fact that the dome height was seen to decrease by 20 - 30 % after testing in these samples. It has been seen in Rainbow ceramics that samples with more curvature exhibit smaller effective coupling coefficients. The geometry change of the Cerambows during testing could have led to the change in this property of the device.

Figure 2 shows a plot of the displacement as a function of temperature under non-loaded conditions. As the temperature was increased, the displacement gradually increased until 100-115°C. After this temperature range, the displacement began to decrease at an accelerated rate until the maximum temperature was reached. The same behavior was observed upon cooling the samples back to room temperature.

The compositions used in this investigation were known to possess piezoelectric properties similar to those of PZT-5. A plot of the change of the  $d_{31}$  coefficient versus temperature was reported by Berlincourt et. al.<sup>5</sup> This diagram showed that a rise in temperature is accompanied by an increase in the  $d_{31}$  coefficient for PZT-5A. It was assumed that the

PLZT materials used had the same variation of their  $d_{31}$  coefficients with temperature. The increase in this material property directly influences the performance of Cerambows because, as stated previously, the lateral contraction perpendicular to the direction of the applied electric field is responsible for the bending motion in these actuators. This factor was considered to be the major contributor to the increase in displacement up to temperatures of approximately 115°C.

Above 115°C, the  $d_{31}$  coefficient does not increase as quickly and other factors begin to dominate the behavior of the samples. The most obvious reason for the decrease in the displacement at high temperatures may have been the fact that the solder bonding layer was rapidly softening. As this softening occurred, the metal and the ceramic layers were able to move relative to each other as opposed to with each other. When the voltage was applied, the deformation of the piezoelectric layer was not entirely transferred to the bending motion because of the overly ductile bonding layer, leading to a decrease in the achieved displacement. Furthermore, as the temperature was continually increased, the bonding layer became more ductile, transferring even less of the piezoelectric strains into bending.

Figure 3 shows a diagram of the temperature-dependent displacement of Cerambow actuators bearing a point load of 200 grams at the dome center. These curves show a similar response to the temperature variation as in Figure 2. In these curves the displacement decrease is much more drastic, and the maximum displacement was found to lie at a lower temperature, ~ 85°C. It was believed that the force of the point loading created nonuniform stress conditions within the ceramic layer which may have led to the more rapid decrease in displacement at a lower temperature. In addition, the amount of shear stress at the interface may have been increased by the application of the point loading. This shear stress may have also played a role in the behavior observed under these testing conditions.

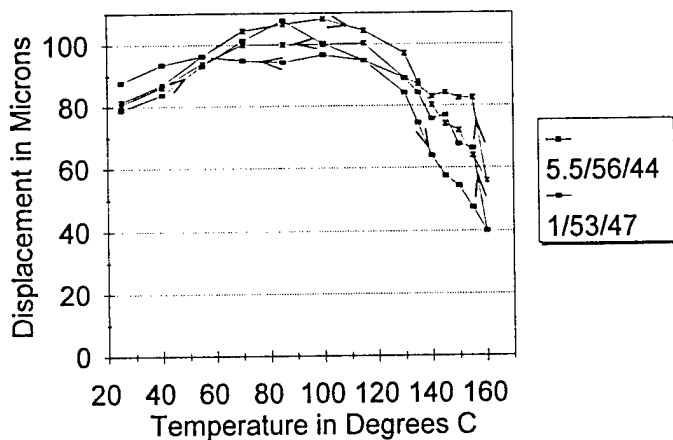


Fig. 2. Displacement as a function of temperature for Cerambow actuators under non-loaded conditions.

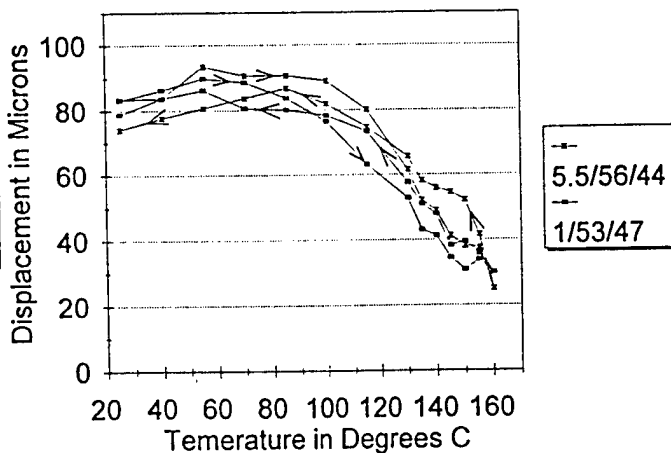


Fig. 3. Displacement as a function of temperature for Cerambow actuators under a 200 gram point loading.

## V. SUMMARY

The temperature dependent displacement capabilities of Cerambow actuators were studied under both loaded and non-loaded conditions. Under both testing conditions, the displacements were found to be fairly temperature independent up to temperatures of approximately 100°C. Past this temperature range, there was a sharp decrease in the observed displacement up to the maximum temperature of 160°C. The softening of the bonding layer was considered to be responsible for this behavior. In addition, temperature cycling of Cerambow actuators did not seem to decrease their room temperature displacement capabilities. The mechanical quality factor was found to decrease more readily in samples that were tested under non-loaded conditions. This was believed to be due to a lack of pressure that was used to fabricate the original structure. The effective coupling coefficient of the dome mode was seen to increase in the loaded samples to a greater extent, and was attributed to a change in the dome curvature after testing.

## V. REFERENCES

- [1] Gene H. Haertling, "Chemically reduced PLZT ceramics for ultra-high displacement actuators," *Ferroelectrics*, vol. 154, pp. 101-106, 1994.
- [2] Y. Sugawara, K. Onitsuka, S. Yoshikawa, Q. Xu, R. E. Newnham, and K. Uchino, "Metal-Ceramic composite actuators," *J. Am. Ceram. Soc.*, vol. 75, pp. 996-998, April 1992.
- [3] Guang Li, "Influence of internal stress on the electromechanical properties of PLZT stress-biased (Rainbow) ceramic actuators," Ph.D. Thesis, Gilbert C. Robinson Department of Ceramic Engineering, Clemson University, 1995.
- [4] Guang Li, "Stress-enhanced displacements in PLZT Rainbow actuators," *to be published*, 1996.
- [5] D. A. Berlincourt, D. R. Curran, and H. Jaffe, "Piezoelectric and piezomagnetic materials and their function in transducers," *Physical Acoustics*, p. 206, 1964.

## PLZT-BASED MULTILAYER COMPOSITE THIN FILMS, PART II: MODELING OF THE DIELECTRIC AND HYSTERESIS PROPERTIES

D. E. DAUSCH,<sup>†</sup> E. FURMAN, F. WANG<sup>‡</sup> and G. H. HAERTLING

*Gilbert C. Robinson Department of Ceramic Engineering, Clemson University,  
Clemson, SC 29634-0907, USA*

*(Received September 21, 1995)*

PLZT-based composite thin films with various compositions were fabricated and characterized in Part I of this study. Similarly to procedures reported in the literature, the low-field dielectric properties in Part II were modeled according to a series capacitor model based on the dielectric constants of the individual composite constituents. In order to model the FE high-field switching properties, AFE-to-FE phase transitions and non-uniform electric field distributions in the composite films, a new hysteresis modeling technique was developed based on a series capacitor model featuring the nonlinear polarizabilities of the individual components as evident from experimental data. The model predicts the behavior of any composite film structure provided the pure component properties are known.

*Keywords: Multilayer composites, thin films, hysteresis model, dielectric properties, series capacitors.*

### INTRODUCTION

An important method of improving the properties of ferroelectric materials has been the development of composite structures. Polymer/ceramic, metal/ceramic and ceramic/ceramic composites have been fabricated; however, the utilization of composite materials in thin film configurations has been infrequently reported. PLZT-based ceramic/ceramic composite thin films containing ferroelectric (FE), antiferroelectric (AFE) and relaxor (i.e., slim-loop ferroelectric) compositions introduced in Part I of this study, "Experimental Investigation of Composite Film Structures," possessed improved properties compared with PLZT thin films of homogeneous composition.<sup>1</sup> Composites were developed with 1) improved AFE-to-FE domain switching with decreased ferroelectric coercive field ( $E_F$ ) and increased saturation polarization ( $P_{sat}$ ) for materials with AFE-type properties, 2) increased induced polarization with decreased coercive field ( $E_C$ ) and remanent polarization ( $P_R$ ) for relaxor-type composites and 3) increased hysteresis loop squareness for ferroelectric memory materials compared with films of homogeneous PLZT composition.

Part II, "Modeling of the Dielectric and Hysteresis Properties," describes the modeling of these devices. In addition to modeling of the low-field dielectric properties of these composites, which has been performed by several authors for bulk ceramic composites, a new hysteresis modeling technique is presented which describes the high-field ferroelectric domain switching properties as well as antiferroelectric-to-ferroelectric phase transitions in the composite thin films. The models

<sup>†</sup> Current address: NASA Langley Research Center, Hampton, VA 23681, USA.

<sup>‡</sup> Current address: NZ Applied Technologies, Woburn, MA 01801, USA.

depict the composite thin films as combinations of series capacitors containing the properties of the individual composite constituents. The dielectric and hysteresis properties over a range of temperatures and frequencies were examined. Modeling of these composite materials provides a method for predicting the low-field dielectric properties and high-field domain switching properties such that composite structures can be designed from known compositions.

## EXPERIMENTAL PROCEDURE

The experimental procedure for thin film fabrication was reported previously in detail<sup>1</sup> and is described briefly here. Thin films of homogeneous and composite composition were fabricated by dip and spin coating from acetate precursor solutions. For thin film production via manual spin coating, the acetate solution was spun onto Pt-coated Si wafer substrates (Pt/Si) using a photoresist spinner at 2000 rpm for 15 seconds and pyrolyzed in a Thermolyne conventional box furnace at 700°C. An automatic dip coater was utilized for the fabrication of thin films on Ag foil substrates. Films were dipped into the solution and raised into a tube furnace for pyrolysis at 700°C. PLZT thin films were also fabricated on Pt/Si with a computer-controlled automatic spin coat reactor/analyzer. Films were spun at 2000 rpm for 30 seconds and heated using rapid thermal processing (RTP) at 700°C. The total film thicknesses, measured with a laser ellipsometer, of the 10 layer spin coated and 24 layer dip coated thin films were between 0.8 and 1.0  $\mu\text{m}$ .

Composite thin films consisted of the following PLZT compositions: ferroelectric 2/55/45 and 7/65/35; antiferroelectric 0/100/0, 0/96/4 and 0/95/5; and relaxor 9.5/65/35 and 12/65/35. Identification of 10 layer spin coated composite films with an initial deposition of  $x$  ferroelectric (F) layers followed by  $10-x$  antiferroelectric (A) layers was denoted by  $F(x)A(10-x)$ . Similarly, 24 layer dip coated composites consisting of  $x$  ferroelectric layers followed by  $24-x$  relaxor (R) layers were identified by  $F(x)R(24-x)$ . Other composite combinations were defined in the same way; i.e.,  $F(x)R(10-x)$ ,  $A(x)F(10-x)$ ,  $R(x)A(10-x)$  and  $R(x)A(24-x)$ . Homogeneous ferroelectric, antiferroelectric and relaxor thin films were also fabricated and were used for modeling of the composites.

For measurement of thin film electrical properties, 1 mm diameter Cu electrodes were vacuum evaporated onto the thin film surfaces. Thin film samples were analyzed using several electrical measurement techniques. Poled and virgin dielectric constants ( $K_{\text{pol}}$  and  $K_{\text{vir}}$ ) were measured on a Leader LCR meter at 1 kHz with a 1 V ac signal. The Curie temperatures ( $T_c$ ) of homogeneous and composite thin film samples were determined by heating the samples in a Delta Design oven. Curie temperatures were indicated by maxima in the measured capacitance. Polarization ( $P$ ) vs. electric field ( $E$ ) hysteresis loops were measured at 1 kHz with a 20 to 40 V ac signal using a Sawyer-Tower circuit and an oscilloscope readout. Thin film capacitance was measured from 100 Hz to 40 MHz using a Hewlett-Packard 4194A impedance analyzer with a 100 mV ac signal.



## DIELECTRIC PROPERTIES

### *Series Capacitor Model*

The low-field dielectric properties of the composite thin films were modeled according to a series equivalent circuit containing linear capacitors based on the dielectric constants of the constituents comprising the composite films. This type of analysis has been performed on bulk ceramic/ceramic composite materials. Shrout and co-workers calculated dielectric, piezoelectric and hysteresis loop properties for AFE/FE multilayer<sup>2</sup> and temperature compensated resonator<sup>3</sup> composites using a linear series capacitor model. Payne and Cross<sup>4</sup> modeled the dielectric properties of polycrystalline dielectric ceramics using an ideal diphasic series capacitor model with a simplified representation of the bulk and grain boundary phases as an alternating layered structure. Effective dielectric constants ( $K_{\text{eff}}$ ) of the composite thin films in this investigation were calculated similarly to the procedures described above for series capacitor configurations. Dielectric constants ( $K$ ) of the two pure components were substituted in the expression

$$K_{\text{eff}} = \frac{K_1 K_2 t_{\text{tot}}}{K_2 t_1 + K_1 t_2}, \quad (1)$$

where  $t_{\text{tot}}$  was the total composite film thickness and  $t_1$  and  $t_2$  were the thicknesses of the individual layers. Equation (1) was derived assuming constant electrode area. Experimental composite dielectric properties were compared with the calculated model for various composite film combinations as a function of temperature and frequency.

### *Comparison with Experimental Data*

At the end of Part I, it was proposed that the composite FE/relaxor thin films could be represented by combinations of series FE and relaxor capacitors.<sup>1</sup> In fact, the effective dielectric constants calculated using Equation (1) for these composites were found to correspond well with the measured  $K_{\text{pol}}$  values for these composites. For the 1  $\mu\text{m}$  2-9 (2/55/45-9.5/65/35), 7-9 (7/65/35-9.5/65/35) and 7-12 (7/65/35-12/65/35) F12R12 composites on Ag foil with 0.5  $\mu\text{m}$  FE and relaxor layers in each, the calculated  $K_{\text{eff}}$ s of 1352, 1870 and 2061, respectively, were only 4 to 8% lower than the measured values of 1424, 2031 and 2160. Dielectric constants of the 7-9 and 7-12 composites are shown in Figure 1 with the series capacitor modeled results which were calculated using Equation (1) over the temperature range from 25 to 180°C. Reasonable agreement was found between composite film behavior and the calculated model. Calculated  $T_{\text{CS}}$ s, however, were 5 to 15°C higher than the experimentally observed values.

Experimental virgin and poled effective dielectric constants of the F(x)A(10-x) composite thin films deposited on Pt/Si along with the series capacitor equivalent circuit representation for the FE/AFE composites are shown in Figure 2. Good agreement between the experimental and modeled results was observed for all of the compositions studied. Additionally, Figure 3 displays the experimental  $K_{\text{eff}}$  of the F5A5 composite measured over a frequency range of 100 Hz to 40 MHz with a 100

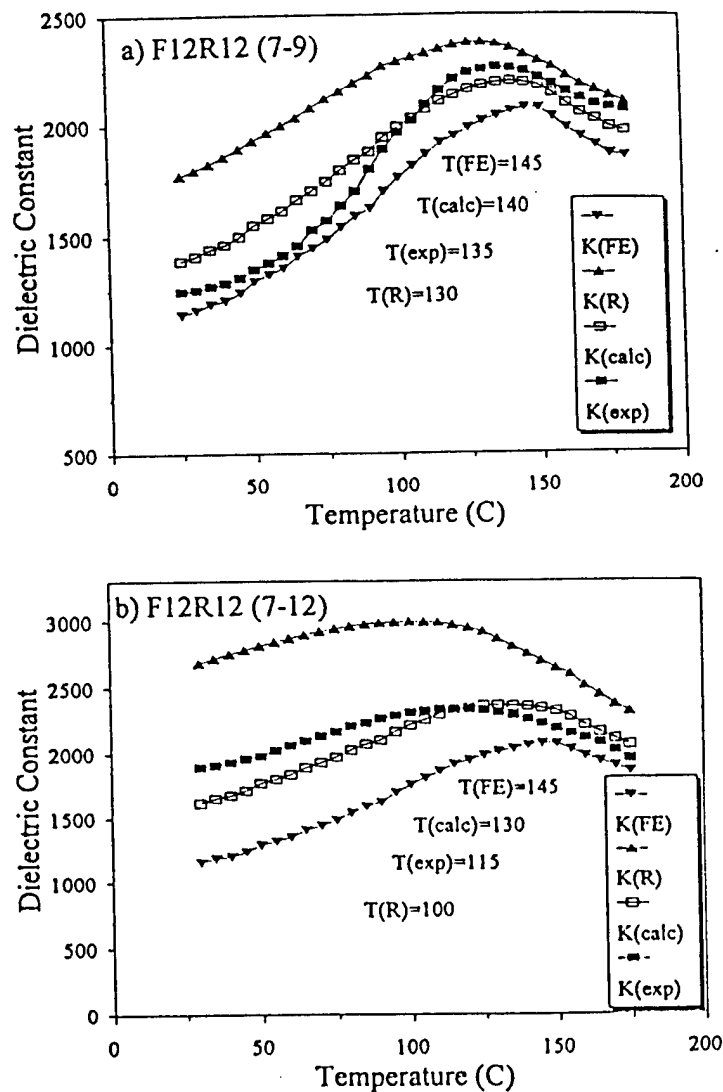


FIGURE 1. Experimental (exp) and calculated (calc) Curie temperature measurements for a) 7-9 and b) 7-12 FE/relaxor composite thin films deposited on Ag. Appropriate homogeneous ferroelectric (FE) and relaxor (R) dielectric constants ( $K$ ) are also shown. The Curie temperatures listed correspond to the temperature ( $T$ ) at which maximum  $K$  was observed.

mV ac signal. A dielectric relaxation at approximately 1 MHz was observed which could be attributed to the effect of an interfacial layer between the PLZT film and adjacent Pt electrode or Si substrate.<sup>5,6</sup> Despite this relaxation, agreement was exhibited between the experimental and modeled F5A5 dielectric properties, and this agreement was observed for all of the F(x)A(10-x) composites. The correspondence of the experimental results with the model at low ac voltage levels suggested that over the observed temperature and frequency ranges, composite films indeed behaved as series combinations of linear capacitors.

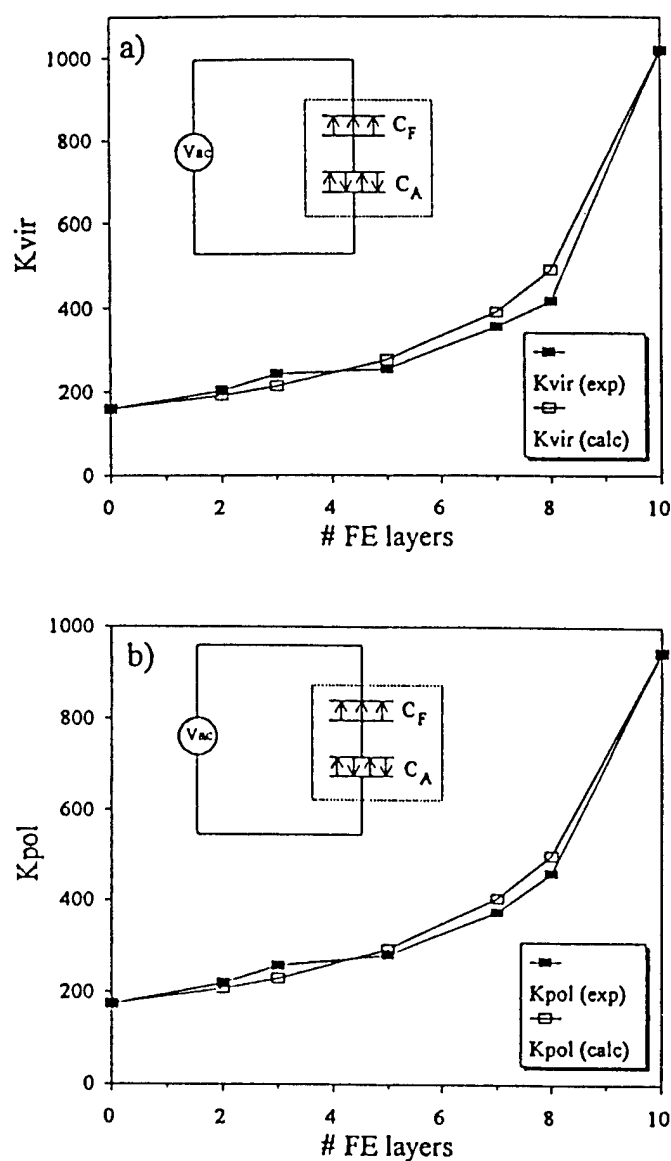


FIGURE 2. a) Virgin and b) poled effective dielectric constants of the  $F(x)A(10-x)$  composite thin films deposited on Pt/Si. Experimental (exp) results were measured at 1 kHz with a 1 V ac signal. The calculated (calc) results displayed were based on the series capacitor model shown.

## HYSTERESIS PROPERTIES

### Graphical Solution

In order to model the FE high-field switching properties and AFE-to-FE phase transitions as well as the non-uniform electric field distributions in the composite films described in Part I,<sup>1</sup> the P-E hysteresis loops of these films were calculated based on the series capacitor model featuring the nonlinear polarizabilities of the individual

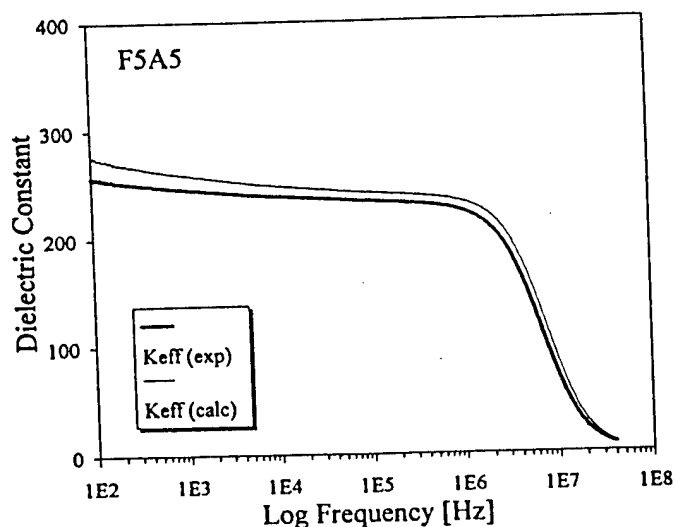


FIGURE 3. Effective experimental (exp) dielectric constant of the F5A5 composite thin film on Pt/Si measured with a 100 mV ac signal. Calculated (calc) results were based on the linear series capacitor model.

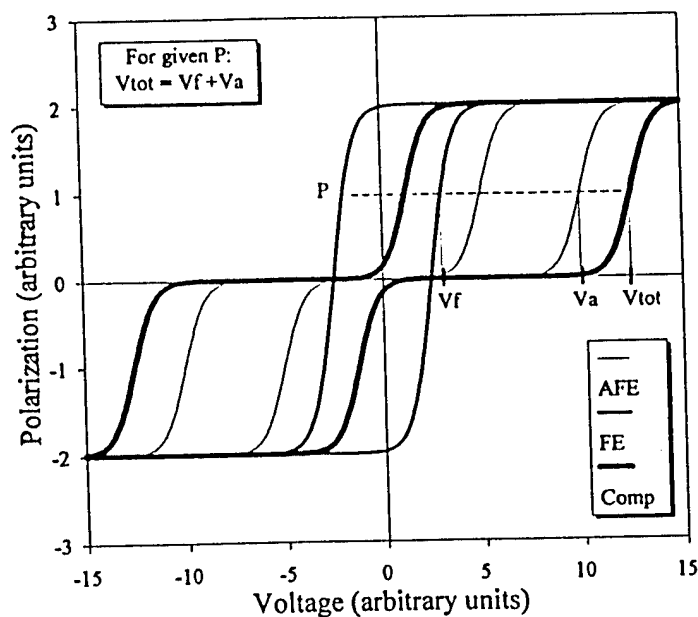


FIGURE 4. Representation of the graphical solution for nonlinear modeling of the hysteresis properties of a FE/AFE composite.

components. Individual component hysteresis loops were combined with series capacitor constraints to obtain the calculated properties of the desired composite thin films. Two techniques were applied for hysteresis modeling—a graphical and an analytical approach. For the graphical solution shown in Figure 4, a FE/AFE composite film hysteresis loop was constructed from the AFE and FE thin film properties

displayed. The boundary conditions applied for capacitors in series were 1) the charges on capacitors in series must be equal, and 2) the sum of the voltages across each capacitor must equal the total voltage. Since polarization is charge divided by area, the polarization in the individual capacitors should be equal and is also equal to the total polarization in the composite assuming spurious sources of charge in the circuit (e.g., leakage currents) are negligible. Hence, as exemplified in Figure 4, the total voltage,  $V_{\text{tot}}$ , across the composite film for a given polarization is calculated by adding the voltages,  $V_a$  and  $V_f$ , required for each individual film to reach the same polarization. This procedure was repeated for various polarization levels for the positive and negative domain switching cycles in the F5A5 and F7A3 composite thin films displayed in Figure 5. As shown, the model agreed fairly well with the experimental data; however, continuous plots of the modeled hysteresis properties were not obtained. Since the graphical approach involved a tedious procedure of computing point-by-point the hysteresis data for the model, the analytical approach was more widely used for modeling of the nonlinear effects in the composite thin films.

#### Analytical Solution

For the FE and AFE capacitors shown in the series capacitor representation in Figure 2,

$$Q_f = C_f V_f \quad (2)$$

and

$$Q_a = C_a V_a \quad (3)$$

where  $Q$  is charge,  $C$  is capacitance and  $V$  is voltage in the FE ( $f$ ) and AFE ( $a$ ) layers. As with the graphical solution, the charge on these series capacitors must be equal. Since charge is proportional to polarization and voltage is proportional to electric field, the first condition of the series model is met when the polarizations ( $P$ ) as functions of electric field ( $E$ ) in the individual layers are equal. This equal polarization condition implies unequal electric fields in the two layers which are related by

$$P_a(E_a) = P_f(E_f) \quad (4)$$

Furthermore, according to the second condition, the sum of the voltages for the series capacitors must be equal to the total voltage,  $V_{\text{tot}}$ . Therefore,

$$V_{\text{tot}} = E_f t_f + E_a t_a \quad (5)$$

where  $t_f$  and  $t_a$  are the thicknesses of the FE and AFE layers. Equations (4) and (5) can be solved simultaneously for the two unknowns,  $E_f$  and  $E_a$ , for any given  $V_{\text{tot}}$  on the composite film. Hysteresis loops of the composite thin films were calculated via this analytical approach by substituting  $E_f$  or  $E_a$  as a function of total voltage into an appropriate expression for polarization for either the FE or AFE layer. This analytical procedure produced a continuous plot of overall composite film polarization versus total voltage.

Miller *et al.*<sup>7</sup> defined ferroelectric hysteresis loops with Equation (6),

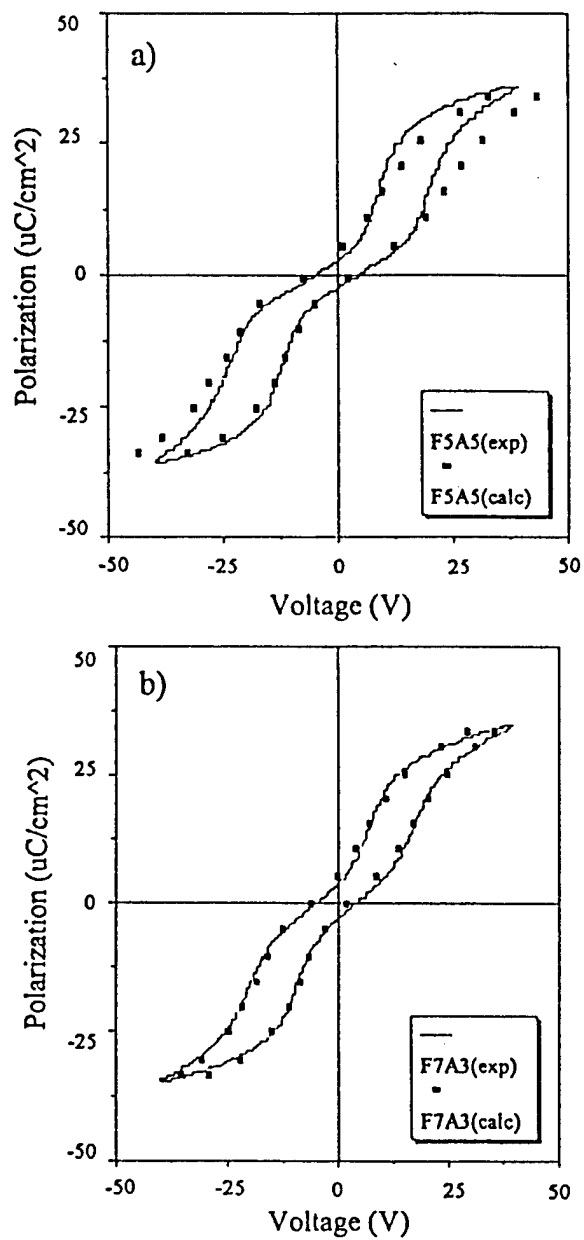


FIGURE 5. Graphical solution of the series capacitor model for the hysteresis properties of a) F5A5 and b) F7A3 composite thin films on Pt/Si.

$$P_d^+(E) = P_{sat} \tanh \left( \frac{E - E_c}{2\beta} \right), \quad (6)$$

for switching dipole polarization,  $P_d^+(E)$ , of the positive domain switching cycle, where

$$\beta = E_c \left[ \ln \left( \frac{1 + \frac{P_R}{P_{sat}}}{1 - \frac{P_R}{P_{sat}}} \right) \right]^{-1} \quad (7)$$

and  $P_R$ ,  $P_{sat}$  and  $E_c$  are the positive remanent polarization, saturation polarization and coercive field quantities of the hysteresis loop. The negative switching cycle of dipole polarization,  $P_d^-(E)$ , was defined as

$$P_d^-(E) = -P_d^+(-E). \quad (8)$$

Miller *et al.* explained that this polarization function does not represent a physical theory of domain switching; it is merely used as a convenient mathematical expression to describe the shape of the FE hysteresis loop.<sup>7</sup> However, this function was found to be consistent with experimental data and was used to predict FE domain switching properties with changing Sawyer-Tower circuit element values. Chai and coworkers<sup>8</sup> additionally used this polarization expression to represent experimental data for a PZT thin film in order to relate local electric field as a function of position in the film with externally measurable voltages. While Equation (6) does not inherently represent the physical process of FE domain switching, the expression can, when depicting experimental data, serve as a model for FE hysteresis properties.

For modeling of the domain switching properties and electric field distributions in the composite thin films in this investigation, Equations (6) through (8) were utilized for experimental data fit of the hysteresis properties of individual components in the composite thin films. In this manner, composite thin film behavior was modeled according to a series combination of the nonlinear individual polarizabilities of the homogeneous constituents comprising the composite structures. FE materials with single hysteresis loops were then defined by

$$P_f^+(E_f) = P_{sat} \tanh \left( \frac{E_f - E_c}{2\beta} \right) \quad (9)$$

and

$$P_f^-(E_f) = -P_{sat} \tanh \left( \frac{-E_f - E_c}{2\beta} \right), \quad (10)$$

where  $P_f$  and  $E_f$  were the FE polarization and electric field, respectively, and  $\beta$  was determined from Equation (7). For the positive domain switching cycle, or  $P_f^+(E_f)$ , the absolute values of  $+P_{sat}$ ,  $-P_R$  and  $+E_c$  obtained from the experimental FE hysteresis loops were substituted into the appropriate equations, while  $| -P_{sat} |$ ,  $| +P_R |$  and  $| -E_c |$  were used for  $P_f^-(E_f)$  calculations. These values were not necessarily equal, as asymmetry was often observed in thin film hysteresis loops. Figure 6 displays a typical FE hysteresis loop with labeled parameters for Equations (9) and (10).

Experimental data for AFE polarization was somewhat more difficult to represent. The high-field hysteresis portions of the double loops were defined by functions similar to those for the FE films; however, for the AFE materials, the hysteresis was offset by an electric field  $E_o$  and a polarization  $P_o$ . These offsets corresponded to the local origins or centers of the hysteresis portions of the loops. Parameters for AFE

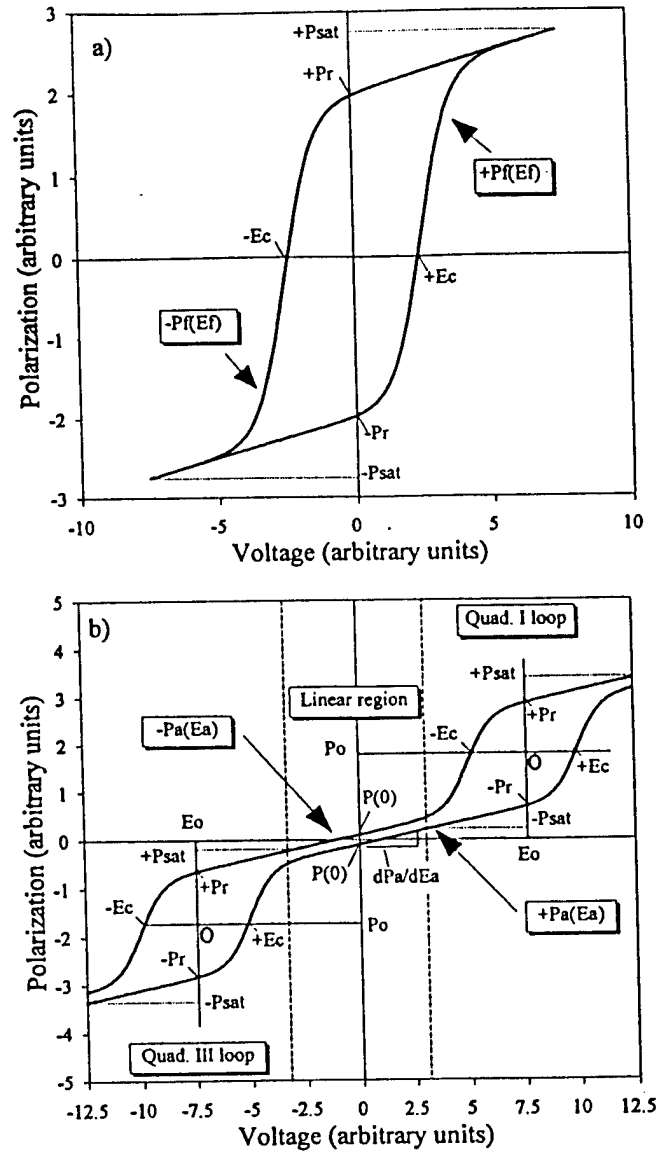


FIGURE 6. Representation of a) FE and b) AFE hysteresis loops with labeled parameters for the polarization functions used in the analytical solution for nonlinear hysteresis property modeling.

hysteresis loop equations are also shown in Figure 6. For hysteresis loops in quadrant I (i.e.,  $+P$ ,  $+E$ ), the AFE-to-FE transitions were determined by

$$P_a^+(E_a) = P_{sat} \tanh \left[ \frac{(E_a - E_o) - E_c}{2\beta} \right] + P_o, \quad (11)$$

while the FE-to-AFE reversions were determined by



$$P_a^-(E_a) = -P_{sa} \tanh \left[ \frac{-(E_a - E_o) - E_c}{2\beta} \right] + P_o \quad (12)$$

Quadrant III (i.e.,  $-P$ ,  $-E$ ) hysteresis regions were defined by

$$P_a^+(E_a) = P_{sa} \tanh \left[ \frac{(E_a + E_o) - E_c}{2\beta} \right] - P_o \quad (13)$$

for the FE-to-AFE reversions and

$$P_a^-(E_a) = -P_{sa} \tanh \left[ \frac{-(E_a + E_o) - E_c}{2\beta} \right] - P_o \quad (14)$$

for the AFE-to-FE transitions.  $P_a$  and  $E_a$  were the AFE polarization and electric field, respectively, and  $\beta$  was again determined from Equation (7).  $|P_R|$ ,  $|P_{sa}|$  and  $|E_c|$  values for these hysteresis portions were obtained from experimental data assuming the local origins corresponded to zero polarization and zero electric field as shown in Figure 6. Equations (11) through (14), which describe the FE hysteresis portions of the AFE double loops, were separated by AFE linear regions defined by

$$P_a^\pm(E_a) = E_a \frac{dP_a}{dE_a} + P_a(0). \quad (15)$$

Linear regression analysis was performed on experimental linear region data to determine the slope of the P-E linear region,  $dP_a/dE_a$ , and the remanent polarization in the linear region,  $P_a(0)$ , with respect to the global origin. Two equations were derived to represent each AFE film— $P_a^+(E_a)$  for the positive domain switching cycle and  $P_a^-(E_a)$  for the negative cycle in the linear region. Equations (11) through (15) were utilized in their appropriate electric field ranges and superimposed in order to accurately depict experimental AFE hysteresis loop properties.

#### Comparison with Experimental Data

**FE/AFE Composites.** The calculated hysteresis loops for automatically spin coated F(x)A(10-x) composite thin films deposited on Pt/Si are displayed with the experimental hysteresis loops in Figure 7. In order to calculate these loops, Equation (4), using the  $P_a(E_a)$  and  $P_f(E_f)$  functions from experimental data fit of the pure FE and AFE films, and Equation (5) were solved simultaneously using Mathsoft Mathcad 3.1 resulting in  $E_a$  and  $E_f$  values corresponding to each input voltage data point ( $V_{tot}$ ) measured on the experimental composite film. These calculated  $E$  values were back-substituted into the polarization functions for the homogeneous films. Since the polarization in the FE and AFE layers as well as the total polarization were assumed to be equal, one of the polarization functions for each composite was plotted versus total composite film voltage in order to produce the modeled hysteresis properties.

As shown in Figure 7, the analytical modeling procedure yielded considerable agreement with the composite film experimental data. Although the modeled data for some of the composites did not converge in the high-field region shown, the model actually predicted this convergence at a higher field saturation region than shown. This lack of complete agreement between the model and the experimental

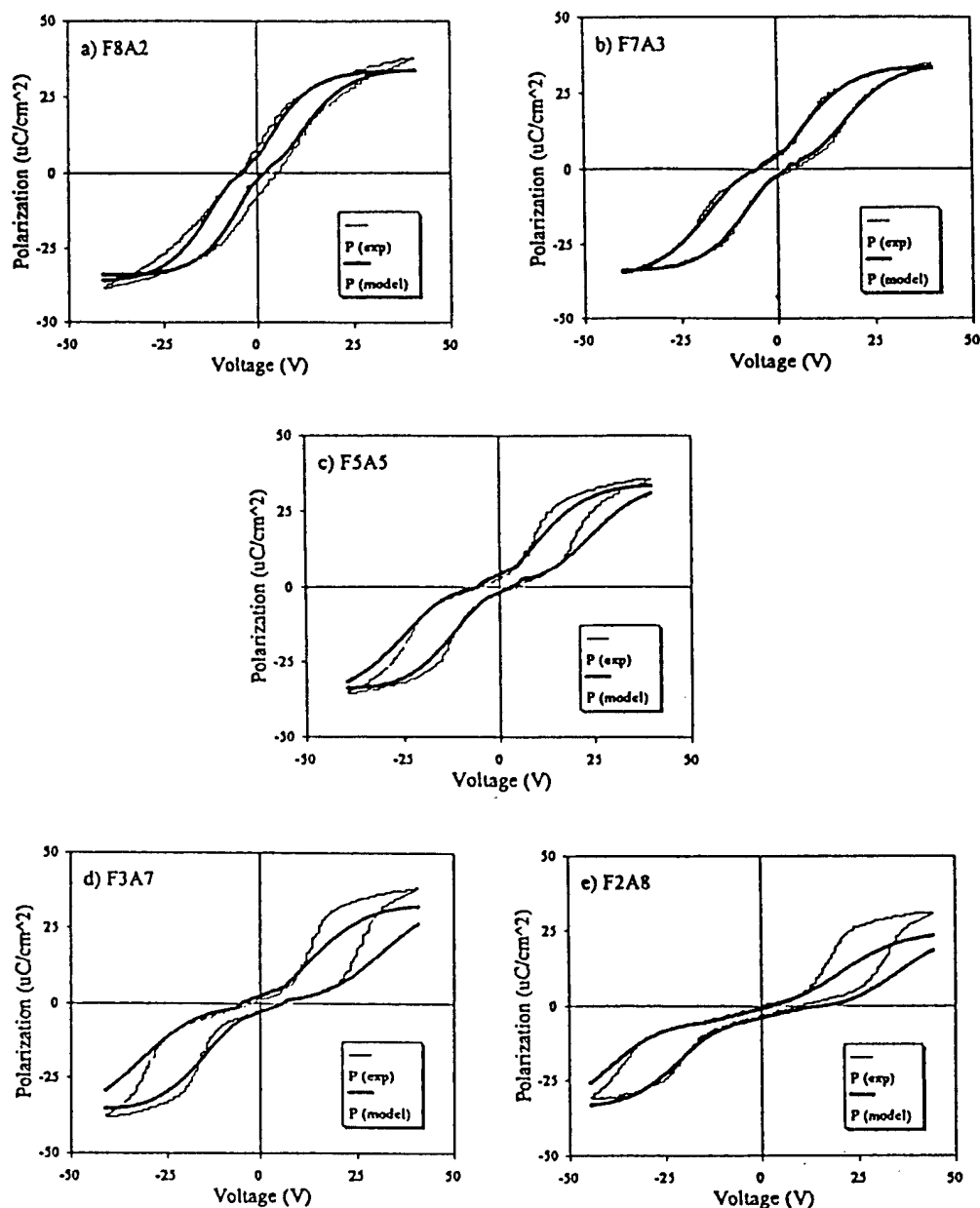


FIGURE 7. Hysteresis loop models for a) F8A2, b) F7A3, c) F5A5, d) F3A7 and e) F2A8 automatically spin coated composite thin films on Pt/Si consisting of FE 2/55/45 and AFE 0/100/0 compositions.

data is not surprising. In the composite structure, one of the electrode-dielectric interfaces is missing for each of the layers. Additionally, the coercive field is known to vary with film thickness, and the thicknesses of the individual composite layers and pure films were not equal.

The analytical models for the F8A2 and F7A3 composites corresponded fairly

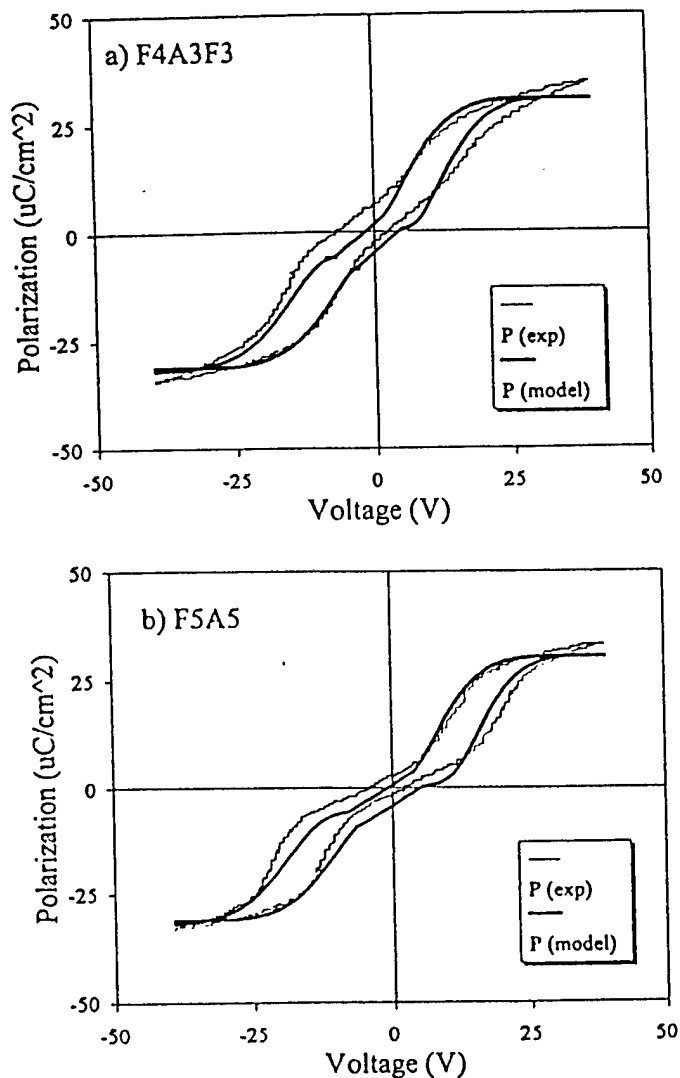


FIGURE 8. Hysteresis loop models for a) F4A3F3 and b) F5A5 manually spin coated composite thin films on Pt/Si consisting of FE 2/55/45 and AFE 0/100/0 compositions.

well with experimental results with the exception of a slightly higher  $E_C$  and  $P_R$  observed in F8A2 than predicted by the model. For the other composites, the modeled results accurately predicted the low-field linear polarization as well as the onset of the AFE-to-FE phase transitions; however, there was some discrepancy for high-field FE domain switching, especially in the F3A7 and F2A8 films. As was shown in the hysteresis properties as a function of temperature in Part I,<sup>1</sup> the presence of the FE layer in the composites significantly sharpened the AFE-to-FE phase transitions compared with the pure AFE films. It is apparent from this modeling work that not only did the addition of FE layer domain switching increase the squareness of the double hysteresis loops, but the AFE layer domain switching improved in these

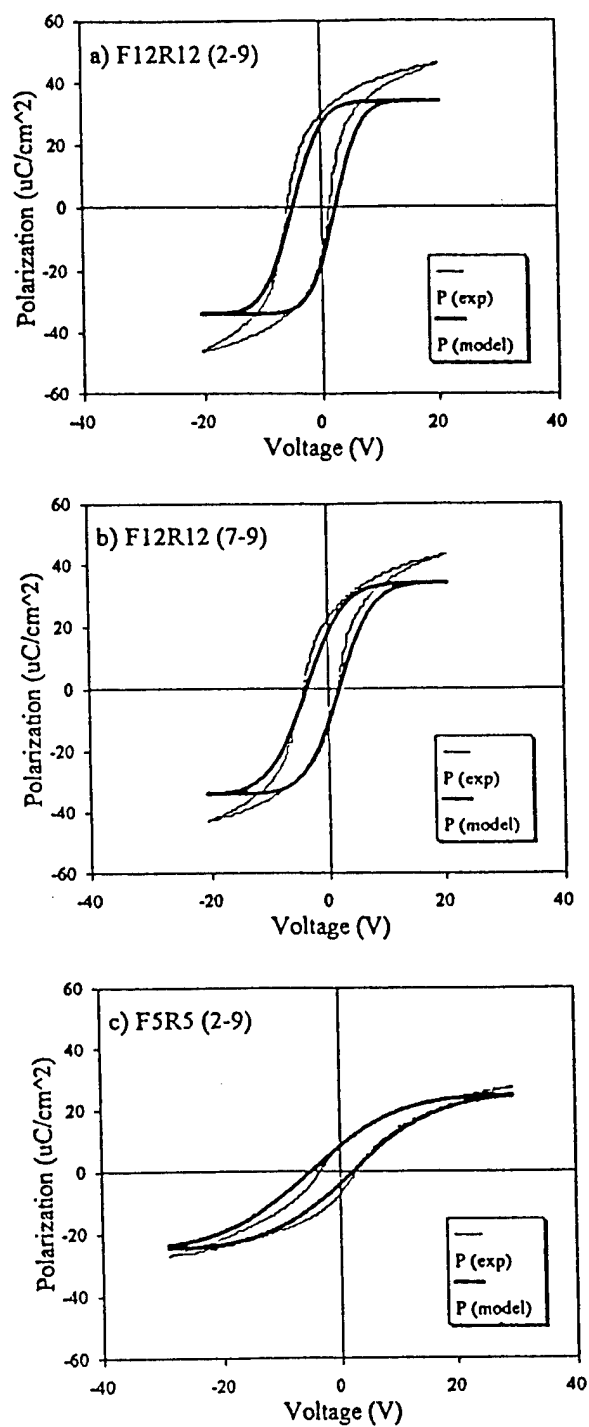


FIGURE 9. Hysteresis loop models for a) 2-9 F12R12 dip coated on Ag, b) 7-9 F12R12 dip coated on Ag and c) 2-9 F5R5 manually spin coated on Pt/Si (2 = 2/55/45, 7 = 7/65/35, 9 = 9.5/65/35 compositions).

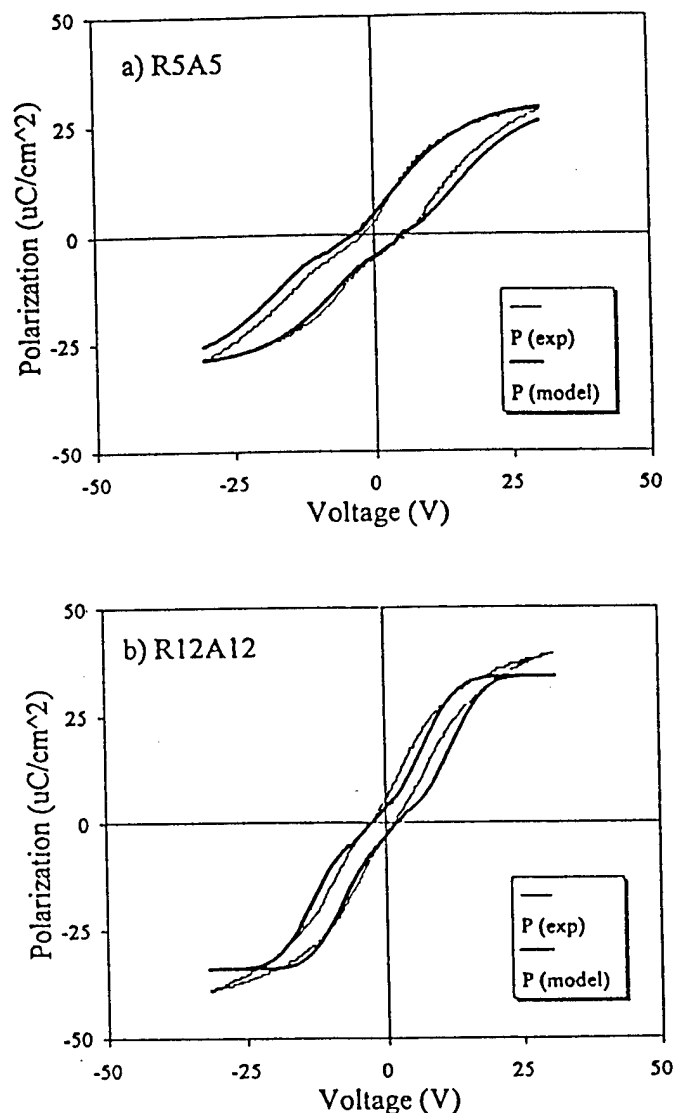


FIGURE 10. Hysteresis loop models for a) R5A5 consisting of AFE 0/96/4 and spin coated on Pt/Si and b) R12A12 consisting of AFE 0/95/5 and dip coated on Ag. The relaxor composition for both composites was 9.5/65/35.

composite structures. Since the model was based solely on the homogeneous AFE and FE experimental results, the fact that more square, better saturated hysteresis loops for the composite films were observed compared with the predicted model suggested that an improvement in AFE layer characteristics occurred. One possible explanation is that the AFE layers in the composite films were in different strain states from that of the pure AFE films. For these  $F(x)A(10-x)$  composite films, enhancement of the AFE-to-FE switching in the AFE layer as well as the ensuing FE

1. A linear series capacitor model accurately described the dielectric properties of composite films for low electric field conditions over wide frequency and temperature ranges.

2. Hysteresis modeling by amending the series model to include the hysteresis properties of the pure constituents and the non-uniform electric field distributions in the composite structures accurately predicted the AFE-to-FE and FE high-field domain switching properties of the composite thin film combinations.

3. The nonlinear series capacitor model predicted the hysteresis properties for the  $F(x)A(10-x)$  thin films; however, the squareness of the double loops in the saturation region for the F2A8 and F3A7 composites was not calculated by the model. This elucidated further the improved domain switching properties in the AFE layer of the composites which was not observed in the homogeneous AFE film used in the model.

4. FE/relaxor and relaxor/AFE composite models accurately predicted the  $E_C$  and  $P_R$  values observed experimentally. An inclusion of a linear polarization term in the model may improve the experimental fit of FE and relaxor film data and modeling of the saturation behavior in these composites.

With this modeling technique, the hysteresis properties of any composite film combination can be predicted provided the experimental properties of the individual homogeneous components in the structure are known; hence, this procedure should be beneficial for the design of composite film devices. Once the desired compositions or range of compositions are chosen for composite fabrication, numerous combinations of composite structures with varying composition and volume % of the constituents can be modeled. A composite, then, with suitable dielectric and/or hysteresis properties can be selected for a proposed application while avoiding the manufacture of superfluous samples with undesirable properties. A similar technique could also be applied for bulk ceramic/ceramic composites for electronic applications which typically require more difficult and time consuming fabrication techniques.

#### ACKNOWLEDGEMENT

This work was supported by ONR under contract no. N00014-94-1-0563.

#### REFERENCES

1. D. E. Dausch, E. Furman, F. Wang and G. H. Haertling, submitted to *Ferroelectrics* (1995).
2. T. Shrout, W. A. Schulze and J. V. Biggers, *Ferroelectrics*, **29**, 129 (1980).
3. T. R. Shrout, W. A. Schulze and J. V. Biggers, *Ferroelectrics*, **34**, 105 (1981).
4. D. A. Payne and L. E. Cross, in "Microstructure and Properties of Ceramic Materials," ed. T. S. Yen and J. A. Pask, Science Press, Beijing, 1991, pp. 380–390.
5. M. Sayer, A. Mansingh, A. K. Arora and A. Lo, *Integrated Ferroelectrics*, **1**, 129 (1992).
6. D. E. Dausch, Ph.D. Dissertation, Clemson University, Clemson, SC, 1995.
7. S. L. Miller, R. D. Nasby, J. R. Schwank, M. S. Rodgers and P. V. Dressendorfer, *J. Appl. Phys.*, **68**, 6463 (1990).
8. F. K. Chai, J. R. Brews, R. D. Schrimpf and D. P. Birnie III, presented at the 9th IEEE International Symposium on Applications of Ferroelectrics, University Park, PA, 1994.

## FABRICATION AND PROPERTIES OF PSZT ANTIFERROELECTRIC RAINBOW ACTUATORS

G. LI, E. FURMAN and G. H. HAERTLING

*Department of Ceramic Engineering, Clemson University, SC 29634-0907, USA*

*(Received January 25, 1996)*

A new type of high-displacement actuator called Rainbow (Reduced And Internally Biased Oxide Wafer) was recently developed, and it shows promising characteristics in a variety of potential applications. The fabrication and properties of Rainbow actuators from PSZT antiferroelectric ceramics with compositions near the antiferroelectric-ferroelectric (AFE-FE) phase boundary were investigated. It was found that the chemical reduction reaction proceeded much more rapidly in PSZT than in PLZT ceramics. The optimum conditions for the processing of PSZT Rainbows were determined to be 850°C for 2–3 hours. Large axial displacements ranging from 102 to 273  $\mu\text{m}$  were obtained from the PSZT Rainbow samples by application of electric fields greater than the AFE-to-FE phase switching levels. The characteristics of the field-induced displacements of the Rainbow samples were dependent on the manner of applying mechanical load on the samples. At room temperature, the antiferroelectric PSZT Rainbows exhibited a concave curvature with respect to the oxide side, which was attributed to the cubic-to-antiferroelectric phase transition in the oxide layer during cooling. The dielectric and AFE-FE phase transition properties of the Rainbow samples were compared with those of the normal ceramics.

*Keywords: Antiferroelectric ceramic, actuator, chemical reduction, ferroelastic domain, internal stress.*

### 1. INTRODUCTION

During the past several years actuators based on ferroelectric ceramic materials have received numerous investigations and undergone remarkable advances.<sup>1</sup> Ceramic actuators offer many advantages including quick response, high induced stress, low energy consumption and low cost which make them very attractive for a number of newer applications. When exposed to an external electric field, a ferroelectric ceramic will change its dimensions through ferroelectric domain reorientation and the intrinsic piezoelectric effect. If the ceramic is in the antiferroelectric state, strains will be developed when the antiferroelectric state is switched to the ferroelectric state under a sufficiently high applied electric field. Since the unit cell of the antiferroelectric state is generally much smaller than that of the ferroelectric state, a significant change in volume occurs during the antiferroelectric-ferroelectric transition. The field-induced dimensional changes in ferroelectric materials provide a useful mechanism for actuation application.

The electric field-induced strains from ferroelectric ceramics are relatively small although the induced stress can be substantial. They are only a few tenths of one percent for most of the compositional systems. This disadvantage considerably limits their use on advanced applications such as active structures, linear motors, cavity pumps and noise-cancelling devices that require a relatively large physical displacement. To achieve a higher displacement from the ceramics, a number of strain magnification mechanisms have been employed. Examples include the traditional uni-

morph and bimorph benders,<sup>2</sup> and the more recent "moonie" structure.<sup>3</sup> A bender is able to transform a small transverse strain of the ceramic into a large displacement in the longitudinal direction, while a "moonie" composite utilizes both the transverse and longitudinal strains in producing a larger axial displacement. Generally, a significant trade-off exists between induced displacement and stress for these structures. That is, an increase of induced displacement is achieved at the expense of lowering generated stress significantly. There is, therefore, a need for mechanisms that can provide large displacements while still sustaining reasonable load or stress. This criterion has been met, to great extent, by a new type of stress-biased, oxide-reduced composite ceramic wafer which was recently developed.<sup>4</sup> Designated as Rainbow (Reduced And Internally Biased Oxide Wafer), the ceramic wafer is obtained via chemical reduction of one major surface of a high lead-containing ferroelectric wafer, such as PLZT, by placing the wafer on a flat carbon block and heat treating it at an elevated temperature. As the partially reduced ceramic wafer is cooled to room temperature, a dome-shaped (sometimes saddle-shaped), internally stressed oxide (unreduced)-reduced layer structure is formed. Very high axial displacement is obtainable from an electroded Rainbow sample by application of an electric field across the ceramic oxide layer. Also, due to the unique dome structure, a Rainbow can sustain a stress higher than normal. Rainbow ceramics have shown promising characteristics for a variety of potential applications.<sup>4-6</sup>

It has been found that the  $\text{Pb}(\text{Sn,Zr,Ti})\text{O}_3$  (PSZT) ceramics with compositions in the vicinity of the FE-AFE phase boundary exhibit very high field-induced strains resulting from the transition from the AFE to the FE state.<sup>7,8</sup> A longitudinal strain of 1.1% (the highest ever reported in the literature for ferroelectric ceramics) was claimed in the PSZT system in a study by Shebanov *et al.*<sup>8</sup> Furthermore, the strain characteristics of these ceramics can be modified through selection of appropriate compositions.<sup>9</sup> For example, a PSZT ceramic may have a shape-memory effect similar to some alloys or digital-like strain characteristics depending on the location of its composition in the phase diagram. Ceramics with specific compositions in the AFE phase region near the AFE-FE phase boundary are easily switched to the ferroelectric state by application of an electric field and remain ferroelectric upon removal of the field. As a result, a shape-memory effect is achieved. The AFE compositions distant from the phase boundary exhibit well-defined AFE characteristics with the digital-like strain characteristics under applied electric fields. A number of possible applications have been proposed to utilize the strain properties of the PSZT ceramics.<sup>9-11</sup>

The objective of this work was to combine the high induced strains of PSZT ceramics with the Rainbow technology to produce high-displacement actuators. In this paper, the fabrication and properties of PSZT antiferroelectric Rainbow actuators with compositions in the vicinity of the FE-AFE phase boundary are described.

## 2. SAMPLE PREPARATION

Bulk PSZT ceramics used for the fabrication of the Rainbow samples were prepared according to the formula  $\text{Pb}_{0.97}\text{La}_{0.02}(\text{Zr}_x\text{Sn}_y\text{Ti}_z)\text{O}_3$ . The samples studied are designated as PSZT X/Y/Z or Rainbow X/Y/Z in the following discussion, where the X,



TABLE I  
Diameter and oxide/reduced thickness ratio of PSZT  
Rainbow samples

Rainbow Sample	Diameter (cm)	Oxide/Reduced ( $\mu\text{m}$ )
66/23/11HP	2.72	302/135
64/26/10HP	2.72	294/135
64/26/10S	2.16	378/140
66/23/11S	2.16	271/190
66/24/10S	2.72	334/165
62/28/10S	2.16	195/165

HP=hot-pressed; S=sintered.

Y and Z are the molar percentage of Zr, Sn and Ti ions in the B site of the perovskite structure, respectively. The letters, HP or S, are also added to the Rainbow designation to indicate that the sample is made from hot-pressed or sintered ceramics. For example, Rainbow 64/26/10S represents a Rainbow made from a sintered PSZT 64/26/10 (Zr/Sn/Ti) wafer. A number of compositions near the AFE-FE phase boundary which were reported to have the highest field-induced strains were selected. Reagent grade  $\text{PbO}$ ,  $\text{ZrO}_2$ ,  $\text{TiO}_2$ ,  $\text{SnO}_2$  and  $\text{La}_2\text{O}_3$  were used as the starting materials. Weighed components were mixed in distilled water for 30 minutes and dried at  $105^\circ\text{C}$  overnight. The dried powders were calcined at  $925^\circ\text{C}$  for 2 hours, and then milled for 8 hours in trichloroethylene using a polyethylene jar and  $\text{ZrO}_2$  balls. Bulk ceramics were obtained either by sintering sample pellets at  $1280\text{--}1320^\circ\text{C}$  for 4 hours or by hot pressing the pellets at  $1200^\circ\text{C}$  for 6 hours at 14 MPa in an oxygen atmosphere. The sintered ceramic slugs were cut and lapped into wafers of various diameters and thicknesses.

In the fabrication of Rainbow samples, a PSZT wafer was chemically reduced on one of the major surfaces by placing the wafer on a graphite block and introducing the assembly into a preheated furnace. A zirconia disk was placed on top of the PSZT wafer to prevent possible thermal shock during processing. After the reduction, the wafer together with the graphite block was removed from the furnace and cooled down in air to room temperature. Epoxy silver electrodes cured at  $200^\circ\text{C}$  were used for determination of the Rainbow's electrical properties. The dimensions of the Rainbow samples are shown in Table I. Samples with two different diameters of 2.16 and 2.72 cm were studied.

### 3. MEASUREMENTS

The crystalline phases of reduced PSZT ceramics were examined with an X-ray diffractometer (Scintag XDS 2000<sup>TM</sup>) using  $\text{Cu K}\alpha$  radiation at a scan rate of 2 degrees per minute. The thicknesses of the reduced layer of the Rainbows were measured from the sample cross-sections by means of an optical microscope. Room temperature dielectric properties of the samples were determined at 1 kHz on an LCR meter (LEADER, 7450-01). Conventional dc hysteresis loop equipment was

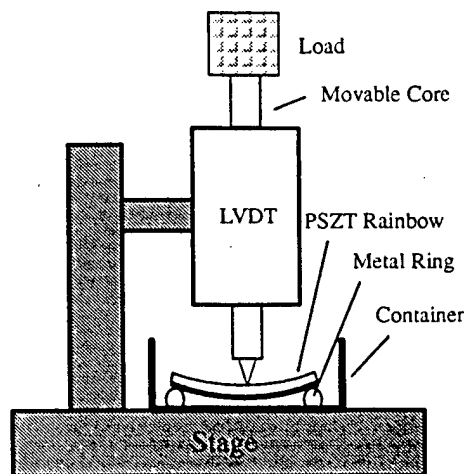


FIGURE 1 Schematic of apparatus for displacement measurement (not to scale).

employed to measure the relationship between polarization and electric field. Electric fields greater than the AFE-to-FE phase transition levels were applied gradually to the samples.

A measuring setup with an LVDT (Linear Variable Differential Transformer, 050 DC-E Lucas Schaeritz Co.), as seen in Figure 1, was used to determine the change of the field-induced displacement with electric field and the change of the dome height of a Rainbow with temperature. A Rainbow sample with electrodes on its major surfaces was placed on a metal ring in a small container. The ring supported only the edge of the sample so that the center part of the Rainbow could move up and down without touching the bottom of the container. The container was filled with silicon oil for insulating and temperature control purposes. The movable core of the LVDT was adjusted to contact the center of the Rainbow sample.

Mechanical loading on the Rainbow samples was accomplished by placing weights on top of the LVDT movable core. The variations of polarization and axial displacement with electric field were measured simultaneously as the samples were loaded.

#### 4. RESULTS AND DISCUSSION

##### 4.1. Chemical Reduction of PSZT Ceramics

Temperature is an important factor in controlling the reduction process during fabrication of Rainbow samples. For PLZT ferroelectric ceramics (the most frequently used Rainbow materials), the optimal reduction temperature was around 975°C. It was found that the reduction reaction was considerably more rapid in PSZT than in PLZT ceramics. A significantly thicker reduced layer in a PSZT than in a PLZT ceramic was produced when they were reduced at the same temperature for a given time. Figure 2(a) shows the reduced layer thickness of a PSZT Rainbow as a function of reduction temperature for a time of one hour. The thickness of the reduced layer began to increase rapidly at about 875°C, and tended to saturate at higher tempera-

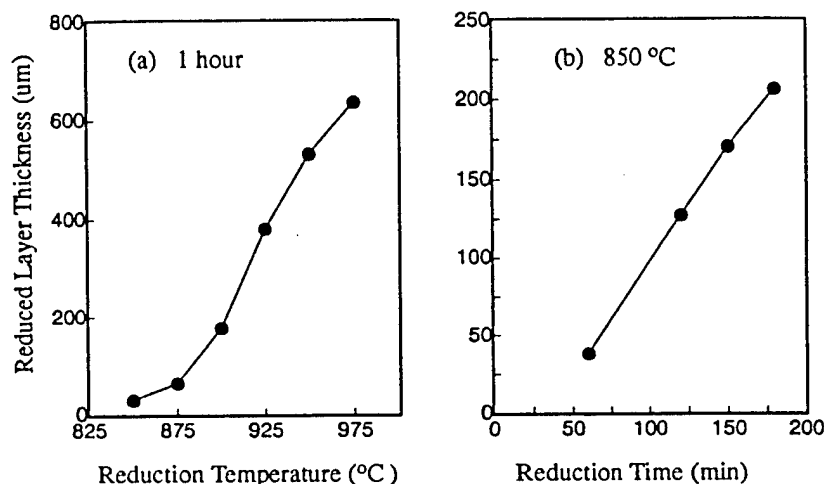


FIGURE 2 Variations of reduced layer thickness with (a) reduction temperature and (b) reduction time for PSZT Rainbow 64/26/10HP.

tures. An approximately 650  $\mu\text{m}$  thick reduced layer was created in the PSZT sample at 975°C, as compared to the 150  $\mu\text{m}$  thick reduced layer in a typical PLZT Rainbow obtained under identical conditions. Further manifestation of the rapid reaction in PSZT ceramics is the enhanced reoxidation of the reduced layers observed at elevated temperatures. For example, a reduced layer 200  $\mu\text{m}$  thick was completely reoxidized almost instantaneously when exposed to air at a temperature used for the reduction. The reasons for the severe reactions occurring in PSZT ceramics have not been fully determined, but they seem to be related to the multivalent nature of the Sn.

Reduction time is another important factor that influences the reduction process. Figure 2(b) shows the change of the reduced layer thickness with time at a constant temperature of 850°C for hot-pressed PSZT 64/26/10. A nearly linear relationship was observed.

Although the reduction reaction is very rapid in PSZT ceramics, the reduction of the PSZT phase, unlike that of PLZT, was found to be incomplete. Figure 3(a) shows the X-ray diffraction pattern from a PSZT sample reduced at 975°C. Even at this high temperature a significant amount of the original PSZT phase remained in addition to the oxide phases such as PbO (massicot),  $\text{ZrO}_2$ ,  $\text{ZrTiO}_4$ , and  $\text{SnO}_2$  which resulted from the reduction process. At 975°C, the rapid reaction led to precipitation of a large amount of lead phase on the sample surface. With the additional loss of lead phase due to reoxidation during cooling, metallic lead was nearly absent from the reduced region. The diffraction pattern in Figure 3(a) was obtained after removal of the lead particles from the surface, and hence the diffraction peaks of the lead phase were not observed. Figure 3(b) shows the X-ray diffraction pattern from a sample reduced at a relatively low temperature of 850°C. At this temperature, only metallic lead and the original PSZT phases are evident, and the lead phase was uniformly distributed within the reduced layer.

As mentioned above, at a high temperature such as 975°C, the rapid reaction in PSZT ceramics leads to the loss of a large portion of lead phase from the reduced region. As a result, the reduced region has poor electrical conductivity or even be-

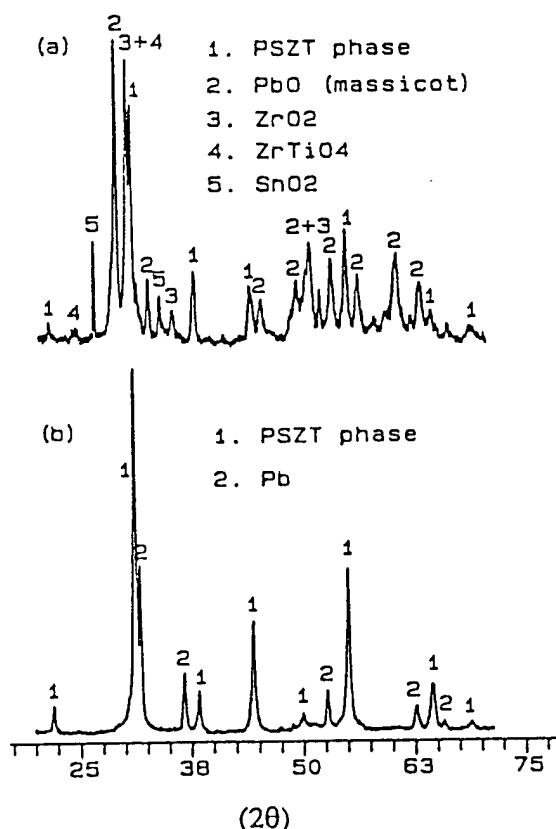


FIGURE 3 X-ray diffraction patterns of PSZT 64/26/10 ceramics reduced at (a) 975°C and (b) 850°C.

comes an insulator. This is detrimental to the performance of Rainbow actuators since the reduced layer must be electrically conductive in order for a Rainbow to operate properly. To prevent the heavy loss of the lead phase from occurring, lower reduction temperatures must be used. However, a very low temperature implies impractical and long reduction times. It was found that the useful temperature range for the production of PSZT Rainbows is actually very narrow, approximately  $850 \pm 30^\circ\text{C}$ . The optimal conditions for producing Rainbow samples from PSZT ceramics were determined to be 850°C for 2–3 hours.

#### 4.2. Properties of PSZT Antiferroelectric Rainbows

Figure 4 shows the polarization (P)-electric field (E) hysteresis loop of Rainbow 64/26/10HP. The hysteresis loop of a normal (non-Rainbow) sample is also given in the figure for comparison. Significant differences between the two loops are seen. First, a finite net polarization  $\Delta p$ , indicating a partially poled ferroelectric state of the sample, was found to exist in the virgin state of the Rainbow sample. This phenomenon, which was also observed in ferroelectric PLZT Rainbows,<sup>12</sup> is believed to be associated with the nonuniform internal stress in Rainbows. Second, the AFE-to-FE phase switching in the Rainbow occurred at a much lower field level and was

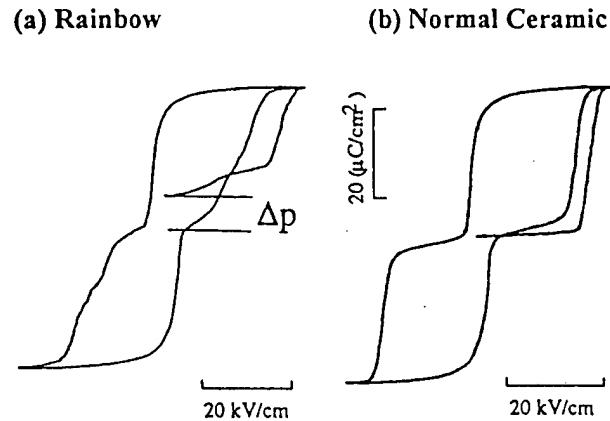


FIGURE 4 Polarization-electric field hysteresis loops of Rainbow 64/26/10HP and normal (non-Rainbow) PSZT 64/26/10 ceramic.

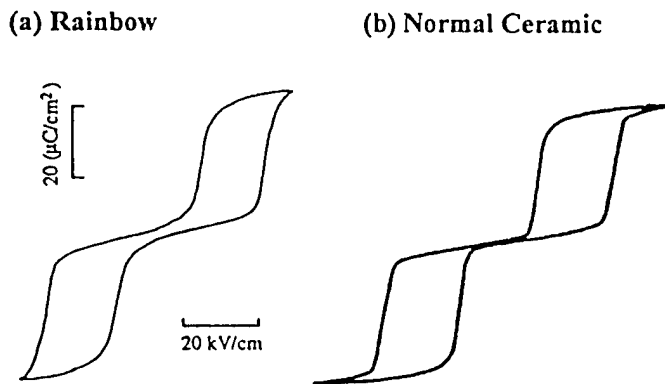


FIGURE 5 Polarization-electric field hysteresis loops of Rainbow 66/24/10S and normal PSZT 66/24/10.

less abrupt compared to the normal sample. Since the composition of PSZT 64/26/10 is located near the AFE-FE phase boundary, an intermediate P-E hysteresis loop characteristic of the two phases, namely a double hysteresis loop with an appreciable remanent polarization, was observed.

The hysteresis loops of Rainbow 66/24/10S and the corresponding normal sample are shown in Figure 5. Because the composition is well inside the AFE phase region, a typical double hysteresis loop with no remanent polarization is seen for the normal sample. The marginal remanent polarization observed in the Rainbow was probably caused by the internal stress, which will be discussed later.

Figure 6 shows the variation of axial displacement with electric field for Rainbows 64/26/10HP and 66/24/10S. A displacement as large as  $273 \mu\text{m}$  was obtained from Rainbow 64/26/10HP accompanying the AFE-FE phase switching. The remanent displacement at zero field was attributable to the remanent polarization as shown in Figure 4(a). Rainbow 66/24/10S also exhibited a large axial displacement resulting from the phase switching, but little remanent displacement was found to exist. The step-like displacement-field relationship of Rainbow 66/24/10S was similar to the field-induced strain curve of the normal sample as indicated in Figure 7.

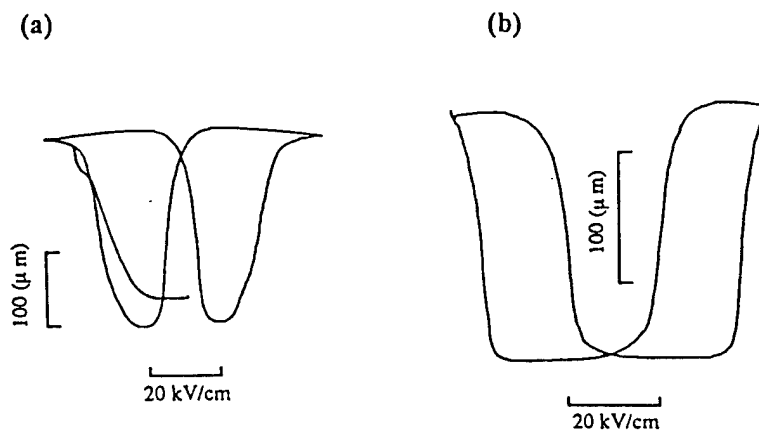


FIGURE 6 Change of axial displacement with electric field for (a) Rainbow 64/26/10HP and (b) Rainbow 66/24/10S.

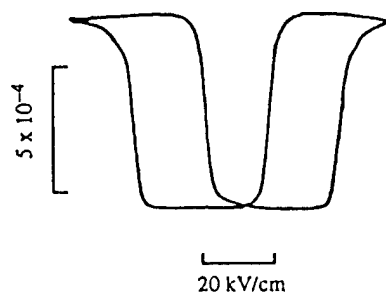


FIGURE 7 Change of transverse strain of PSZT 66/24/10 ceramic with electric field.

The axial displacement- and polarization-electric field relationships of Rainbow 66/23/11HP are given in Figure 8. Of the antiferroelectric samples studied, this sample is closest to the FE phase region. As can be seen in the figure, Rainbow 66/23/11HP is antiferroelectric in the virgin state, but stabilized into the ferroelectric state after being switched by the applied electric field. A large displacement, approximately  $145\text{ }\mu\text{m}$ , was produced during the initial AFE-to-FE phase switching. The reorientation of ferroelectric domains after the initial phase transition led to a butterfly-like loop of typical ferroelectrics and moderate changes in the displacement.

Tables II and III summarize the properties obtained from the PSZT Rainbows and normal ceramics, respectively. The Rainbow samples, in general, possessed a lower dielectric constant and a higher loss factor than the normal samples. The phase switching fields,  $E_{AF}$  and  $E_{FA}$ , of the Rainbow samples were lower than those of the normal ceramics, varying with composition. The saturated polarization, however, was similar in the Rainbows and the normal samples. The total field-induced axial displacement of the Rainbows due to the phase transitions varied from sample to sample and was in the range of 102 to  $273\text{ }\mu\text{m}$  depending on the geometry as well as the material properties of both the oxide and reduced layers. The largest displacement was found in Rainbow 64/26/10HP, which is equivalent to a strain of 0.63 relative to the total thickness of the sample. This is over 200 times larger than the longitudinal strain of the corresponding normal ceramic.

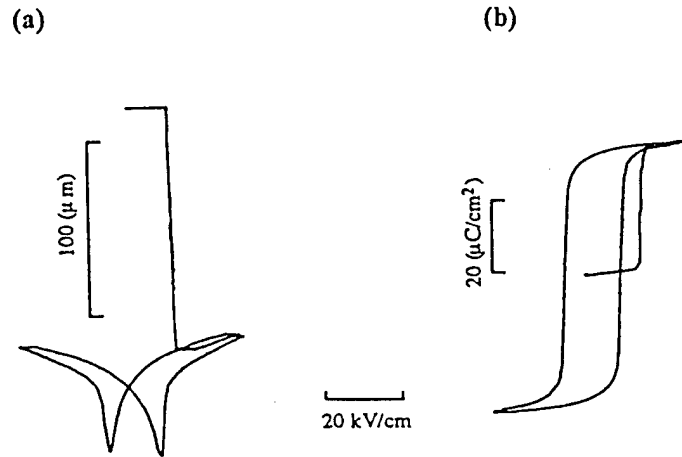


FIGURE 8 Variations of axial displacement and polarization with electric field for Rainbow 66/23/11HP.

TABLE II  
Properties of PSZT Rainbow samples

Rainbow Sample	Dielectric Constant	$\tan\delta$ (%)	$E_{AF}/E_{FA}$ (kV/cm)	$P_S$ or $P_R$ ( $\mu\text{C}/\text{cm}^2$ )	$y_M$ ( $\mu\text{m}$ )	$S_M$ (%)
66/23/11HP	796	2.2	7.5 ( $E_C$ )	35	195*	45
64/26/10HP	730	3.4	19.5/-4.0	33	273	63
64/26/10S	821	3.9	16.5/-3.0	30	187	37
66/23/11S	734	3.1	7.0 ( $E_C$ )	31	102*	22
66/24/10S	626	5.4	28.5/10.0	31	208	42
62/28/10S	826	2.3	27.5/6.5	31	110	31

The effects of axial mechanical loading on the field-induced displacement and P-E hysteresis loops of Rainbow 66/24/10S are shown in Figures 9 and 10 for loads applied to the surfaces of the oxide and reduced layers, respectively. The maximum displacement from each displacement-electric field loop was determined, and plotted against loading in Figure 11. Clearly, the displacement characteristics of the Rainbow are dependent on the manner in which load is applied. There is only a slight change in the displacement up to 570 grams when load was placed on the oxide layer. The displacement with load on the reduced layer, however, decreased continuously with increasing loading. In both cases, it was found that loading has no significant influence on the polarization-electric field hysteresis loop. It is obvious that a PSZT Rainbow is more advantageous when operated with loading on the oxide side.

The different characteristics under the two loading conditions just discussed may be accounted for by the behavior of ferroelastic domains under stress. Ferroelastic domains tend to be in line with the directions in which stress is effectively relieved. When load is applied vertically to the oxide layer surface of a Rainbow, ferroelastic domains are preferably aligned parallel to the surface due to the compressive stress in the planar directions produced by the loading. This occurs because the lattice

TABLE III  
Properties of PSZT normal (non-Rainbow) ceramics

Normal PSZT	Dielectric Constant	$\tan\delta$ (%)	Density ( $\text{g}/\text{cm}^3$ )	$E_{AF}/E_{FA}$ (kV/cm)	$P_S$ or $P_R$ ( $\mu\text{C}/\text{cm}^2$ )	$S_{2,S}$ ( $\times 10^4$ )	$S_{1,S}$ ( $\times 10^4$ )
66/23/11HP	810	2.3	8.11	7.0 ( $E_C$ )	35	5.5	45.2*
64/26/10HP	876	1.6	8.22	23/-2.0	36	6.8	29.5
64/26/10S	913	1.9	8.05	28/1.0	31	7.9	28.0
66/24/10S	990	1.2	7.93	30/11.5	31	8.2	45.3
62/28/10S	882	1.9	7.97	30/9.5	32	8.5	45.7

$E_{AF}$  = Antiferroelectric to ferroelectric switching field.

$E_{FA}$  = Ferroelectric to antiferroelectric switching field.

$P_S$  = Saturated polarization.

$P_R$  = Remanent polarization.

$E_C$  = Coercive field.

$y_M$  = Maximum axial displacement with an applied electric field of  $1.2 \times E_{AF}$ .

$S_M$  = Maximum axial displacement ( $y_M$ ) divided by Rainbow thickness.

$S_{2,S}$  = Transverse field-induced strain.

$S_{1,S}$  = Longitudinal field-induced strain.

\* obtained from initial phase switching.

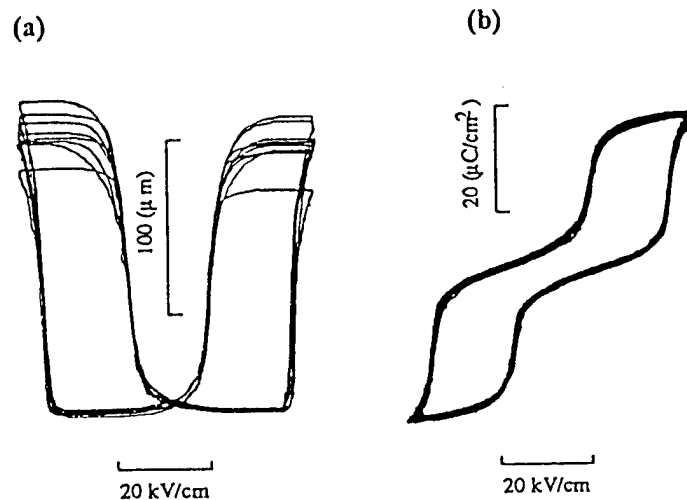


FIGURE 9 Influence of axial mechanical loading on (a) field-induced axial displacement and (b) hysteresis loop of Rainbow 66/24/10S for loads on the oxide layer.

constant of the  $c$ -axis (antipolar direction) is smaller than that of the  $a$ -axis for the PSZT antiferroelectric phase.<sup>8</sup> Similarly, when load is placed on the reduced layer, ferroelastic domains tend to be oriented vertical to the surface as a result of planar tensile stress. These situations are schematically depicted in Figure 12. Since the axial displacement of a Rainbow is dictated by the field-induced transverse strain in the oxide layer, a larger transverse strain should represent a larger axial displacement. Due to the different states of preferential domain alignment under the two loading conditions, different transverse strains occur under an identical applied electric field. As is shown in Figure 12, a sample with load applied to the oxide layer will exhibit



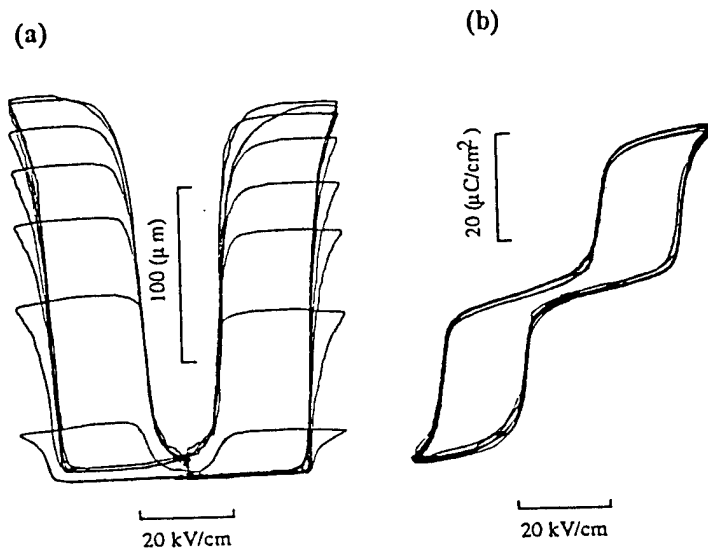


FIGURE 10 Influence of axial mechanical loading on (a) field-induced axial displacement and (b) hysteresis loop of Rainbow 66/24/10S for loads on the reduced layer.

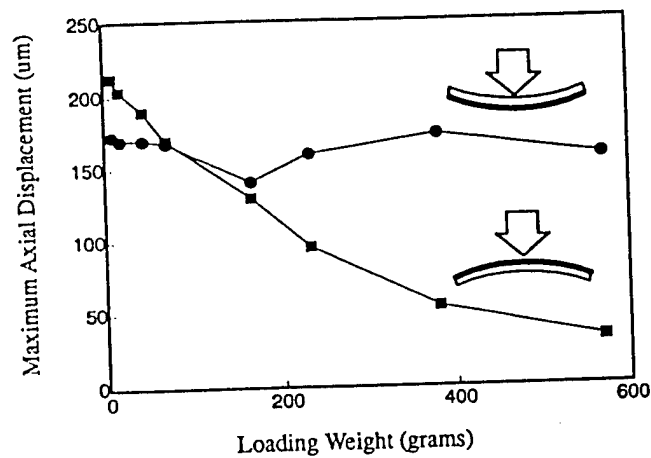


FIGURE 11 Variation of maximum axial displacement with loading for Rainbow 66/24/10S, ● for load on oxide layer and ■ for load on reduced layer.

a larger field-induced displacement than one with load applied to the reduced layer. It should be pointed out that the geometrical stiffness (e.g., the reduced/unreduced layer thickness ratio and the ratio of the total thickness to diameter), dome curvature and initial internal stress of a Rainbow also have influences on the characteristics of displacement versus loading. The combined effects of the geometrical stiffness, curvature and domain alignment lead to the variations of the displacements indicated in Figure 11. Because ferroelastic domains are not polar, the domain alignment under stress will not affect the P-E hysteresis loop, which is in good agreement with the experimental observations.

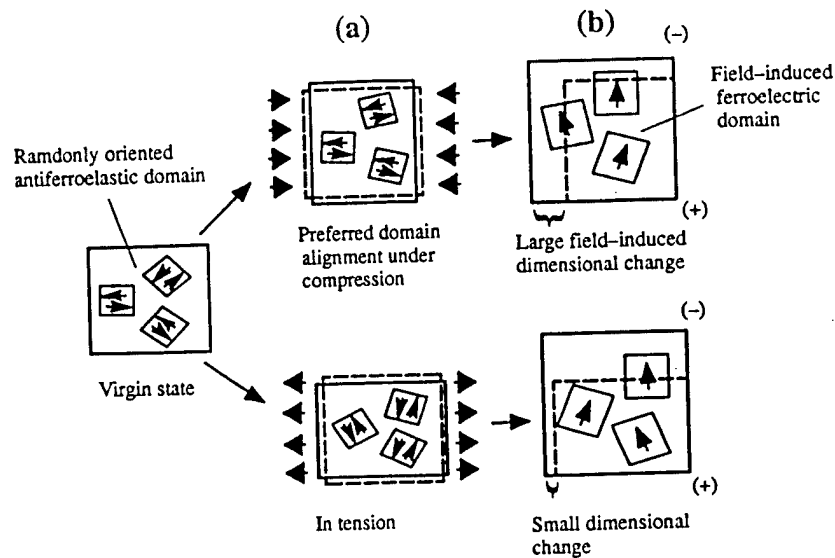


FIGURE 12 Schematic diagram of the transverse dimensional change in the oxide layer due to load-induced stresses and electric field. Dashed lines in (a) and (b) represent the shape of a portion of the oxide layer prior to the application of mechanical loading and electric field, respectively.

#### 4.3. Curvature and Internal Stress of PSZT Rainbows

At room temperature, a typical Rainbow possesses a dome-shaped configuration and an internal stress field as a result of the dimensional mismatch between the oxide and reduced layers produced during processing. Note that the internal stress refers to the stress inside a free Rainbow and is distinguished from the stresses created by loading as described earlier. Many of the characteristics of Rainbows have been found to be closely related to this dome structure and internal stress. The major contributions to the dimensional mismatch are considered to include: (1) the difference in thermal expansion coefficient between the oxide and reduced layers, (2) the dimensional change of the reduced layer due to oxygen (and possibly lead) loss, and (3) the dimensional change of the oxide layer resulting from phase transitions. Generally, Rainbow samples made of ferroelectric ceramics have a concave curvature with respect to the reduced side, which is defined as positive curvature. It was found that all the PSZT Rainbows prepared in this study exhibited a negative curvature, i.e. the reduced side is convex. Negative curvature implies that the oxide layer of a virgin Rainbow is predominantly, or completely, in tension depending on the reduced/unreduced layer ratio. If the composition of a PSZT Rainbow is close to the AFE-FE phase boundary, the internal tensile stress is sufficient to induce a change from the antiferroelectric to ferroelectric phase. The net polarization observed in virgin Rainbow 64/26/10HP and the reduction of the AFE-FE switching fields in the PSZT Rainbows with respect to normal ceramics are probably the consequences of this tensile stress.

The results in Figure 13 are presented to show that the negative curvature in the PSZT Rainbows is attributable to the cubic-to-AFE phase transition. Specifically, the curvature with the concave oxide layer is caused by the fact that the reduction in

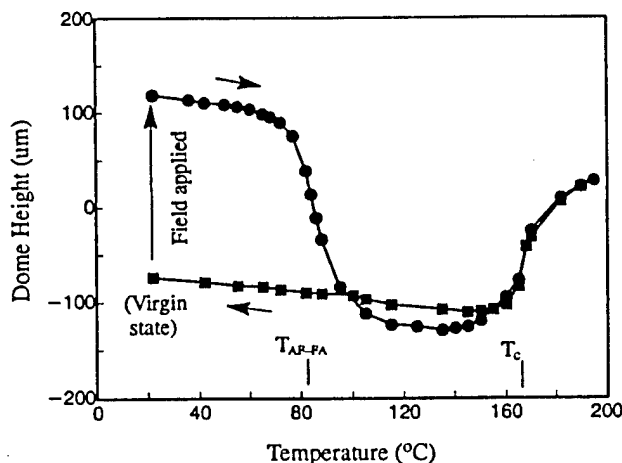


FIGURE 13 Changes of the dome height with temperature for Rainbow 66/23/11HP.

the dimensions of the oxide layer at the cubic-to-AFE phase transition exceeds the dimensional reduction of the reduced layer during cooling of a sample to room temperature. The dome height shown in Figure 13 is defined as the axial height of a Rainbow with respect to the unreduced wafer. Positive dome height corresponds to positive curvature. The curvature of Rainbow 66/23/11HP, which is antiferroelectric, was seen to change from negative to positive when the Rainbow was switched from the virgin antiferroelectric to ferroelectric state by an applied electric field. As the temperature was increased, the positive curvature changed back to a negative value at the FE-to-AFE phase transition  $T_{\text{FE-AFE}}$ . The curvature remained negative within the AFE phase range and became positive again near the Curie point. The reduction of temperature brought the sample back to the original antiferroelectric state and thus a negative curvature, as is indicated in Figure 13. All these clearly show that the antiferroelectric state is responsible for the negative curvature of PSZT Rainbows.

## 5. CONCLUSION

The fabrication and properties of PSZT antiferroelectric Rainbow actuators have been investigated. The reduction reaction in PSZT ceramics proceeds much more rapidly than in PLZT ceramics. The optimal reduction conditions for the fabrication of PSZT Rainbows are 850°C for 2–3 hours. The antiferroelectric-ferroelectric phase transitions occur at a lower field strength in Rainbows as compared to normal ceramics. Large axial displacements in a range of 102 to 273  $\mu\text{m}$  were obtained from the Rainbow samples by application of electric fields exceeding the phase switching levels. The field-induced displacements of the PSZT Rainbows are dependent on the manner of applying load to the samples. When load is placed on the oxide layer, there is only a slight change in the displacements for loads up to 570 grams. The displacement with load on the reduced layer, however, decreases markedly with increasing load. This behavior can be explained by the preferential alignment of

ferroelastic domains under stress. Antiferroelectric PSZT Rainbows generally have negative curvature at room temperature due mainly to the paraelectric to antiferroelectric phase transition in the oxide layer during cooling. The changes of material properties of PSZT Rainbows with respect to normal ceramics are associated with the internal stress resulting from processing.

#### ACKNOWLEDGEMENT

This work was supported by NASA under grant No. NAG-1-1301.

#### REFERENCES

1. K. Uchino, in Proceedings of the Ninth IEEE International Symposium on Applications of Ferroelectrics, pp. 319-324, 1994.
2. J. M. Herbert, "Ferroelectric Transducers and Sensors," Gordon and Breach Science Publishers, New York, 1982, Chap. 6, pp. 227-243.
3. Y. Sugawara, K. Onitsuka, S. Yoshikawa, Q. Xu, R. E. Newnham and K. Uchino, *J. Am. Ceram. Soc.*, **75**, 996 (1992).
4. G. H. Haertling, *Am. Ceram. Soc. Bull.*, **73**, 93 (1994).
5. S. Sherrit, H. D. Wiederick, B. K. Mukherjee and G. H. Haertling, in Proceedings of the Ninth IEEE International Symposium on Applications of Ferroelectrics, pp. 390-393, 1994.
6. E. Furman, G. Li and G. H. Haertling, *Ferroelectrics*, **160**, 357 (1994).
7. W. Pan, C. Q. Dam, Q. M. Zhang and L. E. Cross, *J. Appl. Phys.*, **66**, 6014 (1989).
8. L. Shebanov, M. Kusnetsov and A. Sternberg, *J. Appl. Phys.*, **76**, 4301 (1994).
9. A. Furuta, K. Oh and K. Uchino, *Sensors and Materials*, **3-4**, 205 (1992).
10. L. E. Cross, *J. Intel. Mat. Sys. & Struc.*, **6**, 55 (1995).
11. K. Uchino, *Am. Ceram. Soc. Bull.*, **65**, 647 (1986).
12. G. H. Haertling, in Proceedings of the Ninth IEEE International Symposium on Applications of Ferroelectrics, pp. 313-318, 1994.

# Rainbow actuators and sensors: a new smart technology

Gene H. Haertling

The Gilbert C. Robinson Department of Ceramic Engineering  
Clemson University, Clemson, SC 29634-0907

## ABSTRACT

Recent developments in the technology of ferroelectric, piezoelectric, electrostrictive and antiferroelectric ceramic actuators have clearly demonstrated that the materials required for future applications such as positioners, levelers, pumps, vibration-free structures and variable-focus elements will need to be more sophisticated (multifunctional and smart), more economical and possess a higher degree of performance than presently available. One recently developed method for producing considerably higher-than-normal displacement in these materials is known as the RAINBOW (Reduced and INternally Biased Oxide Wafer) technology. This acronym denotes the basic active structure of the Rainbow device which is produced by a special high temperature chemical reduction process. In its most basic sense, a Rainbow can be considered to be a pre-stressed, monolithic, axial-mode bender; however, because of its unique dome or saddle-shaped configuration, it is able to produce much higher displacements (up to several mm depending on size) and sustain moderate loads (up to 10 kg depending on thickness) than normal benders such as unimorphs and bimorphs. The technology of producing and characterizing such Rainbows as well as methods for increasing their utility by means of stacked actuators for increased linear displacement and matrix arrays for enhanced coverage in wide-area applications such as smart skins, autoleveling structures and deformable coatings are described.

**Keywords:** ferroelectrics, piezoelectrics, electrostrictors, actuators, sensors, Rainbow devices, PLZT, smart structures, actuator arrays, pre-stressed structures

## 1. INTRODUCTION

The recently renewed, worldwide interest in ferroelectric, piezoelectric, electrostrictive and antiferroelectric ceramics by a number of commercial, industrial and government agencies has been brought about as a result of their unique combination of properties (dielectric, electromechanical, photomechanical, electrooptic, memory, etc.) which make them nearly ideal candidates for a variety of actuating and/or sensing applications where small size, low weight, low or high force, small displacement and variable sensitivities are required. Such applications include automobile and home utility improvements, industrial automation, systems for national security, aircraft control and maneuverability, data processing, entertainment, communications and space exploration. Furthermore, since they are capable of the combined functions of actuating, sensing and controlling in response to an external environment or condition, they belong to that special class of multifunctional ceramics known as "smart" materials.<sup>1</sup>

In spite of their many obvious advantages in these applications, such ceramics are still limited in their ability to deliver high energy or power; e.g., a ceramic linear actuator being able to simultaneously generate high displacement and high force under static or quasi-static conditions is still beyond the scope of present ceramic technologies. In general, such actuators can generate significant force ( $>10^3$  N) with very little movement (on the order of microns), or they can deliver millimeters of displacement via strain-amplifying techniques with little or no force; but not both at the same time. The first of these is typified by the monolithic or multilayer, direct extensional actuator while the second is typical of a bimorph (two opposed active ceramic elements) or unimorph (one ceramic element with inactive metal substrate) actuator. Deliverable energy densities per unit mass for the PZT and PMN-based, direct extensional actuators were reported by Giurgiutiu and co-workers<sup>2</sup> to range from 0.2 to 1 J/kg at an overall average electrical-to-mechanical conversion efficiency of 20%.

An assessment of the present-day ceramic actuator technologies for ceramic materials is given in Figure 1. As seen from the figure, direct extensional configurations, composite flexensional structures and bending-mode devices are all used

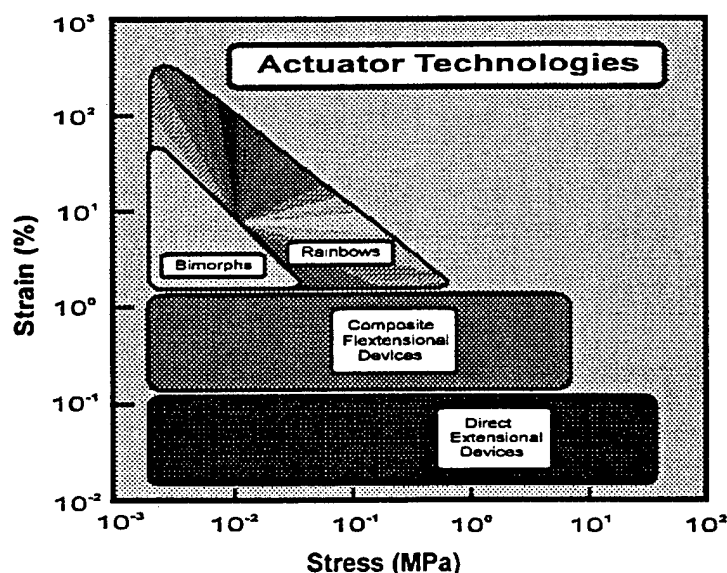


Figure 1. A comparison of ceramic actuator technologies.

to achieve an electromechanical output. Trade-offs between stress generating/load-bearing capability and strain (displacement) must usually be made when designing for particular applications. Maximum displacement can be seen to be achieved with composite or bender structures; however, this is usually accomplished at the expense of less load-bearing capability. A more recently developed strain-amplifying method for piezoelectric and electrostrictive ceramic materials is known as the RAINBOW (Reduced And Internally Biased Oxide Wafer) technology. A complete reference listing for the Rainbow technology is given in references 3 through 17. The properties of the Rainbow are such that it is classified as a pre-stressed, bender actuator which expands the load-bearing capability of the conventional benders while at the same time maintaining or increasing their mechanical displacement characteristics. Key features of the Rainbows are their simplicity, ease of processing, flexibility and surface mountable configuration. Rainbow actuators have been successfully fabricated from all of the common high-lead containing ferroelectric, piezoelectric, electrostrictive and antiferroelectric compositions such as PZT, PLZT, PSZT, PBZT, PNZT, PBiZT, PZT-5A, PZT-5H, PZT-4 and PMN-PT.<sup>9,11,14</sup>

The purpose of this paper is to describe the Rainbow technology in terms of materials, processing, properties and applications. Methods for increasing their utility via cascading arrangements for increased displacement and matrix arrays for wide-area coverage are also described.

## 2. RAINBOW MATERIALS AND PROCESSING

### 2.1 Rainbow materials

Although a number of different compositions have been successfully prepared as Rainbows, those most compatible to the specific processes used and most amenable to achieving the desired properties are in the PLZT solid solution family. Typical high displacement, ferroelectric compositions are 1/53/47 (La/Zr/Ti) and 5.5/56/44 for low and high dielectric constant applications, respectively; whereas, the usual compositions for the electrostrictive-type applications are 9/65/35 or 8.4/70/30. These specific compositions are pointed out in the PLZT phase diagram given in Figure 2. As may be noted, the ferroelectric materials are morphotropic phase boundary compositions, and the non-memory, electrostrictive materials are compositionally located along the ferroelectric-to-paraelectric phase boundary.<sup>9</sup>

### 2.2 Rainbow processing

The Rainbow technology fundamentally consists of a new processing method that is applied to standard, high lead-containing ferroelectric, piezoelectric and electrostrictive ceramic wafers which are transformed by the process into a

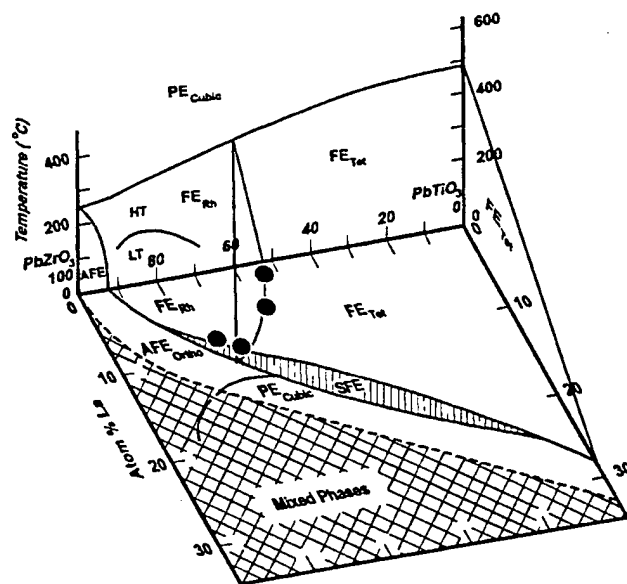


Figure 2. Room temperature phase diagram of the PLZT solid-solution system along with the PZT system vs. temperature. The specific compositions (8.4/70/30, 9/65/35, 5.5/56/44, 1/53/47) are indicated by the bold black circles, left to right, respectively.

monolithic, composite structure consisting of a stressed dielectric and a chemically reduced, electrically conductive layer which acts as the stressing element as one of the electrodes for the final device. Since all of the materials are ferroelectric or electrically-enforced ferroelectric materials, they are multifunctional and smart, by nature, and are thus capable of performing both actuator and sensor functions, simultaneously.

The high temperature chemical reduction process involves the local reduction of one surface of a planar ceramic plate, thereby achieving an anisotropic, stress-biased, dome or saddle-shaped wafer with significant internal tensile and compressive stresses which act to increase the overall strength of the material and also provide its unusually high displacement characteristics. According to previously reported work, the chemical reduction process proceeds via simple reactions consisting of the oxidation of the solid carbon (graphite) block to carbon monoxide and further oxidation of the carbon monoxide gas to carbon dioxide with the associated loss of oxygen from the PLZT oxide in contact or in near contact with the graphite block.<sup>5</sup> Figure 3 shows cross sections of the dome curvature and a fracture surface which are typical of the Rainbow ceramics.



Figure 3. Cross-sectional views of PLZT 5.5/56/44 Rainbow wafer illustrating (a) dome profile and (b) fracture surface of reduced layer (bottom portion) and unreduced PLZT (top portion).

Rainbow ceramics are produced from conventionally sintered or hot pressed ceramic wafers by means of a few simple steps requiring approximately two hours of additional time. A Rainbow is produced from an as-received wafer by

placing it on a flat graphite block, placing a protective zirconia plate of the same size on top of the wafer and introducing the assembly into a furnace held at temperature in a normal air atmosphere. The part is treated at a temperature of 975°C for one hour, removed from the furnace while hot and cooled naturally to room temperature in about 45 minutes. A reduced, cermet layer, approximately 150  $\mu\text{m}$  thick, is produced in the wafer under these treatment conditions. When cool, the dome or saddle-shaped wafer is lifted from the graphite block; brushed and sanded lightly on the reduced (concave) side to remove any metallic lead particles and to expose the electrically conductive, reduced cermet beneath the thin, reoxidized layer; and then electroded for test and evaluation. A variety of electrodes can be used such as epoxy silver, fired-on silver and vacuum-deposited metals. After applying appropriate electrodes, the Rainbow is completed and ready for operation. It should be noted that although Rainbows are processed in bulk wafer form, after heat treatment they may be diced or scribed into smaller elements ( $\sim 1 \text{ mm}^2$ ) for a pick-and-place operation onto a smart hybrid circuit. This technique is possible since each individually diced element possesses a smaller but similar dome structure with a radius of curvature identical to the larger wafer. Even though the displacements of the smaller individual elements are proportionately less than the parent wafer, they nevertheless, are large enough (5 - 50 microns) to be useful in some devices as actuators and sounders or as sensors. Some typical examples of sizes and shapes of Rainbows are shown in Figure 4.

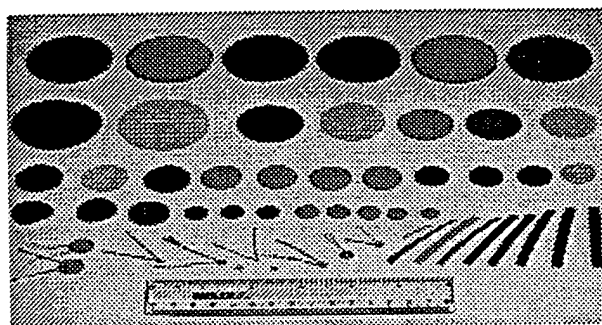


Figure 4. Typical examples of sizes and shapes of Rainbow elements

### 2.3 Rainbow operation

In regard to operation, a Rainbow is similar to a device known in the industry as a unimorph bender. A unimorph is composed of a single piezoelectric element externally bonded to a flexible metal foil which is stimulated into action by the piezoelectric element when activated with a ac or dc voltage and results in an axial buckling or displacement as it opposes the movement of the piezoelectric element. However, unlike the unimorph, the Rainbow is a monolithic structure with internal compressive stress bias on the piezoelectric element; thus producing the dome structure, rendering it more rugged and able to sustain heavier loads than normal. The integral electrode (usually the bottom electrode) consists of metallic lead intimately dispersed throughout the semiconductive, porous oxide layer. The change in shape of the wafer after reduction is believed to be due to (1) the reduction in volume of the bottom reduced layer (largely metallic lead) compared to the unreduced material as a result of the loss of oxygen from the lattice, (2) the differential thermal contraction between the reduced and unreduced layers on cooling to room temperature and (3) any change in volume which may occur on cooling through the Curie point as the material undergoes a phase transformation from a smaller, non-polar, cubic unit cell to a larger, polar, ferroelectric unit cell.

Like other piezoelectric devices, Rainbows may be operated with a dc, pulse dc, or ac voltage; however, when driven with ac, the largest displacements are usually achieved at 100 Hz or less. In operation, the dome height of the Rainbow varies as a function of the magnitude and polarity of the voltage. When a given polarity of voltage is applied, the dome decreases in height depending on the magnitude of the voltage; and alternatively, when the polarity is reversed, the dome increases. The large axial motion of the dome is largely due to contributions from (1) a lateral contraction produced in the material via the  $d_{31}$  coefficient and (2) a stress-directed domain switching process near the top surface wherein c-axis domains lying in the plane of the wafer as a result of the tensile stress are induced by the electric field to switch to a position normal ( $90^\circ$ ) to the plane. It should be remembered that the  $180^\circ$  domains that reorient in the electric field do not cause a change in shape for the Rainbow. A model of this effect is illustrated in Figure 5.



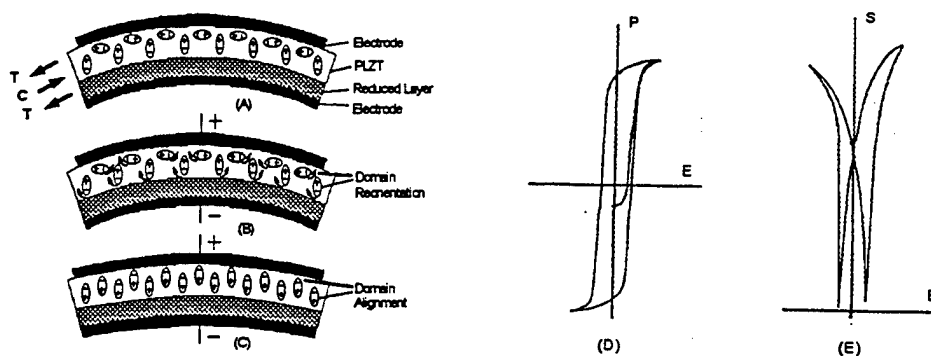


Figure 5. A model of the changes taking place during operation of a Rainbow wafer, depicting various stages of domain alignment and reorientation in a Rainbow actuator: (A) as processed and electroded, (B) first application of voltage causing domain reorientation, (C) complete application of voltage producing near complete domain alignment and flattening of the wafer, (D) the asymmetrical hysteresis loop obtained on the first application of voltage indicating partial, stress-induced (ferroelastic) poling and (E) the asymmetrical strain loop obtained on first application of voltage.

### 3. PROPERTIES

#### 3.1 Dielectric properties

The temperature dependent dielectric behavior for two PLZT compositions; i.e., 1/53/47 and 9/65/35, are shown in Figure 6. It can be seen from the figure that a gradual rise occurs in the relative dielectric constant (1 kHz) of 1/53/47

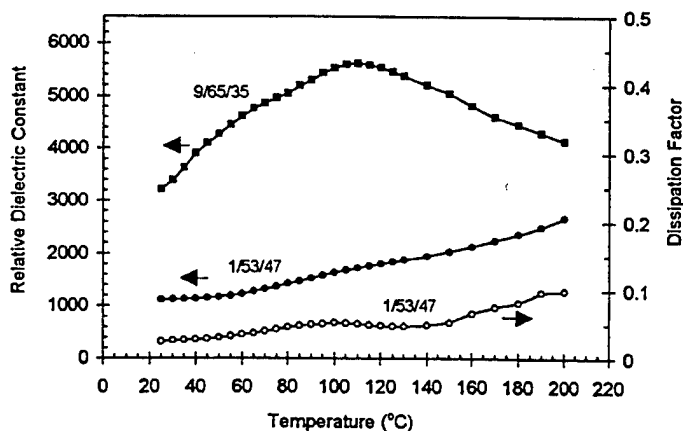


Figure 6. Temperature dependent dielectric properties of PLZT Rainbow wafers.

from a room temperature value of approximately 1100 to about 2700 at 200°C. No peak is observed in this range for this composition because its Curie point is 330°C. On the other hand, composition 9/65/35 shows a change in dielectric constant from 3200 to 5700 over this same temperature range with a peak occurring at 105°C, which is its usual Curie point as determined from small signal measurements. Since this composition is an electrostrictive, relaxor-type material, this Curie point does not coincide with its loss in polarization which occurs at about 20°C; thus, making it one of the most sensitive, high displacement, electrostrictive Rainbow materials. It may be noted that the dielectric constants for both compositions and also the dissipation factor for 1/53/47 are comparable to previously reported values, and this indicates that the Rainbow reduction process does not substantially change the dielectric properties of the unreduced part of the structure.

### 3.2 Hysteresis loops

Typical examples of dc hysteresis loops for compositions 1/53/47 and 9/65/35 are given in Figure 7. The loop in Figure 7(A) was taken on the ferroelectric Rainbow element (1/53/47) in its virgin condition before any other measurements

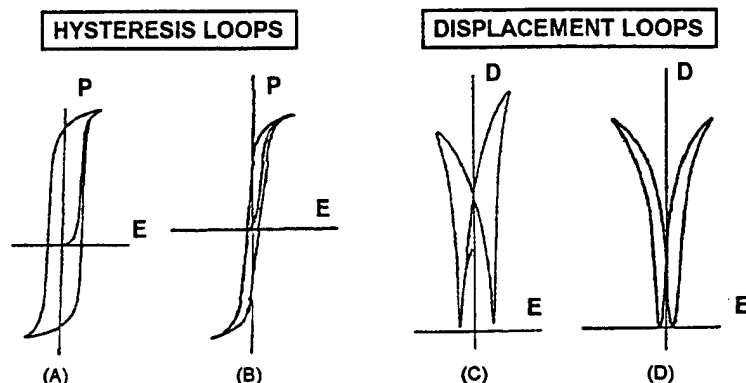


Figure 7. Hysteresis loops (P vs. E) and electromechanical displacement loops (D vs. E) for PLZT Rainbows 1/53/47 (A and C) and 9/65/35 (B and D), respectively.

were made. It should be noted that on the initial application of positive voltage to +450V there was approximately 60% of the total remanent polarization switched rather than the usual 50% one ordinarily observes in a virgin, randomly oriented ceramic. This behavior is highly unusual and indicates that the Rainbow ceramic was partially poled before testing. Additional audio and piezoelectric tests of other virgin parts also indicated that the elements were partially poled to varying degrees; i.e., some very little and others as high as 75%.

One explanation for this condition occurring in the electrically virgin state is that the mechanical compressive and tensile stresses produced in the Rainbow wafer during processing are acting together to switch some of the domains in this soft ferroelectric/ferroelastic material. Since uniform stress is a symmetrical quantity, it is recognized that it alone is insufficient to produce a net polarization in a given direction even though it may be of sufficient magnitude to switch domains; however, a stress gradient such as produced by the Rainbow bending process is a vector quantity and can, indeed, produce the observed effect. This non-uniform stress is believed to be responsible for the partial poling of the Rainbow wafers. Measured properties on the above 1/53/47 wafer were:  $P_R = 44.8 \text{ uC/cm}^2$ ,  $E_C = 7.5 \text{ kV/cm}$ , dielectric constant = 1210 and dissipation factor = 0.047.

The virgin loop of Figure 7(B) is a typical one for the electrostrictive (9/65/35) type of Rainbow materials and is very similar to that obtained on bulk electrooptic material. Measured properties on this wafer were:  $P_{10kV/cm} = 28.3 \text{ uC/cm}^2$ , dielectric constant = 3142 and dissipation factor = 0.085. As a matter of course, no unsymmetrical hysteresis loops were observed in the electrostrictive materials, and none was expected, since there are no stable domains in these materials at zero electric field. Conceivably, a high enough stress could precipitate stable domains in a very near-ferroelectric material, however, this was not experimentally confirmed.

### 3.3 Electromechanical displacement loops

Displacement vs. electric field (butterfly) loops for the Rainbow wafers described above are also shown in Figure 7. Figure 7(C) illustrates the Rainbow axial motion as the sample is electrically switched from zero to +450V, to -450V and back to zero, however, in this case this loop was not taken on the virgin wafer. It may be noted that this loop is remarkably similar to that observed when measuring the direct extensional (longitudinal, lateral) displacements via the piezoelectric  $d_{33}$  or  $d_{31}$  coefficients. The value of displacement in the + voltage direction was measured at 190.5  $\mu\text{m}$ , and the total amount of displacement (+/-) was 432  $\mu\text{m}$ .

Figure 7(D) shows the displacement loop of the electrostrictive Rainbow material (9/65/35) mentioned above. Since 9/65/35 is a relaxor material there should be little or no memory, and the same value and sign of displacement

should be obtained whether a + or a - voltage is applied. One can see by switching this sample through a full voltage loop that a small amount of remanent displacement (strain) is present which is probably due to the close proximity of this composition to a FE phase. A further indication of this incipient FE phase is the higher than normal value of  $P_{10}$  ( $P_{10} = 28.3$  vs. a more normal  $18.0 \text{ uC/cm}^2$ ) as given above. Measured value of total displacement for this wafer was  $178 \text{ um}$ .

### 3.4 Voltage dependent displacement characteristics

The displacement characteristics as a function of applied voltage are given in Figure 8 for some selected compositions. One of the most striking features of this figure is the very high displacements achieved by these Rainbow

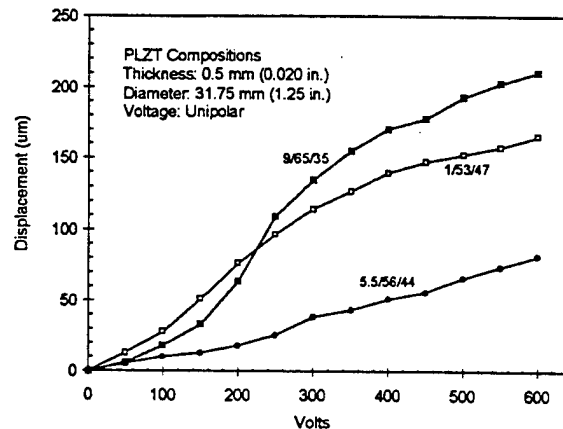


Figure 8. Axial displacement characteristics of Rainbow PLZT compositions as a function of voltage.

ceramics at moderate electric fields; e.g., 400 volts is equivalent to an electric field of  $10 \text{ kV/cm}$ . Composition 9/65/35 is noted to possess the highest displacement of  $210 \text{ um}$  at a maximum voltage of 600 volts, however, its displacement is characteristically non-linear because of its electrostrictive nature. Compositions 1/53/47 and 5.5/56/44 are ferroelectric materials, and thus, are more linear in behavior. As a general rule, the displacements of the ferroelectric materials are lower than those of the electrostrictive compositions, particularly when operated at higher voltages and one polarity; however under bipolar operation, the displacement values of the ferroelectric materials will commonly be double the values shown in the figure.

Figure 9 illustrates the unusually large range of displacements obtained for Rainbows as a function of thickness,

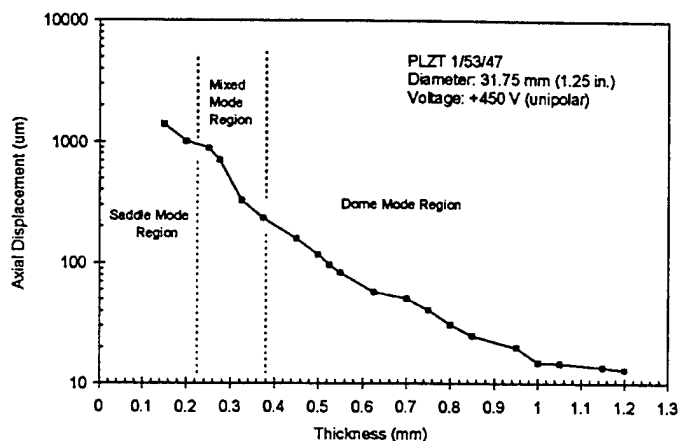


Figure 9. Displacement characteristics of Rainbow PLZT 1/53/47 as a function of wafer thickness.

where thickness is plotted against the log of displacement. Wafer thickness has been found to have a significant effect upon axial displacement primarily because of the change in motional mode; i.e., from dome (spherical) to saddle (cylindrical) flexing, as the wafer thickness is reduced to approximately one-hundredth of the diameter. For example, a 31.75 mm (1.25 inch) diameter wafer usually develops a saddle-mode configuration when its thickness is less than 0.32 mm (0.013 inch). Saddle-mode operation provides maximum displacement with minimum load bearing capability (<100 grams); and therefore, should only be considered for special applications. It can also be seen from the figure that there is a thickness-dependent mixed mode region separating the other two modes. Replotting the data (in the dome-mode region) as displacement vs.  $1/\text{thickness}^2$  reveals a near linear relationship and demonstrates that the displacement is inversely proportional to the square of the wafer thickness as shown in Figure 10.

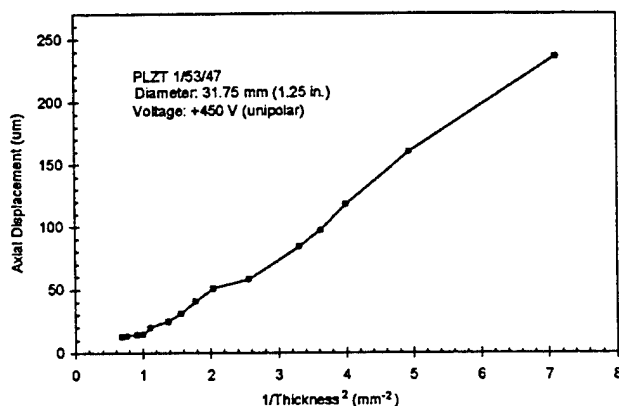


Figure 10. Replot of data from the dome-mode region of Figure 9 for Rainbow 1/53/47

The dependence of the axial displacement of a Rainbow wafer on its diameter is shown in Figure 11 where displacement is plotted against the wafer diameter squared. As can be seen, an excellent linear relationship is obtained.

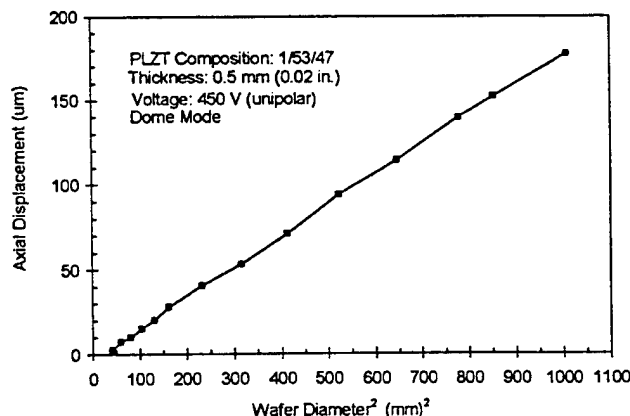


Figure 11. Axial displacement of Rainbow PLZT 1/53/47 as a function of the wafer diameter squared.

Thus, the data from both Figures 10 and 11 confirm that a Rainbow behaves very much like a normal bending actuator according to the equation:<sup>18</sup>

$$y = 3/2 * d_{31} * d^2/t^2 * V$$

or, in general,

$$y = m * d^2/t^2 * V$$

where  $y$  is the axial displacement,  $d_{31}$  is the lateral piezoelectric coefficient,  $m$  is a constant ( $1 \times 10^{-4}$  um/V),  $d$  is the wafer diameter,  $t$  is the wafer thickness and  $V$  is the applied voltage. Maximum displacement is accordingly obtained with larger diameter and thinner wafers. A maximum displacement of 3mm at an operating voltage of 450 V has been obtained, to date, with a single Rainbow wafer having a diameter of 100 mm and a thickness of 0.375 mm.

The effect of an unconstrained axial point load on the displacement of an activated Rainbow is given in Figure 12 for

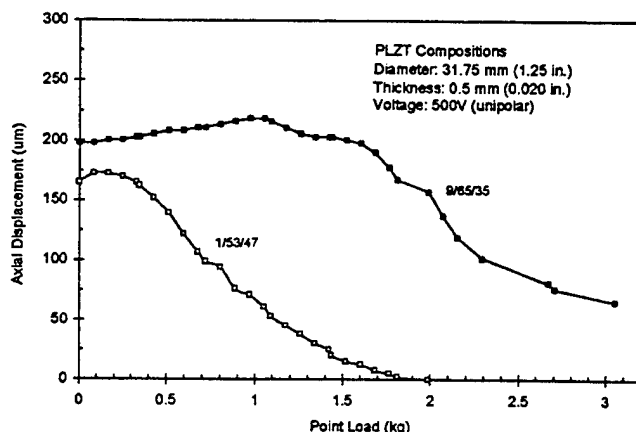


Figure 12. Concentrated (point) load-bearing characteristics of Rainbow PLZT Compositions

compositions 1/53/47 and 9/65/35. PLZT 1/53/47 can be seen to be relatively ineffective when loaded with a dead weight of 1.5 kg (3.3 lbs), whereas, composition 9/65/35 is still effective at a load of over 3 kg. This result is not too surprising since the elastic modulus of 9/65/35 ( $10.9 \times 10^4$  MPa) is noticeably higher than that of 1/53/47 ( $7.8 \times 10^4$  MPa). Another point to note from the figure is the increase in displacement with the introduction of a finite amount of load on the device. This effect was previously reported by Furman, et al.,<sup>8</sup> and is believed to be due to the lowering of the stiffness of the ceramic when the ferroelectric phase is field enforced. This decrease in elastic modulus with field leads to an increased flattening of the wafer under load; however, when the field is removed, the material become stiffer again and the original height (curvature) of the wafer is restored. This phase transformation effect leads to a increased range of displacement up to an amount of loading which can be readily accommodated by the wafer without the electric field. As a function of frequency, 9/65/35 is also superior to 1/53/47 in that its displacement is relatively constant from 0.1 Hz to several hundred Hertz.

Another concern of actuator designers is the amount of force that can be generated by an actuator when voltage is applied. This is shown in Figure 13 for a 1/53/47 Rainbow of standard size. As can be seen, the force generated is a linear

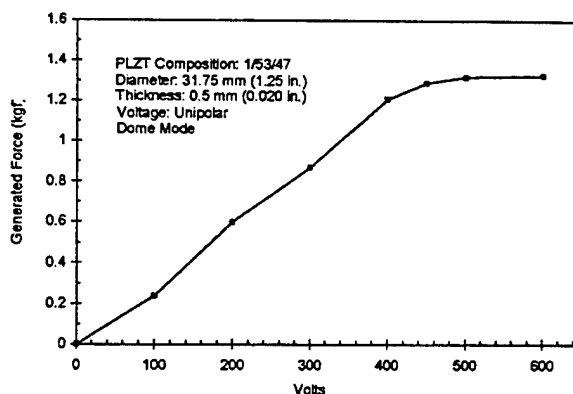


Figure 13. Effect of applied voltage on the force generated by a PLZT 1/53/47 Rainbow wafer.

function of voltage until the onset of saturation for this particular configuration. A maximum force of 1.3 kgf was achieved at 450 volts.

### 3.5 Rainbow stacks and arrays

Previous work on high displacement Rainbow actuators has shown that they possess the capability to be configured into linear stacks for higher displacement devices or into larger area arrays for actuator/sensor functional components. The stacking arrangement consisted of linearly cascading several Rainbow elements together in multiple groups of two in a clamshell arrangement and then bonding these clamshells together into a single unit. Sending/receiving arrays, on the other hand, were individually placed side-by-side (sandwiched between thin layers of ductile metal foil and bonded together with conductive Ag epoxy) in order to maximize their area while minimizing their thickness. Thus, stacks consisted of Rainbows arranged mechanically in series and electrically in parallel while arrays were Rainbows arranged both mechanically and electrically in parallel. Individually addressed elements in some of the arrays were achieved by employing a matrix scheme wherein separate bottom electrodes made up the rows and separate top electrodes were the columns. Operation of a single Rainbow was then obtained by applying voltage between a row and column electrode. Typical examples of stacks and arrays are shown in Figure 14.

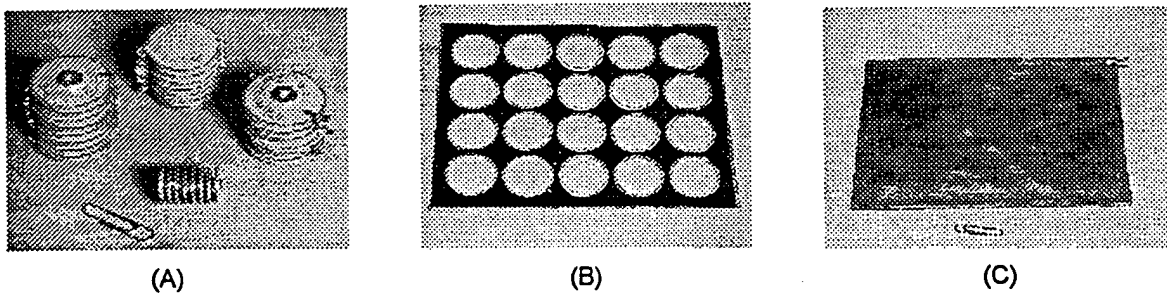


Figure 14. Examples of (A) Rainbow stacks and a Rainbow array showing (B) the individual Rainbow elements before applying the top metal foil and (C) completed smart skin array 1.25 mm thick.

The characteristics of the PLZT Rainbow stacks were evaluated as a function of wafer thickness, wafer diameter, point load-bearing capability and unipolar or bipolar voltage displacement. These data are given in Figure 15. First it can

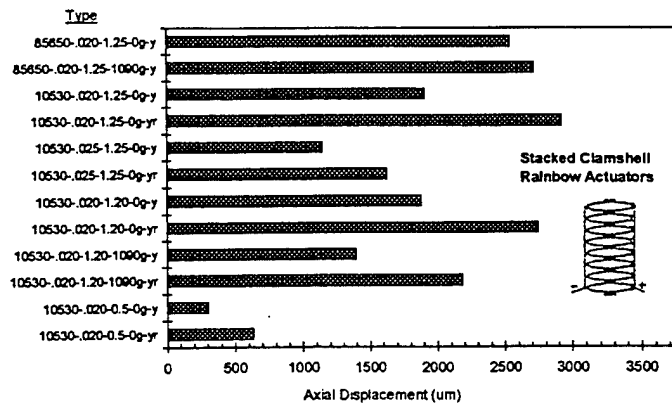


Figure 15. Displacement characteristics of various types of eight-unit Rainbow clamshell actuators. Type legend: composition/wafer thickness in inches/wafer diameter in inches/point load in grams/bipolar (yr) or unipolar (y) voltage displacement.

be seen that bipolar operation always achieves higher displacement by at the expense of higher non-linearity; secondly, in unipolar operation the 8.5/65/35 material achieved higher displacements and could sustain higher loads than the 1/53/47

material; however, in bipolar operation the 1/53/47 was superior in terms of displacement; and thirdly, small compact actuators, 12.7 mm dia. x 24 mm long, were capable of achieving moderate displacements (308  $\mu$ m) under modest loads of 1 kg. or less. In general, total displacements were found to scale linearly with the number of individual Rainbow elements. In regard to the arrays, several different Rainbow arrays consisting of up to 42 Rainbow elements were evaluated

#### 4.0 APPLICATIONS

A number of examples of applications are given in this section in order to demonstrate the versatility of the Rainbow technology. These working models are essentially discrete, proof-of-principle devices which require further engineering, design, miniaturization and modifications in order for them to be suitable for hybrid microelectronics or integrated structures. A number of advantages and features of the Rainbows are: (1) simplicity, (2) solid-state, (3) monolithic, (4) pre-stressed for greater strength and durability, (5) can sustain or generate moderate loads, (6) surface mountable, (7) very high axial displacement, (8) above-the-plane displacement, (9) no bonding layers, (10) temperature compensation possible, (11) can be stacked to multiply displacement and (12) can be fabricated into large area arrays.

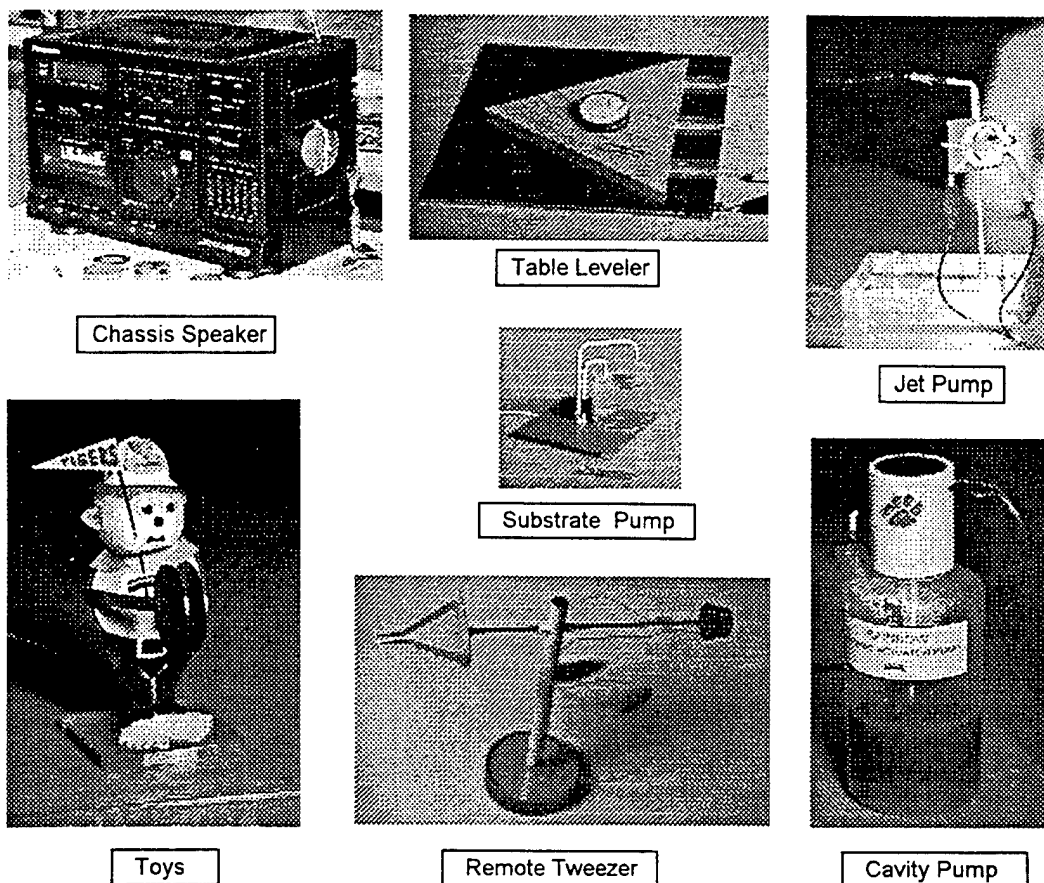


Figure 16. Examples of working model devices using Rainbow ceramics as actuators

The Rainbow devices shown in Figure 16 are typical examples of a number of applications envisioned for this technology. As can be seen, they range from actuators to speakers, and remote handlers to pumps. A more extensive list of applications include (1) linear actuators, (2) cavity/piston pumps, (3) loud speakers, (4) reciprocating motors, (5) relays/switches/thermostats, (6) sensors, (7) hydrophones/hydroprojectors, (8) variable-focus mirrors/lenses, (9) optical deflectors/scanners, (10) vibrating delivery systems, (11) liquid delivery systems, (12) antivibration/noise-cancelling devices, (13) sonic and ultrasonic devices and (14) auto-leveling platforms.

## 5. CONCLUSIONS

The prospects for utilizing Rainbows in discrete hybrid and integrated microelectronics are promising for future applications involving smart ceramics such as ferroelectrics, piezoelectrics, electrostrictive and antiferroelectric materials. Rainbows have opened up a new dimension in high displacement actuators. The key to adapting these materials to specific devices and applications is the manner in which answers are found to questions concerning their reproducibility, reliability, longevity and cost effectiveness. Further development and design work are obviously needed in order to answer these questions.

## ACKNOWLEDGEMENTS

This work was supported by NASA-Langley under Grant No. NAG-1-1301 and ONR under Grant No. N0014-94-1-0563.

## REFERENCES

1. R.E. Newnham and G.R. Ruschau, "Smart electroceramics", *Bull. Am. Ceram. Soc.* **75**, pp. 51-61, 1996.
2. V. Giurgiutiu, Z. Chaudhry and C.A. Rogers, "Energy-based comparison of solid-state actuators", Virginia Tech Report No. CIMSS 95-101, Center for Intelligent Material Systems and Structures, 1995.
3. G.H. Haertling, "Rainbow ceramics - a new type of ultra-high displacement actuator", *Bull. Am. Ceram. Soc.* **73**, pp. 93-96, 1994.
4. G.H. Haertling, "Method for making monolithic prestressed ceramic devices", U.S. Patent No. 5,471,721, December 5, 1995.
5. G.H. Haertling, "Chemically reduced PLZT ceramics for ultra-high displacement actuators", *Ferroelectrics* **154**, pp. 101-106, 1994.
6. E. Furman, G. Li and G.H. Haertling, "An investigation of the resonance properties of rainbow devices", *Ferroelectrics* **160**, pp. 357-369, 1994.
7. S. Sherit, H.D. Wiederick, B.K. Mukherjee and G.H. Haertling, "The dielectric, piezoelectric and hydrostatic properties of PLZT based Rainbow ceramics", *Proc. of the 9th IEEE Intl. Meeting on Appl. of Ferroelectrics*, pp. 390-393, University Park, PA, 1994.
8. E. Furman, G. Li and G.H. Haertling, "Electromechanical properties of Rainbow ceramics", *Proc. of the 9th Intl. Meeting on Appl. of Ferroelectrics*, pp. 146-149, University Park, PA, 1994.
9. G.H. Haertling, "Compositional study of PLZT Rainbow ceramics for piezo actuators", *Proc. of the 9th Intl. Meeting on Appl. of Ferroelectrics*, pp. 313-318, University Park, PA, 1994.
10. C. Elissalde and L.E. Cross, "Dynamic characteristics of Rainbow ceramics", *J. Am. Ceram. Soc.* **78**, pp. 2233-36, 1995.
11. G. Li, E. Furman and G.H. Haertling, "Composition and microstructure of chemically reduced PLZT ceramics", *Ferroelectrics*, **182**, pp. 69-76, 1996.
12. K.M. Nair and V.N. Shukla, *Hybrid Microelectronic Materials*, pp. 71-96, ACerS Ceramic Transactions, Vol. 68., Westerville, OH, 1996.
13. C. Elissalde, L.E. Cross and C.A. Randall, "Structural-property relations in a reduced and internally biased oxide wafer (RAINBOW) actuator material", *J. Am. Ceram. Soc.* **79**, pp. 2041-48, 1996.
14. G. Li, E. Furman and G.H. Haertling, "Fabrication and properties of PSZT antiferroelectric Rainbow actuators", *Ferroelectrics* **188**, pp. 223-236, 1996.
15. D.E. Dausch, "The effects of excess PbO addition and composition variation on the processing and properties of tape cast PLZT Rainbow actuators", *Proc. of the 10th Intl. Meeting on Appl. of Ferroelectrics*, East Brunswick, NJ, 1 1996. (to be published)
16. G. Li and G.H. Haertling, "The piezoelectric, pyroelectric and photoelectric properties of PLZT Rainbow ceramics", *Proc. of the 10th Intl. Meeting on Appl. of Ferroelectrics*, East Brunswick, NJ, 1996. (to be published)
17. G.H. Haertling, "Stress-induced effects in PLZT ceramics", *Proc. of the 10th Intl. Meeting on Appl. of Ferroelectrics*, East Brunswick, NJ, 1996. (to be published)
18. R.C. Buchanan, *Ceramic materials for electronics*, p. 187, Marcel Dekker, Inc., New York, 1991.



# Stress-Induced Effects in PLZT Ceramics

Gene H. Haertling

Gilbert C. Robinson Department of Ceramic Engineering  
Clemson, South Carolina 29634-0907

**Abstract** — Soft, high lead-containing, ferroelectric ceramic materials such as PLZT are known to be highly vulnerable to the effects of mechanical stress at room and elevated temperatures as a consequence of their ferroelastic and pyroplastic natures which are usually manifested in some form of nonlinear behavior within the material. Examples of such behavior include (1) hydrostatic and shock-wave stimulated structural phase transformations as in stress-induced depoling of explosive-to-electrical (EET) transducers, (2) mechanically stimulated domain reorientation as in shape memory effects and Rainbow devices, (3) mechanically stimulated electrooptic effects as in ferroelectric picture (Ferpic) devices and Rainbows, (4) mechanically stimulated strength effects and (5) thermo-mechanically stimulated dimensional changes as in high temperature creep. The improved utility or increased sensitivity of these materials as a result of stress-enhancing techniques is described.

## I. INTRODUCTION

Ferroelectrics have long been known to be highly susceptible to the state of stress existing within the material, regardless of whether that stress is internally or externally generated. This is especially true for the soft (easily electrically switchable) and super-soft PLZT ceramics which commonly possess reduced Curie temperatures of less than 200°C. In such materials, their intrinsic polarization, strain and properties related to domain reorientation are significantly affected by the magnitude, the type and the direction of the stress. Indeed, in many cases, it is this great sensitivity to stress which makes these compositions useful and advantageous in piezoelectric applications such as microphones, sensors and accelerometers; while on the other hand, this same stress vulnerability is undesirable for sonar, ultrasonic actuators and ignitors. Thus, one can easily come to the conclusion that it is important and very knecessary to have a working knowledge of the stress sensitivity of these materials.

Stress sensitivity arises in ferroelectric (polarization vs. electric field) materials because of the piezoelectric coupling between polarization and strain. When this strain (and coupled polarization) can be switched by application of a mechanical stress and there are two or more stable orientational states in the absence of the stress, then a material possessing this characteristic is referred to as a ferroelastic (strain vs. mechanical stress) one [1]. It is this highly sensitive ferroelastic property of the soft ferroelectrics which causes them to be susceptible to all manners of stress.

The effects of stress on piezoelectrics and ferroelectrics have been amply reported in the literature, dating from at least five decades ago [2 - 9]. From this body of work it has been shown that both steady state and transient stress, whether piezoelectrically self-generated or externally generated, can (1) significantly affect properties such as dielectric constant, loss tangent, piezoelectric coefficients, Curie point, elastic modulus and mechanical strength, (2) influence switching behavior, domain reorientation and poling, (3) induce phase changes which lead to substantially altered properties, (4) drastically alter stress-optic and optical birefringent characteristics and (5) change the geometric dimensions of a material by means of high-temperature creep. In many of the cases, these effects are harmful to the performance of the material and the device; however, when prudently designed and properly directed, stress can be used to one's advantage such as in the cases of explosive-to-electrical (EET) transducers and high-displacement Rainbow actuators.

The object of this paper is to review selected examples of the effect of stress on the soft ferroelectric ceramics with special emphasis on the PLZT materials. The specific cases were chosen to describe the positive effects of stress on the enhancement of properties and performance.

## II. STRESS-INDUCED EFFECTS

### A. Stress-Induced Polarization Depoling

Studies on the stress-induced depoling of piezoelectric and ferroelectric ceramics were initiated in the mid-1950s at Clevite Corporation, the company which patented and trademarked the original lead zirconate-lead titanate (PZT) compositions (e.g., PZT-4, PZT-5, PZT-8) that are so familiar to those working in the field of ferroelectric ceramics[10]. In this work, Berlincourt and co-workers first investigated the effects of uniaxial compressive stress on PZT; and later in 1958, they reported on the depoling behavior of a soft, niobia-doped PZT (52/48 Zr/Ti ratio) in response to hydrostatic pressure such as a material might experience in an under water transducer. It was found that these morphotropic phase boundary (MPB) materials release their polarization rather gradually over a pressure range from near zero to greater than 70 MPa and that most of the lost polarization was unrecoverable.

Further studies showed that PZT ferroelectric compositions

located near the FE-AFE phase boundary (PSZT 66/27/7 Zr/Sn/Ti is typical of this type) were more desirable because they released their stored charge more suddenly, and in some cases, at substantially lower pressures. This pressure depoling effect was found to be a result of a pressure-enforced phase transformation from the polar FE state to the nonpolar AFE state. A typical example of such behavior is shown in Fig. 1 where hydrostatic depoling is compared with uniaxial stress depoling [11]. PLZT compositions located along the FE-AFE boundary also exhibit this same behavior.

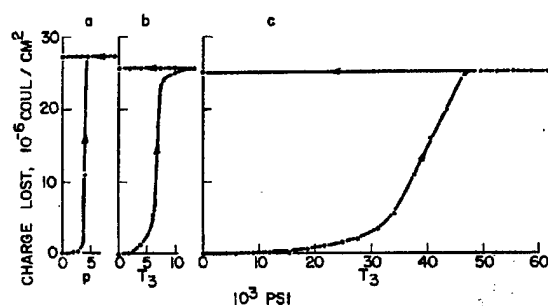


Fig. 1. Electrical depoling behavior of nobia-doped PSZT 66/27/7 (Zr/Sn/Ti) for (a) hydrostatic stress, (b) one-dimensional stress (unclamped) parallel to polar axis and (c) one-dimensional strain (clamped) parallel to polar axis. [11]

When this depoling is accomplished in a transient mode via explosive shock waves or projectile impact, useful electrical pulses of a few hundred kilowatts lasting for several microseconds may be obtained [12]. These one-shot, explosive-to-electrical (EET) power supplies have found a number of uses in primarily military applications.

### B. Stress-Induced Domain Reorientation

One manifestation of stress-induced domain reorientation in ferroelectric ceramics is known as the shape memory effect; i.e. the recovery of a plastically deformed element to its original shape by heating. This effect was discovered by Schmidt and Boczek [13] in PLZT ceramics in 1978 during an investigation of PLZT 8/65/35 (La/Zr/Ti) and was further studied by Kimura, Newnham and Cross [14] while working with PLZT 6.5/65/35.

The effect is easily demonstrated by mechanically bending a PLZT bar at room temperature or at some elevated "characteristic" temperature below the Curie point. After bending the bar, and cooling to room temperature, it will retain its new shape (i.e., possesses memory) indefinitely. However, when the bar is heated above this characteristic temperature, it will return to its original shape. Remarkably high bending angles, larger than 10°, and strains as high as 0.25% have been reported for this reversible effect [13, 15].

Examples of PLZT bars bent at room temperature are given

in Fig. 2.

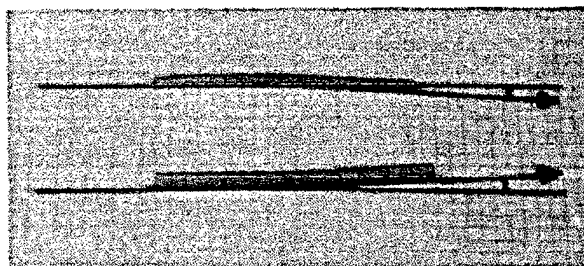


Fig. 2. Two PLZT 7/65/35 ceramic bars which were bent at room temperature.

This effect can be explained in terms of domain reorientation wherein the applied mechanical stress within the material is minimized by the accommodation of the strain relieving 71° and 109° rhombohedral domains. These domains disappear along with the spontaneous polarization when the material is heated above the Curie temperature; and thus, the material reverts back to its original condition. Consequently, it can be seen that the domain reorientation process makes the material more mechanically compliant up to a point where all of the strain relieving domains are reoriented, and beyond that point, the material becomes mechanically stiffer and, once again, acts like a brittle solid. Of course, above the Curie temperature, the material does not display any of these effects.

Another example of stress-induced domain reorientation is exemplified by the RAINBOW (Reduced And Internally Biased Oxide Wafer) actuator. This new type of high displacement bending actuator consists of a high lead-containing ferroelectric material (e.g., PLZT) which is chemically reduced on only one surface in order to render the resulting reduced layer electrically conductive and to impart an overall stress gradient to the wafer. The high compressive radial stress (150 - 200 Mpa) developed in the wafer as a result of differential thermal contraction between the reduced and unreduced layers, as well as any volume change on cool down through the Curie temperature, produces a pronounced spherical (dome) or cylindrical (saddle) curvature to the wafer thereby allowing it to achieve very high displacement when electrically activated.

Studies have shown that, in addition to the normal  $d_{31}$  contribution, the reason for the unusually high displacement resides in the fact that (1) the high stresses (compressive in the interior and tensile on the surface) produce domain reorientation and (2) the high stress gradient produces partial poling of the wafer by means of polarization alignment. This is illustrated schematically in Figure 3 by showing the changing curvature of the wafer as the domains reorient under the influence of stress and electric field. The changing curvature then leads to the axial displacement which is maximized at the center of the wafer.

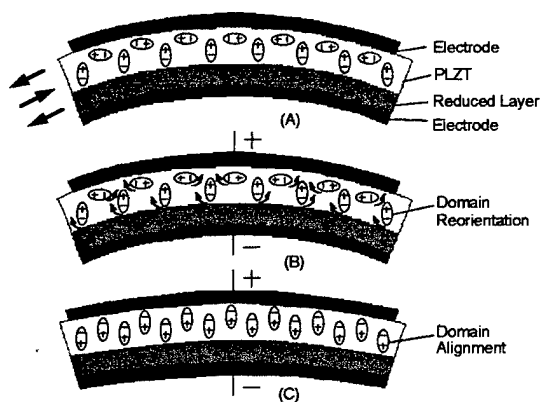


Fig 3. Various stages of domain alignment and reorientation in a Rainbow actuator, depicting conditions: (A) as processed and electroded, (B) first application of voltage and (C) complete application of voltage.

During operation, a ferroelectric Rainbow actuator such as PLZT 1/53/47 achieves the very high displacement by constantly reorienting the lateral, strain-producing domains as the voltage is switched. In the case of an electrostrictive Rainbow actuator, this same effect is involved as the domains change from micro to macro dimensions.

### C. Stress-Induced Electrooptic Effects

One of the most innovative techniques for utilizing stress-induced domain switching in a device is shown in Fig. 4. This permanently stored image in a polished wafer of PLZT 7/65/35 was produced by mechanically bending the wafer while simultaneously applying a bias voltage and

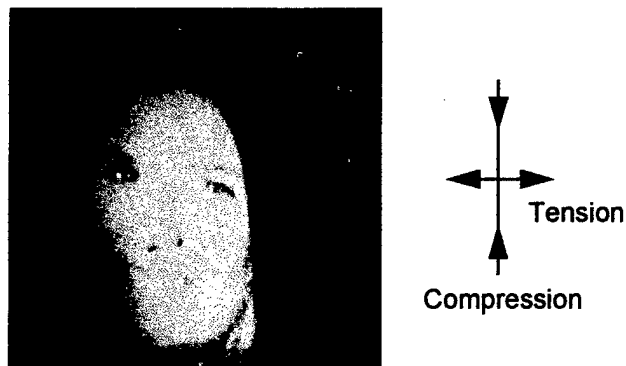


Fig. 4. An example of a stored image with gray-scale capability. The figure shows an image stored in the Ferpic and projected onto the focal plane of a Polaroid camera.

exposing an image with polarized light onto a wafer which possessed a photoconductive film sandwiched between the PLZT and a transparent ITO conductive electrode. Referred to as a strain-biased ferroelectric picture (Ferpic) device by Maldonado and Meitzler [16], this optically birefringent image achieves optical contrast because of the varying domain reoriented positions within the material. Erasure of the image is brought about by simply flooding the device with light as saturation voltage is applied. This reorients all

all of the domains to the same reset position of saturation in the thickness direction.

The strains produced in the Ferpic device are of the order of  $3 \times 10^{-3}$ , and the internal fields associated with strains of this magnitude are estimated to be 90 kV/cm. Internal fields of this magnitude are large enough to not only influence, but in a real sense, control the domain switching process in the ceramic.

Another example of stress-induced birefringence can be demonstrated in the case of a Rainbow actuator. Since the electrostrictive Rainbows are generally fabricated from the optically transparent relaxor PLZT compositions such as 9/65/35, it is quite simple to exhibit this behavior by simply polishing the two side faces of a rectangular Rainbow bar and then placing it under a polariscope consisting of two crossed, linear polarizers and a back light. When this is done as shown in Fig. 5, one can easily locate the neutral stress plane since it appears as a dark line (zero birefringence) running parallel to the major surfaces. This

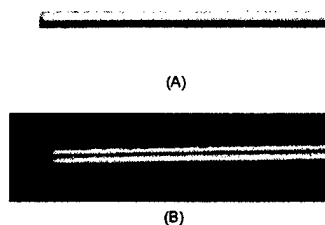


Fig. 5. A PLZT 9/65/35 Rainbow bar as observed with (A) transmitted, unpolarized light and (B) under crossed polarizers. Note in (A) that light is not transmitted in the reduced (bottom) part of the bar and in (B) that the neutral plane separating compressive and tensile stresses is uniform throughout the wafer diameter.

neutral stress plane can be observed to move upward and out of view as voltage is applied to the Rainbow and returns to its original position when the voltage is removed. In reality, the areas appearing white and gray in the above photographs are actually birefringent retardation colors ranging from yellow to red, blue and green as depicted in Fig. 6. A series of color bands are present rather than one uniform color

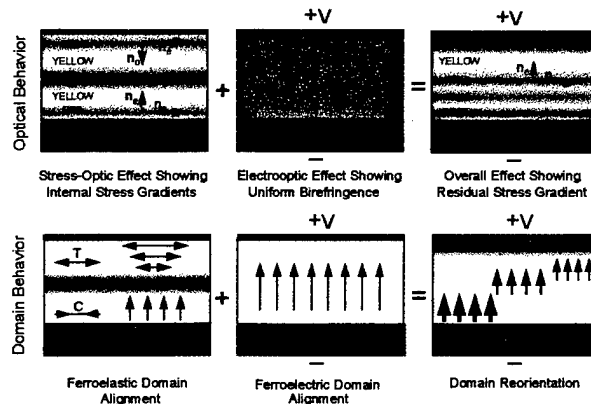


Fig. 6. Stress-optic and electrooptic effects observed in Rainbow ceramics before and during application of voltage.

because the stress (and accompanying strain) is non-uniform, and a stress gradient always exists in a Rainbow. An explanation of what is believed to be occurring in a Rainbow before and during operation is shown in Fig. 6. The top row of Rainbow cross-sections describes the optical behavior, and the bottom row the polarization/domain behavior. The alignment of the domains are a direct result of the Rainbow stresses. Tension toward the top surface aligns the domains (polar axes) parallel to the surface, and compression toward the bottom reduced surface align the domains perpendicular to the surface. When a voltage is applied during operation, the compressively-stressed, perpendicular domains are favored to grow at the expense of the tensionally-stressed, parallel domains; thus leaving the Rainbow in varying degrees of compressive stress which is less than that originally present in the virgin Rainbow. Upon removing the voltage, the original pre-stressed state is restored.

#### D. Stress-Induced Mechanical Properties

It is well known that the pre-stressing of a material can often significantly enhance its mechanical properties and its behavior under service conditions. Notable examples of this effect include the tempering of glass, reinforced concrete, fracture toughening in partially stabilized zirconia (PSZ) and increased chemical durability in compressively stressed glazes on ceramic bodies.

A similar effect has also been observed to occur in pre-stressed ferroelectrics as exemplified by the Rainbow actuators. In these bender-type actuators, it is highly desirable to achieve maximum flexibility in the structure (hence, thinner structure) while still maintaining the highest possible mechanical strength for optimum load-bearing or force-generating properties. Typical values of three-point bending strength and modulus of elasticity for PLZT 9.5/65/35 are given in Table I where normal and Rainbow ceramics are compared. To be noted here is a 55% increase in modulus of rupture accompanied by a 48% decrease in modulus of elasticity. Both of these effects are very desirable for achieving the highest displacements in bending actuators.

TABLE I  
MECHANICAL PROPERTIES OF PLZT RAINBOW CERAMICS

Composition	Reduction Conditions	Modulus of Rupture, MPa	Modulus of Elasticity, MPa
9.5/65/35	as Hot Pressed	87	$10.8 \times 10^4$
9.5/65/35	975°C/60 min.	135	5.6

#### E. Stress-Induced Creep

In super soft, high lead-containing ceramics with point

defects such as exist in the PLZTs ( $\text{Pb}^{+2}$  and  $\text{Zr/Ti}^{+4}$  vacancies), creep at room temperature and also at higher temperatures are issues that need to be addressed. Room temperature creep has not, as yet, received any attention, and high temperature creep has only been dealt with as a means by which it could be used to modify ceramic shapes for conformal piezoelectric patches. Some examples of creep-molded parts which were heat treated at 1100°C for 1 hour are given in Fig. 7. The parts shown in the figure

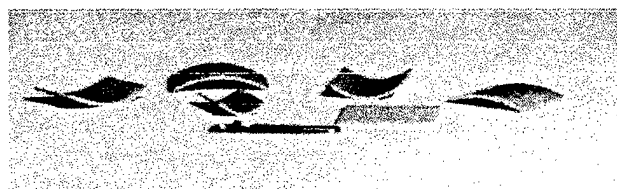


Fig. 7. Examples of PLZT 1/53/47 and 9/65/35 creep-molded ceramics.

possess radii of curvature ranging from 1.25 cm to 12 cm with a thickness of approximately 1 mm.

#### ACKNOWLEDGMENT

This work was supported by NASA and ONR.

#### REFERENCES

- [1] M.E. Lines and A.M. Glass, *Principles and Applications of Ferroelectrics and Related Materials*, Oxford: Clarendon, 1977.
- [2] W.G. Cady, *Piezoelectricity*, New York: McGraw-Hill, 1946.
- [3] H.H. Krueger and D. Berlincourt, "Effects of high static stress on the piezoelectric properties of transducer materials," *J. Acoust. Soc. of Am.*, vol. 33, pp. 1339-1344, 1961.
- [4] H.H. Krueger, "Stress sensitivity of piezoelectric ceramics: Part 1. sensitivity to compressive stress parallel to the polar axis," *J. Acoust. Soc. of Am.*, vol. 42, pp. 636-645, 1967.
- [5] H.H. Krueger, "Stress sensitivity of piezoelectric ceramics: Part 3. sensitivity to compressive stress perpendicular to the polar axis," *J. Acoust. Soc. of Am.*, vol. 43, pp. 583-591, 1968.
- [6] V.A. Isupov, "Some aspects of the physics of piezoelectric ceramics," *Ferroelectrics*, vol. 46, pp. 217-225, 1983.
- [7] H. Arndt, G. Schmidt and N. Vogel, "Influence of uniaxial pressure on the properties of PLZT ceramics," *Ferroelectrics*, vol. 61, pp. 9-18, 1984.
- [8] S.W. Meeks and R.W. Timme, "Effects of one-dimensional stress on piezoelectric ceramics," *J. Appl. Phys.*, vol. 46, pp. 4334-4338, 1975.
- [9] S. Stotz, "Shift of the morphotropic phase boundary in the PZT system under the influence of electric fields and uniaxial stresses," *Ferroelectrics*, vol. 76, pp. 123-132, 1987.
- [10] D. Berlincourt, "Properties of solid solutions of lead titanate - lead zirconate, Clevite Technical Report No. 2, pp. 23-27, May 21, 1956.
- [11] D. Berlincourt, H.H. Krueger and B. Jaffe, "Stability of phases in lead zirconate with variation in pressure, electric field, temperature and composition, *J. Phys. Chem. Solids*, vol. 25, pp 659-674, 1964.
- [12] P.C. Lysne and C.M. Percival, "Analysis of shock-wave-actuated ferroelectric power supplies," *Ferroelectrics*, vol 10., pp. 129-133, 1976.
- [13] G. Schmidt and I. Boczek, "Pseudoelasticity and shape memory of PLZT ceramic, *Phy. Stat. Sol. (a)*, vol. 50, K109-111, 1978.
- [14] T. Kimura, R.E. Newnham and L.E. Cross, "Shape-memory effect in PLZT ceramics," *Phase Transitions*, vol. 2, pp. 113-130, 1981.
- [15] V.K. Wadhawan, M.C. Kemion, T. Kimura and R.E. Newnham, The shape-memory effect in PLZT ceramics," *Ferroelectrics*, vol. 37, pp. 575-578, 1981.
- [16] J.R. Maldonado and A.H. Meitzler, "Strain-biased ferroelectric-photoconductor image storage and display devices," *Proc. IEEE*, vol. 59, pp. 368-382, 1971.

## COMPOSITION AND MICROSTRUCTURE OF CHEMICALLY REDUCED PLZT CERAMICS

G. LI, E. FURMAN and G. H. HAERTLING

*Department of Ceramic Engineering, Clemson University,  
Clemson, South Carolina 29634-0907, USA*

*(Received September 15, 1995)*

Hot-pressed PLZT ceramic wafers were chemically reduced by a special processing technique on one of the major surfaces to form oxide-reduced layer composite structures. Devices based on such structures have promising characteristics for actuator use. The composition and microstructure of the reduced layer from several PLZT ceramics of different compositions as well as the oxide-reduced layer interface were examined and analyzed by means of X-ray diffraction (XRD) and scanning electron microscopy (SEM). A variety of the oxide phases, such as PbO, ZrO<sub>2</sub>, ZrTiO<sub>4</sub>, and LaTiO<sub>3</sub>, were revealed in the reduced PLZT samples by XRD in addition to the anticipated metallic lead phase. SEM micrographs showed that the reduced PLZT ceramics were composed of various fine-grained particles, and the metallic lead formed a continuous phase. It was found that the oxide-reduced layer interface region was composed of a mixture of unreduced and reduced phases. The thickness of the mixed phase region was primarily associated with the grain size of the original unreduced PLZT ceramics.

*Keywords: Ferroelectric ceramic, chemical reduction, microstructure, actuator.*

### 1. INTRODUCTION

A new type of ultra-high-displacement, multi-function actuator, named RAINBOW (Reduced And INternally Biased Oxide Wafer), has recently been developed by using a special processing method. This technique involves chemical reduction of one of the major surfaces of a high lead-containing ferroelectric ceramic wafer by heat treating the wafer on a flat carbon block at an elevated temperature, thus producing a dome-shaped, oxide-reduced layer composite structure. When an electric field is applied across such a composite wafer, large axial displacement is generated. Detailed descriptions of Rainbow ceramics and their potential applications can be found in References 1 and 2. Since the electromechanical properties of a Rainbow actuator are dependent upon the physical properties such as thermal expansion, elasticity, and electrical conductivity of its reduced layer, a thorough investigation of the microstructure of reduced PLZT ceramics is significant for the characterization and application of Rainbow actuators. The PLZT ceramics were chosen for this work because they are easily reduced and have excellent electromechanical characteristics.

The phase components and microstructure of the reduced layer as well as the configuration of the oxide-reduced layer interface for several PLZT Rainbow samples have been investigated by means of X-ray diffraction technique and scanning electron microscopy.

### 2. SAMPLE PREPARATION AND EXPERIMENTAL PROCEDURES

The Rainbow samples used were prepared from PLZT ceramics 1.0/53/47, 5.5/57/43 and 9.5/65/35, where the numbers denote the atom ratios La/Zr/Ti of the PLZT

compositions. Conventional processing techniques combined with hot-pressing were employed to produce highly dense PLZT slugs. The ceramic wafers obtained from the PLZT slugs were chemically reduced by placing them on a graphite block and heat treating them under the conditions of 975°C/60 min (reduction temperature/time).

Fractured, polished, and etched surfaces of the samples were used in both XRD and SEM analyses. For X-ray diffraction, the reduced side of the Rainbow samples were lapped off approximately 50  $\mu\text{m}$  and slightly polished to expose the internal structures. This procedure was employed because a thin reoxidized layer is often formed on reduced surfaces during processing. X-ray diffraction was first performed on the polished surfaces. Then, the same surfaces were etched with an HCl/HF solution for further study. X-ray diffraction patterns of fractured surfaces were obtained from the powders prepared by crushing the completely reduced PLZT wafers.

Cross-sectional surfaces of the Rainbow samples were usually used for the SEM analysis in this study. The fractured surfaces were obtained by breaking the Rainbow along their diameters. The surfaces were also polished by using progressively finer diamond pastes with a finish of 0.25  $\mu\text{m}$ . The polished surfaces were then etched, cleaned, and coated with a carbon or gold film before examination. In some cases, the polished surfaces were directly examined under SEM.

All of the X-ray diffraction experiments were performed on an X-ray diffractometer (Scintag XDS 2000™) with Cu K $\alpha$  radiation at a scan rate of 2 degrees per minute. A JOEL scanning electron microscope operating at an accelerating voltage of 15 keV was used for the SEM analyses.

### 3. EXPERIMENTAL RESULTS

#### 3.1 X-Ray Diffraction Analysis

Figures 1(a)–1(c) show the X-ray diffraction patterns from the polished surface of the reduced layer of Rainbow samples 1.0/53/47, 5.5/57/43 and 9.5/65/35, respectively. The Rainbow samples in this work are indicated by their original PLZT composition; for example, Rainbow 10/53/47 represents a sample produced from PLZT 1.0/53/47 wafer. It was found that in all cases the strongest peaks in the diffraction patterns were produced by the metallic lead phase. The remaining weaker peaks were caused by a number of oxide phases formed during the reduction process. The number and composition of the phases observed in the reduced PLZT ceramics were dependent on the unreduced PLZT compositions. As is indicated in the figures, the oxide phases identified include PbO (litharge),  $\text{ZrO}_2$ ,  $\text{ZrTiO}_4$ ,  $\text{TiO}_2$ ,  $\text{LaTiO}_3$ , and  $\text{La}_{0.66}\text{TiO}_{2.993}$  (JCPDS 26-827).

The X-ray diffraction pattern of the etched reduced surface of Rainbow 5.5/57/43 is given in Figure 2. It can readily be seen by comparing Figure 2 with Figure 1(b) that, upon etching, almost all of the Pb peaks were greatly depressed while those of the oxide phases underwent little change. This result suggests that it is primarily the Pb phase that was etched away from the surface.

It should be noted that the intense diffraction peaks of the Pb phase shown in Figures 1(a)–1(c) may partly result from the grinding and polishing treatments on

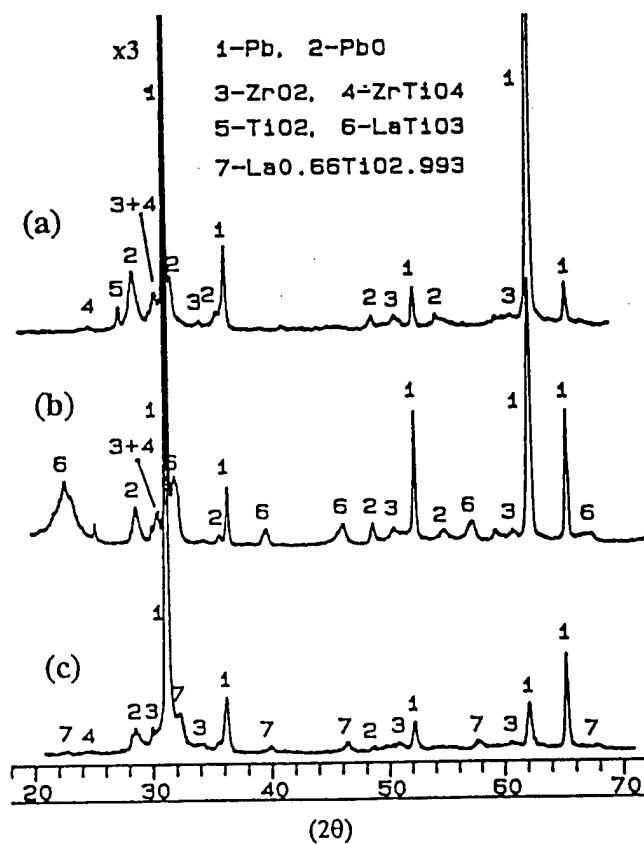


FIGURE 1 X-ray diffraction patterns from the polished surface of the reduced layer of Rainbows (a) 1.0/53/47, (b) 5.5/57/43 and (c) 9.5/65/35.

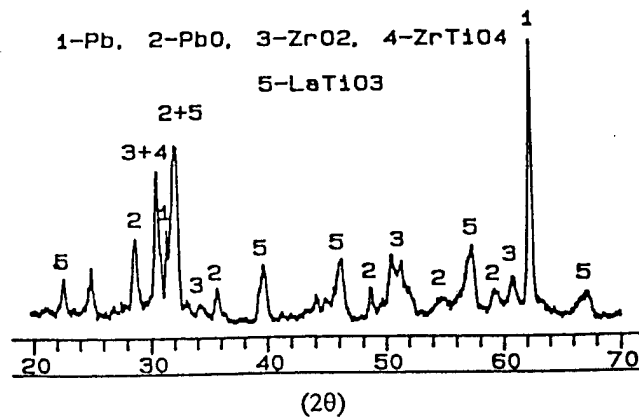


FIGURE 2 X-ray diffraction pattern from etched reduced surface of Rainbow 5.5/57/43.

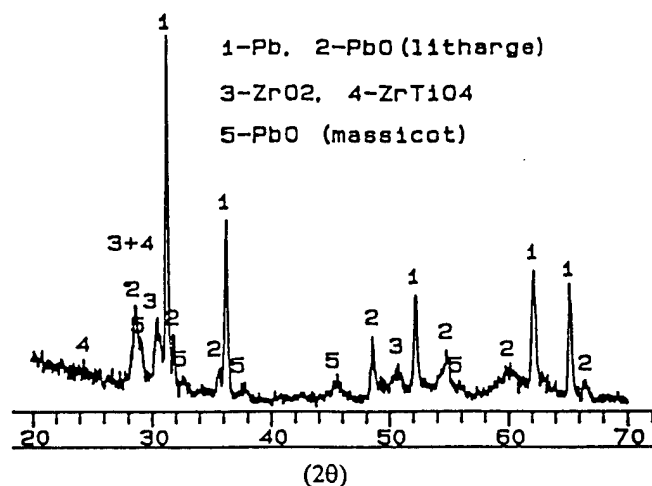


FIGURE 3 X-ray diffraction pattern of the powder obtained from reduced PLZT 1.0/53/47 sample.



FIGURE 4 SEM micrograph of fractured cross-sectional surface of Rainbow 1.0/53/47 near the PLZT-reduced layer interface.

the sample surfaces prior to analysis. Since the metal Pb is a very soft material relative to the oxide phases, when a reduced sample is ground or polished, the Pb phase is deformed and smeared over the surface. Consequently, the relative amount of Pb phase on the surface is increased, thereby enhancing the intensity of the Pb diffraction peaks.

For this reason, the X-ray diffraction of fractured surfaces better reflects the actual states of the various phases in a sample. Since it is difficult, in practice, to obtain a large fracture surface of the reduced layer, the powders from completely reduced wafers which contain various small fracture surfaces were used instead. The diffraction pattern of such powder for Rainbow 1.0/53/47 is shown in Figure 3. As can be seen, the intensity ratios of the major metallic lead peaks to the oxide phase peaks are considerably reduced compared to those of the polished surface shown in Figure 1(a), indicating the presence of smearing in the polished samples. It is, however, worth noting that the Pb diffraction peaks from the powder remain the strongest,



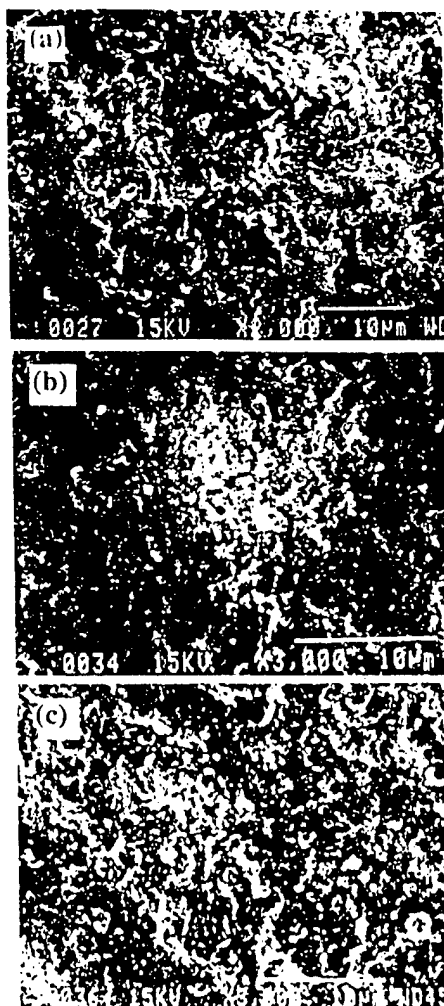


FIGURE 5 SEM micrograph of the reduced layer of Rainbows (a) 1.0/53/47, (b) 5.5/57/43 and (c) 9.5/65/35.

and this is also true for the other PLZT Rainbow samples studied. Figure 3 also shows the existence of PbO (massicot) phase which was not observed in Figures 1(a)–1(c).

### 3.2 SEM Analysis

Figure 4 shows the SEM micrograph of the fractured cross-sectional surface of Rainbow 1.0/53/47. The upper portion of the micrograph shows the PLZT layer, and the lower portion is the reduced layer. These layers are separated by a PLZT-reduced layer interface where both the unreduced and reduced phases were found. A micrograph of higher magnification on the reduced region, which is given in Figure 5(a),

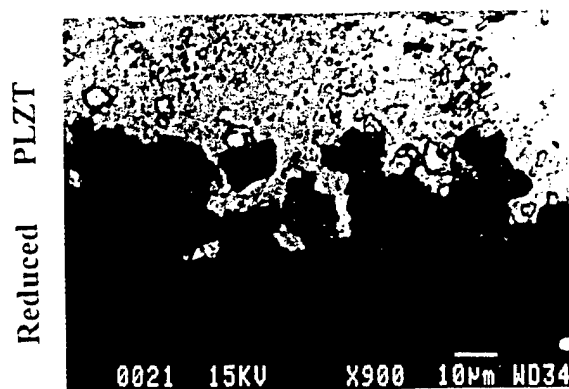


FIGURE 6 Backscattered electron image of Rainbow 1.0/53/47 near the PLZT-reduced layer interface.

indicates that the region was composed of various fine-grained particles. A similar microstructure was also observed in Rainbows 5.5/57/43 and 9.5/65/35, as is shown in Figures 5(b) and 5(c) respectively. The small uniformly distributed particles, about  $0.2\ \mu\text{m}$  in diameter, as can be seen in the figures, were identified to be the Pb grains by means of X-ray diffraction coupled with an extraction technique. The microstructure of the reduced layer seems relatively insensitive to the microstructure of the original PLZT composition.

The secondary electron image of a polished surface of the reduced layer is usually featureless. It was, however, found that some characteristics of the polished surfaces can be revealed via a backscattered electron imaging technique. Figure 6 is a backscattered electron image of Rainbow 1.0/53/47 near the PLZT-reduced layer interface. Again the lower portion is the reduced layer. The darkest areas seen in Figure 6 are most likely the thoroughly reduced regions. This is because the reduction process leads to a relatively loose structure by decomposing the original dense PLZT phase with an accompanying oxygen loss, thereby contributing less to the backscattered electron signals. From the morphology of the oxide-reduced layer interface it can be deduced that the reduction reaction was initiated along the PLZT grain boundaries and then proceeded toward the center of the grains.

The SEM image of the etched reduced surface of Rainbow 5.5/57/43, whose X-ray diffraction pattern has been given in Figure 2, is displayed in Figure 7. The grains exposed by etching, which can be seen in Figure 7, are considered to be the oxide phases identified in the corresponding X-ray diffraction pattern. The fact that the oxide grains appear isolated indicates that the Pb grains, which were mostly etched away from the surfaces, form a continuous phase. The continuity of the lead phase is further supported by high electrical conductivity of the reduced layers.

#### 4. DISCUSSION

The results of the aforementioned X-ray diffraction analyses indicate that a number of different phases are produced as a result of the chemical reduction of a PLZT ceramic in forming the Rainbow structure. The phases found include the metallic lead phase and seven oxide phases: PbO (litharge), PbO (massicot),  $\text{ZrO}_2$ ,  $\text{ZrTiO}_4$ ,

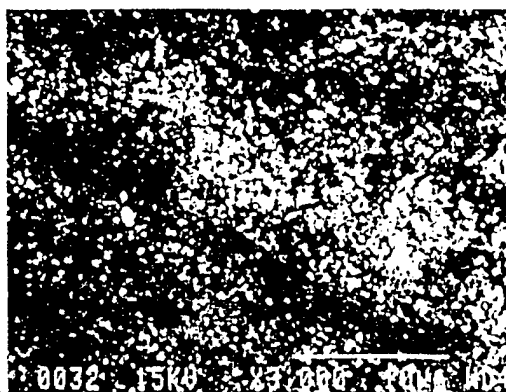


FIGURE 7 SEM micrograph of etched reduced layer of Rainbow 5.5/57/43.

$\text{TiO}_2$ ,  $\text{LaTiO}_3$  and  $\text{La}_{0.66}\text{TiO}_{2.993}$ . The original PLZT phase was not observed in the reduced samples. It is noted that while the exact number and composition of the phases in a particular reduced PLZT sample depend on the original PLZT composition, the phases of Pb, PbO (litharge),  $\text{ZrO}_2$  and  $\text{ZrTiO}_4$  are common among the samples studied.

Many investigations of chemical reduction of ferroelectric materials were concerned with the influence of reduction atmosphere on the electrical and optical properties of the materials.<sup>3-7</sup> In these studies, defects, generally vacancies, were introduced into the crystal lattice during chemical reduction, but the framework of the crystal structure underwent no substantial changes. Current work dealt with intense chemical reduction of high-lead containing ferroelectric ceramics in which the original crystal structure was completely destroyed. In his investigation of PLZT ceramics reduced by graphite blocks,<sup>8</sup> Haertling showed that the reduction reaction is accomplished via the interaction between carbon monoxide and loosely held oxygen atoms in the PLZT perovskite lattice. It is therefore considered that, except for the oxygen and slight Pb losses during reduction, the reduced layer should contain the same amount of chemical elements as the unreduced PLZT ceramic. In other words, the chemical reduction simply decomposes the PLZT crystal structure by attacking the lattice oxygen ions and, at the same time, produces new phases by rearranging the constituent elements.

Based on this consideration, the volume fraction of the lead phase in a reduced PLZT sample may not be as large as it seems in the X-ray diffraction as, for example, shown in Figure 3. This is reasonable since along with the volume fraction of each phase many other factors may contribute to the relative peak intensities of the X-ray diffraction pattern in a multiphase material. In fact, for the conceivable uses of Rainbow actuators, it is not critical whether the Pb phase is dominant or not. The main concern is that the Pb phase must be a continuous phase so that the reduced layer has good conductivity. The fact that the metallic lead in the reduced layer occurs with very fine particles, as was shown in the SEM micrographs, suggests that even a small volume fraction of lead phase can render the reduced layer electrically conductive. This may explain why the reduced PLZT ceramic exhibits excellent conductivity.

There is a region along the PLZT-reduced layer interface where both PLZT and

reduced phases exist. The dimension (normal to the interface) of the region is defined as the thickness of the interface in a Rainbow. It was found that the interface thickness was related to the grain size of the phase before reduction. This is easily understood considering that the reduction process is initialized along grain boundaries as illustrated in Figure 6. For Rainbow 1.0/53/47, whose PLZT layer displays a larger grain size, the thickness was found to be approximately 20  $\mu\text{m}$ . Rainbows 5.5/57/43 and 9.5/65/35 have an interface thickness of about 2  $\mu\text{m}$  and 5  $\mu\text{m}$ , respectively. The configuration of the PLZT-reduced layer interface is probably important for some specific properties of Rainbow actuators such as fatigue and loading capability and will be investigated further.

## 5. SUMMARY

A number of different crystalline phases have been found in the PLZT ceramics reduced via the RAINBOW process. The phases found include metallic lead and seven oxide phases: PbO (litharge), PbO (massicot),  $\text{ZrO}_2$ ,  $\text{ZrTiO}_4$ ,  $\text{TiO}_2$ ,  $\text{LaTiO}_3$  and  $\text{La}_{0.66}\text{TiO}_{2.993}$ . The original PLZT phase was not observed. While the exact number and composition of the phases for a particular reduced sample are dependent on the PLZT composition, the phases of Pb, PbO (litharge),  $\text{ZrO}_2$  and  $\text{ZrTiO}_4$  are commonly observed, with the Pb phase producing the strongest X-ray diffraction.

The reduced PLZT ceramics are composed of various fine-grained particles, and the smallest grains, about 0.2  $\mu\text{m}$ , correspond to the lead phase. This microstructural characteristic is relatively insensitive to the PLZT composition. It is shown that the metallic Pb grains constitute a continuous phase in the reduced PLZT ceramics, which is consistent with the good electrical conductivity of these materials.

Near the interface between the PLZT and reduced phases of a Rainbow, the two phases coexist. The thickness of the interface was found to be associated with the grain size of the PLZT phase. The values of the interface thickness for Rainbows 1.0/57/43, 9.5/65/35 and 5.5/57/43 are approximately 20, 4, and 2  $\mu\text{m}$ , respectively.

## ACKNOWLEDGEMENT

This work was supported by NASA under grant No. NAG-1-1301.

## REFERENCES

1. G. H. Haertling, *Bull. Am. Ceram. Soc.*, **73**, 94 (1994).
2. E. Furman, G. Li and G. H. Haertling, *Ferroelectrics*, **160**, 357 (1994).
3. S. Ikegami and I. Ueda, *J. Phys. Soc. Jpn.*, **19**, 159 (1964).
4. S. Ducharme and J. Feinberg, *J. Opt. Soc. Am.*, **B**, **3**, 283 (1986).
5. N. P. Rajopadhye, S. V. Bhoraskar, S. Badrinarayan and A. P. B. Sinha, *J. Mat. Sci.*, **23**, 2631 (1988).
6. A. Dhar and A. Mansingh, *J. Phys. D: Appl. Phys.*, **24**, 1644 (1991).
7. S. M. Mukhopadhyay and T. C. S. Chen, *J. Mat. Res.*, **10**, 1502 (1995).
8. G. H. Haertling, in Proceedings of 4th International SAMPE Electronics Conference (Society for the Advancement of Materials and Process Engineering Covina, GA), Vol. 4, p. 699, 1990.

## THICKNESS DEPENDENT PROPERTIES OF ACETATE-DERIVED PLZT FILMS

GENE H. HAERTLING

Clemson University, Clemson, SC, 29634-0907

*(Received March 18, 1996; in final form August 15, 1996)*

**Abstract** The present trend in ferroelectric memories toward lower operating voltages, and consequently, thinner (less than 0.3  $\mu\text{m}$ ) films is offset by other applications requiring thicker films in the range of 5 to 25  $\mu\text{m}$ . This wide range of film thicknesses imposes significantly different restraints on the films and their properties. The present investigation involved a study of selected properties of acetate-derived, multiply dip-coated PLZT films ranging in thickness from 0.3  $\mu\text{m}$  to 11.5  $\mu\text{m}$ . Films were deposited on Ag and Pt/Si substrates via a dip coating process and subsequently sintered at a temperature of 700°C for 3 minutes. Various properties (film smoothness, dielectric constant, hysteresis loop characteristics, etc.) of the films were determined as a function of film thickness. Coercive field was examined in more detail over the thickness range from 0.3  $\mu\text{m}$  to bulk material.

## INTRODUCTION

Ferroelectric ceramic films are now emerging as a truly viable class of materials for a variety of electronic and electrooptic applications ranging from integrated DRAMs and non-volatile memories to discrete sensors, actuators, resonators and optical modulators. Of these, the trend in DRAMs and memories is toward lower operating voltages, and consequently, thinner (less than 0.3  $\mu\text{m}$ ) films; whereas, many of the other applications require thicker films in the range of 5 to 25  $\mu\text{m}$  and utilize somewhat higher voltages. Traditionally, this latter group of applications have always been served by bulk materials which were thinned by various means to the appropriate thickness. There is, however, a practical limit to such bulk thinning techniques for free-standing elements at approximately 50  $\mu\text{m}$ , thus leaving a thickness gap between the films and bulk.

There are good reasons to believe that the gap between the bulk materials and thin films will eventually be filled with materials suitably designed and appropriately processed. Indeed, the difficulty in fabricating films in this thickness range is the primary reason for their notable lack of availability. Previous investigators have employed multiple dip coating, multiple spin coating and chemical vapor deposition techniques with limited success on films up to 25  $\mu\text{m}$  in thickness.<sup>1-3</sup> From experience, one quickly learns that films thicker than about 2 or 3  $\mu\text{m}$ , which have been prepared via solution deposition techniques, have a tendency to undergo cracking, debonding from the substrate, loss of transparency and/or increased surface roughness; any one of which will, most often, render the film useless. Recognizing that this thickness range is a problem in regard to materials fabrication, it still holds promise as a fruitful area of research since it is generally recognized that certain phenomena such as electromechanical (piezoelectricity)

and electrooptic effects could be profitably applied to devices within this range.

Bulk PLZT electrooptic shutter and modulator ceramics, for example, are expensive because they must be fabricated fully dense and transparent; and then sliced, lapped, polished and annealed in order to be acceptable for use in optoelectronic devices. Thin films, on the other hand, are considerably faster, easier and less costly to prepare; but they are too thin to achieve the necessary optical retardation required for transverse-mode devices. Hence, the need arises for the development of suitable techniques for preparing high quality "thick" thin films for both large and small area applications.

For want of a better term, solution-derived films within the range of 5 to 25  $\mu\text{m}$  are referred to as thick films, as are also the more conventional hybrid microelectronic thick films which are fabricated from polymer-suspended ceramic powders using screen printing techniques; however, one should not confuse these two basically different approaches to the problem. In the former case, the resulting films are usually transparent and may be oriented to a considerable degree, whereas in the latter case, the films are translucent-to-opaque and randomly oriented. While most investigators have chosen to use modified thin film techniques in order to achieve the thicker films, Chen and co-workers<sup>4</sup> were also successful in producing PZT films in the range of 12  $\mu\text{m}$ , using a screen printing technique.

Since much of the information already reported on the characteristics of thin films leads one to believe that thin films are substantially the same as the bulk (e.g., polarization, dielectric constant and phase stability) with the exception of the influence of the substrate (e.g., stress and chemical interaction), the object of this investigation was to study the thickness dependence of the properties of a soft ferroelectric composition such as PLZT in the range from submicron to greater than 10  $\mu\text{m}$ . This was an attempt to bridge the property gap between thin films and bulk materials, and hopefully, demonstrate a continuity between the two. Of particular interest was coercive field since  $E_c$  values for films reported in the literature are always substantially higher than those of the bulk.

## EXPERIMENTAL

A morphotropic phase-boundary PLZT composition, 1/53/47 (La/Zr/Ti), was chosen for this investigation. A stock solution for this MOD process was prepared by weighing the required amounts of acetate precursors of lead, lanthanum, zirconium and titanium and mixing them together with the appropriate amount of methyl alcohol for viscosity control. This simple operation yielded a clear, light-yellow solution which was water soluble and stable for long periods of time. Details on the acetate process are given in previously published work.<sup>5</sup> The solution was then deposited on the selected substrate via automatically controlled dipping and withdrawal operations. Drying occurred in a matter of a few seconds, immediately followed by the introduction of the coated substrate into a furnace preheated to the sintering temperature of 700°C. Multiple dipping, drying, sintering and cooling cycles were automatically performed in a hands-off environment as shown in Figure 1. At the dilution ratio selected, individually dipped layer thicknesses were approximately 0.3  $\mu\text{m}$  per layer, yielding films as thick as 12  $\mu\text{m}$

1/3 rpm Motor Driven Rotor

Roller Guides

1700°C

Kanthal Furnace

Substrate

Solution

FIGURE 1. Thin/thick film automated dipping apparatus.

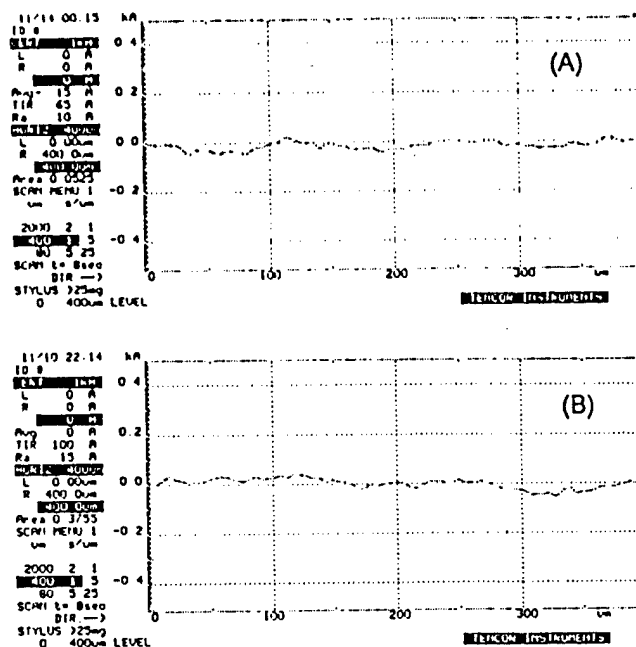


FIGURE 2. Examples of surface finish for (A) Si/Pt wafer and (B) 20 layer, 3.8  $\mu\text{m}$  thick, acetate-derived PLZT 1/53/47 film deposited on Pt/Si.

For the dielectric and hysteresis loop measurements on the films, top copper electrodes, one mm diameter, were deposited through a mask via vacuum evaporation. Fired-on Ag electrodes were used on the bulk samples. Small-signal dielectric measurements consisting of capacitance and dissipation factor were carried out on a digital LCR meter at 1 kHz. Hysteresis loops (P vs. E) were measured on films using a modified Sawyer-Tower circuit at a driving signal of  $\pm 100$  volts and a frequency of 1 kHz. All samples were tested to a voltage which was approximately three times  $E_c$ . The loop data were photographically recorded by means of an oscilloscope readout, although selected loops on the bulk material were also obtained from a Radiant Technology RT66A tester equipped with a high voltage interface which was capable of  $\pm 4000$  volts.

## RESULTS AND DISCUSSION

### Relative Dielectric Constant

The relative dielectric constants of the PLZT 1/53/47 films deposited on Ag and Pt/Si showed strikingly different behavior as a function of thickness. As shown in Figure 3, the Ag-substrate dielectric constant exhibited only a slightly increasing dependence on film thickness, from 550 to 645, in the thickness range from 0.3  $\mu\text{m}$  to 8  $\mu\text{m}$ , whereas the Pt/Si-substrate dielectric constant significantly increased in value from 500 to 1320 throughout this same thickness range. Considering that the bulk value was measured at 1161, these results indicate that the substrate and its effect on internal stress and domain alignment in the films has a significant influence on this small-signal property. It is now well known that high thermal expansion substrates such as Ag and MgO ( $\alpha = 18 \times 10^{-6}/^\circ\text{C}$  and  $12 \times 10^{-6}/^\circ\text{C}$ , respectively) put the PZT film ( $\alpha = 5.5 \times 10^{-6}/^\circ\text{C}$ ) in compression thereby producing mainly c-oriented domains of lower dielectric constant, whereas a low thermal expansion substrate such as Si ( $\alpha = 2.3 \times 10^{-6}/^\circ\text{C}$ ) does just the opposite in producing mainly a-oriented domains of higher dielectric constant.<sup>6,7</sup> Under these circumstances, these results are quite understandable. Previous work has confirmed similar findings specifically for PLZT films on Ag and Pt/Si substrates.<sup>8</sup>

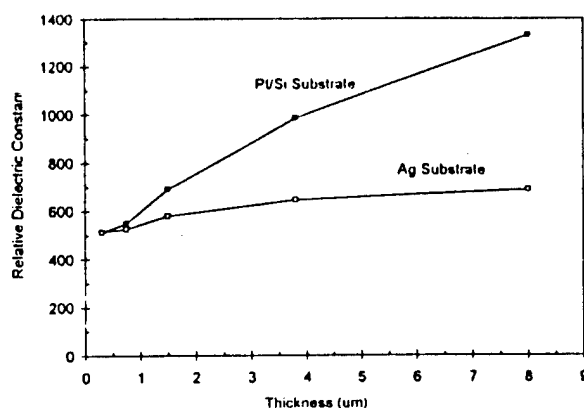


FIGURE 3. The effect of film thickness on relative dielectric constant for PLZT 1/53/47 films on Pt/Si substrates.



### Hysteresis Loop Characteristics

Selected hysteresis loops for films deposited on both Pt/Si and Ag substrates are shown in Figure 4. All of the loops were taken to a voltage of approximately three times  $E_c$  for

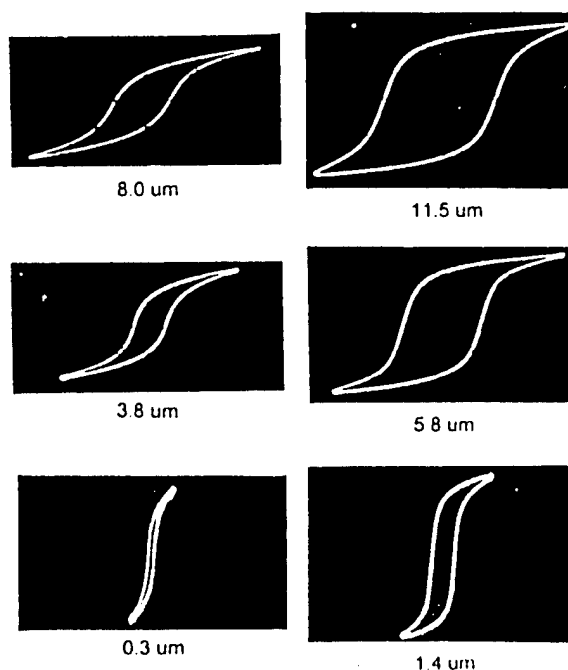


FIGURE 4. Hysteresis loops of PLZT 1/53/47 films multiply dip-coated to the indicated thicknesses on Pt/Si (left column) and Ag (right column) substrates. (Y axis = 15  $\mu\text{C}/\text{cm}^2$  and X axis = 20 V/div.)

the particular film thickness. The most noticeable characteristics of these loops is the more rounded appearance and lower  $P_R$  of the Pt/Si loops as compared to those on Ag which are more square and of higher value. These values can be compared in Figure 5.

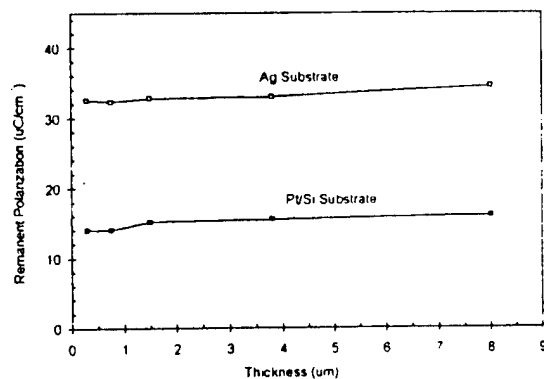


FIGURE 5. The effect of film thickness on  $P_R$  for PLZT 1/53/47 on Ag and Pt/Si.

One can easily see in this figure that the Ag substrates produce films with substantially higher  $P_R$  values (approx.  $32 \text{ uC/cm}^2$ ) than do the Pt/Si substrates (approx.  $15 \text{ uC/cm}^2$ ); and furthermore, the values are relatively constant throughout the film thickness range. As mentioned in the case of dielectric constant, it is believed that film stress is again the primary cause of this effect since the Ag-substrate, c-oriented domains are non-strain producing entities and switch more easily with higher total polarization than the Pt/Si-substrate, a-oriented domains which involve strain during switching. In fact, on Pt/Si the tensile stress significantly suppresses switching in the thickness direction while on Ag the compressive stress enhances switching in the thickness direction. A comparative value of remanent polarization for the randomly oriented, bulk material is  $40 \text{ uC/cm}^2$ .

As was just shown, and other investigators have previously reported, it is relatively easy to obtain bulk-type values of  $P_R$  from films when they are appropriately stressed or even when they are in a stress-free condition; however, this is not the case in regard to  $E_c$ . All reported values of  $E_c$  for films are substantially higher than corresponding values for the same composition in bulk form. The data presented in Figure 6 also bear this out, where

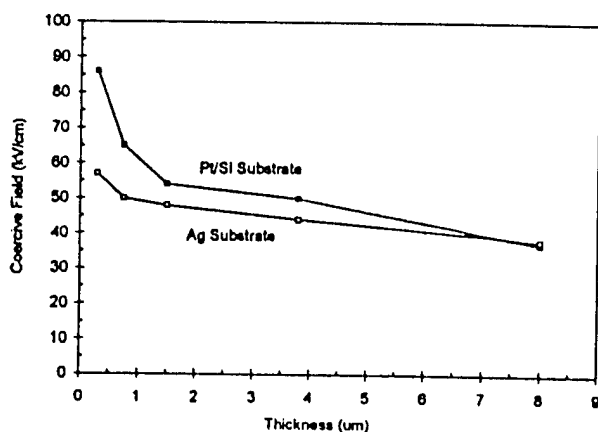


FIGURE 6. The dependence of  $E_c$  on film thickness for PLZT 1/53/47 on Pt/Si and Ag substrates.

a highly nonlinear relationship is observed between  $E_c$  and film thickness. Values of  $E_c$  approach 90 kV/cm for films on Pt/Si and 60 kV/cm for Ag substrates. This same data, plotted on a thickness scale large enough to include a bulk material value, is given in Figure 7 along with an equation for the curve; i.e.,  $E_c = t^{-0.25}$ . Although it not yet known what the significance of this thickness exponent is, the fact that a curve such as this can fit the data adequately may well indicate a continuum of  $E_c$  values for films as a function of thickness rather than a discontinuity between the films and the bulk material.

With the thought in mind that there existed a continuum of  $E_c$  values between films and the bulk, it was postulated that the thickness effect should also be observed in the bulk material, albeit, on a much smaller scale. The data obtained on hot-pressed samples with thicknesses ranging from 0.25 to 1 mm, are shown in Figure 8. Here it can be seen

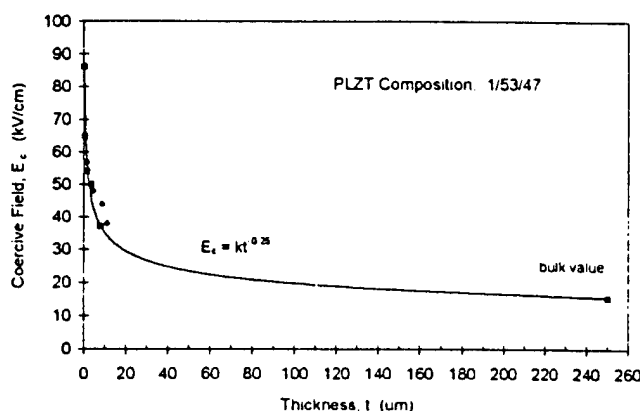


FIGURE 7. The thickness dependence of  $E_c$  for PLZT 1/53/47 (curve extended to bulk value, squares = Pt/Si and diamonds = Ag substrate).

that a definite trend exists even in the bulk for both small and large grain size material, and furthermore, the higher  $E_c$  values are associated with the thinner samples, as one

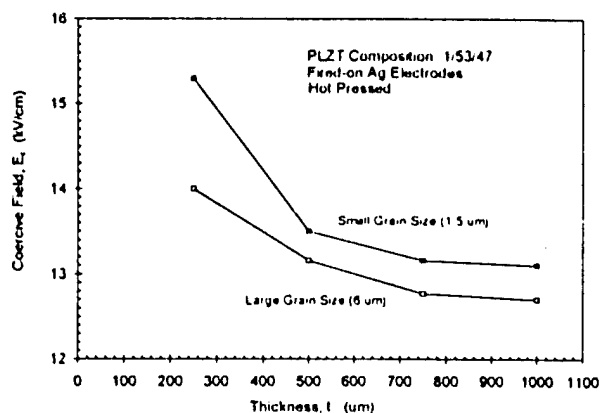


FIGURE 8. The dependence of  $E_c$  on wafer thickness for bulk PLZT 1/53/47

would predict. A similar dependence of  $E_c$  on thickness for a bulk ferroelectric (TGS) was reported many years ago (1962) by Kay and Dunn.<sup>9</sup>

A replot of this data on a log-log scale, along with the film data, yielded the information shown in Figure 9. Here it can be seen more clearly that a single relationship (and perhaps, a single dominant mechanism or condition) may describe the behavior of all of the data obtained from the films in the present study. Understanding the basic cause or causes for this behavior has yet to be determined, however, a more thorough investigation of this effect was beyond the scope of the present work.

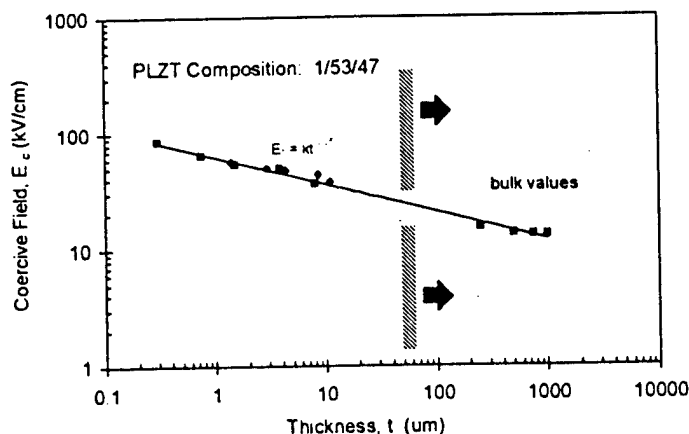


FIGURE 9. Log-log plot of  $E_c$  vs.  $t$  over the thickness range from thin films (0.3 μm) to bulk material (1000 μm).

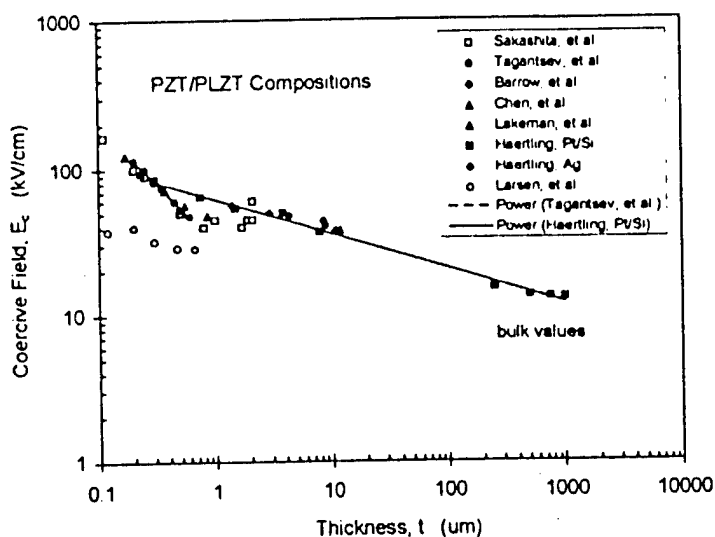


FIGURE 10. Thickness dependence of  $E_c$  for a variety of PZT and PLZT materials studied by the indicated investigators over the thickness range from 0.1 μm to 1 mm.

Although the same general trends just mentioned can also be seen in work reported by previous investigators, the situation, in this case, is not nearly so clear.<sup>2,3,4,10-12</sup> In a similar log-log plot of all data (including that of the present study) as shown in Figure 10, it can be seen that a wider range of  $E_c$  values have been obtained over a narrower range of thicknesses than in the present study. In fact, no single relationship appears to be able to describe the behavior, especially when one considers the data of Larsen, et al.<sup>12</sup> Possible reasons for this result are still not adequately understood, even in the

truly thin film region where thicknesses are less than 1  $\mu\text{m}$ . Although several mechanisms or conditions have been proposed such as a dielectric interfacial layer, stress, a depletion layer, space charge, nucleation effects and possible combinations of these, better designed and more controlled experiments are still needed in order to bring order out of the present chaos. Tagantsev and co-workers<sup>13</sup> have devoted a substantial amount of work and attention to this problem with considerable success; however, their conclusion that a limiting value of  $E_c$  is already achieved at only modest thicknesses of approximately twice the depletion layer thickness (approximately 0.5  $\mu\text{m}$ ) does not agree with the results of the present investigation. Obviously, additional work needs to be done in order to solve the problem; and in doing so, we may finally bridge the gap between the films and bulk material.

### CONCLUSIONS

1. PLZT films with bulk-like properties were obtained from multiply dip-coated Ag and Si/Pt substrates prepared via the water-soluble, acetate MOD process. Thicknesses of the films ranged from 0.3  $\mu\text{m}$  to 11.5  $\mu\text{m}$ .
2. The average surface roughness of a 3.8  $\mu\text{m}$  (20 layer) thick film on Pt/Si was 100 angstroms (0.4 microinches).
3. Relative dielectric constants were observed to increase to bulk values as a function of increasing film thickness for the film on Pt/Si; the differences between Ag and Pt/Si substrate results are believed to be due to differing stresses in the films.
4. Remanent polarization values remained relatively constant at 32  $\mu\text{C}/\text{cm}^2$  throughout the film thickness range.
5. Coercive field was found to decrease as a function of film thickness according to the relationship:  $E_c = t^{-0.25}$  kV/cm. The reason for this behavior is not yet known.
6. Bulk material of the same composition (PLZT 1/53/47) was also found to exhibit a changing  $E_c$  as a function of thickness, varying from 14.0 to 12.7 kV/cm in the thickness range of 0.25 mm to 1 mm, respectively, for the large grain size (6  $\mu\text{m}$ ) material; and from 15.3 to 13.1 kV/cm over the same thickness range for the small grain size (1.5  $\mu\text{m}$ ) material.

### ACKNOWLEDGMENT

This work was supported by ONR under Grant No. N00014-94-1-0563.

### REFERENCES

1. G.H. Haertling, *Integrated Ferroelectrics*, **3**, 207 (1993).
2. Y. Sakashita, H. Segawa, K. Tominaga and M. Okada, *J. Appl. Phys.*, **73**, (11) 7857 (1993).
3. D.A. Barrow, R. Noteboom and M. Sayer, *Integrated Ferroelectrics*, **8**, 1 (1995).